Probing topological properties of Bloch bands with ultracold atoms in a honeycomb optical lattice

Lucia Duca

München, 2015

Probing topological properties of Bloch bands with ultracold atoms in a honeycomb optical lattice

Lucia Duca

Dissertation
an der Fakultät für Physik
der Ludwig–Maximilians–Universität
München

vorgelegt von
Lucia Duca
aus Ancona, Italien

München, Juli 2015

Erstgutachter: Prof. Dr. Immanuel Bloch

Zweitgutachter: Prof. Dr. Wilhelm Zwerger

Tag der mündlichen Prüfung: 18 September 2015

Zusammenfassung

Vor über 30 Jahren beschrieb Berry die Effekte, die durch die geometrische Struktur des Hilbertraums auf die adiabatische Bewegung quantenmechanischer Systeme wirken. Seit dem hat das Konzept der geometrischen Phasen, die mit der adiabatischen Bewegung verbunden werden sogenannten Berry-Phasen in einer grossen Anzahl physikalischer Systeme Anwendung gefunden. In der Festkörperphysik sind analoge topologische Eigenschaften von Bändern für eine Vielzahl von Vielteilcheneffekten verantwortlich, zum Beispiel für den ganzzahligen Quanten-Hall-Effekt und die Existenz robuster leitender Randzustände in topologischen Isolatoren. Die Berry-Krümmung, jener Parameter der die Geometrie der Eigenzustände der Bänder beschreibt, ist von fundamentaler Bedeutung für die Charakterisierung physikalischer Eigenschaften von Elektronenzuständen in der Festkörperphysik und bestimmt die topologische Invariante eines Bandes, die sogenannte Chern-Zahl. Obwohl die Berry-Phase und die Berry-Krümmung eine zentrale Rolle in der Bestimmung topologischer Eigenschaften von Bändern spielen, bleibt die Messung der kompletten geometrischen Struktur eines Bandes eine grosse experimentelle Herausforderung.

Diese Arbeit berichtet über die experimentelle Realisierung eines hexagonalen optischen Gitters für ultrakalte Atome, dessen Eigenschaften denen von Graphen ähneln. Diese Gitterstruktur besitzt eigenartige topologische Merkmale, die mit den konischen Schnittpunkten zweier Bänder, den sogenannten Dirac-Punkten, in Verbindung stehen. Die topologischen Eigenschaften eines Bloch-Bandes manifestieren sich, wenn ein Teilchen adiabatisch in einem geschlossenen Kreis im Impulsraum um einen solchen konischen Schnittpunkt zweier Bänder des Energiespektrums bewegt wird. Analog zum Aharonov-Bohm-Effekt, bei dem ein Elektron durch die Bewegung um eine Zylinderspule einen Phasenversatz erhält, erhält ein Teilchen bei dieser Bewegung eine geometrische Phase. Diese Arbeit präsentiert eine interferometrische Technik zur Detektion der topologischen Eigenschaften dieser Kegel sowie der Verteilung der Berry-Krümmung im reziproken Raum mit einer hohen Quasiimpulsauflösung.

Im ersten Teil dieser Arbeit werden das hexagonale Gitter sowie der experimentelle Aufbau zum Erzeugen eines Gases ultrakalter Atome erläutert. Dann wird analog zum Aharonov-Bohm-Effekt ein interferometrisches Protokoll für ultrakalte Atome im reziproken Raum entwickelt, mit dem die mit den Dirac-Kegeln assoziierte geometrische Phase detektiert werden kann. Diese interferometrische Technik kombiniert die Bewegung der Atome im Band mit Spin-Echo-Interferometrie und erlaubt die Charakterisierung topologischer Eigenschaften des untersten Bandes im optischen Gitter durch Bestimmung der räumlichen Verteilung der Berry-Krümmung eines einzelnen Dirac-Kegels. Der detektierte, scharfe Phasensprung von π und die starke Reduktion des Interferenzkontrasts am Dirac-Kegel demonstrieren die nichttriviale Verwindung der Bandeigenzustände und die starke Lokalisierung der Berry-Krümmung an den Kegeln. Des Weiteren wird die Interferometrie dazu genutzt

die Bewegung im reziproken Raum und die Annihilation der topologischen Eigenschaften durch ein unausgeglichenes Gitter zu detektieren. Das beobachtete Verschwinden der π Berry-Phase demonstriert den übergang zu einer topologisch trivialen Bandstruktur.

Der letzte Abschnitt dieser Arbeit präsentiert vorläufige Ergebnisse zur Interferometrie in den untersten beiden Bändern des Gitters. Die Stückelberg-Interferometrie, realisiert durch die diabatische Bewegung der Atome im reziproken Raum, wird dazu genutzt, die Dispersion der Bänder zu bestimmen und die Symmetrie der Bandeigenzustände zu erforschen. Erweiterungen dieser Arbeit würden die Charakterisierung topologischer Invarianten von Mehrbandsystemen erlauben, wie zum Beispiel die $\mathbb{Z}_2$ invariant of the quantum spin Hall effect. Invariante des Quanten-Spin-Hall-Effekts.

Die Ergebnisse, die in dieser Arbeit präsentiert werden, demonstrieren die nichttriviale Verwindung der Bandeigenzustände um die Dirac-Kegel eines optischen Bienenwabengitters für ultrakalte Atome. Durch den hohen Grad an Kontrolle über die Gitterparameter eignet sich das System um topologische Eigenschaften von Energiebändern in einer gut kontrollierten Umgebung zu erforschen. Die beiden präsentierten interferometrischen Techniken stellen mögliche Wege zur Rekonstruktion der lokalen topologischen Eigenschaften und dadurch der topologischen Invarianten eines optischen 2D-Gitters dar.

Abstract

More than thirty years ago, Berry delineated the effects of the geometric structure of Hilbert space on the adiabatic evolution of quantum mechanical systems. Since then, the concept of geometrical phases – the Berry phases – associated with adiabatic evolution has been applied to a large variety of physical systems. In condensed matter, analogous topological properties of the energy bands are responsible for a wide range of many-body phenomena, such as the integer quantum Hall effect and the existence of robust conducting edge states in topological insulators. The Berry curvature, the parameter which describes the geometry of the band eigenstates, is of fundamental importance to the characterization of the physical properties of electronic states in condensed matter systems and it determines the topological invariant of a band, the Chern number. Despite the central role of Berry phases and Berry curvature, fully mapping out the geometric structure of an energy band remains a major challenge for experiments.

This thesis reports on the experimental realization of a honeycomb optical lattice for ultracold atoms which has properties similar to those of solid state graphene. This lattice structure presents peculiar topological features associated with conical intersections of energy bands, the Dirac cones. The topological properties of a Bloch band can manifest themselves when a particle is adiabatically moved in a closed loop in reciprocal space around one of the conical intersection of bands present in the energy spectrum. By doing so, the particle acquires a geometric phase which is analogous to the phase shift experienced by electrons moving around a solenoid, the well known Aharonov-Bohm effect. This thesis presents an interferometric technique to detect the topological properties of such cones and to probe the distribution of Berry curvature in reciprocal space with high quasimomentum resolution.

The first part of this thesis introduces the honeycomb optical lattice and the experimental setup for cooling ultracold atoms. Then, an interferometric protocol for ultracold atoms, analog of the Aharonov-Bohm effect in reciprocal space, is developed to detect the geometric phase associated with the Dirac cones. The interferometric technique combines the motion of atoms in the band with spin-echo interferometry and it allows the topological properties of the lowest band of the optical lattice to be characterized by probing the localization of the Berry curvature of an individual Dirac cone. The detected sharp phase jump to π and the strong reduction in interference contrast at the Dirac cones demonstrate the winding of the band eigenstates and the strong localization of the Berry curvature at the cones. Moreover, the interferometry is used to detect the movement in reciprocal space and the annihilation of the topological features upon lattice imbalance. The observed disappearance of the π Berry phase confirms the transition to a topologically trivial band structure.

The last part of this thesis presents preliminary results concerning interferometry in the two lowest bands of the lattice. The Stückelberg interferometry, realized by

diabatic motion of atoms in reciprocal space, is used to map the dispersion of the bands and to probe the symmetry of the band eigenstates. Extensions of this work would allow the characterization of topological invariants of multi-band systems, like the $\mathbb{Z}_2$ invariant of the quantum spin Hall effect.

The results reported in this thesis demonstrate the non-trivial winding of the band eigenstates around the Dirac cones of an optical honeycomb lattice for ultra-cold atoms. The high degree of control over the lattice parameters makes the system suitable for investigating topological properties of energy bands in a well controlled environment. The two interferometric techniques presented constitute possible approaches for reconstructing the local topological properties of a 2D optical lattice and, thereby, of its topological invariant.

Contents

Chapter 1.

Introduction

The concept of topology was first introduced in mathematics to classify manifolds that can be continuously deformed one into an other [1, 2]. These curved spaces, despite being very different in shape, have the same total curvature and they are part of the same topological class which is defined by an integer, the topological invariant. Deeply connected to topology is the concept of holonomy: a vector which is parallel transported on a manifold can twist and turn if the surface is curved. After a motion in a closed loop, it might happen that its final orientation is different from the initial one. This rotation of the transported vector is of purely geometric origin. Geometrical properties of curved manifolds were for long just a mathematical concept. It was not until the end of the 20th century that the idea of topology entered into the description of physical phenomena thanks to the studies of Berry about the adiabatic evolution of a quantum mechanical system [3]. As Berry pointed out more than thirty years ago, when eigenfunctions adiabatically evolve with respect to a time dependent Hamiltonian in a closed path in the parameter space they can acquire a phase of geometric origin – the Berry phase. This phase factor might seem irrelevant as it is just an additional phase multiplying the original state. On the contrary, it has physical consequences on the adiabatically transported quantum state. The generality of the geometric phase suggest its depth: its effects have been observed experimentally in a great variety of systems, from photons [4, 5], to NMR [6–8] and molecules [9], just to mention a few. A well known example is the geometrical interpretation of the Aharonov-Bohm effect [10], where a magnetic flux in a confined region of space influences the eigenstates everywhere via the magnetic vector potential. Berry's idea of geometrical phases has been widely generalized [11–13] and it has become essential to our understanding of the most diverse physical phenomena.

Topology is of fundamental importance to the understanding of macroscopic properties of condensed-matter systems as well. As realized by Thouless and coworkers in their seminal work [14], the physical properties of a solid are encoded not only in the scalar dispersion of the bands, but also in the geometry of the band eigenstates. The Berry curvature, a parameter which characterizes such topological features of an energy band, determines the physical properties of electronic states as well as the

topological invariant of the band, the Chern number [14]. The Berry curvature is responsible for a wide range of many-body phenomena such as, the quantized conductivity in the integer quantum Hall effect (IQHE) [14–16], the Hall conductivity of graphene in a magnetic field [17] and the existence of robust edge and surface states in 2D and 3D topological insulators [18, 19]. The origin of all these phenomena is deeply rooted in the topological properties of the bulk and they are well understood at the single particle level when the geometric properties of the bands are taken into account. Several works also pointed out that the quantized conductance and a non-zero Chern number do not necessarily need time reversal symmetry to be broken with an external magnetic field as for the IQHE. As illustrated by the Haldane model [20], developed for a honeycomb lattice, and subsequently by the Kane and Mele model [21, 22], the quantized conductance can be an intrinsic property of the system. This is the case of the quantum spin-Hall effect [23, 24], where the Hall response is created by spin-orbit interactions in the bulk and described by a topological invariant, the $\mathbb{Z}_2$ invariant, extension of the concept of Chern number for multi-band systems. The properties of topological bands become even richer when interactions between particles are added, an example being the fractional quantum Hall effect [25, 26].

The direct investigation of real materials is often complicated by imperfections of the lattice structure, anisotropies and strong inter-particle correlations which make it hard to describe a real solid with a simple theoretical model. Recently, new experimental techniques, developed in very diverse physical systems, allowed recreating the physical properties of solid state materials in an environment that can be well controlled to a great extent. Among these techniques, ultracold atoms have become of fundamental importance as they proved to be very versatile at simulating a disparate range of condensed matter systems over the recent years. The strength of simulations with ultracold atoms relies on the high degree of control over the system's parameters and on the essentially defect-free nature of the engineered potentials. The fundamental building block of this field was the first creation of a Bose-Einstein condensate (BEC) in atomic gases [27, 28]. After that, the field developed to study properties of superfluidity in a systematic manner. Vortices were observed [29, 30] and excitations of the superfluid where studied in depth [31, 32]. Soon after the Bose-Einstein condensation, the quantum degenerate regime was reached for fermionic alkali metal atoms as well [33]. By combining quantum degeneracy with the possibility of tuning interactions via Feshbach resonances [34, 35], the study of the BEC to BCS crossover became experimentally accessible [36].

After these results, ultracold atoms experiments soon developed towards the simulation of the properties of solid state systems with optical lattices. The underlying idea is to replace the role of electrons in a solid with bosonic or fermionic atoms in a periodic optical potential formed by interfering laser beams [37]. Even if the details of the potentials and the energy scales of these systems are quite different,

the underlying models that describe them are formally equivalent. After the proposal of D. Jaksch and coworkers for realizing the Bose-Hubbard model with cold atoms [38], the first observation of the quantum phase transition from a superfluid to a Mott insulating state [39] was a crucial result for the field. It demonstrated the possibility of entering strongly interacting regimes with ultracold atoms in optical lattices and, in contrast to condensed matter, the ability to engineer Hamiltonians in a defect-free environment. Soon after this remarkable result, systems with lower dimensionalities were studied, like the Tonks-Girardeau gas [40, 41], and Mott insulators for degenerate fermionic atoms were realized as well [42, 43].

These seminal results further strengthened the field of simulations with ultracold atoms, which soon diversified in many different directions to investigate a broad range of condensed matter phenomena, such as: Anderson localization in a disordered potential [44], ultracold ground state molecules and Rydberg atoms for studies on long-range and anisotropic dipolar interactions [45–47], strong effective magnetic fields in optical superlattices [48–50], just to mention a few. These results highlighted the remarkable control over the engineered synthetic materials and the wide range of possibilities for quantum simulations in well tailored quantum systems. Moreover, several techniques have been developed to manipulate and probe the properties of such systems and provide direct information about the quantum states. Some well known examples are in-situ single-site resolved detection and manipulation [51–53], few-sites resolved imaging [54], atom interferometry [55–58] and Bragg spectroscopy [59].

Among the many directions of novel studies with cold atoms, a notable one is engineering topological band structures. The high tunability of cold atom systems would allow a rich variety of exotic topological phenomena to be explored, especially when interactions are added to the systems. Reaching the fractional quantum Hall regime [60, 61] and studying the interplay of topology and interactions in a systematic manner [62] are major goals in the cold atoms community. Furthermore, tailoring the topological features of Bloch bands might enable one to realize systems which are out of the reach of real solid state materials, a famous example being the Haldane model [20]. To this end, theoretical and experimental effort has been put into developing techniques to imprint geometrical phases on cold atomic clouds or to engineer topological bands in these highly-controllable quantum systems. First results were realized with rotating BECs [63]. Then, novel schemes were proposed and implemented to increase the flux of the effective magnetic field or to engineer spin-orbit coupling by driving the system using external fields [64–66]. Some of these methods are based on Raman transitions [67–69], which proved to be a promising research direction as shown by recent experimental results about synthetic Hall effects [67, 70, 71] and gauge fields in synthetic dimensions [72, 73]. In the context of standard optical lattices, geometrical features and artificial magnetic fields have been recently implemented in driven systems [74–76], where complex tunnelings between the different lattice sites are engineered either by time-periodic modulation

of the lattice [77], or Raman-assisted tunneling [64, 78]. These complex hoppings allowed for the creation of such topological bands. Some examples are lattice ladders with a net magnetic flux per plaquette [79], the Hofstadter bands in optical superlattices [80, 81] and the realization of the Haldane model in brick-wall lattices [20, 82]. Additionally, artificial magnetic fields can also be created by deformations of the lattice potential, in analogy to the case of strained graphene [83, 84]. Despite its fundamental role in describing the physical properties of real and synthetic materials, fully mapping out the geometric structure of an energy band remains a major challenge for ultracold atoms experiments, as well as for solid state ones. Experimental techniques capable of revealing and characterizing the topological features of Bloch bands are under development. Among the ones proposed, like analysis of transport measurements [81, 82, 85, 86], quench dynamics [87, 88] or edge states [89, 90], recent results demonstrated how the geometrical properties of bands can be inferred by using interferometry [57] which allowed the Zak phase to be measured in a 1D superlattice potential [58].

This thesis presents an experimental apparatus for studying ultracold atoms, bosons and fermions, in a honeycomb optical lattice. The growing interest in the properties of such lattice relates to the peculiar geometrical features of its band structure, the Dirac cones of its energy spectrum, which are linked to the bipartite nature of the lattice potential. Analogous Dirac cones can be found in a wide variety of physical systems, like molecules featuring conical intersections of energy surfaces [91], photonic waveguides [92] and polaritons [93], as well as in optical lattices. While earlier experiments investigated the Mott insulator transition in honeycomb lattices [94, 95], only recently experimental results drew attention to the relevance of probing topological properties of such lattice structure by realizing the Haldane model with ultracold atoms [82]. The advances in synthetic gauge fields might enable one to explore a rich variety of exotic topological phenomena in the honeycomb lattice that remain hard or even impossible to implement in condensed matter systems, like the Kane-Mele model [22], chiral bosonic superfluid phases [96], the Hofstadter spectrum [97], and Floquet topological insulators [98, 99].

Large part of this thesis deals with the development of the experimental setup for studying ultracold atoms, the bosonic ^{87}Rb and the fermionic ^{40}K, in the optical lattice. The implementation of techniques to cool the atoms to degeneracy and condensation, the experimental realization of the honeycomb optical lattice and of techniques to manipulate the state of the atoms via Bloch oscillations were key steps to start the studies on topological Bloch bands. This involved the development of an entire apparatus in which the alkali atoms are cooled by standard techniques and then trapped in a honeycomb lattice potential.

To confirm the topological character of the synthetic lattice potential, the Berry phase associated with the winding of the eigenfunctions at the individual Dirac cones of the optical honeycomb lattice has been directly measured. In solid state graphene,

the presence of a localized π-flux associated with a Dirac cone has been observed via the polarization dependence in photoemission spectra [100, 101], measurements of a half-integer shift in the positions of quantum Hall plateaus and the phase of Shubnikov-de Haas oscillations [17, 102]. In our experimental realization, we instead make use of interferometry to directly observe the singular π flux of the cones. The versatile interferometric technique for a BEC of ^{87}Rb [57, 58] is the analog of the Aharonov-Bohm effect, as it maps the Berry curvature enclosed by arbitrary closed paths in reciprocal space. The observed Berry phase of π demonstrates the winding of the band eigenstate at the Dirac cones and highlights the capability of the developed interferometric technique to detect local topological features that are challenging to observe by alternative techniques based on transport measurements. Furthermore, this thesis reports on the direct observation of the annihilation of the Dirac points [103, 104]. Here we make use of the cold atoms interferometry to directly observe the motion of the Berry fluxes and detect the change of topology of the band. The Aharonov-Bohm interferometry is a key technique for the complete characterization of 2D topological lattices [57] and for monitoring the change of topology of an energy band when artificial magnetic fields and complex tunnelings are engineered in the honeycomb lattice.

Analogous geometrical phase factors can be defined in multi-band systems as well. In the last part of this thesis we present preliminary results concerning interferometry in the two lowest bands of the lattice as a first step towards the reconstruction of topological invariants of multi-band systems. Specifically, we implemented Stückelberg interferometry [105, 106], which allows us to reconstruct the dispersion of energy bands as well as to provide insight into the symmetries of the topological features of the two-band model. By combining Stückelberg interferometry with several existing techniques topological invariants of multi-band systems could be fully reconstructed, as suggested in [107].

Outline

In Chapter 2, the concepts of topology and geometrical phases associated with adiabatic transport of quantum systems are introduced. Particular attention is paid to the topological properties of Bloch bands and of conical intersections of energy bands.

In Chapter 3, the model of interest, the honeycomb lattice, is presented. First we derive and discuss its main features, i.e. energy bands and winding of the eigenstates, from the tight-binding model of the lattice. Then, the optical lattice potential created by interfering three running waves is described. The interference pattern is set to realize a time-reversal and inversion symmetric lattice with tunable tunnelings along three main hopping directions. Finally, the Hamiltonian describing non-interacting atoms in such optical potential is derived and we illustrate how it simulates the model of interest.

In Chapter 4, we present the experimental setup which allows the cooling of bosonic ^{87}Rb and fermionic ^{40}K atoms to condensation and degeneracy. The different cooling steps and typical clouds parameters at the end of each evaporation cycle are briefly summarized.

In Chapter 5, the lattice setup is presented. Mapping techniques to detect the quasimomentum distrubution of the atoms loaded in the lattice are illustrated. We also describe Bloch oscillations of bosonic atoms in the honeycomb lattice under the presence of an external force.

In Chapter 6, the interferometric technique used to map the topological features of the lattice is described. After illustrating the protocol for the Aharonov-Bohm interferometry and some experimental details, the results are presented. The interferometry is used to detected a sharp phase jump to π at the Dirac cones and observe the motion of the cones followed by the annihilation of the Berry fluxes.

In Chapter 7 we present preliminary results concerning interferometry in a two-band model. The Stückelberg interferometry protocol along with experimental results are described.

Conclusions and future prospects are in Chapter 8. In the appendices, additional details about the system parameters and the Aharonov-Bohm interferometry are presented.

Publication

The following reference has been published in the context of this thesis

- **An Aharonov-Bohm interferometer for determining Bloch band topology**
  Lucia Duca, Tracy Li, Martin Reitter, Immanuel Bloch, Monika Schleier-Smith, Ulrich Schneider.
  Science 347, 288-292 (2015).

Chapter 2.

Topological properties of Bloch bands

The idea of topological properties of energy bands originates from description of curved manifolds in differential geometry which soon generalized to the description of generic abstract spaces, including the Hilbert space of quantum mechanical systems. Many reviews and books cover the subject in detail, we reference to [2, 108–111] for a more complete introduction to the topic. In this chapter, the concepts of topology and geometrical phases are briefly introduced. These notions will be needed to understand the features of the optical lattice we aim at characterizing. In Section 2.1, the concepts of parallel transport and geometric phases on a real and on the Hilbert space are introduced. In Section 2.2, the effects of the geometric structure of Hilbert space on the adiabatic evolution of quantum mechanical systems are presented. Here we introduce the Berry phase [3] and its generalization to degenerate eigenstates done by Wilczek and Zee [12]. The concept of topology is then translated to the case of Bloch bands where analogous phase factors can be found which relate to winding of the band eigenstates, Section 2.3. Finally, we comment on topological features of a conical intersection that will be needed to understand the features of the model of solid-state graphene, Section 2.4.

2.1. Introduction on geometrical properties

In differential geometry, manifolds are equivalent if they can be adiabatically deformed one into an other [2]. To classify these topologically equivalent manifolds, one can analyze the parallel transport of a vector $\mathbf{v}$ on the surface of a manifold. The vector is constrained to lie in the plane tangent to the surface of the manifold which is parametrized by the vector normal to the surface $\mathbf{n}$, so that $\mathbf{v} \cdot \mathbf{n} = 0$. Moreover, the vector $\mathbf{v}$ as well as the reference frame of the tangent plane, parametrized by the orthogonal vectors $\mathbf{e}_1$, $\mathbf{e}_2$, can not rotate around the normal axis as the vector moves on the surface of the manifold, i.e. $\boldsymbol{\omega} \cdot \mathbf{n} = 0$ where $\boldsymbol{\omega}$ is the angular velocity of the reference frame, $\boldsymbol{\omega} = \mathbf{n} \times \dot{\mathbf{n}}$. These conditions fix the pointing direction of the vector as it moves on the surface, $\dot{\mathbf{v}} = \boldsymbol{\omega} \times \mathbf{v}$ [112]. These geometrical constrains
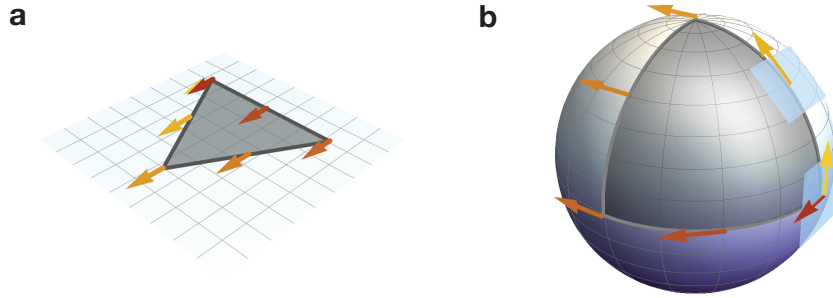
Figure 2.1.: Examples of parallel transport of a vector on different manifolds, a plane and a sphere. The vector is constrained to lie on the plane tangent to the surface of the manifold. Few tangent planes are shown for the case of the sphere to illustrate how the vector tilts together with them. Final vector (red) is rotated compared to the starting vector (yellow) when moving on a curved manifold.

set the law of parallel transport. As the vector is transported, its orientation can change only if the orientation of the local tangent plane changes along the path. After a closed loop C on a surface S, the orientation of the vector might be not parallel to the original one if the vector moved on a curved manifold, as illustrated in Fig. 2.1. The angle φ by which the transported vector is rotated compared to the initial orientation is the holonomy [112]

$$\varphi = \text{Im} \oint_C \mathbf{u}^* \dot{\mathbf{u}} \, dt = \oint_C \mathbf{A}(\mathbf{r}) d\mathbf{r} \tag{2.1}$$

where $\mathbf{u}$ is a complex unit vector which specifies the local basis of the vector $\mathbf{v}$ and accounts for the local rotation of the reference frame on a curved manifold [112]. The connection $\mathbf{A}(\mathbf{r})$, describing how the vector has to rotate to move from one point to an other on the curved surface, is gauge dependent but the angle φ is not because of the integration on a loop. To understand this gauge independence, we can imagine to rotate the reference frame at some specific point $\mathbf{r}$ by doing the following gauge transformation $\mathbf{u}(\mathbf{r}) \to \mathbf{u}(\mathbf{r})e^{i\chi(\mathbf{r})}$. By doing so, the connection will also change to account for the different choice of gauge and it transforms as $\mathbf{A}(\mathbf{r}) \to \mathbf{A}(\mathbf{r}) + \nabla_{\mathbf{r}}\chi(\mathbf{r})$, with an additional term that is not necessarily zero. However, the integral is $\oint_C \nabla_{\mathbf{r}}\chi = 0$ when initial and final points coincide and the equation 2.1 is gauge independent.

For a 2D closed manifold, the angle φ can be rewritten in terms of the Gaussian curvature $\Omega(\mathbf{r})$ enclosed during the loop by using the Stokes' theorem, $\varphi = \int_S \Omega(\mathbf{r}) d^2 r$, where $\Omega(\mathbf{r}) = \kappa_1 \kappa_2$ and κ_1, κ_2 are the principle curvatures of the surface. The integration done over the complete manifold M is an integer multiple of 2π that

measures the total curvaure, or the genus g, of the manifold [2]

$$\int_M \Omega(\mathbf{r})d^2r = 2\pi n_C = 2\pi(2 - 2g).\tag{2.2}$$

The integer n_C is the topological invariant that classifies different types of adiabatically connected manifolds. This relation which connects local geometry and global topology has evolved through mathematical abstraction to generic abstract spaces, like the Hilbert space of quantum mechanical systems.

2.2. Manifestations of topology in quantum mechanical systems

Following the discussion given by Berry [3], here we summarize the most important parameters and observables that characterize the topological properties of a quantum mechanical system.

2.2.1. Geometric phase factors related to cyclic adiabatic transport

We start by considering a quantum system described by a Hamiltonian $\hat{H}(\mathbf{r})$ that depends on a parameter $\mathbf{r}(t)$ which can be changed over time. Its discrete spectrum is given by $\hat{H}(\mathbf{r})|\phi_n\rangle = E_n(\mathbf{r})|\phi_n\rangle$, $|\phi_n\rangle$ being a set of eigenfunctions. The evolution of the system is described by the Schrödinger equation for the generic wavefunction $|\psi\rangle$

$$i\hbar\frac{d|\psi\rangle}{dt} = \hat{H}(\mathbf{r})|\psi\rangle.\tag{2.3}$$

The system, initially prepared in the state $|\psi(0)\rangle = |\phi_n(0)\rangle$, is adiabatically transported in the parameter space. The adiabaticity condition requires that the rate of variation of the Hamiltonian is low enough to make the probability of transition to an other state $|\phi_m\rangle$ vanishingly small [113]

$$\hbar|\langle\phi_m|\dot{\phi}_n\rangle| \ll |E_n - E_m|.\tag{2.4}$$

This means that the system will remain in the instantaneous eigenstate $|\phi_n\rangle$ throughout the adiabatic motion. During this transport the state will adiabatically evolve and acquire a phase factor η

$$|\phi_n(0)\rangle \to e^{i\eta(t)}|\phi_n(\mathbf{r})\rangle.\tag{2.5}$$

This condition together with the Schrödinger equation for the state $|\phi_n\rangle$ defines how the state evolves during the adiabatic motion and it is the analog of the parallel transport we already introduced. From eq. 2.3 and eq. 2.5, the accumulated phase η is obtained which is composed of two terms

$$\eta(t) - \eta(0) = -\int_0^t \frac{E_n(t)}{\hbar} dt' + i \int_{\mathbf{r}_0}^{\mathbf{r}(t)} \langle \phi_n | \nabla_{\mathbf{r}} \phi_n \rangle d\mathbf{r} = \varphi_{dyn} + \varphi_{geom}. \qquad (2.6)$$

The dynamical phase, φ_{dyn}, describes the evolution of the particle in a state with a certain energy E_n. The second phase term, φ_{geom} is purely geometrical as it depends only on how the state has changed along the path the system followed. The phase φ_{geom} is generally gauge dependent: suppose that we make a different gauge choice, i.e. $\phi_n(\mathbf{r}) \to e^{i\chi(\mathbf{r})}\phi_n(\mathbf{r})$. The Berry connection defined by eq. 2.6 as

$$\mathbf{A}_n(\mathbf{r}) = i\langle \phi_n | \nabla_{\mathbf{r}} \phi_n \rangle \qquad (2.7)$$

will pick an additional contribution: $\mathbf{A}_n(\mathbf{r}) \to \mathbf{A}_n(\mathbf{r}) + \nabla_{\mathbf{r}}\chi(\mathbf{r})$ which does not cancel in eq. 2.6. As illustrated earlier for the case of parallel transport, the phase φ_{geom} is gauge independent only when a periodic condition is applied, i.e. when the particle moves in a closed loop C. In this case, this geometric phase is a gauge-invariant quantity called the Berry phase, quantum mechanical analog of eq. 2.1

$$\varphi_B = i \oint_C \langle \phi_n | \nabla_{\mathbf{r}} \phi_n \rangle d\mathbf{r}. \qquad (2.8)$$

By applying Stokes theorem to the integral of eq. 2.8, we introduce the Berry curvature which is analogous to the Gaussian curvature $\Omega(\mathbf{r})$

$$\Omega_n(\mathbf{r}) = \nabla \times \mathbf{A}_n(\mathbf{r}) = i\langle \nabla_{\mathbf{r}} \phi_n | \times | \nabla_{\mathbf{r}} \phi_n \rangle. \qquad (2.9)$$

The Berry phase might seem irrelevant as it is just additional phase factors multiplying the original state. On the contrary, this phase has physical consequences on the quantum mechanical state and its effects have been observed experimentally in a great variety of physical systems. A well known example is the Aharonov-Bohm effect [10, 114, 115] where two electron wavepackets moving around a solenoid, on the left and right of it, pick up a phase difference which is the geometrical phase associated with the presence of a net flux of magnetic field inside the interferometer loop. Generalizations of the concept of Berry phase have been carried out in several works. Aharonov and Anandan focused on non-adiabatic transport [13], Wilczek and Zee on the transport in degenerate eigenstates [12] and Simon generalized the concept of geometric phase as a holonomy [11].

The concept of Berry phase can be extended to multilevel systems as well. This extension can be intuitively understood by considering a particle that has an internal

structure. In this case, the motion in the parameter space may result in a coherent transformation of its internal states which we need to account for. In this scenario, the adiabatic evolution has to be described by a unitary transformation instead of just a phase factor, which describes how all the internal states change during the adiabatic transport. Wilczek and Zee where the first to generalize the findings of Berry for multilevel systems by considering Hamiltonians with N-fold degenerate eigenstates [12]. For each one of them, a new adiabatic condition analogous to eq. 2.4 is defined such that the evolution of the system is restricted to the set of degenerate states while being adiabatic with respect to all other states. The transformation which time-evolves the initial state within the degenerate subspace includes the usual dynamical phase factor and a geometrical term that is a Wilson line [116]. The generalization of the Berry phase is the Wilson loop matrix, calculated for closed paths in the parameter space and the gauge invariant quantities are the eigenvalues of the Wilson loop matrix [116].

Origin of gauge freedom in quantum mechanical systems

The state $|\psi\rangle$ of a quantum mechanical system is not uniquely defined as it is possible to make a change of basis and describe the system in a new reference frame. The unitary transformation that changes the basis states can not change the physical properties of the system as they do not depend on an arbitrary choice of gauge. This arbitrariness in the choice of such frame is a gauge freedom. Since the dynamics of a state is determined by equation of motion which have the form of differential equations, we need to find a way of redefining derivatives to preserve the gauge invariance of the theory.

As a simple illustrative example, we can look at the Schrödinger equation for the state $|\psi(\mathbf{r})\rangle$ of a free particle of mass m, $i\hbar\partial_t|\psi\rangle = (-i\hbar\nabla_{\mathbf{r}})^2/(2m)|\psi\rangle$. The effect of a local gauge transformation of the state of the following kind $|\psi\rangle \to |\psi'\rangle = e^{i\chi(\mathbf{r})/\hbar}|\psi\rangle$ is to change the derivative which becomes $\nabla_{\mathbf{r}}|\psi'\rangle = ie^{i\chi(\mathbf{r})/\hbar}\nabla_{\mathbf{r}}\chi(\mathbf{r})/\hbar\,|\psi\rangle + e^{i\chi(\mathbf{r})/\hbar}\nabla_{\mathbf{r}}|\psi\rangle$. The gauge transformation introduces an additional term in the Hamiltonian because of the spatial dependence of $\chi(\mathbf{r})$. To guarantee the gauge invariance of the equation of motion we need to introduce a gauge potential $\mathbf{A}(\mathbf{r})$ in the Hamiltonian which changes under a gauge transformation of the state according to $\mathbf{A}(\mathbf{r}) \to \mathbf{A}'(\mathbf{r}) = \mathbf{A}(\mathbf{r}) + \nabla_{\mathbf{r}}\chi(\mathbf{r})$. This term allows us to redefine the derivative $\nabla_{\mathbf{r}}$ in the Hamiltonian by introducing the covariant derivative $\mathbf{D}_{\mathbf{r}} = \nabla_{\mathbf{r}} - i\mathbf{A}(\mathbf{r})/\hbar$ which changes as the wavefunction under a gauge transformation such that $\mathbf{D}_{\mathbf{r}}|\psi\rangle \to \mathbf{D}'_{\mathbf{r}}|\psi'\rangle$. With this new definition of derivative, the Schrödinger equation is written as

$$i\hbar\partial_t|\psi'\rangle = \frac{(-i\hbar\nabla_{\mathbf{r}} - \mathbf{A}(\mathbf{r}))^2}{2m}|\psi'\rangle \tag{2.10}$$

and the wavefunction $|\psi'\rangle$ is always a solution of the same Schrödinger equation no matter what gauge we choose. The geometric phases can thereby be interpreted

as a consequence of the local gauge invariance of the system which introduces a gauge potential $\mathbf{A}(\mathbf{r})$ in the equations of motion. In the case of adiabatic motion considered by Berry, the gauge of the state can be transformed by a U(1) local gauge transformation as it moves in the parameter space. The U(1) gauge freedom results in a Berry connection $\mathbf{A}(\mathbf{r})$ which can be viewed as a U(1) gauge field. The non-zero Berry phase is the consequence of the additional non-zero vector potential $\mathbf{A}(\mathbf{r})$. If the state consists of a linear combination of N eigenstates, belonging to one N-fold degenerate eigenvalue, the state is invariant with respect to a SU(N) gauge transformation which gives rise to a SU(N) gauge potential.

2.3. Geometric phases in Bloch bands

Analogous geometric factors can be introduced for Bloch bands of a solid where the manifold is now the Brillouin zone (BZ). In this systems, the distribution of Berry curvature over the Brillouin zone characterizes the energy bands and uniquely determines their topological invariants.

2.3.1. Single particle in a periodic potential

To understand the main features of the lattice we can solve the Schrödinger equation for a single particle in a periodic potential $V_L(\mathbf{r})$, which we assume to be two dimensional. A generic lattice is described by the following non-interacting Hamiltonian

$$\hat{H}_L = \frac{\hat{\mathbf{p}}^2}{2m} + V_L(\mathbf{r}) \tag{2.11}$$

with a potential periodic in $\mathbf{r}$, $V_L(\mathbf{r}) = V_L(\mathbf{r} + \mathbf{R})$, and $\hat{\mathbf{p}} = -i\hbar\nabla_{\mathbf{r}}$ the momentum operator. Given the periodicity of the potential in real space, the eigenstates are the Bloch waves [117]

$$\psi_{\mathbf{k}}^n(\mathbf{r}) = e^{i\mathbf{k}\mathbf{r}}u_{\mathbf{k}}^n(\mathbf{r}) \tag{2.12}$$

product of a plane wave and the cell-periodic part of the wave-function, $u_{\mathbf{k}}^n(\mathbf{r}) = u_{\mathbf{k}}^n(\mathbf{r} + \mathbf{R})$, which inherits the periodicity of the lattice potential. The index n indicates the band number and $\mathbf{k}$ the quasimomentum that can be chosen to be periodic by making a periodic gauge choice. The periodicity of $\mathbf{k}$ reads $\mathbf{k} = \mathbf{k} + \mathbf{G}$, $\mathbf{G}$ being a reciprocal lattice vector that describes the periodicity of the Hamiltonian in the reciprocal space. The k-vector can be restricted to the first Brillouin zone [117]. The Schrödinger equation for the Bloch wave is

$$\left(\frac{\hat{\mathbf{p}}^2}{2m} + V_L(\mathbf{r})\right)\psi_{\mathbf{k}}^n(\mathbf{r}) = E_{\mathbf{k}}^n\psi_{\mathbf{k}}^n(\mathbf{r}). \tag{2.13}$$

The eigenvalues $E_{\mathbf{k}}^n$ are the Bloch bands that compose the discrete energy spectrum of the single-particle in the periodic potential. By inseting the ansatz of eq. 2.12 into the Schrödinger equation 2.13, the eigenvalue equation for the waves $u_{\mathbf{k}}$ is derived

$$\hat{H}_L(\mathbf{k})u_{\mathbf{k}}^n(\mathbf{r}) = E_{\mathbf{k}}^n u_{\mathbf{k}}^n(\mathbf{r}) \tag{2.14}$$

where

$$\hat{H}_L(\mathbf{k}) = \frac{(\hat{\mathbf{p}} + \hbar\mathbf{k})^2}{2m} + V_L(\mathbf{r}). \tag{2.15}$$

The Bloch waves of eq. 2.12 have a fixed quasimomentum and they are completely delocalized in real space. This representation is not convenient when one wants to describe the system in terms of localized states on the different lattice sites. In this case one could use an alternative representation in real space by transforming the Bloch basis into an new orthonormal one, the Wannier basis [118, 119]. This basis choice is particularly suited to describe deep lattices where the particles are localized on a lattice site and decoupled from particles in neighboring wells. The Wannier function of a particle localized at a lattice site $\mathbf{r}_0$ in the band n is defined as the following combination of Bloch waves

$$w^n(\mathbf{r} - \mathbf{r}_0) = \frac{1}{\sqrt{N}} \sum_{k \in BZ} e^{-ik\mathbf{r}_0} \psi_k^n(\mathbf{r}), \tag{2.16}$$

where N is the number of lattice sites.

2.3.2. Topological properties of a single band

In analogy to what we did in Section 2.2.1 for particles in real space, we can define the Berry connection in reciprocal space for particles in a Bloch band.

First of all, we should note that the Berry connection and curvature of a band are a property of the periodic part of the Bloch waves, $u_{\mathbf{k}}^n$. This is because the Schrödinger equation for $u_{\mathbf{k}}^n$ is explicitly dependent on the quasimomentum $\mathbf{k}$, see eq. 2.14 and 2.15. This is not the case for the Schrödinger equation of a Bloch wave, eq. 2.13, where the quasimomentum $\mathbf{k}$ is just labeling the eigenvalues. While the Bloch waves at different $\mathbf{k}$-points are orthogonal to each other by definition, this is not necessarily true for the eigenfunctions $u_{\mathbf{k}}^n$ calculated at different quasimomenta as they are solutions of different eigenvalue equations. The Berry connection of a band n is thus defined as

$$\mathbf{A}_n(\mathbf{k}) = i\langle u_{\mathbf{k}}^n|\nabla_{\mathbf{k}}|u_{\mathbf{k}}^n\rangle \tag{2.17}$$

and it describes how to change the eigenfunctions $u_{\mathbf{k}}^n$ when moving from one point to the next in the reciprocal space. The corresponding Berry curvature is

$$\Omega_n(\mathbf{k}) = \nabla \times \mathbf{A}_n = i\langle \nabla_{\mathbf{k}} u_{\mathbf{k}}^n| \times |\nabla_{\mathbf{k}} u_{\mathbf{k}}^n\rangle \tag{2.18}$$

which is analogous to a synthetic magnetic field with vector potential $\mathbf{A}_n$ in reciprocal space. By using eq. 2.14, the Berry curvature can also be rewritten as [3]

$$\Omega_n(\mathbf{k}) = i \sum_{n \neq m} \frac{\langle u_{\mathbf{k}}^n | \nabla \hat{H}_L(\mathbf{k}) | u_{\mathbf{k}}^m \rangle \times \langle u_{\mathbf{k}}^m | \nabla \hat{H}_L(\mathbf{k}) | u_{\mathbf{k}}^n \rangle}{(E_n - E_m)^2} \tag{2.19}$$

which is a useful expression to calculate Berry phases. These geometrical concepts can also be extended to three dimensional lattices, but the Berry curvature must be treated vectorially in this case.

In analogy to the case of adiabatic motion in real space, we can now imagine to move a particle in an arbitrary closed loop in our new parameter space which is the reciprocal space of the lattice. At the end of the motion the particle has acquired a geometric phase which is

$$\varphi_{\text{Berry}} = \oint_C \mathbf{A}_n(\mathbf{k}) \, d\mathbf{k} = \int_S \Omega_n(\mathbf{k}) \, d^2k \tag{2.20}$$

where S is the area of the Brillouin zone enclosed by the path $C = \partial_S$ [120]. Although the Berry connection is not uniquely defined, see Section 2.2.1, the geometric phase is gauge independent, and is therefore an observable that encodes information on the geometrical properties of a Bloch band. We should also point out that, since the reciprocal space can be chosen to be periodic by making a periodic gauge choice, a closed loop can also be performed by moving straight in the Brillouin zone, i.e. when the quasimomentum changes by one reciprocal lattice vector as $\mathbf{k} - \mathbf{G}/2 \to \mathbf{k} + \mathbf{G}/2$. The geometrical phase in this scenario is called Zak phase [121] that is specific to the case of systems with periodic boundary conditions and it is defined as

$$\varphi_{\text{Zak}} = \int_{\mathbf{k} - \mathbf{G}/2}^{\mathbf{k} + \mathbf{G}/2} \mathbf{A}_n(\mathbf{k}) \, d\mathbf{k}. \tag{2.21}$$

This geometric phase is not completely gauge-independent as it depends on the choice of the origin of the coordinate system which changes the Bloch waves as $\psi_{\mathbf{k}}^n(\mathbf{r}) \to \psi_{\mathbf{k}}^n(\mathbf{r} + \mathbf{r}')$ and the eigenvectors as $u_{\mathbf{k}}^n(\mathbf{r}) \to e^{i\mathbf{k}\mathbf{r}'} u_{\mathbf{k}}^n(\mathbf{r} + \mathbf{r}')$ [58]. The geometrical phases of a band are linked to its topological invariant, analog of the invariant of eq. 2.2. For a 2D lattice, the invariant is the Chern number n_C defined as the Berry phase acquired for a loop which covers the entire Brillouin zone, $n_C = \int_{BZ} \Omega_n(\mathbf{k})/(2\pi) \, d^2k$ [14]. The Chern number is an integer which characterizes the topology of the energy band.

It is natural to extend the notion of geometric phases and topological invariants to the case of multiple degenerate bands by using the notion of Wilson loops and lines which depend on diagonal and off-diagonal Berry connections [121]. For multiple bands the variety of topological classes can become very rich. One important exam-

ple is the $\mathbb{Z}_2$ invariant of topological systems with time-reversal (TR) symmetry, e.g. the quantum spin Hall effect (QSHE) [21, 22]. In this systems the winding of the phase of the eigenfunctions is different for spin up and down particles. This information is encoded in the $\mathbb{Z}_2$ invariant, which has been mathematically formulated in different ways depending on the observable [22, 122–124]. One of these [124] relates it to the difference in the Zak phase of each band and the difference between eigenvalues of the Wilson loop for specific paths along time-reversal invariant momenta which cover only half of the Brillouin zone [107].

2.3.3. Role of symmetries

The distribution of Berry curvature of a band and the value of the Chern number are linked to symmetries of the lattice. Particularly important are time-reversal and inversion symmetries which dictate the form of Berry curvature.

Time-reversal symmetry is a transformation that reverses the arrow of time, $\mathcal{T} : t \to -t$. For spinless particles $\mathcal{T}$ commutes with the position operator but not with the momentum operator, $\mathcal{T}\hat{x}\mathcal{T}^{-1} = \hat{x}$ and $\mathcal{T}\hat{p}\mathcal{T}^{-1} = -\hat{p}$. Thereby, we have that $\mathcal{T}[\hat{x}, \hat{p}]\mathcal{T}^{-1} = -i\hbar$ and the operator $\mathcal{T}$ is an anti-unitary operator corresponding to the complex-conjugation [111]. For the case of particles in a lattice, the operator $\mathcal{T}$ changes the Bloch Hamiltonian of a spinless particles according to $\mathcal{T}\hat{H}_L(\mathbf{k})\mathcal{T}^{-1} = \hat{H}_L(-\mathbf{k})$ while the eigenfunctions transform as $\mathcal{T}u_{\mathbf{k}}^n = u_{-\mathbf{k}}^{n,*}$ [111]. By using these relations and the definition of the Berry curvature, eq. 2.18, it directly follows that the Berry curvature is an odd function of the quasimomentum $\mathbf{k}$ under time invariance, i.e. $\Omega_n(\mathbf{k}) = \mathcal{T}\Omega_n(\mathbf{k}) = -\Omega_n(-\mathbf{k})$. As a result, the Chern number has to be zero for time reversal symmetric Hamiltonians and it can only be changed if time reversal symmetry is broken. This is what happens in the Hall effect, for example, where the time reversal symmetry is broken by the presence of an external magnetic field [14].

Inversion symmetry is, instead, a unitary operator which reverses the spatial direction, $\mathcal{I} : \mathbf{r} \to -\mathbf{r}$, thereby it changes both position and momentum. For particles in a lattice, the effect of this operator is to change the eigenvectors according to $\mathcal{I}u_{\mathbf{k}}^n = u_{-\mathbf{k}}^n$ [111]. If the lattice is inversion symmetric, the Berry curvature is an even function of $\mathbf{k}$, $\Omega_n(\mathbf{k}) = \Omega_n(-\mathbf{k})$.

When a lattice has both inversion and time-reversal symmetries, Ω_n has to be zero or a delta function singularity to fulfill the symmetries conditions and $\Omega_n(\mathbf{k})$ is robust against deformations that preserve these symmetries of the lattice. Moreover, when there is $\mathcal{T}\mathcal{I}$ invariance, the eigenfunctions $u_{\mathbf{k}}^n$ transform as $\mathcal{T}\mathcal{I}u_{\mathbf{k}}^n = u_{\mathbf{k}}^{n,*}$ and they can be chosen to be purely real by making the appropriate gauge choice. As a result of $\mathcal{T}\mathcal{I}$ invariance, the state can only have a phase factor which is an integer multiple of π to maintain the reality of the eigenstates. This can also be seen by noting that the factors from the adiabatic evolution must coincide when we reverse the arrow of time or of space, i.e. $e^{i\varphi_{\text{Berry}}} = e^{-i\varphi_{\text{Berry}}}$. Since a phase is well-defined

up to modulo 2π, the Berry phase transforms as $\mathcal{TI}\varphi_{\text{Berry}} = -\varphi_{\text{Berry}} + 2n\pi$ and the Berry phase φ_{Berry} has to be an integer multiple of π.

2.4. Conical intersection of energy bands

Not all the bands with time-reversal invariance and inversion symmetry have a vanishing Berry curvature. Berry flux singularities are allowed by $\mathcal{TI}$-symmetry and they can be found, as an example, in a time-inversion symmetric lattice with conical intersections of energy bands [125]. These degeneracy points of the energy spectrum commonly arise in bipartite lattices, e.g. hexagonal lattices [126], superlattices [64] or dimers in the case of molecules [9].

For a two dimensional system, a conical intersection in a two-band model is most generally described by an Hamiltonian of the kind

$$\hat{H}_C(\mathbf{k}) = \mathbf{h} \cdot \boldsymbol{\sigma} \tag{2.22}$$

which resembles the Hailtonian of a spin-1/2 particle in a magnetic field. In the definition, $\boldsymbol{\sigma}$ are the Pauli matrices $\boldsymbol{\sigma} = (\hat{\sigma}_x, \hat{\sigma}_y, \hat{\sigma}_z)$ and $\mathbf{h}(\mathbf{k}) = (h_x, h_y, h_z)$ is a vector function of $\mathbf{k}$. For simplicity we parametrize the conical intersection by setting $h_x = \alpha k_x$ and $h_y = \alpha k_y$. We can allow for a finite gap at the intersection point between the two bands by introducing $h_z \neq 0$. The vector $\mathbf{h}$ is conveniently written in spherical coordinates as

$$\mathbf{h}(\mathbf{k}) = \begin{pmatrix} h_x \\ h_y \\ h_z \end{pmatrix} = |\mathbf{h}| \begin{pmatrix} \sin\Phi_{\mathbf{k}}\cos\Theta_{\mathbf{k}} \\ \sin\Phi_{\mathbf{k}}\sin\Theta_{\mathbf{k}} \\ \cos\Phi_{\mathbf{k}} \end{pmatrix} \tag{2.23}$$

where we introduced the azimuthal $\Theta_{\mathbf{k}}$ an polar $\Phi_{\mathbf{k}}$ angles

$$\tan\Theta_{\mathbf{k}} = \frac{h_y}{h_x} = \frac{k_y}{k_x}$$

$$\cos\Phi_{\mathbf{k}} = \frac{h_z}{|\mathbf{h}|}. \tag{2.24}$$

The eigenstates of $\hat{H}_C$ with eigenenergies $E_\pm = \pm|\mathbf{h}|$ are the spinors $u_{\mathbf{k}}^\pm$, which can be written in spherical coordinates and with a specific gauge choice as

$$u_{\mathbf{k}}^- = \begin{pmatrix} \sin(\Phi_{\mathbf{k}}/2) \\ \cos(\Phi_{\mathbf{k}}/2)e^{i\Theta_{\mathbf{k}}} \end{pmatrix}, \quad u_{\mathbf{k}}^+ = \begin{pmatrix} -\cos(\Phi_{\mathbf{k}}/2) \\ \sin(\Phi_{\mathbf{k}}/2)e^{i\Theta_{\mathbf{k}}} \end{pmatrix}. \tag{2.25}$$

The Berry connections of eq. 2.17, describing the change of the eigenvectors' orien-

tation, are derived from the definition of $u_{\mathbf{k}}^{\pm}$ and they are

$$\mathbf{A}_{-}(\mathbf{k}) = \nabla_{\mathbf{k}}\Theta_{\mathbf{k}}\cos^2(\Phi_{\mathbf{k}}/2) \quad \text{and} \quad \mathbf{A}_{+}(\mathbf{k}) = \nabla_{\mathbf{k}}\Theta_{\mathbf{k}}\sin^2(\Phi_{\mathbf{k}}/2). \tag{2.26}$$

The winding of the phases $\Phi_{\mathbf{k}}$ and $\Theta_{\mathbf{k}}$ indicates the non-trivial Berry connection of the cone. The Berry curvature $\Omega_{\pm}$ is directly calculated from eq. 2.26 and it relates to the winding of the polar and azimuthal angle according to

$$\Omega_{\pm}(\mathbf{k}) = \mp\frac{\sin\Phi_{\mathbf{k}}}{2}\nabla_{\mathbf{k}}\Theta_{\mathbf{k}} \times \nabla_{\mathbf{k}}\Phi_{\mathbf{k}}. \tag{2.27}$$

When both $\mathcal{T}$ and $\mathcal{I}$ symmetries are present, the Hamiltonian commutes with the $\mathcal{TI}$ operators and the $\hat{\sigma}_z$ term has to be zero. $\hat{H}_C(\mathbf{k})$ reduces to the Dirac form

$$\hat{H}_C(\mathbf{k}) = \alpha(k_x\hat{\sigma}_x + k_y\hat{\sigma}_y). \tag{2.28}$$

Since the mass term h_z is zero, the energy gap between first and second band vanishes at intersection point between the two conical bands. The crossing point is called Dirac point. Given the new form of the Hamiltonian 2.28, the eigenfunctions of the two bands simplify to

$$u_{\mathbf{k}}^{\pm} = \frac{1}{\sqrt{2}}\begin{pmatrix} \mp 1 \\ e^{i\Theta_{\mathbf{k}}} \end{pmatrix} \tag{2.29}$$

Correspondingly, the Berry connections 2.17 reduce to

$$\mathbf{A}_{+}(\mathbf{k}) = \mathbf{A}_{-}(\mathbf{k}) = i\langle u_{\mathbf{k}}^{\pm}|\nabla_{\mathbf{k}}|u_{\mathbf{k}}^{\pm}\rangle = \frac{1}{2}\nabla_{\mathbf{k}}\Theta_{\mathbf{k}}. \tag{2.30}$$

The winding of the phase $\Theta_{\mathbf{k}}$ by 2π when moving in a loop C of arbitrary size around the conical intersection results in the following Berry phase

$$\varphi_B = \oint_C \frac{1}{2}\nabla_{\mathbf{k}}\Theta_{\mathbf{k}}d^2k = \pm\pi, \tag{2.31}$$

as we expect from the symmetry constrains analyzed in the previous section. It follows that the Berry curvature associated with the degeneracy point of a conical intersection has the following singular form when the system has $\mathcal{TI}$-symmetry

$$\Omega_{\pm}(\mathbf{k}) = \pm\pi\delta(\mathbf{k}). \tag{2.32}$$

The degeneracy point and its π Berry flux are stable against perturbations that preserve the $\mathcal{TI}$-symmetry, i.e. which do not add a $\hat{\sigma}_z$ term in the Hamiltonian, because of the constrains that the symmetries impose. The effect of such perturbation is to shift the location of the crossing point by a certain vector $\boldsymbol{\kappa}$. The new
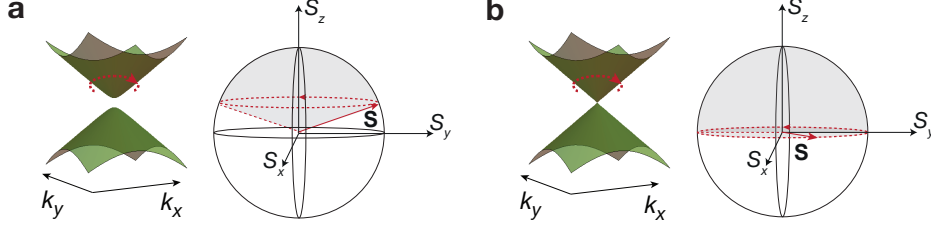
Figure 2.2.: Adiabatic transport around a gapped **(a)** or ungapped **(b)** cone results in different solid angles (shaded area) enclosed by the winding of the pseudospin **S** (red arrow) on a unitary sphere.

Hamiltonian with this additional perturbation becomes

$$\hat{H}'(\mathbf{k}) = \hat{H}_C(\mathbf{k}) + \kappa_x \sigma_x + \kappa_y \sigma_y. \tag{2.33}$$

2.4.1. Interpretation in terms of rotation of a pseudospin

The meaning of Berry curvature and connection can be better understood by picturing the winding of the eigenvectors as the winding of a pseudospin on a unitary sphere. The spinors $u_{\mathbf{k}}^{\pm}$ may be visualized in terms of the expectation value of the Pauli operator $\boldsymbol{\sigma}$ [3, 126]. According to our definitions of $u_{\mathbf{k}}^{\pm}$ and $\mathbf{h}$, eq. 2.23-2.25, the pseudospin is

$$\mathbf{S}(\mathbf{k}) = \pm \langle u_{\boldsymbol{k}}^{\pm}| \, \boldsymbol{\sigma} \, |u_{\boldsymbol{k}}^{\pm}\rangle = \pm \frac{\mathbf{h}}{|\mathbf{h}|} \tag{2.34}$$

and the angles $\Theta_{\mathbf{k}}$ and $\Phi_{\mathbf{k}}$ parametrize the orientation of the vector $\mathbf{S}(\mathbf{k})$ on a unitary sphere. The rotation of this vector is pictured in Fig. 2.2 for a particle moving around the cone. When $h_z = 0$, i.e. $\Phi_{\mathbf{k}} = \pi/2$, the pseudo-spin $\mathbf{S}$ is confined to the equatorial plane. As it moves in a loop, the azimuthal angle $\Theta_{\mathbf{k}}$ rotates by 2π and $\mathbf{S}(\mathbf{k})$ undergoes a full rotation in the $S_z = 0$ plane. If $h_z \neq 0$, $\mathbf{S}(\mathbf{k})$ is not constrained to the equatorial plane and it will undergo a rotation around some axis defined by $\hat{H}_C(\mathbf{k})$ enclosing a smaller solid angle on the sphere.

To better understand the relation between the winding of $\mathbf{S}(\mathbf{k})$ and the Berry curvature, we can make use of the eq. 2.19 for the Berry curvature, the definition of the Hamiltonian 2.33 and the commutation properties of the Pauli matrices to rewrite the curvature as a function of the pseudospin [3]. The winding of $\mathbf{S}(\mathbf{k})$ gives rise to the following Berry curvature

$$\Omega_{\pm}(\mathbf{k}) = i\nabla_{\mathbf{k}} \times \langle u_{\mathbf{k}}^{\pm}| \nabla_{\mathbf{k}} |u_{\mathbf{k}}^{\pm}\rangle = \frac{\mathbf{S}}{2} \cdot \left(\frac{\partial \mathbf{S}}{\partial k_x} \times \frac{\partial \mathbf{S}}{\partial k_y} \right). \tag{2.35}$$

It is thus clear that the Berry phase φ_B measures half of the solid angle enclosed by the rotation of the pseudospin $\mathbf{S}(\mathbf{k})$ when the k-vector wraps in a loop around the

conical intersection of bands. Consequently, the Chern number can be interpreted as an integer counting the number of times the pseudospin wraps around the unit sphere when the loop encloses the entire Brillouin zone.

Chapter 3.

The optical honeycomb lattice and its topological features

In the previous chapter, Section 2.3, the generic Hamiltonian describing a particle in a periodic potential has been introduced and the Berry connection and curvature of an energy band have been derived. In this chapter, the lattice model of our interest, the honeycomb lattice, is presented. The peculiarity of this model is the presence of conical intersections in the energy spectrum. In Section 3.1, the honeycomb lattice model is introduced. Its energy bands and topological features associated with the Dirac cones, both essential to the full characterization of a Bloch band, are described for the most relevant configurations of the lattice: with/without AB offset and with imbalanced hoppings. In Section 3.2, the properties of the optical potential created by three interfering waves are discussed and we present how the honeycomb interference pattern is experimentally realized. Starting from it, the single-particle Hamiltonian is derived and the properties of non-interacting particles in such lattice potential are described, Section 3.3.

3.1. The honeycomb lattice model

Here the specific model of our interest, a honeycomb lattice, is introduced. This two-dimensional lattice structure has been extensively investigated over the past years both theoretically and experimentally [17, 102, 127, 128]. We reference to the following reviews [126, 129] for a more detailed description of the properties of graphene-like lattices and recent experimental results obtained in solid state systems. In this section, we will illustrate how this model relates to the features of conical intersections of bands and which are its topological properties.

3.1.1. Lattice symmetries and useful definitions

The minima of the honeycomb lattice potential are arranged as illustrated by the scheme in Fig. 3.1a. The peculiarity of this lattice structure is that its unit cell is composed of two inequivalent sites, A and B. The lattice can thus be decomposed
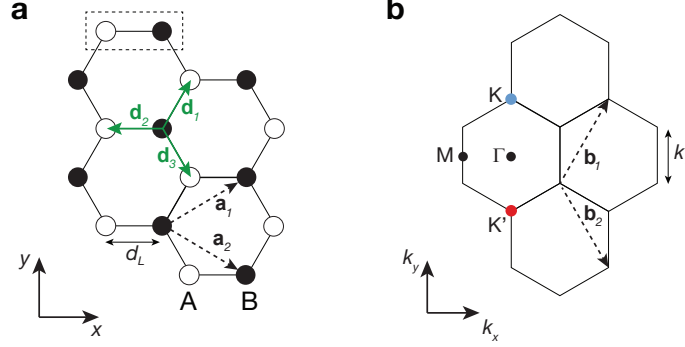
Figure 3.1.: Lattice in real **(a)** and reciprocal **(b)** space. The unit cell, dashed rectangle in **(a)**, composed by two lattice sites A and B is illustrated. The primitive lattice vectors $\mathbf{a}_1, \mathbf{a}_2$, the reciprocal lattice vectors $\mathbf{b}_1, \mathbf{b}_2$ and the nearest-neighbor hopping directions $\mathbf{d}_i$ (green arrows) connecting A and B sites are shown. The three high symmetry points (Γ, $\mathbf{M}$, $\mathbf{K}^{(')}$) of the first Brillouin zone are depicted in **(b)**.

into two triangular sublattices connecting the equivalent sites. The primitive lattice vectors connecting the sites of the A sublattice can be defined as

$$\mathbf{a}_1 = d_L \left(\frac{3}{2}, \frac{\sqrt{3}}{2}, 0 \right), \quad \mathbf{a}_2 = d_L \left(\frac{3}{2}, -\frac{\sqrt{3}}{2}, 0 \right) \tag{3.1}$$

where d_L is the distance between the neighboring A-B sites composing the unit cell. The lattice constant is given by $a_L = |\mathbf{a}_i| = \sqrt{3}d_L$. The A and B sites are connected via the vectors $\mathbf{d}_j = d_L(\cos(j\pi/3), \sin(j\pi/3))$ with $j = 1, 2, 3$, describing the three possible hopping directions as illustrated in Fig. 3.1a. The positions of the A and B sites can be chosen to be written as

$$\mathbf{r}_a = n\mathbf{a}_1 + m\mathbf{a}_2, \quad \mathbf{r}_b = n\mathbf{a}_1 + m\mathbf{a}_2 + \mathbf{d}_3, \quad n, m \in \mathbb{Z}. \tag{3.2}$$

As we have seen in the previous chapter, a periodic potential in real space results in a periodic quasimomentum due to the periodicity of the Bloch wavefuncitons. The reciprocal lattice vectors $\mathbf{b}_j$ describing the periodicity of the reciprocal space are defined by the well known relation $\mathbf{a}_i\mathbf{b}_j = 2\pi\delta_{i,j}$ as

$$\mathbf{b}_1 = \frac{4\pi}{3\sqrt{3}d_L} \left(\frac{\sqrt{3}}{2}, \frac{3}{2}, 0 \right), \quad \mathbf{b}_2 = \frac{4\pi}{3\sqrt{3}d_L} \left(\frac{\sqrt{3}}{2}, -\frac{3}{2}, 0 \right). \tag{3.3}$$

Important points in reciprocal space are the $\mathbf{K}$ and $\mathbf{K}'$ points, corners of the Brillouin zone which are depicted in Fig. 3.1b. Their location is given by

$$\mathbf{K}^{(')} = \frac{4\pi}{3\sqrt{3}d_L}\left(\cos\left(\pm\frac{\pi}{2}+\frac{2n\pi}{3}\right),\ \sin\left(\pm\frac{\pi}{2}+\frac{2n\pi}{3}\right)\right)\quad\text{with}\ \ n\in\mathbb{Z}, n\in[0,3[. \tag{3.4}$$

These two sets of points are inequivalent as they are not connected by a reciprocal lattice vector.

Here some definitions have been introduced for the honeycomb lattice structure, this notation will be used throughout the rest of this thesis.

3.1.2. The model

The origin of the Berry fluxes in the honeycomb lattice can readily be understood in the tight-binding limit. The main features of this model and its physical properties are briefly presented in this section. By analyzing the eigenenergies and eigenstates we will relate the features of the lattice with those of a conical intersection, described in Sec. 2.4.

The honeycomb lattice is modeled by the following Hamiltonian in the tight-binding limit

$$\hat{H}_{tb} = -\sum_{\langle\mathbf{r}_a,\mathbf{r}_b\rangle} J_{\mathbf{r}_a,\mathbf{r}_b}(\hat{c}^\dagger_{\mathbf{r}_a}\hat{c}_{\mathbf{r}_b} + h.c.) + \frac{\Delta}{2}\sum_{\mathbf{r}_{a,b}} \hat{c}^\dagger_{\mathbf{r}_a}\hat{c}_{\mathbf{r}_a} - \hat{c}^\dagger_{\mathbf{r}_b}\hat{c}_{\mathbf{r}_b}. \tag{3.5}$$

The first term describes the hopping of a particle between two neighboring sites connected by the vectors $\mathbf{d_i}$, illustrated in Fig. 3.1a. We consider only the hopping between neighboring sites and assume that all the other higher hopping terms are negligible. The hopping amplitudes $J_{\mathbf{r}_a,\mathbf{r}_b}$ can be different along the three hopping directions $\mathbf{d_i}$. The operators $\hat{c}^\dagger_{\mathbf{r}_a}$ and $\hat{c}^\dagger_{\mathbf{r}_b}$ create a particle in the sublattice site A or B in the Wannier orbital centered at a certain position $\mathbf{r}_a$ and $\mathbf{r}_b$ defined by eq. 3.2. For our purposes we can consider them to be bosonic operators. The second term describes an energy offset of magnitude Δ between the two sublattices.

From the symmetry of the Hamiltonian, which has a unit cell composed by two inequivalent lattice sites A and B, we can write an ansatz for the eigenstates of the Hamiltonian as a superposition of Bloch waves of the two sublattices and they are

$$\psi_\mathbf{k}(\mathbf{r}) = \sum_{\mathbf{r}_a} a_\mathbf{k}e^{i\mathbf{k}\mathbf{r}_a}w(\mathbf{r}-\mathbf{r}_a) + \sum_{\mathbf{r}_b} b_\mathbf{k}e^{i\mathbf{k}\mathbf{r}_b}w(\mathbf{r}-\mathbf{r}_b). \tag{3.6}$$

The $w(\mathbf{r}-\mathbf{r}_{a,b})$ are the Wannier functions at site $\mathbf{r}_a$ and $\mathbf{r}_b$, see eq. 2.16, and $\mathbf{k}$ is the quasimomentum restricted to the first Brillouin zone which is defined by the reciprocal lattice vectors $\mathbf{b}_1$, $\mathbf{b}_2$ defined by eq. 3.3. With this ansatz, the cell-periodic

a

b
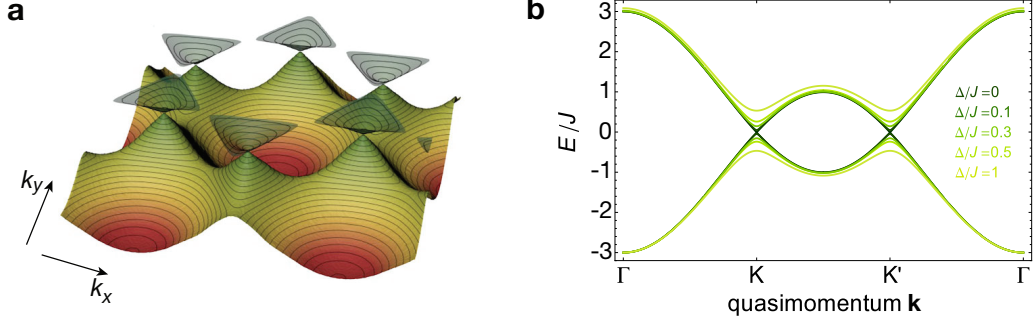
Figure 3.2.: **(a)** Dispersion relation of the honeycomb lattice, showing the arrangement of the conical intersections between the first and second band in the reciprocal space. **(b)** Energy spectrum along a straight path connecting Γ, $\mathbf{K}$ and $\mathbf{K}^{(\prime)}$ points. An energy gap opens at the Dirac points when an energy offsets Δ is introduced. The gap increases with increasing Δ, from dark to bright green.

wavefunction $u_{\mathbf{k}}$ is a two-component spinor $u_{\mathbf{k}} = (a_{\mathbf{k}}, b_{\mathbf{k}})^T$. By using the ansatz of eq. 3.6 and the lattice Hamiltonian defined by eq. 3.5, the Schrödinger equation for the wave $\psi_{\mathbf{k}}(\mathbf{r})$ is solved. From the Schrödinger equation, an eigenvalue equation for the coefficients $a_{\mathbf{k}}$ and $b_{\mathbf{k}}$ is derived and it reads

$$\hat{H}_{tb}(\mathbf{k})(a_{\mathbf{k}}, b_{\mathbf{k}})^T = E(\mathbf{k})(a_{\mathbf{k}}, b_{\mathbf{k}})^T. \tag{3.7}$$

The Hamiltonian $\hat{H}_{tb}(\mathbf{k})$ is the following 2×2 matrix

$$\hat{H}_{tb}(\mathbf{k}) = \begin{pmatrix} \Delta/2 & -t_{\mathbf{k}} \\ -t_{\mathbf{k}}^* & -\Delta/2 \end{pmatrix} \tag{3.8}$$

where Δ is an energy offset between the sublattices and the parameter $t_{\mathbf{k}}$ is given by

$$t_{\mathbf{k}} = J_1 e^{i\mathbf{k}\cdot\mathbf{d_1}} + J_2 e^{i\mathbf{k}\cdot\mathbf{d_2}} + J_3 e^{i\mathbf{k}\cdot\mathbf{d_3}} = |t_{\mathbf{k}}| \, e^{i\theta_{\mathbf{k}}}, \tag{3.9}$$

J_i being the hopping amplitudes along the three hopping directions $\mathbf{d_i}$ which are equal if the lattice potential has C_3 symmetry. The Hamiltonian of eq. 3.8 has the following form $\hat{H}_{tb} = \mathbf{h}(\mathbf{k}) \cdot \boldsymbol{\sigma}$, where the vector $\mathbf{h}$ can be parametrized in spherical coordinates as done in the previous chapter, see eq. 2.23.

Eigenvalues

The matrix 3.8 is diagonalized to find the eigenenergies of the two bands

$$E_{2,1}(\mathbf{k}) = \pm |\mathbf{h}| = \pm\sqrt{(\Delta/2)^2 + |t_{\mathbf{k}}|^2}. \tag{3.10}$$

If the lattice has inversion and time-reversal symmetries, i.e. $\Delta = 0$, and equal tunnelings along the three hopping directions, $J_i = J$, the dispersion can be further simplified. By using the definition of the parameter $t_{\mathbf{k}}$, eq. 3.9, and the one of the eigenvalues, eq. 3.10, the eigenenergies are written as

$$E_\pm(\mathbf{k}) = \pm J\sqrt{3 + 4\cos(3k_x d_L/2)\cos(\sqrt{3}k_y d_L/2) + 2\cos(\sqrt{3}k_y d_L)}. \qquad (3.11)$$

In this case the bandwidth of each band is $3J$. The bands are periodic with the periodicity given by the reciprocal lattice vectors $\mathbf{b}_i$, as it can also be seen from the plots of the energy bands in Fig. 3.2a. Moreover, when $\Delta = 0$ and $J_i = J$, there are degeneracy points between the bands that are located at the $\mathbf{K}$ and $\mathbf{K}^{(')}$ points, corners of the Brillouin zone. In this scenario, the Hamiltonian reduces to massless case in proximity of the Dirac points, see eq. 2.28. The linear dispersion of the bands can be calculated by expanding eq. 3.11 to first order in $\mathbf{k} - \mathbf{K}^{(')}$, distance to the crossing point. The dispersion is given by

$$E_\pm(\mathbf{k} - \mathbf{K}^{(')}) \approx \pm v_F \left| \mathbf{k} - \mathbf{K}^{(')} \right|, \qquad (3.12)$$

with a slope of $v_F = 3J d_L/2$. If $\Delta \neq 0$, instead, the degeneracy is lifted at the Dirac points. The resulting bands are shown in Fig. 3.2b where they are plotted for different energy offsets Δ and equal tunnelings J_i. It can be seen that the effect of the energy offset is to open a gap of size Δ. This is not surprising since the Hamiltonian has the form of the Hamiltonian of a conical intersection presented Section 2.4 with mass term $h_z = \Delta/2$.

Imbalanced tunnelings

A relative change in the tunneling rates along the three hopping directions ($J_1 \neq J_2 \neq J_3$) results in a modification of the energy bands [97, 104, 130]. The imbalanced tunneling breaks the rotational symmetry of the lattice potential but it does not introduce an energy offset between the A and B sites. Its effect is analogous to the perturbation for a conical intersection which preserves time-reversal and inversion symmetry, see eq. 2.33, and it results in a shift of the position of the Dirac cones. This can be readily understood by looking at the dispersion of the energy bands when the hoppings are imbalanced. By using eq. 3.9 and eq. 3.10, the bands with arbitrary hoppings J_i are given by

$$E_\pm(\mathbf{k}) = \pm \mid J_1 e^{i\mathbf{k}\mathbf{d_1}} + J_2 e^{i\mathbf{k}\mathbf{d_2}} + J_3 e^{i\mathbf{k}\mathbf{d_3}} \mid, \qquad (3.13)$$

in the tight binding limit. Here Δ is set to zero for simplicity. The three terms can be interpreted as vectors of lengths J_1, J_2, J_3. The bands will have degeneracies in the energy spectrum only when $E_\pm(\mathbf{k}') = 0$, which means that the three vec-

tors need to add up to zero at a certain $\mathbf{k}'$. By using triangle inequalities for the norm of the vectors, the following condition for the tunneling amplitudes is derived: $||\, J_1 \,| - |\, J_2 \,||\,\leq\,|\, J_3 \,|\,\leq\,|\, J_1 \,| + |\, J_2 \,|$. If this condition is met, the imbalanced hopping amplitudes do not open a gap at the Dirac point but only shift the zeros of eq. 3.13 to a different $\mathbf{k}$ point in the Brillouin zone. If the inequality is violated, instead, the degeneracy between the first and second band is lifted. This happens when two Dirac points meet.

Eigenstates and topological features

We have seen that the bipartition of the lattice results in a spectrum which presents conical intersection of bands and, depending on the system parameters, degeneracy points in the energy spectrum. As discussed earlier, these features result in a non-trivial winding of the phase of the eigenstates of the two bands $u_{\mathbf{k}}^{2,1}$ in proximity of the conical intersection.

The eigenstates $u_{\mathbf{k}}^{\pm}$ of $\hat{H}_{tb}$ are obtained from eq. 3.7 and they are superpositions of the states of the A and B sublattices

$$u_{\mathbf{k}}^{\pm} = \frac{\frac{\Delta}{2} \pm |\mathbf{h}|}{\sqrt{2(|\mathbf{h}| \pm \frac{\Delta}{2})\,|\mathbf{h}|}} \begin{pmatrix} -1 \\ \frac{t_{\mathbf{k}}^{*}}{\Delta/2 \pm |\mathbf{h}|} \end{pmatrix}, \qquad (3.14)$$

which are more and more localized to the A or B sites with increasing Δ. In the case of $\Delta = 0$ they reduce to an equal superposition of the wavefunctions of the A and B sites, analogous to the eigenfunctions that we have presented for a conical intersection, see eq. 2.25.

Following the treatment of the conical intersection done in Section 2.4, the spinors $u_{\mathbf{k}}^{\pm}$ may be visualized in terms of the pseudospin $\mathbf{S}(\mathbf{k})$, see eq.s 2.25 and 2.34. The orientation of $\mathbf{S}(\mathbf{k})$ is parametrized by the azimuthal $\Theta_{\mathbf{k}}$ an polar $\Phi_{\mathbf{k}}$ angles 2.24, with

$$\tan\Theta_{\mathbf{k}} = \frac{\mathrm{Im}(t_{\mathbf{k}}^{*})}{\mathrm{Re}(t_{\mathbf{k}}^{*})} \;\; \text{and} \;\; \cos\Phi_{\mathbf{k}} = \frac{\Delta}{2\epsilon_{\mathbf{k}}}. \qquad (3.15)$$

These angles vary with the parameters of the Hamiltonian and the position in the Brillouin zone. The Dirac points correspond to the phase $\mathrm{Arg}(t_{\mathbf{k}}^{*})$ being ill-defined. The rotation of $\Theta_{\mathbf{k}}$ and $\Phi_{\mathbf{k}}$ is illustrated in the plots of Fig. 3.3a-b for a specific path in the Brillouin zone. When $\Delta = 0$, the angle $\Phi_{\mathbf{k}}$ is constant, i.e. $\Phi_{\mathbf{k}} = \pi/2$. In this case, the pseudospin $\mathbf{S}$ is confined to the equatorial plane at an angle $\Theta_{\mathbf{k}} = \mathrm{Arg}(t_{\mathbf{k}}^{*})$. This is not true when $\Delta \neq 0$. The spinor can wind anywhere on the unitary sphere and it is not confined to the equator, see the plot in Fig. 3.3a.

The angle $\Theta_{\mathbf{k}}$ is changed by modifying the hopping amplitudes along the three hopping directions. As shown in the plots of Fig. 3.3b-c, the discontinuity in the phase associated with the Dirac cones and the crossing point between the two bands
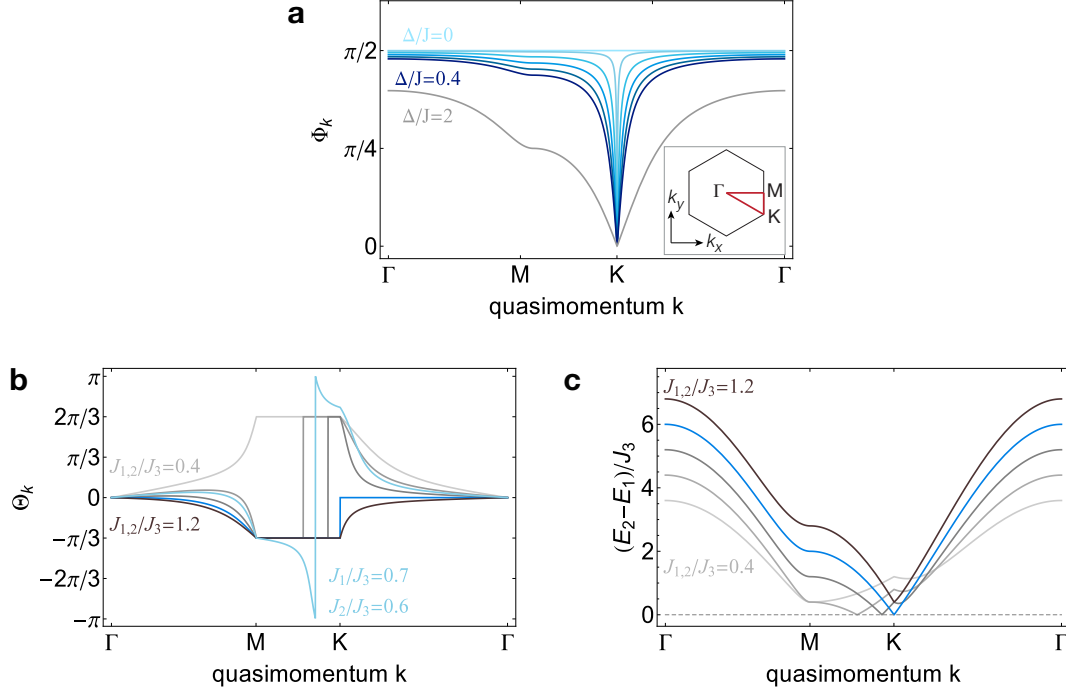
Figure 3.3.: Orientation of the pseudospin. **(a)** Winding of the angle $\Phi_{\mathbf{k}}$ (eq. 3.15) along the path depicted as an inset. Curves are calculated for different AB offsets Δ, $\Delta/J = 0, 0.05, 0.1 - 0.4, 2$. When $\Delta = 0$ the angle is fixed anywhere along the path and the pseudospin lies on the equatorial plane. The bigger Δ the more it will precess away from the equatorial plane in proximity of the **K** point. The eigenstate acquires more and more the character of the bare states on the A and B sites with increasing Δ, approaching $\Phi_{\mathbf{k}} = 0$. **(b)** Angle $\Theta_{\mathbf{k}}$ and **(c)** energy difference between first and second band along the same path for $\Delta = 0$. A discontinuity of the angle $\Theta_{\mathbf{k}}$ and a vanishing energy difference between first and second band indicate the presence of a Dirac cone. By changing the tunnelings $J_{1,2}$ relative to the third the angle and the location of the band crossing is modified. The Dirac cone moves closer to the **M** point with decreasing $J_{1,2}/J_3$. Balanced hopping case is in dark blue in **(b)** and **(c)**. When the Dirac point lies inside the area of the path taken – light blue curve calculated for $J_1/J_3 \neq J_2/J_3$ in **(b)** – the spinor undergoes a full rotation in the x-y plane.

move when the hoppings $J_{1,2}$ are changed relative to the third, J_3. The Dirac point moves along the path towards the **M** point for decreasing ratios $J_{1,2}/J_3$. From the plot in Fig. 3.3b it can be seen that the angle $\Theta_{\mathbf{k}}$ changes by 2π when the Dirac point lies inside the area of the path, which corresponds to the following parameters $J_1/J_3 = 0.7$ and $J_2/J_3 = 0.6$ in the graph. This indicates that the pseudospin undergoes a complete a full rotation when a closed path encircles a single Dirac

Figure 3.4.: **(a)** Berry curvature of the first band for $\Delta = 0.5J$, for visualization purposes. The curvature spread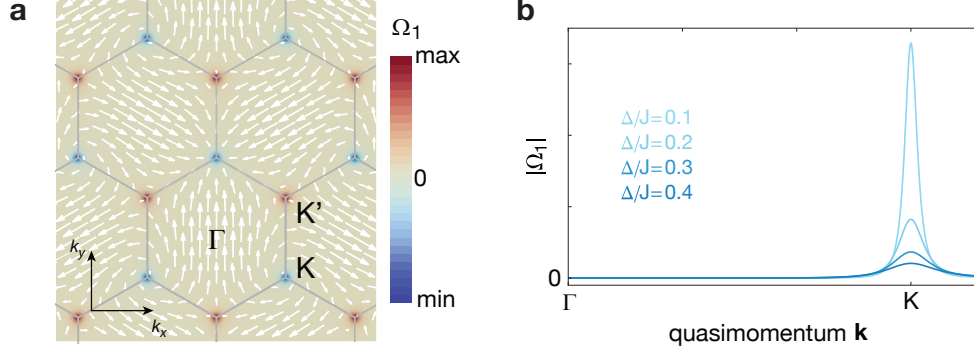s over a finite area and it alternates in sign at the $\mathbf{K}$ and $\mathbf{K}'$ points. White arrows are a pseudospin representation of the Bloch states with orientation indicating the phase of the coupling between sublattices according to the definition in 3.15. Lengths of the arrows indicate the energy gap in the two-band model, i.e. $|\mathbf{h}|$. **(b)** Distribution of Berry curvature with different energy offsets Δ/J. The distribution spreads over a larger area with increasing Δ.

cone. The momentum-dependent orientation of the pseudospin $\mathbf{S}(\mathbf{k})$ on the entire Brillouin zone is also depicted in Fig. 3.4a.

When $\Delta = 0$ the Berry connections of the two bands are obtained from eq.s 2.17 and 3.14

$$\mathbf{A}^{1,1}(\mathbf{k}) = \mathbf{A}^{2,2}(\mathbf{k}) = \frac{1}{2}\nabla_{\mathbf{k}}\theta_{\mathbf{k}}. \tag{3.16}$$

while the off-diagonal Berry connections are

$$\mathbf{A}^{1,2}(\mathbf{k}) = \mathbf{A}^{2,1}(\mathbf{k}) = i\langle u_{\mathbf{k}}^n|\nabla_{\mathbf{k}}|u_{\mathbf{k}}^{n'}\rangle = -\frac{1}{2}\nabla_{\mathbf{k}}\theta_{\mathbf{k}} \tag{3.17}$$

with 1(2) labeling the $E_{-(+)}$ band. The topological features of first and second band are the same because of symmetry of the two bands in the tight-binding limit. The vector $\mathbf{S}(\mathbf{k})$ undergoes a full rotation in the $S_z = 0$ plane in an infinitesimal loop around a Dirac point and the Berry curvature takes the following singular form $\Omega_n(\mathbf{k}) = \pm\pi\delta(\mathbf{k} - \mathbf{K}_{\pm})$, which is imposed by the time-reversal $\mathcal{T}$ and inversion $\mathcal{I}$ symmetries of the lattice potential. As shown in Fig. 3.4a, the Berry curvature alternates in sign at the $\mathbf{K}$ and $\mathbf{K}'$ points such that the Chern number of the band is zero. Despite this fact, the winding of the vector $\mathbf{S}(\mathbf{k})$ produces a sign change in the wave function of a particle that adiabatically encircles a single Dirac point. This phase factor of π is the Berry phase φ_B defined by eq. 2.31 and it is related to the singular Berry flux of the conical intersection.

When the energy offset is $\Delta \neq 0$, both angles $\Theta_{\mathbf{k}}$ and $\Phi_{\mathbf{k}}$ vary in proximity of the

Dirac point and the spinor is not constrained to the equatorial plane anymore. The less trivial winding of the spinor is described by the Berry connection of eq. 2.26, introduced in the previous chapter. The Berry curvature can also be calculated from the rotation of the spinor, eq. 2.35. For the honeycomb lattice with nearly degenerate sublattices ($\Delta/J \ll 1$), as in the case of our experiment, $\Omega_\pm$ is well localized at the $\mathbf{K}, \mathbf{K}'$ points. By using the expression for the Berry curvature of eq. 2.19, the curvature is approximated by first order perturbation theory in the vicinity of each Dirac point as

$$\Omega_\pm(\mathbf{k}) \approx i \frac{\langle u^\pm | \nabla_\mathbf{k} H_{\mathrm{tb}} | u^\mp \rangle \times \langle u^\mp | \nabla_\mathbf{k} H_{\mathrm{tb}} | u^\pm \rangle}{(E_+ - E_-)^2}. \tag{3.18}$$

By using the definition of the Hamiltonian, eq. 3.8, and the one of its eigenstates, eq. 3.14, the distribution for the Berry curvature of a single Dirac cone at the $\mathbf{K}^{(')}$ point is directly derived from eq. 3.18

$$\Omega_\pm(\mathbf{k}) \approx \pm \frac{1}{2\gamma^2} \left(1 + \left| \frac{\mathbf{k} - \mathbf{K}^{(')}}{\gamma} \right|^2 \right)^{-\frac{3}{2}}, \tag{3.19}$$

where $\gamma = \frac{1}{3d_L}\frac{\Delta}{J}$ parametrizes the distribution of Berry curvature. We quantify the spread in Berry curvature in terms of the half-width at half maximum of the distribution $\Omega_n(\mathbf{k})$, the parameter $\delta k_\Omega = (\gamma^{2/3} - \gamma^2)^{1/2}$, throughout the rest of this thesis. The distribution of eq. 3.19 of a cone is preserved for a small imbalance of the hopping amplitudes J_i up to when the Dirac points overlap and annihilate. The distribution of Berry curvature in the reciprocal space is illustrated in Fig. 3.4a where it can be seen that Ω_- has a finite extent and it alternates in sign at the $\mathbf{K}$ and $\mathbf{K}'$ points, as described by eq. 3.19. The Berry curvature spreads over a larger area in reciprocal space when the offset Δ is increased, as illustrated by the graph in Fig. 3.4b.

3.2. Implementation with ultracold atoms in an optical lattice

An optical lattice for neutral atoms is created by interfering running waves: the spatially dependent intensity pattern realizes a periodic potential for the atoms which simulates the periodic potential experienced by electrons in a solid [37]. This section focuses on how the honeycomb lattice potential has been realized by interfering three running waves.

3.2.1. The optical dipole potential

Alkali atoms can be trapped and manipulated by their interaction with light which is off resonance from the D_1 and D_2 transitions [131]. The optical dipole force, arising from dispersive interactions with far-off-resonant light, allows for optical trapping of particles. The effect of this interaction is well understood in the dressed-state picture [132, 133] where the energy shift of the new dressed states arising from the coupling of two, or more, energy levels is modeled by an optical potential U_{dip}. When the detuning of the light of frequency ω_L is large compared to the splitting between the hyperfine levels of an alkali atom in the $|F, m_F\rangle$, the hyperfine transitions of the multi-level atom are not resolved. Therefore, the light shifts of all possible transitions are summed up to obtain the following dipole potential [134]

$$U_{\text{dip}}(\mathbf{r}) = U_0 I(\mathbf{r}) \tag{3.20}$$
$$= \frac{3\pi c^2}{2} \left(\frac{\Gamma_1}{\omega_1^3} \frac{1 - \mathcal{P}g_F m_F}{\Delta_1} + \frac{\Gamma_2}{\omega_2^3} \frac{2 + \mathcal{P}g_F m_F}{\Delta_2} \right) I(\mathbf{r})$$

where we have defined an effective detuning which is

$$\frac{1}{\Delta_i} = \frac{1}{\omega_i - \omega_L} + \frac{1}{\omega_L + \omega_i}. \tag{3.21}$$

The parameters $\omega_{1,2}$ are the resonance frequencies of the center of the D_1 and D_2 hyperfine manifolds and $\Gamma_{1,2}$ are the corresponding spontaneous decay rate of the excited states. The dependence on the m_F-state and on polarization, $\mathcal{P} = 0, \pm 1$ for $\pi, \sigma_\pm$ polarizations, is explicit. Since the intensity profile $I(\mathbf{r})$ is generally position dependent, the spatially dependent energy shift gives rise to a dipole force acting on the atoms which is $F_{\text{dip}}(\mathbf{r}) = -\nabla_{\mathbf{r}} U_{\text{dip}}(\mathbf{r})$ and it is used to trap the particles. The sign of the potential and, consequently, the direction of the dipole force depend on the sign of the effective detunings Δ_i and on polarization. For linearly polarized light, the atoms will be attracted and trapped at the maxima of the intensity profile $I(\mathbf{r})$ when the light is red detuned, i.e. $1/\Delta_1 + 2/\Delta_2 < 0$. For blue detuning, $1/\Delta_1 + 2/\Delta_2 > 0$, the atoms will be repelled by the maxima and trapped at the minima of the intensity pattern.

Gaussian beams as an harmonic trap

The harmonic traps needed for the experiment are created by tightly focused Gaussian beams, red-detuned from the atomic transition. The intensity profile of a focused Gaussian beam propagating along the x-axis is described by

$$I(x, y, z) = \frac{2P}{\pi w_y w_z} e^{-\frac{2y^2}{w_y^2} - \frac{2z^2}{w_z^2}}, \tag{3.22}$$
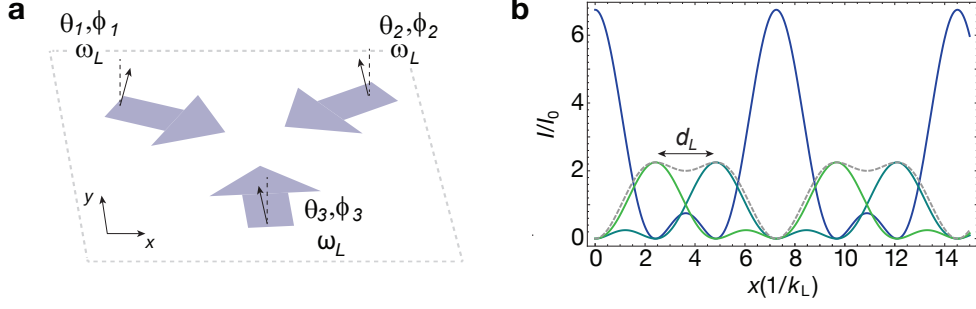
Figure 3.5.: **(a)** Configuration of the lattice beams (purple arrows) in real space. Their polarizations (black arrows) are also illustrated. **(b)** Plot of the intensity pattern (eq. 3.27-3.28) along $y = 0$ created by the three interfering beams with a tilt in polarization of $\theta_i = \pi/6$ and $\phi_i = 0$. I_0 is the intensity of each beam. The periodic potentials from the s-component (blue) and the p-component (dashed) of the polarization are shown separately. Dark and bright green represent the intensity patterns of the $\sigma_\pm$ components which create the p-polarized lattice.

where, the $1/e^2$ radii w_y and w_z are a function of the distance x from the focal point and their dependence is $w_{y,z}(x) = w_0\sqrt{1 + x^2/x_R^2}$, $x_R = \pi w_{y,z}^2/\lambda_L$ being the Rayleigh length characterizing the focused beam. If the spatial extend of the atomic cloud along x is much smaller than x_R, the waists can be assumed to be constant along the x-axis. P is the total power of the laser beam. Assuming that the atoms are trapped at the intensity maxima due to the dipole potential of eq. 3.20, the trap is approximated by an harmonic trap by expanding the Gaussian intensity profile of eq. 3.22 about its maximum to first order. The trapping frequencies $\omega_{y,z}$ are obtained from this approximation and they are given by

$$\omega_{y,z} = \sqrt{\frac{4U_0 I_0}{m w_{y,z}^2}} \tag{3.23}$$

where m is the mass of the trapped atoms, $I_0 = 2P/(\pi w_y w_z)$ is the intensity maxima and U_0 is defined by eq. 3.20.

3.2.2. The periodic potential from three interfering beams

Thanks to the intensity dependence of the dipole force, a periodic potential for the atoms is generated by interfering laser beams. In our experimental realization, the interference pattern that realizes the honeycomb lattice is created by superimposing three running waves which have the same frequency and which are interfering on a plane at a $120(1)°$ angle from each other, as illustrated in Fig. 3.5a. The wavevectors of the three beams are lying on the xy-plane and are described by the

following vectors

$$\mathbf{k}_1 = k_L \left(\frac{\sqrt{3}}{2}, -\frac{1}{2}, 0 \right), \ \ \mathbf{k}_2 = k_L \left(-\frac{\sqrt{3}}{2}, -\frac{1}{2}, 0 \right), \ \ \mathbf{k}_3 = k_L \left(0, 1, 0 \right), \qquad (3.24)$$

where $k_L = 2\pi/\lambda_L = \omega_L/c = |\mathbf{k}_i|$ is the wavenumber of the lattice beams. Lets assume next that our quantization axis, given by a magnetic field offset, is pointing along the z-direction. This will define the polarizations of the three interfering waves. Most generally each running wave is described by a combination of s and p polarizations, where s is the component out of plane of intersection, i.e. along the z-axis, and p is the in-plane component. The electric field of a running wave is given by

$$\mathbf{E}_i(\mathbf{r}) = \sqrt{I_i} e^{i\mathbf{k}_i\mathbf{r} - i\omega_L t}(\cos(\theta_i)\hat{\mathbf{z}} + \sin(\theta_i)e^{i\phi_i}(\hat{\mathbf{z}} \times \hat{\mathbf{k}}_i)), \qquad (3.25)$$

where I_i is the beam's intensity, the parameter θ_i sets the angle of the polarization relative to the z-axis, thereby fixing the ratio between the s and p components of the polarization vector of the wave. The parameter ϕ_i, instead, sets the phase shift between the s and p components in case of elliptical polarizations. In eq. 3.25, the overall global phase of the beam has been set to zero since it does not affect the shape of the potential and the properties of the lattice. Choosing a different global phase results only in a shift of the interference pattern.

The total electric field, combination of the electric fields of the s and p polarization components of the three waves, is $\mathbf{E}(\mathbf{r}) = \sum_{i=1}^{3} \mathbf{E}_i = \mathbf{E}_s + \mathbf{E}_p$. The component $\mathbf{E}_p$ of the electric field can also be decomposed into σ_+ and σ_- polarizations components by making the following basis transformation $\hat{e}_+ = \frac{1}{\sqrt{2}}(\hat{x} + i\hat{y})$, $\hat{e}_- = \frac{1}{\sqrt{2}}(\hat{x} - i\hat{y})$. The corresponding electric fields can be written in this new basis as

$$\mathbf{E}_{\sigma_\pm} = \frac{1}{\sqrt{2}} e^{-i\omega_L t} \left(\sin\theta_1 e^{i\mathbf{k}_1\mathbf{r} + i\phi_1} + \sin\theta_2 e^{i\mathbf{k}_2\mathbf{r} \pm i4\pi/3 + i\phi_2} + \sin\theta_3 e^{i\mathbf{k}_3\mathbf{r} \pm i2\pi/3 + i\phi_3} \right).$$

$$(3.26)$$

The electric fields of the $\sigma_\pm$ polarizations are spatially shifted relative to each other, as well as relative to the s-polarized component of the total electric field. The polarization decomposition is particularly important if the atoms are not in a $m_F = 0$ state, as the polarization dependent light shift of the dipole potential might be significant depending on the detuning of the light, see eq. 3.20.

The total intensity pattern generated by the three interfering waves is given by the interference patterns of the s and p polarization components, $I(\mathbf{r}) = I_s + I_p$, where

$$I_s(\mathbf{r}) = |\mathbf{E}_s|^2 = \sum_{i=1}^{3} I_i \cos^2\theta_i + \sum_{i,j=1}^{3} \sqrt{I_i I_j} \cos(\theta_i)\cos(\theta_j)\cos((\mathbf{k}_i - \mathbf{k}_j)\mathbf{r}) \qquad (3.27)$$
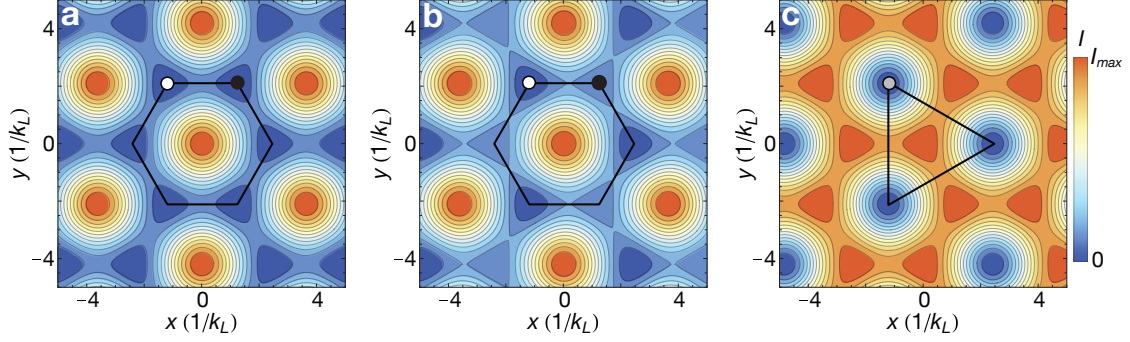
Figure 3.6.: Total intensity patterns created by setting the beams' polarizations at the same angle $\theta_i = \theta$, with $\theta = 0, \pi/4, \pi/2$ from left to right. Angles ϕ_i are fixed to $\phi = (0, 2\pi/3, 4\pi/3)$, settings that maximize the energy offset between the A and B sites (see eq.s 3.27 and 3.28). The minima of the intensity pattern create a honeycomb potential **(a)** when polarizations are out-of-plane, $\theta = 0$, or triangular for in-plane polarizations $\theta = \pi/2$ **(c)**. The two minima, the A and B sites (black and white dots), of the honeycomb potential and the single minima (grey dot) of the triangular one compose the unit cell. **(b)** Intermediate tilts can create a honeycomb lattice with AB offset.

$$I_p(\mathbf{r}) = |\mathbf{E}_+|^2 + |\mathbf{E}_-|^2 =$$

$$= \sum_{i=1}^{3} I_i \sin^2 \theta_i - \frac{1}{2} \sum_{i,j=1}^{3} \sqrt{I_i I_j} \sin \theta_i \sin \theta_j \cos((\mathbf{k}_i - \mathbf{k}_j)\mathbf{r} + \phi_i - \phi_j). \qquad (3.28)$$

The optical lattice potential is given by $V_L = \sum_i U_{0,i} I_i(\mathbf{r})$, where the sum runs over the three possible polarizations, π and $\sigma_\pm$, and $U_{0,i}$ is the polarization dependent dipole potential of eq. 3.20. If the $\sigma_\pm$ polarizations terms contributing to the interference pattern are not negligible, the total the optical lattice potential has to be separated into a state-independent part, proportional to $|\mathbf{E}_+|^2 + |\mathbf{E}_-|^2 + |\mathbf{E}_s|^2$, and a state-dependent part, proportional to $|\mathbf{E}_+|^2 - |\mathbf{E}_-|^2$. The complete derivation of the state-dependent optical potential can be found in the appendix A. As we will see later on, the state-dependent part of the potential can be safely neglected for the results presented in this thesis because of the choice of wavelength, i.e. large detuning, and of beams' polarizations.

The intensity patterns created by the different polarization components are plotted in Fig. 3.5b and the total interference pattern is illustrated in Fig. 3.6. For the case of tilted and linear polarizations, i.e. $\phi_i = 0$ in eq. 3.26, the minima of the s-component create a pattern that has a honeycomb symmetry while the maxima are arranged in a triangular pattern. The opposite happens for the p-polarized component and its maxima are overlapped with the minima of the s-polarized potential when $\phi_i = 0$, as in the example presented in Fig. 3.5b. Depending on the tilts θ_i and

on the wavelength, triangular or honeycomb lattices can be implemented. When the phases ϕ_i of the electric fields $\mathbf{E}_i$ are different for the three beams, the two potentials created by the interferences I_s and I_p are shifted relative to each other. This adds an energy offset between the A and B sites, minima of the honeycomb lattice potential, as illustrated by the plots of the interference pattern in Fig. 3.6b. The control of the s and p polarization components of the lattice beams allows for a precise tuning of the energy offset between the A and B sublattices, as suggested in [95], and, consequently, of the spread in Berry curvature. The good control on polarization tilts could also be used for creating flux lattices, as proposed in [68, 135], or dynamic optical superlattices [136].

3.2.3. The honeycomb optical lattice

In order to create a honeycomb lattice potential with no energy offset between the lattice sites, the frequency of the lattice beams is far detuned from the D-lines of the alkali atoms (^{87}Rb and ^{40}K) that we are using in our experimental realization. The light is blue detuned from the atomic transitions (λ_L=755nm) and the beams' polarizations are linear and pointing along the z-axis, i.e. $\theta_i = \phi_i = 0$. With this settings, the atoms will be trapped in the minima of the honeycomb potential described by eq. 3.27 due to the optical dipole force. The optical lattice potential is given by

$$
\begin{aligned}
V_L(\mathbf{r}) =& U_0 \left| \sum_{i=1}^{3} \sqrt{I_i} e^{-i\mathbf{k}_i \cdot \mathbf{r}} \right|^2 \\
=& V_1 + V_2 + V_3 + 2\sqrt{V_1 V_2} \cos((\mathbf{b}_1 - \mathbf{b}_2)\mathbf{r}) \\
& + 2\sqrt{V_1 V_3} \cos(\mathbf{b}_2 \mathbf{r}) + 2\sqrt{V_3 V_2} \cos(\mathbf{b}_1 \mathbf{r}),
\end{aligned}
\tag{3.29}
$$

where the $V_i \propto I_i$ is the ac Stark shift produced by the ith beam. The reciprocal lattice vectors of the honeycomb optical lattice are given by $\mathbf{b}_1 = \mathbf{k}_2 - \mathbf{k}_3$ and $\mathbf{b}_2 = \mathbf{k}_1 - \mathbf{k}_3$. From this definition and eq. 3.3, the distance between the A and B sites is obtained, $d_L = \frac{2}{3\sqrt{3}} \lambda_L$. The values of the potentials V_i are typically given in unit of the recoil energy, $E_r = \hbar^2 k_L^2 / (2m)$, which is about $E_r \sim 4$ kHz for ^{87}Rb. If the intensities of the beams are all the same, $I_{1,2,3} = I_0$, and $\Delta = 0$ the lattice is a perfect hexagon. The corresponding intensity pattern is illustrated in Fig. 3.6a. In this case, the lattice depth is set by the barrier height between neighboring sites which is given by the single beam light shift V_0. If the lattice beams have different intensities, instead, the rotational symmetry of the lattice potential is broken and the resulting potential looks stretched, as illustrated by the schematics of Fig. 3.7a and as explained in Section 3.1.2. In the graph, the intensities of two lattice beams are changed relative to the third by setting $I_{2,3} = f I_1$ in eq. 3.29. The lower the
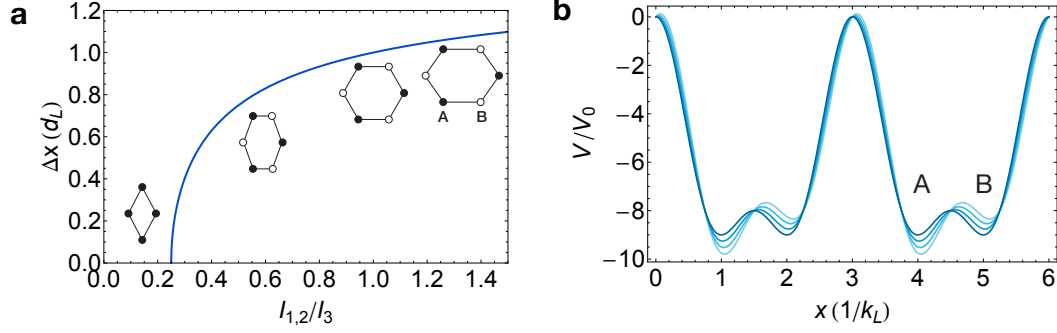
Figure 3.7.: **(a)** A relative intensity imbalance between the lattice beams $(I_{1,2}/I_3)$ modifies the separation between between two wells Δx_0 along a certain direction. The insets illustrate how the real space lattice potential is modified by the imbalance. **(b)** Lattice potential for different energy offsets Δ between the A and B sites ($\Delta = 0 - 1.5\ E_r$, from dark to light blue), introduced via the potential of eq. 3.30.

imbalance factor f, the smaller the separation between two lattice sites will be along the merging direction. As the imbalance gets stronger ($f \ll 1$), two lattice sites move towards each other and merge, and the lattice becomes a rhomboid, as illustrated in figure. In the other limit, when $I_3 = 0$, the lattice is a 1D lattice.

Effect of imperfect polarizations

In practice, experimental imperfections, such as the birefringence of the glass cell or imperfect polarizers, can break the inversion symmetry of the lattice by introducing an additional potential created by the p-polarized component of the light. As described by equations 3.27 and 3.28, a tilt of the polarization angles θ and ϕ in at least two beams is enough to introduce an energy offset Δ between the A and B sites. To allow for a small energy offset, and therefore for a finite Berry curvature in our model, we add to the potential of eq. 3.29 a 1D lattice potential created by two running waves that have imperfect polarizations. This potential is modeled, without loss of generality, using the following equation

$$V_p(x) = \frac{\Delta}{\sqrt{3}} \sin(\sqrt{3}k_L x) \tag{3.30}$$

where Δ depends on the polarizations' angles θ_i and ϕ_i. The eq. 3.30 is derived in appendix A. The effect of this additional 1D lattice on the A and B wells is to add an energy offset between the two sites, as illustrated in the plot of Fig. 3.7b. The potential of eq. 3.30 is not the most homogeneous way of introducing an AB offset as it also introduces a distortion of the lattice geometry. If one is interested in maximizing the offset between the A and B sites, it would be best to add not a

1D lattice but a triangular one, which has the same periodicity of the honeycomb potential by construction.

3.3. Single particle in the honeycomb optical lattice

In this section, the Schrödinger equation is solved numerically for a non-interacting particle in the optical potential. As our experiments are performed outside the tight-binding regime, all theoretical modeling of the system is based on ab initio band-structure calculations which incorporate the full lattice potential described by the equations 3.29 and 3.30. The corresponding energy spectrum and the topological features are then derived from it.

3.3.1. Solving the Schrödinger equation

Given the periodic potential of eq. 3.29, the Hamiltonian of a non-interacting particle is

$$\hat{H}_0(\mathbf{r}) = \frac{\hat{\mathbf{p}}^2}{2m} + V_L(\mathbf{r}). \tag{3.31}$$

According to the Bloch theorem, the eigenfunction of the nth band with quasimomentum $\mathbf{k}$ are the Bloch waves, see eq. 2.12. The eigenfunction $u_k^n(\mathbf{r})$ has the same translational symmetry as the honeycomb lattice potential: $u_k^n(\mathbf{r}) = u_k^n(\mathbf{r} + \mathbf{R})$ with $\mathbf{R} = \sum_i n_i \mathbf{a}_i$. By making this ansatz for the wavefunctions, the Schrödinger equation is simplified to derive the eigenvalue equation for the periodic part of the Bloch waves, see eq. 2.14 and eq. 2.15. The potential $V_L(\mathbf{r})$ and the periodic part of the Bloch functions $u_k^n(\mathbf{r})$ can be written as the following Fourier series

$$V_L(\mathbf{r}) = \sum_j v_j e^{i\mathbf{G}_j \mathbf{r}} \quad \text{and} \quad u_k^n(\mathbf{r}) = \sum_j c_j^{n,k} e^{i\mathbf{G}_j \mathbf{r}}. \tag{3.32}$$

Contrary to the case of a square lattice, the Hamiltonian for the honeycomb lattice is not separable and the summations in equations 3.32 run over all combinations of reciprocal lattice vectors $\mathbf{G_j} = \sum_{j \in \mathbb{Z}} n_j \mathbf{b}_1 + m_j \mathbf{b}_2$, where n_j, m_j are integers and $n_j + m_j = j$. We keep the short notation for the sake of clarity. Using this expansions, the Schrödinger equation results in an equation for the coefficients $c_j^{n,k}$

$$E_k^n c_j^{n,k} = \frac{\hbar^2 (\hat{\mathbf{G}}_j + \mathbf{k})^2}{2m} c_j^{n,k} + \sum_{j'} v_{j-j'} c_{j'}^{n,k}. \tag{3.33}$$

Finally, the Schrödinger equation is further simplified by noting that the expansion of the potential has few nonzero terms due to the simple form of the lattice potential described by eq. 3.29. These non-vanishing terms correspond to $j = \pm 1, 0$. As an
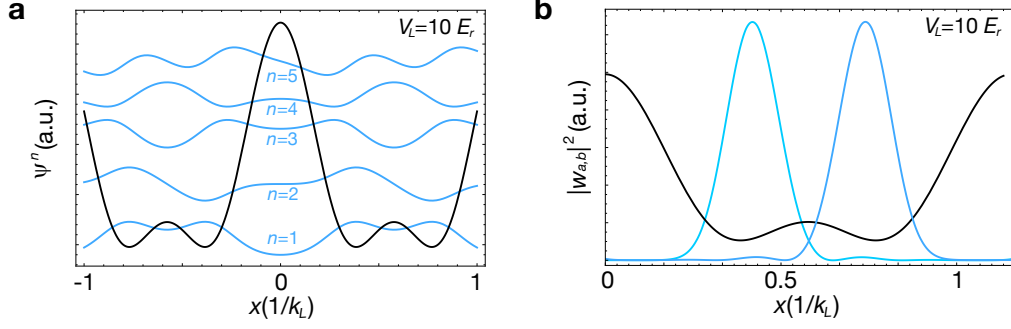
Figure 3.8.: **(a)** Potential (black) with the corresponding Bloch wavefunctions (blue) for the first six bands calculated at the Γ-point, i.e. $\mathbf{k} = 0$. Bloch waves are ordered by their energies, increasing from bottom to top. **(b)** Wannier functions localized on the A and B sites, $w_A(\mathbf{r})$, $w_B(\mathbf{r})$, (blue) together with the potential (black). With a 10 E_r lattice depth there is a small but finite overlap between the two localized functions.

example, the coefficients for a balanced honeycomb lattice are $v_{\pm 1} = v_{\pm \mathbf{k}_1} = v_{\pm \mathbf{k}_2} = v_{\pm \mathbf{k}_1 \mp \mathbf{k}_2}$ and $v_0/v_{\pm 1} = 3$. The equation 3.33 is therefore rewritten in a simple matrix form as $E_k^n c_j^{n,k} = \sum_{j'} H_{j,j'} c_{j'}^{n,k}$. The matrix elements $H_{j,j'}$ are given by

$$H_{j,j'}(\mathbf{k}) = \left(\frac{\hbar^2 (\hat{\mathbf{G}}_j + \mathbf{k})^2}{2m} + v_0 \right) \delta_{j,j'} + v_{\pm 1}\ \delta_{j,j'\pm 1}. \tag{3.34}$$

where one has to remember that the index j labels a combination of reciprocal lattice vectors. The eigenenergies and eigenvectors are numerically evaluated by diagonalizing such matrix which is truncated to some finite n. This truncation corresponds to the number of bands that we need to include to make a good enough approximation of the Hamiltonian, eq. 2.15, or, equivalently, the high frequency components of the Fourier series which can be truncated because they have small enough weights $c_j^{n,k}$.

3.3.2. Wannier functions and tight-binding limit

The Bloch basis is not always the most convenient one. The Wannier basis can also be used to describe the properties of the lattice and it is particularly convenient when we want to rewrite the Hamiltonian of eq. 3.34 in terms of local operators acting on the different lattice sites, as we have seen in Section 3.1. The Wannier function of a particle localized at a lattice site $\mathbf{r}_{a,b}$ of the A or B sublattice in the band n is defined by eq. 2.16. For a symmetric honeycomb configuration and deep lattice potential, the Wannier functions localized on the A or B sites can be constructed as an equal superposition of the Wannier functions of the first and second band, w^1

and w^2, according to

$$w_A(\mathbf{r}) = \frac{1}{\sqrt{2}}(w^1(\mathbf{r}) - w^2(\mathbf{r})) \tag{3.35}$$

$$w_B(\mathbf{r}) = \frac{1}{\sqrt{2}}(w^1(\mathbf{r}) + w^2(\mathbf{r})). \tag{3.36}$$

For an asymmetric potential, instead, the Wannier functions need to be found by maximizing the localization of the functions numerically [137]. Plots of the localized Wannier functions and of the delocalized Bloch wavefunctions are shown in Fig. 3.8 for the honeycomb lattice with balanced beams' intensities.

The Bloch states on the A or B sublattice are rewritten as

$$\psi_{a,b}^{n,k}(\mathbf{r}) = \frac{1}{\sqrt{N}} \sum_{\mathbf{r}_{a,b}} e^{ik\mathbf{r}_{a,b}} w^n(\mathbf{r} - \mathbf{r}_{a,b}). \tag{3.37}$$

By making an ansatz for the field operator, which is generally given by a superposition of field operators for particles in the A and B sites, the Hamiltonian can be rewritten in terms of the creation and annihilation operators $\hat{c}_{\mathbf{r}_{a,b}}^\dagger, \hat{c}_{\mathbf{r}_{a,b}}$ of an atom in the Wannier state $w(\mathbf{r}_{a,b})$ localized at the site $\mathbf{r}_{a,b}$. By increasing the lattice depth, the Wannier functions get more and more localized to a lattice site. The tight-binding limit is reached when the Wannier functions have a significant overlap only with the ones of the nearest neighboring lattice sites. In this case, only the hopping between nearest neighboring sites is relevant and the Hamiltonian will reduce to the one of the the tight-binding model of the hexagonal lattice, eq. 3.5. The tunnelings $J_{\mathbf{r}_a,\mathbf{r}_b}$, describing the hopping between neighboring A-B sites, are defined as

$$J_{\mathbf{r}_a,\mathbf{r}_b} = -\int_{-\infty}^{\infty} w^*(\mathbf{r} - \mathbf{r}_a)\left(-\frac{\hbar^2}{2m}\nabla_{\mathbf{r}}^2 + V_L(\mathbf{r})\right)w(\mathbf{r} - \mathbf{r}_b)d\mathbf{r}. \tag{3.38}$$

Finally, it is interesting to note that there is a relation between the topological features of a band and the center of mass position defined via the Wannier functions of that band. This connection becomes clear when we write down the matrix elements of the position operator in reciprocal space. By making use of the definition of the Wannier functions and of Bloch waves, see eq. 2.12 and 2.16, and the definition of the position operator $\hat{\mathbf{r}} = i\hbar\nabla_{\mathbf{r}}$, we can note that

$$\hat{\mathbf{r}}\left|w^n(\mathbf{r} - \mathbf{r}_0)\right\rangle = \frac{1}{\sqrt{N}} \sum_{\mathbf{k}} i\nabla_{\mathbf{k}}(e^{i\mathbf{k}(\mathbf{r} - \mathbf{r}_0)}\left|u_{\mathbf{k}}^n\right\rangle). \tag{3.39}$$

By writing the Wannier functions in an explicit form, the matrix elements of the

position operator simplify to [137, 138]

$$\langle w^n(\mathbf{r} - \mathbf{r}_0)| \,\hat{\mathbf{r}}\, |w^n(\mathbf{r})\rangle = \frac{1}{\sqrt{N}} \sum_{\mathbf{k}} e^{i\mathbf{k}\mathbf{r}_0} \mathbf{A}_{\mathbf{k}}^n, \tag{3.40}$$

where the Wannier functions are calculated at different lattice sites $\mathbf{r}_0$ and $\mathbf{A}_{\mathbf{k}}^n$ is the Berry connection. We can thus describe the Berry connection in terms of these matrix elements according to

$$\mathbf{A}_{\mathbf{k}}^n = \frac{1}{\sqrt{N}} \sum_{\mathbf{r}} e^{-i\mathbf{k}\mathbf{r}} \langle w^n(\mathbf{r})| \,\hat{\mathbf{r}}\, |w^n(0)\rangle . \tag{3.41}$$

These relations illustrate the close connection between the localization of the Wannier functions and the topological properties of bands which can be seen as a way of mapping of the density distribution of particles in the lattice. If the Wannier states can be chosen to be exponentially localized in real space, the only non-zero element of the position operator would be the one with $\mathbf{r}_0 = 0$, see eq. 3.40. In this case the Berry connection is trivial because it is independent on $\mathbf{k}$ and the Chern number of that band is zero. This is not true when the off-diagonal elements of the position operator cannot be set to zero, i.e. when the Wannier states can not be simultaneous eigenstates of the band projected coordinate operators in all three directions and thus can not be exponentially localized to a lattice site. This relation between localization of Wannier states and topological properties of bands has been derived in the context of polarization of crystalline solids [120, 137, 139] where the charge polarization is given by the sum of the center of charge of the Wannier states, see eq. 3.40, summed up over all contributing bands [139]. The change of polarization for loops covering the entire Brillouin zone gives an intuitive understanding of how the quantized Hall response relates to the Chern number of a band and to the properties of its Wannier functions.

3.3.3. Energy bands from the full model

The energy bands can be calculated directly from the Hamiltonian described by eq. 3.34 for any lattice depth. Since the wavefunctions repeat themselves by a reciprocal lattice vector $\mathbf{b}_1, \mathbf{b}_2$, it is enough to restrict the bands and the states to quasimomenta within the first Brillouin zone, which can be chosen to have honeycomb symmetry. In the case of no energy offset between the sublattices and equal tunnelings, $J_i = J$, the energy bands present degeneracy points between two consecutive bands as a direct consequence of the bipartite nature of the honeycomb lattice. For the example, the first and second band touch at the $\mathbf{K}$ and $\mathbf{K}'$ points, corners of the Brillouin zone, the third and fourth touch at the Γ-point and so on. This degeneracies are shown in the plots of the energy bands of Fig. 3.9. It is important
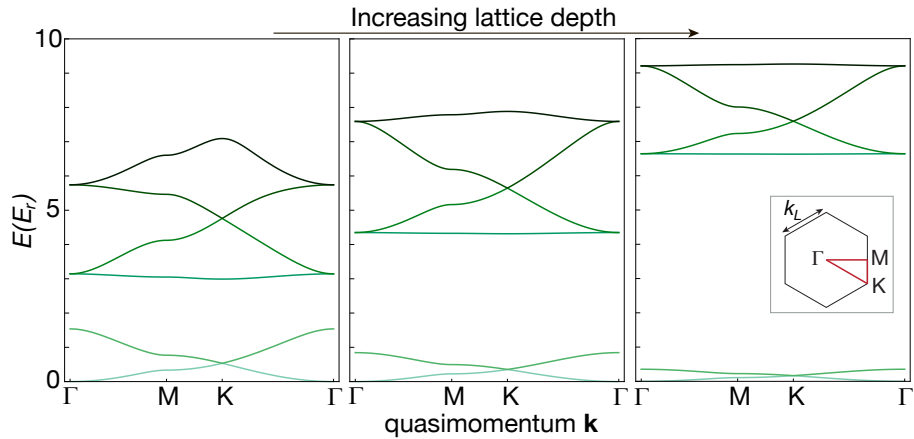
Figure 3.9.: Plots of the first six bands along the path in the BZ depicted in red in the inset. The lattice depths are 2-5-10 E_r from left to right.

to note that the degeneracy points, consequence of the symmetries of the lattice, are present at any lattice depth. When the lattice depth increases the energy difference between the first and the second band decreases, as we expect from the Hamiltonian of eq. 3.8 since the tunneling J between the A and B sites sets the energy difference between the first and second band. The same happens for any pair of 'mirror' bands with higher energies. For a deep enough lattice the Hamiltonian reduces to the one of the tight-binding limit. The system is deeply in the tight binding regime when the ratio of nearest-neighbor and next-nearest-neighbor tunneling is $J_{n.n.n.}/J_{n.n.} \sim 10^{-2}$, corresponding to a lattice depth of $\sim 15\ E_r$ for the honeycomb lattice, as illustrated by the graph in Fig. 3.10a. The dispersion of two lowest bands approaches the tight-binding solution with increasing lattice depth, as the plot in Fig. 3.10b shows.

The degeneracy at the Dirac points is a consequence of the combined time-reversal and inversion symmetry of the lattice potential. The introduction of any asymmetry between the A and B sublattices is liable to open an energy gap of size Δ at the degeneracy points. This can occur when the beams' polarizations have some in-plane polarization component, which can be set on purpose or can be introduced when the beams' polarizations are imperfect. Such imperfection can add the potential of equation 3.30 which breaks inversion symmetry of the lattice. An energy gap at the Dirac points can also be introduced by breaking time-reversal symmetry. This has been done in cold-atoms experiments by circularly shaking the lattice potential [82], which adds complex next-nearest-neighbor tunnelings and realizes the Haldane model [20].

Moving and merging the Dirac cones

As we have seen in Section 3.1.2, the location of the Dirac points in the Brillouin zone can be changed by modifying the nearest-neighbor tunnelings along the three
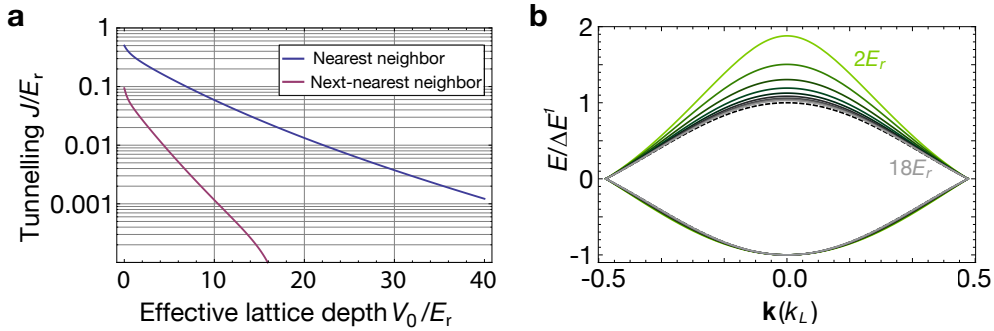
Figure 3.10.: Tight binding limit for the honeycomb lattice. Plots of **(a)** the nearest-neighbor and next-nearest-neighbor tunnelings and **(b)** first and second bands along a path connecting the two Dirac points and for different lattice depths V_0. Energy bands are in units of the bandwidth of the first band $\Delta E^1(V_0)$. The tight binding solution, dashed line in **(b)**, is plotted.

hopping directions. In solid state graphene this can be done by strain [140], but moving and merging the Dirac points is not easily achieved in solid state systems due to fracture under tensile stress of the samples [126]. Ultracold atoms in a honeycomb lattice are, instead, a favorable setup for observing the effect of strain thanks to the high degree of control on the optical potential, as the experimental work in [141] showed. In our setup, the distortion of the lattice structure is introduced via a relative imbalance of the beams' intensities which modifies the lattice potential, see Section 3.2.3. The power imbalance results in a modification of the tunneling rates along the three hopping directions and, consequently, of the energy bands which are obtained from the ab initio calculations described in Section 3.3.1.

For simplicity, we assume that the intensities of two lattice beams are changed relative to the third, setting $V_{1,2} = fV_3$. The lower the power imbalance factor f, the smaller the separation between the Dirac points along the y direction becomes, as illustrated in the sequence of plots of Fig. 3.11. At a critically low imbalance factor f_c, the Dirac points merge and a gap opens at the **M** point for $f < f_c$. For the lattice depth of 1 E_r, which is considered in Fig. 3.11, $f_c \simeq 0.25$. As illustrated by the graph of Fig. 3.11c, this critical imbalance f_c depends on the chosen lattice depths V_i that set the tunneling rate J_i. This dependence indicates that the merging of the Dirac points does not relate to the change of symmetry in real space: the lattice is still a honeycomb lattice but it has no degeneracy points when the hopping rates are strongly imbalanced. From the graph of Fig. 3.11c one can also note that the deeper the lattice the more crucial it is to stabilize the relative intensities of the lattice beams, since a small relative change of powers can lead to a substantial modification of the energy bands.
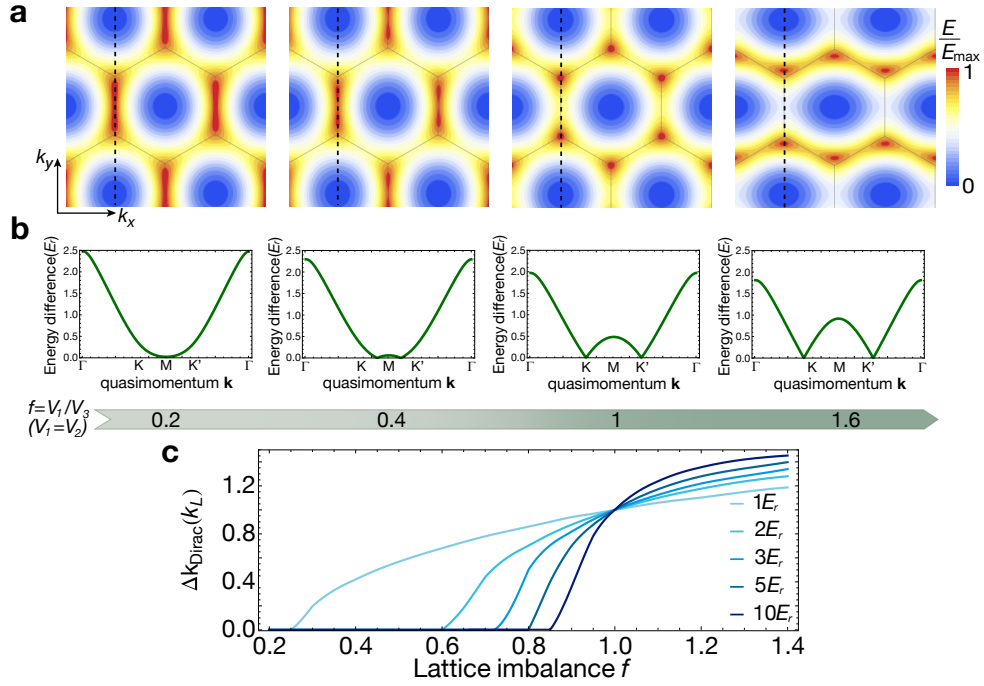
Figure 3.11.: Energy spectrum and movement of the Dirac points. **(a)** 2D plots of the lowest energy band for a $1\,E_r$ lattice from *ab initio* calculations as a function of intensity imbalance $f = V_{1,2}/V_3$ for $V_1 = 1\,E_r$. The color scale on each plot is normalized to the band width $E_{\max}$. The dashed lines indicate the merging direction for this specific choice of power imbalances. **(b)** Energy splitting between the two lowest bands for a cut along the merging direction ($k_x^{\mathrm{fin}}{=}0$) which shows the motion of the Dirac points. **(c)** Distance between two Dirac points, $\Delta\mathbf{k}_{\mathrm{Dirac}}$, versus lattice imbalance f for different lattice depths.

3.3.4. Topological features

The Berry curvature and Berry connection can be computed from the eigenvectors of the full model presented in Section 3.3.1 even away from the tight-binding limit. The distribution of Berry curvature in the Brillouin zone and the winding of the Berry connection are illustrated in Fig. 3.12 for different lattice imbalances f. It can be seen from the plot in Fig. 3.12a that the distribution of the Berry curvature obtained from ab initio calculations resembles the one we derived in Section 3.1. The Berry fluxes move together with the degeneracy points when the lattice balance is changed, as illustrated in Fig. 3.12b. At a critically low imbalance factor f_c the Dirac points merge and the corresponding Berry fluxes of opposite sign annihilate, leaving a gapped spectrum with no topological features for $f < f_c$, as it can be seen from the last plot of Fig. 3.12 which illustrates that there is no winding of the spinor's phase anywhere in the reciprocal space. In this last scenario, we expect to
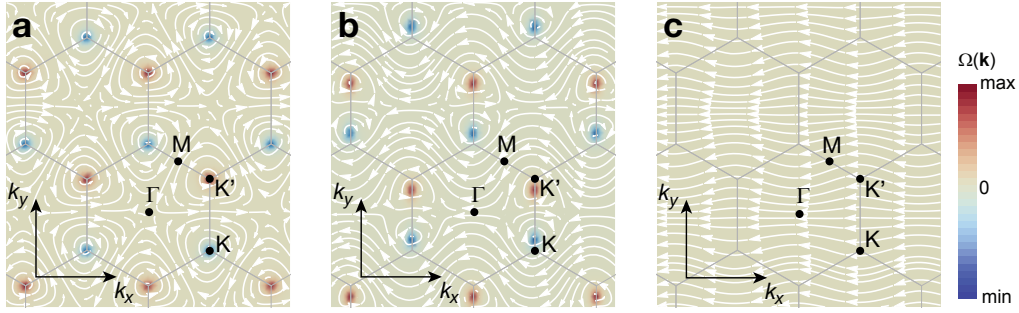
Figure 3.12.: Berry curvature Ω_1 and Berry connection $\mathbf{A}_1$ (white arrows). Lattice depth is 1 E_r and $\Delta = 0.5$ J for visualization purposes. The power imbalance increases from left to right: $f = 1, 0.8, 0.2$. **(a)** For $f = 1$ the Dirac points and the corresponding fluxes are located at the corners of the Brillouin zone (gray hexagons). Upon imbalance, the fluxes move together with the Dirac cones **(b)**. When the Dirac points have merged **(c)**, the topological features related to the winding of the spinor are lost.

measure a Berry phase of zero for any closed loop in the Brillouin zone.

Chapter 4.

Ultracold atoms: the experimental setup

Since the first realization of Bose-Einstein condensation [27, 28] there has been an increasing number of experiments with ultracold atoms studying bosonic or fermionic species at ultracold temperatures. The techniques for cooling and manipulating alkali metal atoms are quite standard by now. A comprehensive description of the physical processes behind the different cooling schemes can be found in numerous references [142–144]. In our experimental realization, we cool bosonic Rubidium (^{87}Rb) and fermionic Potassium (^{40}K) atoms to condensation and degeneracy. Since the cooling techniques for this particular mixture have been studied in depth in the past, we reference to previous works for a comprehensive description of the cooling processes and of the challenges to face [145–149]. In this chapter, our experimental setup is presented focusing on specific details of our apparatus. Many technical details regarding our new setup can be found in the following theses [150–152] which mostly focus on the early stage of the building process: the design of vacuum setup and transport coils [150], the characterization of the MOTs [151] and the dipole trap design [152]. These details are briefly summarized here. After a short intorduction on ultracold atoms and on the techniques to manipulate them, Section 4.1, the setup and the different cooling stages for ^{40}K and ^{87}Rb are presented, Sections 4.2 and 4.3. Finally, standard detection techniques are introduced, Section 4.4.

4.1. Ultracold atoms

4.1.1. Bosons and fermions

Indistinguishability of particles is a fundamental concept in quantum theory as quantum statistics determines how the many-particle wavefunctions should be constructed. The behavior of an ideal gas of N indistinguishable bosonic atoms differs fundamentally from the fermionic case because of their different exchange statistics [153–158]. For N non-interacting spinless bosons, the many-body ground state is the one where all the particles occupy a single-particle ground state. In the case of

fermions, instead, each single-particle state can only be occupied by a single fermion, thus the many-particle ground state is realized when the lowest N single-particle states are completely filled up to the Fermi energy ϵ_F, energy of the last occupied single-particle state. In reality, the systems we are studying have always a finite temperature. It is thus necessary to take into account the statistical distribution of the particles in the different energy levels ϵ_i when describing the properties of the system. At finite temperature, the mean occupation of a single particle eigenstate ϵ_i for a thermalized system of non-interacting bosons and fermions is described by the distributions

$$f_{B,F}(\epsilon_i) = \frac{1}{e^{(\epsilon_i-\mu)/k_BT} \mp 1} \tag{4.1}$$

where k_B is the Boltzmann constant, T the temperature of the gas and μ the chemical potential. Reaching condensation and degeneracy depends on all the properties of the system, as temperature, dimensionality, densities and atom numbers as they determine the single particle density of states and the chemical potential.

Here we consider the gases to be confined in a three-dimensional harmonic trapping potential

$$V_{ho}(x, y, z) = \frac{m}{2}(\omega_x^2 x^2 + \omega_y^2 y^2 + \omega_z^2 z^2) \tag{4.2}$$

where ω_i denote the trap frequencies along the three directions and m the mass of the particles. The energy levels are given by eigenenergies of the harmonic oscillator and the properties of the system can be calculated analytically since the density of states takes the simple form $g(\epsilon_i) = \epsilon_i^2/(2\hbar^3\bar{\omega}^3)$, with $\bar{\omega} = (\omega_x\omega_y\omega_z)^{1/3}$ being the geometrical mean of the trap frequencies. The most relevant distributions for harmonically trapped fermions and bosons are summarized in the appendix B.

Some parameters of the trapped gases are particularly important when condensation or degeneracy has to be reached. For fermions, the important energy scale is the Fermi energy ϵ_F. In the case of a harmonic trap [144, 159, 160], ϵ_F is easily derived from the density of states $g(\epsilon_i)$ and the statistical distribution for particles at zero temperature. The Fermi energy for N particles is described by

$$\epsilon_F = \hbar\bar{\omega}(6N)^{1/3} \tag{4.3}$$

and the corresponding Fermi temperature is given by $T_F = \epsilon_F/k_B$. When the temperature of fermionic gas decreases, more and more atoms will occupy the lowest energy states in an ordered manner and the Fermi-Dirac distribution will approach a step function. We can infer the degeneracy of the gas by the ratio T/T_F which is indicative of the amount of particles with energy above the Fermi level and of their Fermi-Dirac distribution.

The behavior of gas of bosonic particles at low temperatures is very different from the fermionic one [155, 156, 161]. When the temperature decreases, the ground state of the system of energy ϵ_0 becomes macroscopically occupied. The origin of

this phase transition is deeply linked to the Bose-Einstein distribution. Since the distribution f_B can not be negative, the chemical potential is bounded, $\mu < \epsilon_0$. The upper bound of μ results in a saturation of the thermal distribution when the number of particles is increased and μ reaches its maximum value. The critical temperature T_c of this phase transition is given by [142]

$$T_c \approx 0.94\hbar\bar{\omega}(N)^{1/3} \tag{4.4}$$

for non interacting particles in a harmonic trap. From a semiclassical approximation, one can also derive a value for the density at which the phase transition occurs which is $n_c = 2.612\lambda_{dB}^3$, λ_{dB} is the de Broglie wavelength. Below T_c, the occupation of the ground state N_0 becomes macroscopic. The many-body ground state is described by a macroscopic wavefunction, or order parameter, proportional to the ground state wavefunction of the harmonic oscillator $\psi_0(\mathbf{r})$ [142]

$$\phi_0(\mathbf{r}) = \sqrt{N}\psi_0(\mathbf{r}). \tag{4.5}$$

4.1.2. The contact potential

The scattering between two particles is a standard quantum mechanical textbook problem [162], here we focus on the case of collisions with low scattering energies, i.e. ultracold temperatures. In this case, the mean distance between the particles is typically much larger than the range of the interaction and the details of the molecular potential are not resolved. Consequently, the collisional properties, that generally involve calculating a very complex interatomic potential, can be simplified by taking into account incoming waves with small wave-vector, $\mathbf{k} \to 0$. To solve the scattering problem it is enough to consider s-wave collisions [163]. The entire scattering problem is modeled by a single parameter, the s-wave scattering length a_s, and the interaction potential U_I is described by an effective contact interaction which is a delta-function

$$U_I = g\delta(\mathbf{r}) \tag{4.6}$$

where $\mathbf{r}$ is the interparticle distance, g is the scattering amplitude which is

$$g = \frac{2\pi\hbar^2 a_s}{\mu_{1,2}} \tag{4.7}$$

for collisions between particles with mass m_1 and m_2 with reduced mass of the two colliding particles $\mu_{1,2} = m_1 m_2/(m_1 + m_2)$. The scattering length a_s depends on the atomic species and the states involved in the collision process. A final important aspect to consider is the symmetry. The spatial part of the two-body scattering wavefunction, solution of the two-body scattering problem, is radially symmetric for s-wave scattering. Therefore, fermions in the same spin state have a vanish-

ing s-wave scattering length due to their quantum statistics and the lowest partial wave contributing to the scattering problem is the p-wave term that is negligible at ultracold temperatures. This means that a single component Fermi gas is non-interacting. The situation is different for a mixture of fermions in different hyperfine states [144, 160].

4.1.3. Weakly interacting Bose gas

The exchange of energy and momentum due to collisions between ground-state atoms can excite particles to higher energy levels, out of the condensate. Due to the interaction term, the ground state can not be the same as the ground state of the non-interacting Hamiltonian, eq. 4.5, but it has to include the finite overlap with the excited states. A weakly interacting BEC is modeled by the Gross-Pitaevskii equation. An in depth review of interaction effects in a Bose gas can be found in [143, 164, 165]. To derive the Hamiltonian of the interacting system, the bosonic field operator $\hat{\psi}(\mathbf{r})^{\dagger}$ that creates a particle at the position $\mathbf{r}$ is introduced. The Hamiltonian with the interaction term given by the potential of eq. 4.6 is

$$H = \int \hat{\psi}^{\dagger}(\mathbf{r}, t) \left(-\frac{\hbar^2 \nabla^2}{2m} + V_{ho}(\mathbf{r}, t) \right) \hat{\psi}(\mathbf{r}, t) + \frac{g}{2} \hat{\psi}^{\dagger}(\mathbf{r}, t) \hat{\psi}^{\dagger}(\mathbf{r}, t) \hat{\psi}(\mathbf{r}, t) \hat{\psi}(\mathbf{r}, t) \; d\mathbf{r}.$$

(4.8)

For simplicity we considered a single component Bose gas and dropped the spin dependence of the field operator. For a dilute weakly interacting system, the Schrödinger equation is solved with a mean field approximation of the field operator, which is decomposed in a mean field condensate contribution and a correction term describing atoms in excited states, i.e. $\hat{\psi}(\mathbf{r}, t) = \langle \hat{\psi}(\mathbf{r}, t) \rangle + \delta\hat{\psi}(\mathbf{r}, t)$. By neglecting the perturbation term, the Gross-Pitaevskii equation for the order parameter, $\langle \hat{\psi}(\mathbf{r}, t) \rangle = \phi_0(\mathbf{r}, t)$, is derived

$$i\hbar \; \partial_t \phi_0(\mathbf{r}, t) = \left(-\frac{\hbar^2 \nabla^2}{2m} + V_{ho}(\mathbf{r}) + g|\phi_0(\mathbf{r}, t)|^2 \right) \phi_0(\mathbf{r}, t).$$

(4.9)

This differential equation can be further simplified for the stationary case to obtain an approximated solution for the many-body wavefunction as well as the density profile of atoms in the trap, $n(\mathbf{r}) = |\phi_0|^2$, that takes the well known inverted parabola profile for an harmonic trapping potential [166, 167]. More on the Thomas-Fermi profile and distributions of atoms in a harmonic trap can be found in the appendix B. By including the perturbation term $\delta\hat{\psi}(\mathbf{r}, t)$, a set of differential equations for the excitations, the Bogoliubov modes, is derived to study the stability of the condensate and to find the collective modes and elementary excitations that can be populated during its dynamics [164, 168]. Depending on the system parameters, the superfluidity can even be lost. One well known example is the loss of superfluidity

for particles moving at a constant velocity v greater than the critical velocity of the superfluid, $v > v_c = min|\epsilon(p)/p|$ where $\epsilon(p)$ is the spectrum of the excitations [164, 169]. This is only one example of possible types of excitations that can be activated by collisions and dynamics. For most of the results presented in this thesis the effects of weak interactions can be safely neglected. However, we will see in the following chapters concerning the lattice that superfluidity and, consequently, the coherence of the many-body wavefunction can be lost when the condensate is moving with a finite velocity in the lattice potential. This effect will put a limit on experimental timescales. Properties of the weakly interacting gas in the honeycomb lattice are derived in the appendix C.

4.1.4. Tuning interactions with a magnetic field

Magnetic fields are a valuable tool for ultracold atoms' experiments as they can be used as a trapping potential or as a homogeneous energy offset to tune interactions between atoms. Given the electronic configuration of alkali-atoms, the interaction of a weak magnetic field $B(\mathbf{r})$ with the total atomic angular momentum F lifts the degeneracy between the m_F sublevels. The Zeeman energy shift is

$$E_Z(\mathbf{r}) = \mu_B g_F m_F |B(\mathbf{r})| \tag{4.10}$$

where μ_B is the Bohr magneton, g_F is the Landé g-factor for the specific hyperfine state m_F of an alkali-atom. For stronger magnetic fields the Breit-Rabi formula has to be used to compute the correct energy shifts. Depending on their m_F state the atoms will lower or rise their energy in presence of the external field.

Coils in anti-Helmholtz configuration create an inhomogeneous magnetic field of the kind $B(\mathbf{r}) \propto B'|\mathbf{r}|$ which is used to magnetically trap atoms in a low-field seeking state at the minimum of the magnetic field. Coils in Helmholtz configuration can be used, instead, to apply a constant and homogeneous field offset which allows to tune the contact potential of eq. 4.6 by tuning the magnitude and sign of the scattering length a_s when a Feshbach resonance is available. The basic idea is to approach a scattering resonance between an open channel, constituted by two incoming atoms in the hyperfine states $|F_1, m_{F1}\rangle$ and $|F_2, m_{F2}\rangle$, and one (or more) closed channels, $|F_3, m_{F,3}\rangle$ and $|F_4, m_{F,4}\rangle$, with $m_{F,1} + m_{F,2} = m_{F,3} + m_{F,4}$. The channels can couple thanks to the additional spin-dependent interaction term present in the interatomic potential at short distances. Open and closed channels are offset in energy and this energy difference is tuned with an external magnetic field which shifts the energy of each state according to eq. 4.10. The open channel is thus tuned close to resonance with the last molecular bound state of the closed channel [170, 171]. By approaching this Fano-Feschbach resonance the scattering length can be adjusted at will [172, 173], from attractive to repulsive. In proximity of the resonance of width Δ_F happening at a magnetic field offset of magnitude B_0, the scattering length is

given by

$$a(B) = a_{bg} \left(1 - \frac{\Delta_F}{B - B_0} \right) \tag{4.11}$$

where a_{bg} is the background scattering length far away from resonance, for $B = 0$. We reference to [35] for a complete overview on Feshbach resonances in ultracold gases.

4.2. Experimental setup

4.2.1. ^{87}Rb and ^{40}K

In our setup the bosonic ^{87}Rb and the fermionic ^{40}K species are the alkali-metal atoms we want to cool down to condensation and degeneracy. The details of their atomic properties and optical transitions can be found in the following references [174, 175]. The lowest hyperfine manifolds are shown in Fig. 4.1 together with the relevant optical transitions that are used to manipulate and cool the atoms. The ^{87}Rb-^{40}K mixture has good collisional properties that allow ^{87}Rb to be used as a coolant for the fermions, even without tuning interactions via a Feshbach resonance. In particular, the interspecies scattering length for the true ground-states, $|F = 1, m_F = +1\rangle$ for ^{87}Rb and $|F = 9/2, m_F = -9/2\rangle$ for ^{40}K, is attractive, $a_{K,Rb} = -184\ a_0$ [176, 177], $a_0 = 0.0529$ nm being the Bohr radius. The collisional properties between the states $|F = 2, m_F = +2\rangle$ and $|F = 9/2, m_F = +9/2\rangle$ are also favorable for sympathetic cooling, $a_{K,Rb} \sim -300\ a_0$ [178]. The attractive interactions with a fairly large scattering length ensure a good spatial overlap of the clouds in the traps during the different stages of evaporation and, consequently, good thermalization. The background scattering length for the groundstate of ^{87}Rb is instead repulsive, $a_{Rb,Rb} = 100.4\ a_0$ [179, 180]. This prevents the collapse of the condensate once the temperature goes below the critical temperature T_c [181, 182]. The ^{87}Rb Feshbach resonances are not experimentally accessible, nonetheless condensation can be reached without tuning interactions thanks to the good scattering rate. Several Feshbach resonances are instead available for ^{87}Rb-^{40}K mixtures [177, 183, 184] and for different mixtures of hyperfine states of ^{40}K [185–188].

4.2.2. Vacuum setup

The vacuum setup consists of three different chambers in which three different cooling stages are performed, see Fig. 4.2. The first part of the setup is a self made chamber for the 2D+ MOT pre-cooling stage, details on the design can be found in [150]. The atomic sources consist of Rubidium and Potassium (4% enriched) vials placed in separate bellows connected to the rest of the apparatus via valves so that the flux of atoms and the pressure in the 2D chamber can be adjusted at
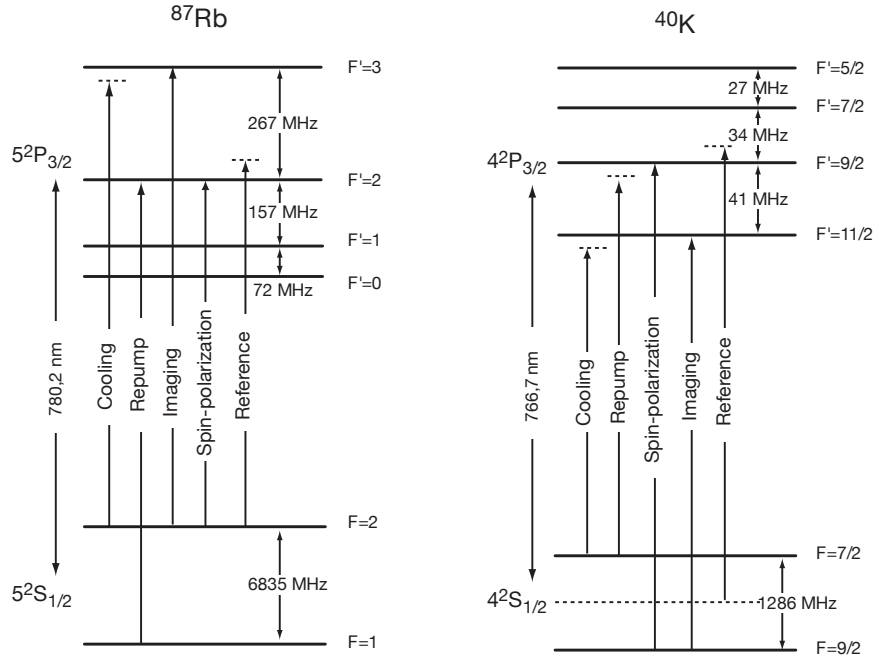
Figure 4.1.: Level structure of the D_2 lines of ^{87}Rb and ^{40}K. The most important optical transitions used in the experiment for the MOT cooling and repumping, spin-polarization and absorption imaging are shown. We reference to [151, 152] for the precise value of the detuning during the cooling in the MOTs. The reference lasers are locked to the crossover lines of the $F = 2 \rightarrow F' = 1, 3$ transitions of ^{87}Rb and the crossover $F = 1, 2 \rightarrow F'$ of ^{39}K.

will. This chamber is connected to the rest of the setup via a differential pumping tube which keeps a difference in pressure between the two chambers of about two orders of magnitude. The background vapor pressure in the 3D MOT chambers is $\sim 9 \times 10^{-11}$ mbar. The 3D MOT chamber connects to the science cell via a differential pumping section (6mm in diameter) which keeps a constant pressure gradient between the chambers and, combined with the ion getters pumps, it allows us to reach $\sim 5 \times 10^{-12}$ mbar in the last section of the vacuum setup. To obtain a rather low vacuum pressure we also pre-baked the stainless steel parts at about 400°C which reduced the outgassing rate of hydrogen from the stainless steel and improved the final vacuum pressure. The rather long distance from the MOT to the science cell has been designed to keep a large optical access around the glass cell.

Experimental coils

The experimental coils have been designed to provide a strong trapping potential when set in anti-Helmholtz configuration (gradient of 3 G/(A cm) along z-axis) and
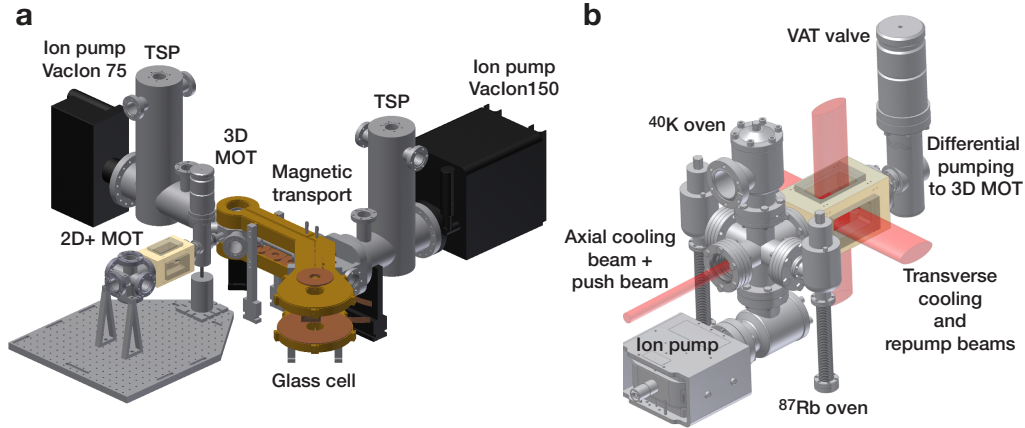
Figure 4.2.: **(a)** Full vacuum setup. The system is pumped via two ion-getter pumps. Titanium sublimation pumps (TSP) are also used to coat part of the chambers with titanium which absorbs residual gas in the system. **(b)** Zoom on the 2D+ MOT chamber. The different beams (red) used for pre-cooling the atoms are sketched.

a homogeneous offset field when they are in Helmholtz configuration (field offset of 11.8 G/A and curvature of $0.7 \times 10^{-6} \mathrm{mG/A} \, \mu\mathrm{m}^2$), suitable for tuning ^{40}K Feshbach resonances [150]. The experimental coils' design is determined by the glass cell dimensions, the 250 G/cm gradient necessary for evaporative cooling, and the large aperture at the center needed to place a high resolution objective close to the glass cell. To improve the thermal contact with the cooling block, the coils have been made out of ribbon wire. One side of each coils has been milled flat and pressed on the cooling block with a layer of thermally conducting paste (Duralco 134, Polytec PT) in between to ensure a good heat exchange with the cooling block.

4.3. Cooling steps

In this section we will briefly summarize the different cooling steps performed to reach ultracold temperature regimes.

4.3.1. Pre-cooling in the 2D+ MOT and 3D MOT

Double species 2D+ MOT

The cooling sequence starts with a pre-cooling stage in a 2D+ MOT where ^{40}K and ^{87}Rb are cooled together. The setup is illustrated in Fig. 4.2b. The working principle of a 2D+ MOT is no different from the well known 3D MOT setup [131] as it combines the slowing down of atoms due to radiation pressure force, arising from

absorption and emission cycles of near-resonant light, with the spatial-dependence of the optical force due to a magnetic field gradient. Four rectangular coils create a 2D quadrupole field such that the cooling from the MOT occurs only in the transversal direction. An additional axial beam is used for axial colling via optical molasses which increases the efficiency of the transversal cooling, as also observed in [189–191], and decreases the mean velocity as well as the width of the velocity distribution of the atoms. Additionally, we superimpose a push beam which pushes the colder atoms into the next chamber. The differential pumping section connecting the two chambers acts as an additional velocity filter for the atoms, selecting only the ones with low enough transversal velocity. The atomic flux strongly depends on the parameters of the axial cooling beam and on the vapor pressure of the two species which indicates that K-Rb collisions between trapped K and background Rb atoms are the dominant loss processes, as reported in detail in [151]. This did not prevent us from having a good flux of cold atoms out of the double species 2D+ MOT.

3D MOT

In the 3D MOT we load to saturation $\sim 10^{10}$ ^{87}Rb atoms and $2 \sim 10^8$ ^{40}K atoms. These are typical parameters for cooling ^{40}K to degeneracy. For the experiments described in the following chapters, instead, only $\sim 10^9$ ^{87}Rb atoms are loaded in the MOT. Due to the large intensities needed for the Doppler cooling of ^{40}K, a large percentage of ^{40}K atoms are in the excited state during the cooling in the 3D MOT. Atoms can exchange energy via collisions between ground and excited state atoms and these collisions put a limit on density and temperature of the ^{40}K MOT. We added a dark spot (9 mm diameter at the atoms' position) to the repumping beam [192] to reduce the collisional losses between K-K* at the center of the trap where the densities are highest. The dark-spot MOT increased the ^{40}K atom number by a factor of two [152]. Spin changing collision between ^{40}K and ^{87}Rb atoms are not suppressed by the dark-spot [193, 194] therefore the cold clouds are spatially displaced in the trap by few millimeters to reduce the detrimental effect of ^{87}Rb on the ^{40}K MOT.

After the MOT loading, the atoms are released from the trap and ^{87}Rb is further cooled via an optical molasses. During this stage, the cooling laser is detuned by -90 MHz from resonance and the intensity is reduced to about 10% of the total power to reach a sub-Doppler temperature for ^{87}Rb of about 40μK. The molasses phase is crucial for the transport and evaporation, especially when working with ^{40}K where efficient sub-Doppler cooling is harder to achieve [195–197]. Since molasses cooling is not efficient for ^{40}K, its temperature is mostly lowered by thermalization with the colder ^{87}Rb cloud when the atoms are recaptured and trapped in a strong quadrupole trap. We experimentally found an optimal detuning of -30 MHz from resonance for ^{40}K during the molasses phase. With this setting we observed moderate colling and no atoms' loss during the molasses phase.

Spin polarization

After molasses the atoms are spin polarized. A perfectly polarized sample is important not only for a good transfer of the cold sample into a magnetic trap but also for an efficient sympathetic cooling. In fact, hyperfine changing collisions can happen in a mixture of alkali atoms in different hyperfine states. The energy gained after the spin-changing collision is stored by ^{40}K and the ^{87}Rb atoms as kinetic energy and it causes heating as well as losses in the sample. During the polarization sequence we apply a homogeneous field offset along the z-direction to lift the degeneracy between the hyperfine states. The atoms are then polarized with pulse of σ_+ light resonant with the $|^2S_{1/2}, F = 2\rangle \rightarrow |^2P_{3/2}, F' = 2\rangle$ for ^{87}Rb and $|^2S_{1/2}, F = 9/2\rangle \rightarrow |^2P_{3/2}, F' = 9/2\rangle$ for ^{40}K. A σ_+-polarized repumper light is also applied during the spin polarization for a more efficient pumping. The pulse pumps all the atoms in the low-field seeking states in the $^2S_{1/2}$ manifold, $|F = 2, m_F = +2\rangle$ for ^{87}Rb and $|F = 9/2, m_F = +9/2\rangle$ for ^{40}K. These atoms are magnetically transported to the science cell. The spin-polarization pulse is quite efficient: $\sim 80 - 70\%$ of the atoms are pumped in the correct hyperfine states and recaptured in the magnetic trap. This recapture efficiency is limited by the cloud density in the case of ^{87}Rb. For ^{40}K, instead, the main limitation is temperature: not all the atoms spend enough time in the spin-polarization light to be pumped in the correct state and they either fly out of the trap or they are pumped in a high-field seeking state. No spurious hyperfine states are captured and transported to the science cell.

4.3.2. Transport and evaporation in a plugged quadrupole trap

The transport of the atoms to the science cell is done magnetically. The transport coils are designed such that the trap geometry is not affected during the transport sequence to avoid parametric heating [150, 198]. Given the size of the differential pumping section and the gradients we can achieve with the transport coils, we found that the pumping section acts as a temperature filter for the atomic clouds. As a result, we typically transport only the $\sim$20% colder ^{87}Rb atoms and $\sim$10% of the ^{40}K cloud while removing the hot atoms which are located further away from the zero of the quadrupole trap according to their Boltzmann distribution. By transporting the atoms back and forth through the pumping section, we observed a narrowing of the distribution of atoms in the trap which is indicative of a selective removal of hot atoms. The measured temperature is decreased by a factor of two after crossing the pumping section. This evaporation is not harmful as we reached condensation and degeneracy with good atom numbers in the end.

The first stage of evaporation in the glass cell happens in an optically plugged quadrupole trap [142]. Here a blue-detuned plug beam of wavelength λ=760 nm and beam waist 30 μm at the atoms position, prevents Majorana spin flips at the center of the quadrupole trap where the field is zero [199]. The plug beam is not
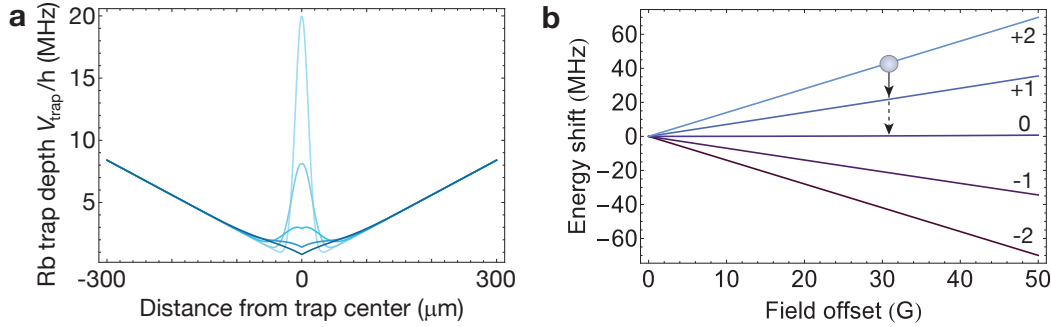
Figure 4.3.: **(a)**: Trapping potential for ^{87}Rb atoms in the $|F = 2, m_F = +2\rangle$ state along the direction of magnetic transport together with the plug potential. The displacement from the center of the experimental coils along the transport direction increases from 0 cm to 1 cm (steps of 2 mm) from the light to dark blue curve. The tightly focused plug has a moderate effect on the trapping potential of the magnetic transport as its barrier falls down rapidly away from the focal point of the plug. **(b)**: Working principle of the RF evaporation. Energy splitting of the hyperfine levels (m_F number on the side) of the $F = 2$ manifold of ^{87}Rb as a function of magnetic field offset B_0. An RF wave resonantly couples atoms in the $|2, +2\rangle$ state sitting at a specific trap position, i.e. at a certain field B_0, (gray sphere) to anti-trapped states.

coming along the symmetry axis of the coils, as most standard setups, but it travels along the direction of the transport. Since the beam is tightly focus at the atoms' position, its barrier height decreases away from the center of the experimental coils and it does not significantly affect the trapping potential of the magnetic transport, as shown in the plot of Fig. 4.3a.

The RF-evaporation works by selective removal of the hotter ^{87}Rb atoms via a radio frequency (RF) sweep which transfers the atoms from a trapped to an untrapped state, $|F = 2, m_F = 2\rangle \rightarrow |F = 2, m_F = 0\rangle$, in an energy-selective way. The selection in energy is given by the spatially dependent Zeeman shift of the quadrupole trap (gradient of ~ 240 G/cm) combined with the thermal distribution of atoms in the trap by which hotter atoms are located further away from the center. When the RF frequency matches the energy difference between different hyperfine states, atoms with a certain temperature T are transferred to anti-trapped states and removed from the trap, see Fig. 4.3b. The ^{40}K atoms are unaffected by the RF sweep because of their different magnetic moment. As the ^{87}Rb cloud thermalizes to colder temperatures, the ^{40}K atoms are sympathetically cooled by thermal contact with the bosonic cloud. At the end of the evaporation ramp (from 30 MHz to 2 MHz) we typically reach a temperature of 6 μK with $\sim 1 \times 10^7$ ^{87}Rb atoms and $\sim 5 \times 10^6$ ^{40}K atoms. Typical lifetimes in the plugged trap (gradient of 240 G/cm) are on the order of 30 s after the evaporation.
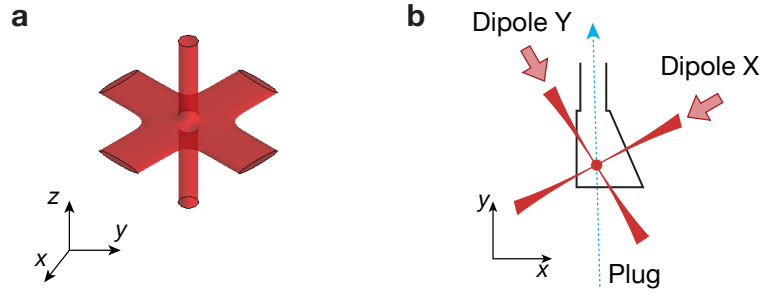
Figure 4.4.: **(a)** Crossed dipole trap created by overlapping three red detuned beams. The strong aspect ratio of the beams X and Y creates a pancake-like trapping potential. **(b)** Orientation of the dipole beams relative to the glass cell.

4.3.3. Crossed dipole trap

After the RF-evaporation, the quadrupole gradient is lowered and the atoms are loaded in an optical dipole trap to continue the evaporation. The crossed optical dipole trap is composed of two main beams and a vertical pinning beam, as illustrated in Fig. 4.4. Red-detuned light of wavelength 1064 nm (Nufern fiber laser) is used to trap the atoms at the intensity maxima, as discussed in Section 3.2.1. The two main axis of the crossed dipole trap, dipole X and Y, have a waist of ~ 300 μm in the horizontal direction and ~ 35 μm in the vertical one. The strong aspect ratio creates a pancake-like trap that can potentially be used for studies of two dimensional systems [152]. The vertical beam, which has more moderate intensities, provides additional confinement in the xy-plane which is used to increase the clouds' density during evaporation and to better pin the atoms in the trap when experiments are performed in a shallow dipole trap. The dipole Z is radially symmetric with a waist of 180μm. Maximum total trapping frequencies are on the order of $\omega_{x,y} \sim 2\pi \times 60$ Hz and $\omega_z \sim 2\pi \times 600$ Hz for ^{87}Rb. They have been calibrated by monitoring the center of mass motion of the BEC after a displacement in the trap. The experimental results are summarized in Fig. 4.5. When the dipole trap is weak, the gravitational potential can not be neglected as its magnitude is comparable to the dipole trap potential. The total potential $U_{\text{tot}} = U_{\text{dip}} + mgz$ and the vertical gravitational sag of the atoms in the spatially inhomogeneous trapping potential modify the trap frequencies, as illustrated in the graphs. Given the different masses of the two atomic species, the dipole trapping potential is higher for ^{40}K compared to ^{87}Rb by a factor of $\sim (m_{\text{Rb}}/m_{\text{k}})^{1/2}$ which means that for low dipole powers the two atomic species will experience a different gravitational sag. The tight confinement along z of our trap geometry reduces the relative sag almost up to the end of the ^{87}Rb evaporation down to a BEC, ensuring a good spatial overlap between the clouds for the sympathetic cooling of ^{40}K.
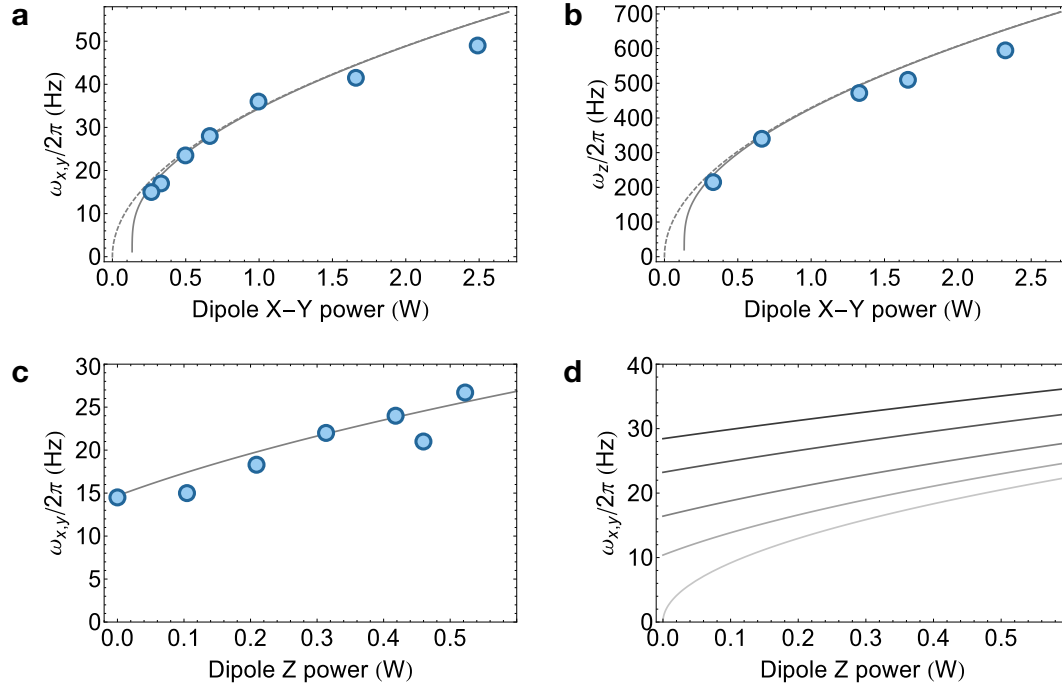
Figure 4.5.: **(a)** Horizontal ($\omega_{x,y}$) and **(b)** vertical (ω_z) total dipole trap frequencies for ^{87}Rb as a function of the power of dipole X and Y. Dipole Z intensity is set to zero. Frequencies are measured by monitoring the center of mass motion of the BEC after a sudden displacement from the trap center. Expected trap frequencies for the combined dipole and gravitational potentials (thick lines) and trap frequencies without gravitational potential (dashed lines) are shown. The effect of the gravity becomes relevant at low dipole powers. Due to the vertical sag in the spatially inhomogeneous dipole potential both horizontal and vertical trap frequencies are affected by the presence of gravity. **(c)** Calculated and measured horizontal dipole trap frequencies for ^{87}Rb as a function of dipole Z intensity. Dipole X and Y are set to $\sim$ 300mW. **(d)** Calculated total trap frequencies for different powers of dipole X and Y, from 0 W (light gray) to 750 mW (dark gray). The effect of the additional dipole Z is more pronounced when dipole X and Y powers are low.

4.3.4. Forced evaporation in the dipole trap

To continue the evaporation in the dipole trap, the atoms are transferred to the ground states, $|1, +1\rangle$ for ^{87}Rb and $|9/2, -9/2\rangle$ for ^{40}K, by rapid adiabatic passage. The evaporation ramp is sketched in Fig. 4.6a, typical density profiles during the evaporation are plotted in Fig. 4.6b. The evaporation in the dipole trap works similarly to the one in the magnetic quadrupole trap: hot atoms are removed by lowering the trap depth. The colder atoms that remain trapped rethermalize, if the

Figure 4.6.: **(a)** Schematic of the evaporation ramp performed in the dipole trap together with the most important steps of the evaporation sequence. **(b)** Absorption images of ^{40}K and ^{87}Rb atoms after TOF taken at different stages of the evaporation in the dipole trap. The sympathetic cooling ends after 8 s, after that the bosonic cloud is removed from the trap and cooling proceeds with a ^{40}K spin mixture.
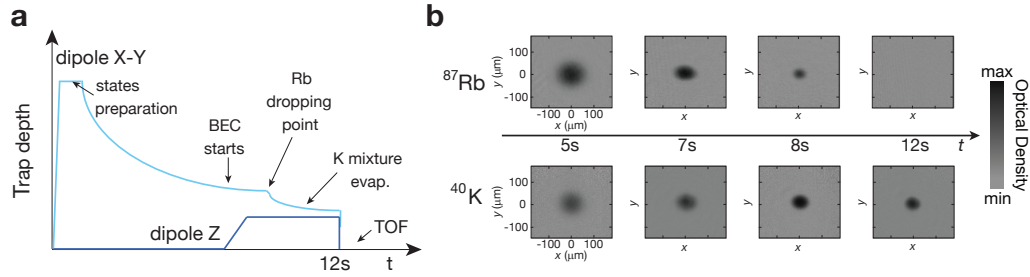
collision rates are favorable, and the velocity distribution narrows. A disadvantage of this scheme is that by decreasing the trap depth the trap frequencies decrease and so does the collision rate. Given the different mass of the two species, the bosonic specie is the one that is directly evaporated out of the trap and cooled by the forced evaporation, while the ^{40}K atoms see a deeper trap and they are sympathetically cooled by collisions with the colder ^{87}Rb atoms. By increasing the phase space density of ^{87}Rb, the condensation is reached for the bosonic specie with typically a maximum of $N \sim 3 \times 10^5$ atoms in an almost pure BEC (condensate fraction of $\gtrsim 90\%$). Lifetimes of the ultracold atoms in the dipole trap are on the order of 20 s.

Thermalization of ^{40}K with ^{87}Rb is efficient thanks to the favorable background scattering length. At the end of the 8 s evaporation ramp with final trap frequencies of $\omega_z \sim 2\pi \times 200$ Hz and $\omega_{x,y} \sim 2\pi \times 15$ Hz for ^{87}Rb, we have 5×10^5 ^{40}K atoms at a $T \sim 100$ nK. We experimentally found that, as observed in other works [147], sympathetic cooling is more efficient when the bosonic cloud is only partially condensed, since the heat capacity of the bosonic species is still higher than the fermionic one [200]. The sympathetic cooling ramp ends before pure condensation is reached for ^{87}Rb, after that the BEC is released from the trap and the evaporation proceeds further with a 50/50 mixture of ^{40}K atoms in the hyperfine states $|9/2, -9/2\rangle$ and $|9/2, -7/2\rangle$. To enhance the collision rate between the two states, a constant magnetic field is applied to increase the scattering length to about $a_s \sim +250$ a_0. At the end of the evaporation ramp (4 s) we typically reach a degenerate Fermi gas with $T = 0.13(2)$ T_F and $N \sim 3 \times 10^5$ atoms in the spin mixture. Lifetime of the degenerate mixture in the trap is typically 20 s, while it is 80 s long for a single component Fermi gas.
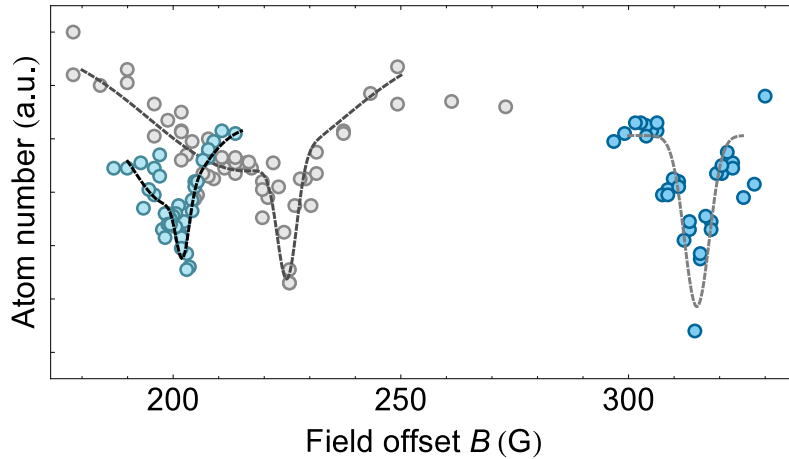
Figure 4.7.: Some relevant Feshbach resonances of ^{40}K [188]. Gray data correspond to the overlapping s and the p resonances of the mixture $|9/2, -9/2\rangle + |9/2, -5/2\rangle$. Light blue data are taken for a mixture of $|9/2, -9/2\rangle$ and $|9/2, -7/2\rangle$, the overlapping loss features correspond to the resonances for the mixtures $|9/2, -9/2\rangle + |9/2, -7/2\rangle$ and $|9/2, -7/2\rangle + |9/2, -7/2\rangle$. Both mixtures can be used for sympathetic cooling. Dark blue points correspond to the resonance for $|9/2, +5/2\rangle + |9/2, +7/2\rangle$ which can be potentially used for optical flux lattice scheme [201]. Lines are bimodal Gaussian fits as guides to the eye. Atom numbers of the data sets have been scaled for visualization purposes.

4.3.5. Tuning interactions

Several Feshbach resonances are available for the ^{87}Rb-^{40}K mixture and for mixtures of hyperfinestates of ^{40}K. To prove the capability of our setup of studying cold atoms with tunable interactions, we probed the Feshbach resonances of ^{40}K for different input channels. Some relevant Feshbach resonances of ^{40}K are shown in Fig. 4.7. By approaching a resonance the scattering rate is enhanced and the fraction of atoms lost from the trap increases. The Feshbach resonance is detected by measuring the loss of atoms at different magnetic field offsets. The measured position of the different loss features associated with the resonances agrees with the positions reported in literature to better than 1% [188]. The resonance for the mixture $|9/2, -9/2\rangle$, $|9/2, -7/2\rangle$ is used to increase the scattering rate during the last evaporation stage of ^{40}K.

4.4. Detection techniques

4.4.1. Absorption imaging

Absorption imaging is one of the most standard techniques in ultracold atoms experiments. To obtain the density distribution of the cloud, light resonant with an atomic transition is shine onto the the atoms. For a beam of intensity I_0 propagating along z which samples a medium of density $n(x, y, z)$, its intensity is reduced by the absorption of the medium according to the Beer-Lambert law

$$I(x, y) = I_0 e^{-OD(x,y)} \tag{4.12}$$

with an optical density $OD(x, y)$

$$OD(x, y) = \sigma_0 \int n(x, y, z) dz. \tag{4.13}$$

Here we assumed the light to be on resonance with an atomic transition that has a polarization-averaged scattering cross section of $\sigma_0 = 3\lambda^2/(2\pi)$. The intensity of the imaging beam is also assumed to be weaker than the saturation intensity of the chosen transition, $I \ll I_s$. As our atomic clouds are three dimensional, when the imaging beam is recorded on a CCD camera we obtain an intensity profile which carries the information about the column density $n_c(x, y) = \int n(x, y, z) dz$. To correctly evaluate the spatial distribution of density of the atomic cloud, we also take an image without atoms, I_{bg}, so that the spatially dependent intensity profile of the imaging beam is removed. From the images we extract the following distribution

$$n_c(x, y) = -\frac{C_{CG}}{\sigma_0} \ln \left(\frac{I(x, y)}{I_{bg}} \right) \tag{4.14}$$

C_{CG} being an average of the squared Clebsh-Gordan coefficients of all the transitions which can be excited by the polarized light. By calibrating the CCD, the measured intensity per pixel is related to an atom number.

Images of the atomic clouds can be taken in situ or at a certain time of flight (TOF) during which the atomic clouds freely expand. By performing long enough TOF, the momentum distribution of atoms in the harmonic trap is directly mapped onto real space density distribution. The column density n_c is thereby used to discern a thermal gas from a condensed Bose gas or a degenerate Fermi gas. The density distribution of atoms after TOF can be obtained from a semiclassical approximation. As they are well known for the case of an harmonic trapping potential [142–144] they are summarized in appendix B. For a thermal cloud following Maxwell-Boltzmann statistic, the density profile is a Gaussian which expands isotropically according to its temperature. This is not the case for a gas at ultracold temperatures. Some
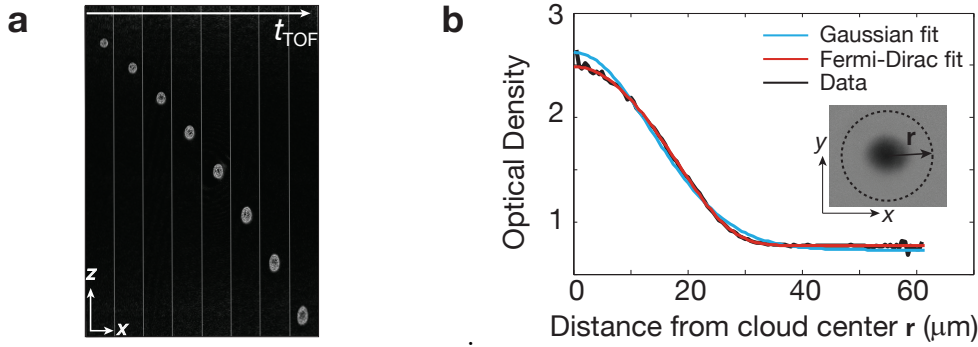
Figure 4.8.: **(a)**: Images of a pure ^{87}Rb BEC during TOF. The inversion of the aspect ratio of the cloud during the free fall is a clear indication of condensation. **(b)**: Plot shows the azimuthally averaged density profile of the degenerate Fermi gas of ^{40}K (inset image) after ballistic expansion together with Gaussian and Dirac-Fermi fits (distribution for degenerate fermions, see appendix B for details). The column density of the degenerate gas is better fitted by the Fermi-Dirac distribution with $T/T_F \sim 0.15$ and $N \sim 3 \times 10^5$.

examples of measured density profiles of bosons and fermions are shown in Fig. 4.8. For a BEC, the free-fall expansion depends on the ground state energy and, thereby, it is significantly affected by the shape of the trap: the cloud expands faster along the axis where the harmonic confinement is stronger. For a degenerate Fermi gas, instead, the density distribution is not well described by a Gaussian distribution at such low temperatures. The distribution is best fit by a Fermi-Dirac distribution which models a degenerate Fermi gas trapped in an harmonic potential. For decreasing temperatures, the Fermi-Dirac distribution does not differ much from the distribution at zero temperature, thereby the fitting is not reliable for temperatures below $\sim 0.1T_F$ as it relies on minimal changes on the wings of the distribution. Finally, it is important to note that for short TOF the density distribution n_c is always a convolution of the in situ size and momentum distribution, no matter what the state of the atomic cloud is.

High resolution objective

A high resolution objective (Special optics Inc.) placed below the glass cell is used to image the atoms along the z-axis. The objective has a NA=0.5, f-number $f_N = 1$, and focal length $f = 25$ mm. It is AR coated for a range of 532-1064 nm wavelengths. It can be moved for focusing via a motorized stage (Custom Micro-Z Objective Positioner MCL) in a range of about 5.3 mm. A protection ring fixes the highest position of the stage.

Any imaging system has an intrinsic resolution limit which is due to its finite aperture. As a result, some frequency components of the imaged object are filtered
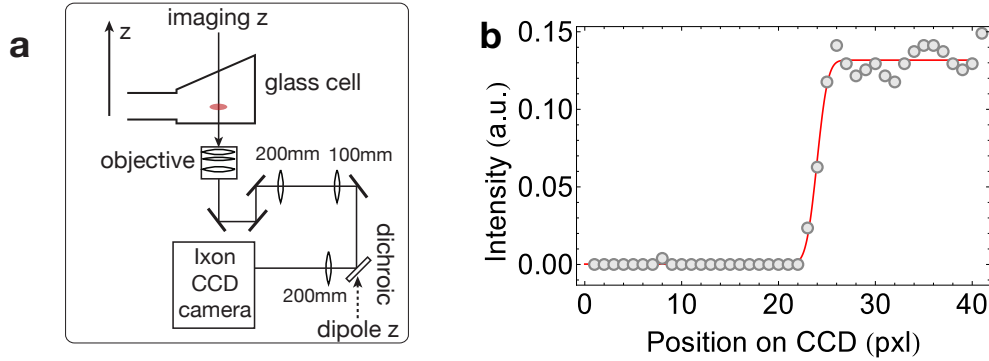
Figure 4.9.: **(a)**: Schematic of the vertical imaging setup. **(b)**: Example of one data set used to extract the diffraction limit of the objective by imaging a sharp object. Line is an errorfunction fit to the sharp change in intensity.

out. The effect of the aperture is modeled by the point spread function (PSF) which describes how a point source is imaged by the system. An image $O_I(\mathbf{r})$ of any object $O(\mathbf{r})$ is described by a convolution of the PSF and the object itself, $O_I(\mathbf{r}) = \int O(\mathbf{r}_0) \mathrm{PSF}(\mathbf{r}_0 - \mathbf{r}) d\mathbf{r}_0$ [202]. For a circular aperture, as in the case of our objective, the PSF is an Airy disk whose width depends on the wavelength of light and on the NA. The resolution limit of the imaging system, the minimum distance at which two point-like objects can be distinguished, is $\sigma_{DL} = 1.22\,\lambda f_N$ according to the Rayleigh criterion. By imaging a test target (razor blade) the resolution of the objective has been tested. The image is a convolution of a step function with the PSF and the sharpness of the imaged razor edge gives information about the width of the Airy disk directly. From the images, we estimate an average diffraction limit of $\sigma_{DL} = 1.0(3)\sigma_{specs} = 0.92(29)$ μm for a 780 nm imaging wavelength which agrees with the specified value σ_{specs} and it is on the order of three lattice sites. The resolution can also be tested by imaging a thermal cloud of atoms and by computing its autocorellation function [203] which carries information about the PSF and the aberrations of the optical setup. Calibrating them is particularly important when the high resolution imaging system is used for correlation measurements.

4.4.2. Stern-Gerlach imaging

To extract information about the hyperfine state composition of the atomic sample, a state dependent force is applied during the TOF which spatially separates the different state components before imaging them. This Stern-Gerlach imaging, is realized with a field gradient created by a single coil described by $B(\mathbf{r}) = B_0 + B'_{SG}\mathbf{r}$. The spatially dependent magnetic field results in a spatially dependent Zeeman shift, eq. 4.10, and, therefore, in a force of different strength for atoms in different m_F
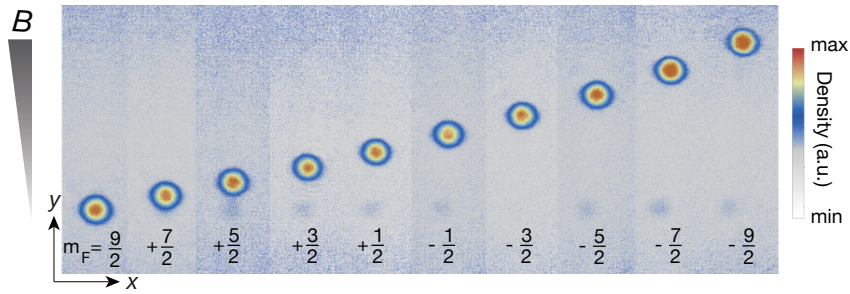
Figure 4.10.: A Stern-Gerlach pulse spatially separates atoms in different hyperfine states. Here ^{40}K in the state $|F = 9/2, m_F\rangle$ is imaged, labels correspond to the m_F level.

states. Its magnitude is

$$F_{SG} = \mu_B g_F m_F B'_{SG} \tag{4.15}$$

and it points along $\mathbf{r}$. In our setup we use two identical Stern-Gerlach coils placed orthogonally to each other. The coils have a conical geometry which is less obstructive so that they can be placed closer to the atoms. They have been designed to produce a rather homogeneous field gradient, B'_{SG}=0.5 G/(A cm), over the extension of the atomic cloud. The curvature, $B''_{SG} \sim 2 \times 10^{-3}$mG/(A μm^2) results in a change of gradient of $\lesssim 1\%$ across the cloud, which can be safely neglected. The force acting on the atoms is well approximated by eq. 4.15. By adding the fields of the two coils, the direction of the combined gradient can be adjusted at will. Examples of Stern-Gerlach images of different hyperfine states of ^{40}K are shown in Fig. 4.10.

4.5. Final remarks

In this chapter we have introduced the experimental setup which allows us to cool ^{87}Rb to condensation and ^{40}K to degeneracy. A possible improvement would be to perform a more efficient sub-Doppler cooling for ^{40}K [195, 197] which would increase the atom number after transport and, consequently, the efficiency of the evaporation ramps. Moreover, adding a gradient to the dipole potential can help in keeping the densities high throughout the cooling sequence since the trap can be tilted during the evaporation instead of being lowered in depth [204, 205].

Given that bosonic and fermionic species are available, both of them can be loaded in an optical lattice depending on the features that we aim at studying. Particularly interesting is the possibility of using the Feshbach resonances of ^{40}K to study the effect of interactions for atoms in topological bands, which is still mostly unknown for both bosons and fermions in a honeycomb lattice [95, 96, 206, 207]. In the following chapters we will focus on bosonic atoms in the honeycomb lattice as they

are an ideal local probe for mapping out the local topological features of a Bloch band.

Chapter 5.

Lattice setup, detection and manipulation techniques

In this chapter, the setup for creating the honeycomb lattice potential is presented and the experimental techniques used to manipulate and to detect the properties of the atoms loaded in the lattice are introduced. The setup is described in Section 5.1 and standard mapping techniques are presented in Section 5.2. In Section 5.3, we describe Bloch oscillations which are used to manipulate the state of atoms in the lattice. Finally, in Section 5.3.4 we comment on the effect of weak interactions which can result in instabilities as the atoms move in an energy band and which set a limit on the experimental timescales for such motion. All the results presented here and in the following chapters are obtained with a ^{87}Rb BEC.

5.1. The experimental setup for the optical lattice

The honeycomb optical lattice is created by interfering three laser beams. The optical setup for the lattice is schematized in Fig. 5.1. A MBR110 single-frequency Ti:Sapphire Laser (Coherent) pumped by a 10W Verdi laser (Coherent) at 532nm provides the laser light for the optical potential. The total output power is about 1.4W, the linewidth is $\sim$500 kHz when the Ti:Sa cavity is locked. The etalon locking electronics for this specific laser design also introduces a $\sim$1% intensity noise peak to peak, mostly at 88 kHz and higher harmonics. The advantage of the Ti:Sa system compared to other types of lasers is that the wavelength can be tuned over a rather wide range. This allows us to have a flexible setup in which the detuning can be tuned to be red or blue for ^{40}K and ^{87}Rb. Thanks to the absence of amplified spontaneous emission, main issue for tampered amplifier lasers, this setup could be used for addressing the Raman transitions required for the optical flux lattices scheme [68] where resonant scattering needs to be avoided given the already prohibitive scattering rate of the nearly resonant Raman beams. For the experiments described in the following chapters, the wavelength of the light is set to $\lambda_L = 755$ nm, blue-detuned from ^{87}Rb transitions. The laser light is split into three beams controlled by acousto-optical modulators (AOMs) and sent to the
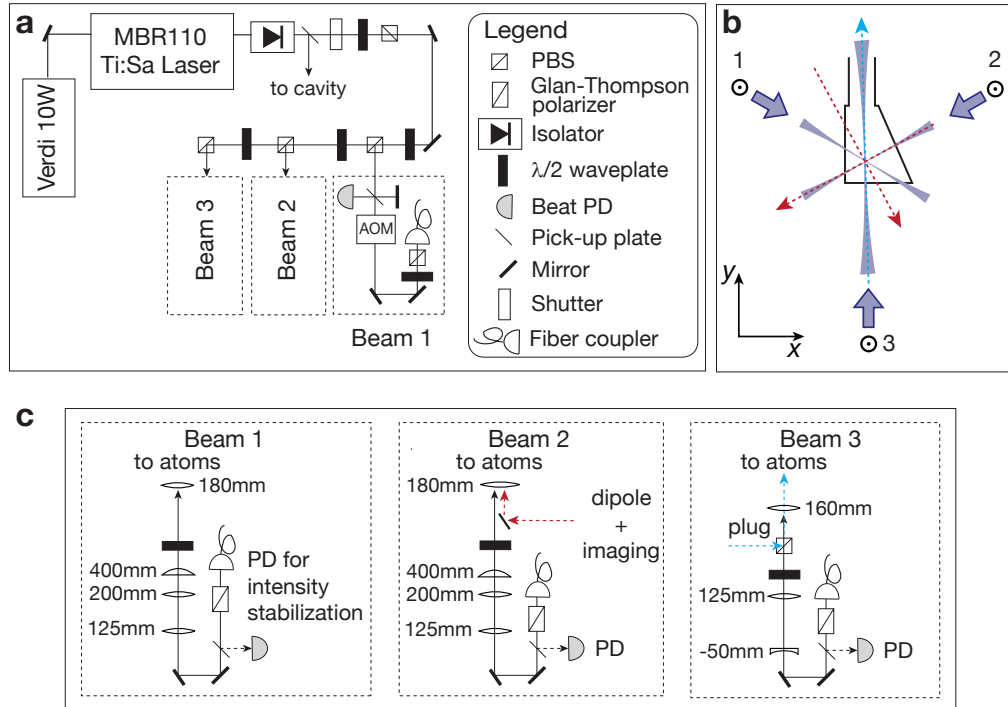
Figure 5.1.: Simplified lattice setup. **(a)** Schematic of the laser setup on the experimental table where each lattice beam is separately prepared and controlled via AOMs. **(c)** Schematic of the optical setup of each beam on the experimental table. **(b)** Orientation of the lattice beams (purple) relative to the glass cell. Dipole (dashed red) and plug (dashed blue) beams overlapping with the ones of the lattice (violet) are also shown.

experimental table via separate fibers, as depicted in Fig. 5.1a. The AOMs are driven by separate synthesizers (Agilent MXG N5182A, at 198 MHz) such that the frequency and intensity of each beam can be tuned independently. The synthesizers are locked to a common reference local oscillator (LO) to reduce relative frequency and phase noise among the beams related to the use of separate drivers. The beams' intensity is stabilized via a standard closed loop controller (PID controller) which actively regulates the AOM RF-power.

The geometric arrangement of the beams on the experimental table is illustrated in Fig. 5.1b. Two lattice beams are overlapped with, respectively, a dipole beam (lattice beam number 2) and the plug beam (nr. 3), the third one is independent (nr. 1). The schematics of optical setups in Fig. 5.1c illustrate how each beam is prepared and how the overlap with the dipole and plug beams is realized on the experimental table. The polarizations of the beams are first set with a Glan−Thompson polarizer and then controlled via polarizers to be linear and out of plane of intersection to create a interference pattern with honeycomb symmetry.
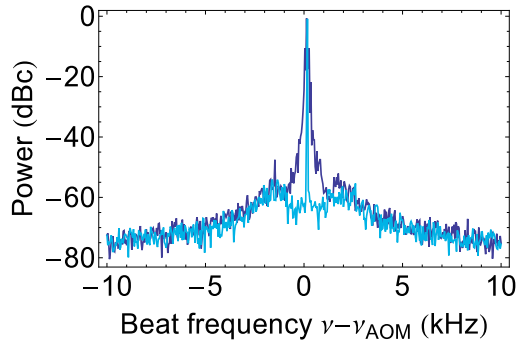
Figure 5.2.: Comparison between the power spectrum of the AOM driver (light blue) and the beat signal between the light before and after the fiber of one lattice beam (dark blue). Phase noise appears as a broadening of the original spectrum. Powers are referenced to the corresponding carrier peaks.

The lattice is created by interfering beams with a Gaussian intensity profile described by eq. 3.22 which are focused onto the atomic cloud. The beams are shaped by telescopes and the horizontal and vertical waists at the atoms position are $w_1 = (35~\mu m, 430~\mu m)$, $w_2 = (36~\mu m, 480~\mu m)$ and $w_3 = (41~\mu m, 490~\mu m)$ for each beam respectively. The aspect ratio is chosen to match the one of the dipole trap potential. This choice of waists gives a rather homogeneous lattice potential over the extension of the cloud and, at the same time, gives a broad range of lattice depths, up to $\sim 12E_r$ for a 10W pump power. Since the atoms are trapped at the minima of the periodic potential, the only effect of the Gaussian envelope is to spatially vary the lattice depth away from the crossing point of the lattice beams. This inhomogeneity of the optical potential introduces, in first approximation, an effective anti-trapping harmonic potential superimposed with the one of the dipole trap. The spatially varying on-site frequencies depend on the intensities of the three lattice beams and can even be radially asymmetric when the lattice potential is imbalanced. Typical measured anti-trapping frequencies for a $1E_r$ lattice are on the order of $\omega_{xy}^{ac} \sim 2\pi \times 10 \text{Hz}$ and $\omega_z^{ac} \sim 2\pi \times 80$ Hz.

The optical potential has no additional periodic confinement along the z-axis and it results in a periodic array of 1D tubes instead of a single 2D plane as in solid state graphene. During the experimental runs, the cloud of $\sim 5 \times 10^4$ atoms populates ~ 7000 tubes with an average of ~ 7 atoms per tube and a peak of ~ 30 atoms in the central tube. More details on the tubes' parameters can be found in appendix C.

Even if the lattice beams are generated by the same optical source and their AOM drivers have a common reference, noise on the laser source, on the optical fibers and mechanical vibrations can introduce phase and intensity noise on the three interfering beams that generate the optical potential. This would result in parametric heating and in an exponential increase of energy over time [208, 209].
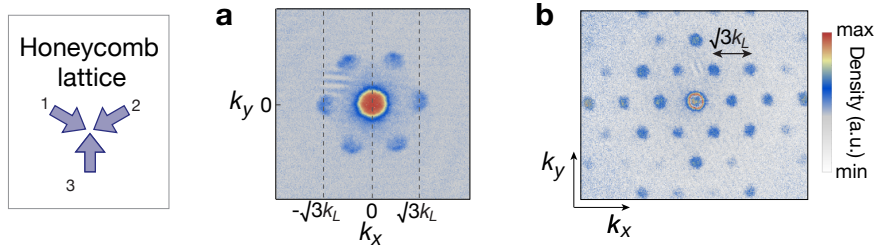
Figure 5.3.: **(a)** Image of a condensate loaded in the honeycomb lattice in a super-fluid state after a sudden switch off of the trapping potentials and TOF. Lattice depth is $5E_r$. **(b)** Image of BEC after pulsing the lattice and TOF. The momentum distribution after the expansion presents many orders of diffraction peaks separated by multiples of the reciprocal lattice vectors.

To this end, a Phase-Locked Loop (PLL) [210, 211] has been developed to reduce the phase noise coming from the use of separate fibers. The main idea is to use the beat between the light before and after the optical fiber as an input signal for the feedback loop. In the ideal noiseless case, the beat has a power spectral density which is a delta function. Phase noise composed of many frequency components, usually low in frequency, effectively broadens the spectrum of the beat signal, as illustrated in Fig. 5.2. By feedbacking this noise signal onto the AOM frequency, the phase noise can be reduced. More details on our Phase-Locked Loop can be found in the following thesis [211]. We experimentally found that this PLL has a negligible effect on the atoms' lifetime because of the intensity noise ($\simeq 1\%$) of the Ti:Sa etalon lock. This is the most important source of noise in our setup and it also couples to the input signal of the PLL lock. When the Ti:Sa cavity is locked, the condensate lifetime decreases with increasing lattice depth from $\lesssim 5$ s to $\lesssim 100$ms for a range of $1 - 10E_r$. In comparison, when the laser is running single-mode with the locking electronics turned off the lifetimes are longer, ~ 6 s to ~ 500 ms.

5.2. Measurement techniques

5.2.1. Interference pattern after time-of-flight

The Bloch wavefunctions of eq. 2.12 reflect the periodicity of the lattice in real space. If we let the atoms freely expand, the resulting real-space density distribution carries information about the quasimomentum distribution of the atoms loaded in the lattice and the symmetry of the reciprocal space [198, 212, 213]. This mapping technique is realized by an instantaneous switch off of the lattice potential followed by free expansion of the atomic cloud in the gravitational potential. The real space density distribution after TOF directly maps on the quasimomentum distribution
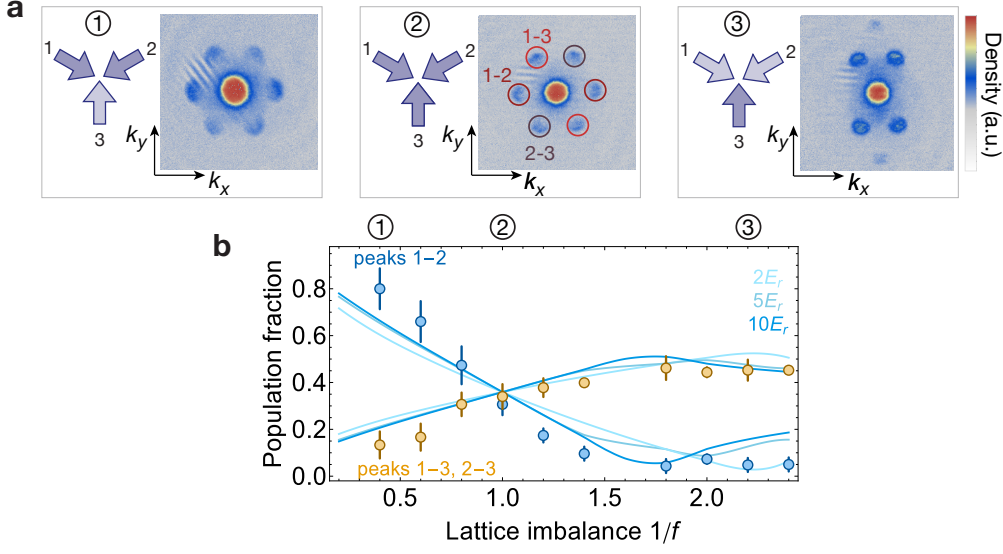
Figure 5.4.: Interference peaks and lattice balancing: The population imbalance of the first order peaks relates to the relative imbalance of the lattice beams, i.e. to the intensities I_i. **(a)** Images from 1-3 show examples of TOF pictures taken at different relative imbalances of the lattice beams, as illustrated by the schematics on the side. Each pair of peaks relates to the interference of a pair of lattice beams, numbered in the image 2. **(b)** Fraction of atoms in each pair of peaks as a function of lattice imbalance, $1/f = I_3/I_{1,2}$, theory lines are calculated for different lattice depths from ab initio calculations which incorporate the full lattice potential, eq. 3.29. Data are taken at a $5E_r$ lattice depth and follow the expected trend for the populations of the different interference peaks. The balancing of the lattice is inferred from the balancing of the interference peaks.

and it reads [212]

$$n(\mathbf{r}) = \left(\frac{m}{\hbar t}\right)^3 |\tilde{w}(\mathbf{k})|^2 \sum_{i,j} e^{i\mathbf{k}(\mathbf{r}_i - \mathbf{r}_j)} \langle \Psi | \hat{c}_i^\dagger \hat{c}_j | \Psi \rangle, \qquad (5.1)$$

where the envelope is given by $\tilde{w}(\mathbf{k})$, which is the Fourier transform of the Wannier function, and Ψ is the many-body wavefunction describing the state of the atoms loaded in the lattice. The operator $\hat{c}_i^\dagger$ is the bosonic operator which creates a particle at the site i. The summation in eq. 5.1 gives the quasimomentum distribution and, since it depends on a two-point correlation function, it also carries information about the coherence between particles at different lattice sites. For bosons in a superfluid state, as an example, the interference pattern presents sharp interference maxima which directly reflect the high degree of phase coherence of the system. A typical image taken with this mapping technique for condensed atoms loaded in the

honeycomb lattice is shown in Fig. 5.3a. It can be seen that the resulting density pattern, composed of sharp density peaks, repeats itself after a reciprocal lattice vector because of the periodicity of the Bloch waves. The optical potential can also be pulsed on to reveal the symmetries of the lattice. As a result, the BEC diffracts as radiation does when it is shone onto a crystalline solid [214]. The interference pattern after TOF is composed of many diffraction orders as illustrated in Fig. 5.3b which are periodically spaced according to the periodicity of the lattice potential.

As illustrated in Fig. 5.4, the populations of the first order diffraction peaks are linked to the balancing of the lattice as they depend on the depth of the potential crated by each pair of interfering beams. The peaks are labeled in Fig. 5.4a according to the corresponding pair of lattice beams that generates them. If one beam is stronger (weaker) than the others the corresponding peaks will be more (less) populated because of the increased (lowered) coupling strength, as illustrated by the examples in Fig. 5.4. We typically monitor only the first order diffraction peaks to infer the balance of the lattice potential.

5.2.2. Band mapping technique

The drawback of the previous detection scheme is that the atomic population of the different bands, if populated, cannot be resolved. To obtain this information together with the quasimomentum distribution a different mapping technique has to be employed which is called band mapping technique [198]. To realize it, the lattice depth is ramped down to zero instead of being suddenly turned off before the ballistic expansion of the cloud takes place. Some conditions apply for the duration of the ramp to ensure a correct mapping of the quasimomentum: To avoid excitations to other bands during the mapping sequence, the ramp has to be adiabatic with respect to the energy difference with the higher bands. Moreover, the ramp has to be fast compared to the band width to avoid the redistribution of the atoms in the bands during the ramp. If these conditions are met, the Bloch waves of the nth band with quasimomentum $\mathbf{k}$ are adiabatically mapped onto plane waves with free-space momentum $\mathbf{p}$ in the nth Brillouin zone. The geometry of the zones for our lattice configuration are illustrated in Fig. 5.5b. The occupations of the different bands and the quasimomentum distribution of the particles are obtained from the expansion images. An example of an image taken after band mapping and TOF is shown in Fig. 5.5a. In a honeycomb lattice, the conditions on the ramp timescales are harder to fulfill with increasing lattice depth for atoms in the lowest energy band because the separation between the first and second band decreases with increasing lattice depth, as discussed in Section 3.3.3.

Finally, it is important to mention the effect of the finite size of the weakly interacting BEC on these mapping techniques. As already mentioned, weakly interacting bosons at T=0 in a harmonic trap spatially redistribute compared to the non-interacting case where the particles are localized at the minima of the trapping
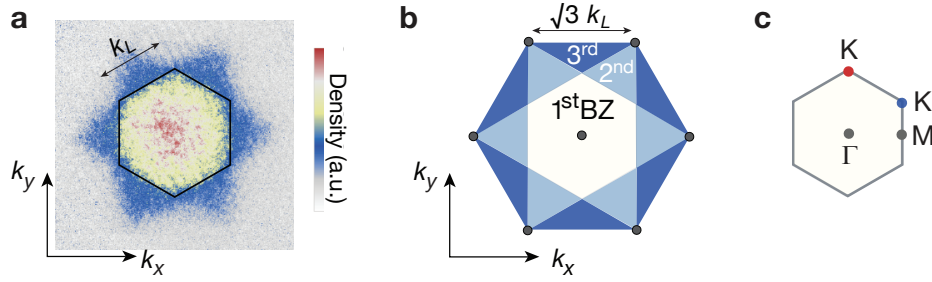
Figure 5.5.: Images after band mapping: **(a)** Thermal atoms loaded in the lattice and imaged after band mapping and TOF. First (hexagon) and second bands are completely filled. **(b)** Schematic of the first three Brillouin zones which correspond to different bands being populated. **(c)** Relevant high-symmetry points in the first Brillouin zone.

potential with a spatial distribution given by the ground state of the harmonic trap. This in-situ density distribution of interacting atoms, described by the Thomas-Fermi parabolic profile, cannot be neglected for short TOF. This is the case in our experiment where the observed density distribution is a convolution of the quasimomentum and real-space distributions. The real quasimomentum distribution can be extracted by extrapolating the cloud's density profile to long TOF durations.

5.2.3. Lattice calibration via parametric heating

The lattice depth can be calibrated by exciting the atoms via a periodic modulation of the intensity of the lattice beams [208, 209]. When the modulation V_{mod} is weak compared to the energy difference between the bands, its effect can be treated as a perturbing periodic potential which is added to the one of the static lattice

$$V(t, \mathbf{r}) = V_L(\mathbf{r}) + V_{mod} \cos(\omega t). \tag{5.2}$$

The effect of the modulation is to add a coupling between two different bands. When the frequency ω matches the energy difference between the bands the atoms are resonantly excited and energy is pumped into the system. Atoms can therefore be lost from the trap after some long waiting time. The resonance feature associated with the enhancement of the atomic loss due to parametric heating gives an estimate of the energy difference between two bands. A comparison between the resonance frequencies and the band structure calculation gives an estimate of the lattice depth, as the plot in Fig. 5.6b shows. The broadening of the resonance feature is given by the transitions bandwidths and the inhomogeneity of the lattice over the extension of the cloud. As long as the modulation is weak, the measured resonance frequency will correspond to the energy difference between the bands. If that is not the case, deformations of the lattice potential can broaden and shift the resonance.
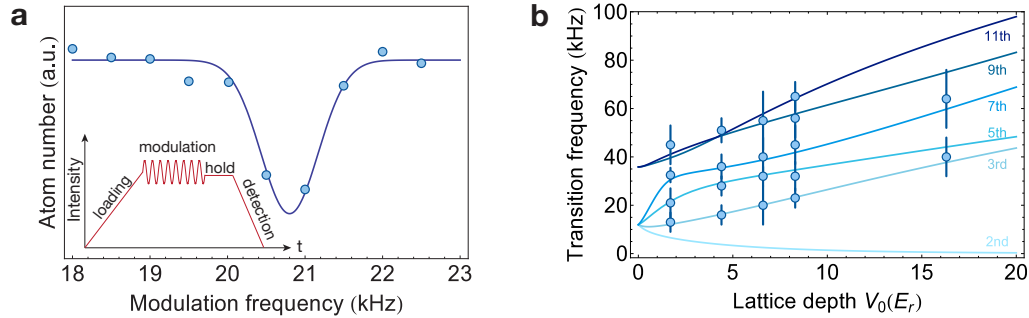
Figure 5.6.: **(a)** Example of a resonance feature measured by amplitude modulation together with a Gaussian fit. The experimental sequence is depicted in the inset. **(b)**: Measured resonance frequencies for transitions from the first band to higher bands for atoms loaded at $\mathbf{k} = 0$. Data are overlapped with calculated theory lines to estimate the lattice depth.

5.3. Bloch oscillations

When atoms of a weakly interacting BEC are adiabatically loaded in a lattice they will macroscopically populate the $\mathbf{k} = 0$ state which has the lowest energy. Analogously to electrons in a solid under the influence of an electric field, the addition of a force results in a change of the atoms' quasimomentum and in a motion of the atoms in the Brillouin zone. For strong enough forces, interband tunneling becomes possible. Bloch oscillations are by now a standard technique to probe properties of band structures with cold atoms [215, 216]. In this section, we focus on our experimental realization via lattice acceleration and field gradient and on the specifics of Bloch oscillations in a honeycomb lattice.

5.3.1. Force from a field gradient

A standard way of introducing an external force acting on the atoms is to add a potential gradient via a magnetic field. The spin-dependent potential for an atom of magnetic moment μ in a magnetic field gradient described by $B(\mathbf{r}) = B_0 + \mathbf{r} \cdot \nabla B$ is

$$V_B = \mu B(\mathbf{r}) = \mu B_0 + \mathbf{F} \cdot \mathbf{r}. \tag{5.3}$$

The force $\mathbf{F} = \mu \cdot \nabla B$ experienced by the atoms can be considered constant if the curvature of the magnetic field is negligible at the atoms' position. This is the case in our experiment where the homogeneous gradient is created by the pair of Stern-Gerlach coils presented in Section 4.4. The two coils also allow to fine tune the direction of the force, if needed.
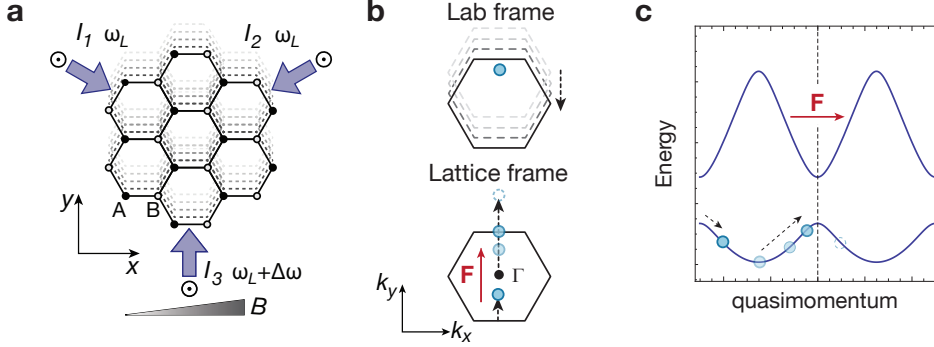
Figure 5.7.: **(a)** Sketch of the honeycomb lattice in real space. A linear frequency sweep of the third lattice beam creates a uniform lattice acceleration along the y-direction. A magnetic field gradient can create an additional spin-dependent force along the x direction. **(b)** Schematic of the motion of the particles (blue circles) in the first BZ (hexagons) when the lattice is accelerated. In the lab frame of reference, the BZ is moving relative to the atoms. The opposite happens in the frame co-moving with the lattice. **(c)** Schematic motion of the particles in the lowest band in the adiabatic case. The quasimomentum of particles changes in time according to eq. 5.11.

5.3.2. Force from lattice acceleration

A force can also be realized by moving the lattice potential relative to the atoms. This motion is implemented experimentally by controlling the relative phase of the lattice beams that generate the optical potential. The effect of a phase difference between the lattice beams is to create a spatial displacement of the lattice potential. As an illustrative example, we can consider a 1D lattice created by two counter-propagating lattice beams with electric fields $\mathbf{E}_1 \propto e^{ik_L r}$ and $\mathbf{E}_2 \propto e^{-ik_L r}$ which generate the following optical potential $V_L = U_0 I(r) \propto \cos^2(k_L r)$. If the phase of one lattice beam is changed relative to the other, e.g. $E_1 \to E_1 e^{i\Delta\phi}$, the optical potential becomes $V_L \propto \cos^2(k_L r + \Delta\phi/2)$ and the additional phase results in a shift of the periodic pattern along r. The same effect happens in the honeycomb optical lattice when the phase of one lattice beam is changed relative to the other two.

The phase difference between the beams is experimentally tuned by changing the frequency of a lattice beam relative to the others, i.e. by making the following substitution $\omega_L \to \omega_L + \Delta\omega$ for one of them. If the change of the frequency $\Delta\omega$ is small, it will not affect the k-vector in first approximation and we can model its effect by adding the term $\Delta\omega$ to the electric field of one running wave generating the honeycomb potential defined by eq. 3.29. If $\Delta\omega$ is time-independent, the electric field of the lattice beam which is modified becomes $E_i \propto e^{i\mathbf{k}_i \mathbf{r} - i(\omega + \Delta\omega)t}$. The phase difference $\Delta\phi$ between the beams is given by $\Delta\phi(t) = \Delta\omega\, t$, hence the optical potential moves with a constant velocity proportional to $\Delta\omega$. If the frequency difference

is time-dependent, instead, the lattice is accelerated. The phase shift $\Delta\phi(t)$ is given by the following equation in this case

$$\Delta\phi(t) = \int_0^t \Delta\omega(t')dt'. \tag{5.4}$$

If $\Delta\omega(t)$ is linearly ramped over time, the lattice has a constant acceleration and a constant inertial force acts on the atoms in the reference frame co-moving with the lattice. We parametrize this linear ramp as

$$\Delta\omega(t) = 2\pi\frac{\delta\nu}{\delta t}t \tag{5.5}$$

where $\frac{\delta\nu}{\delta t} = const.$ is the constant rate of frequency change and $\nu = 2\pi\omega$. The effect of the additional time-dependent phase $\Delta\phi(t)$ is to move the lattice potential along the direction of the running wave which is frequency shifted. For example, if the beam with wave-vector $\mathbf{k}_3$, see the labeling in Fig. 5.7a, is changed, we obtain the following displacement along the the y-axis from the definition of the honeycomb potential, eq. 3.29,

$$y(t) = y_0 + \frac{2}{3k_L}\Delta\phi(t). \tag{5.6}$$

The interference pattern moves as illustrated in Fig.5.7a. Given this displacement, we can directly infer the magnitude of the acceleration of the lattice from eq. 5.5 and eq. 5.6 and derive the force experienced by an atom of mass m. The acceleration is described by

$$|\mathbf{a}_L| = \frac{2}{3}\lambda_L\frac{\delta\nu}{\delta t} = \frac{|\mathbf{F}|}{m}. \tag{5.7}$$

By tuning the parameter $\frac{\delta\nu}{\delta t}$, the strength of the force can be adjusted at will. The direction of the force is given by the pointing direction of the lattice beam which is changed, i.e. by the k-vectors defined in Section 3.2. Moreover, if more than one lattice beam is frequency-shifted, the total inertial force experienced by the atoms will be given by the vector sum of the individual forces and it can point in any arbitrary direction. Furthermore, non-constant forces can also be easily implemented. For example, circular motion can be realized with a sinusoidal modulation of the frequency of two lattice beams, appropriately phase shifted relative to each other. The circular motion can be used to break time-reversal symmetry of the lattice potential [82].

5.3.3. Time dependent Hamiltonian

To understand the effect of the forces we can now derive the time-dependent Hamiltonian in the lab frame describing the evolution of the atoms when the magnetic

field gradient of equation 5.3 and an orthogonal acceleration of the lattice $\mathbf{a}_L \perp \nabla B$ are combined. In the lab frame of reference, the resulting Hamiltonian for an atom of magnetic moment μ and mass m is

$$H(t) = \frac{\mathbf{p}^2}{2m} + V_L\left[\mathbf{r} - \mathbf{R}\left(t\right)\right] - \mu\,\mathbf{r}\cdot\nabla B - \mu B_0, \qquad (5.8)$$

where $V_L(\mathbf{r})$ describes the lattice potential at $t = 0$, see eq. 3.29, and $\mathbf{R}(t) = \mathbf{a}_L t^2/2$ is the time-dependent displacement given by the lattice acceleration defined by eq. 5.7. Here we neglect the presence of the external harmonic trapping potential as we are interested in small spatial displacements of the atoms about the center of the trap where the trapping potential can be considered as constant in first approximation. For larger displacements, the presence of a trap can not be neglected and one needs to account for the restoring force of the harmonic potential as well. The dynamics of the Hamiltonian 5.8 can be most conveniently analyzed in a frame co-moving with the lattice by making a unitary transformation $U(t) = e^{-i\mathbf{r}\cdot m\mathbf{a}_L t/\hbar}e^{i\mathbf{p}\cdot\mathbf{a}_L t^2/(2\hbar)}$. This transformation takes into account the real space displacement $\mathbf{R}(t)$ as well as the finite velocity of the atoms in the accelerated lattice, $\mathbf{v} = m\mathbf{a}_L t$. The time-dependent Schrödinger equation for the wavefunciton ψ is then equivalently expressed as $i\hbar\dot{\tilde{\Psi}} = \tilde{H}\tilde{\Psi}$ in the co-moving frame, where $\tilde{\Psi} = U\psi$. The new hamiltonian is

$$\tilde{H} = UHU^\dagger + i\hbar\dot{U}U^\dagger = \frac{\mathbf{p}^2}{2m} + V_L(\mathbf{r}) - \boldsymbol{\mathcal{F}}_\mu \cdot \mathbf{r} + \varepsilon_\mu(t) + \varepsilon_{cm}(t). \qquad (5.9)$$

The total force

$$\boldsymbol{\mathcal{F}}_\mu = \mu\nabla B - m\mathbf{a}_L \qquad (5.10)$$

includes both the force from the field gradient and the fictitious force experienced by the atoms in the non-inertial lattice frame. The factor $\varepsilon_{cm} = \frac{1}{2}m|\mathbf{a}_L t|^2$ describes an additional kinetic energy offset which takes into account the fact that the atoms are moving at a finite velocity in the lab frame. The term $\varepsilon_\mu(t) = -\mu[\mathbf{R}(t)\cdot\nabla B + B_0]$ describes the Zeeman energy due to the presence of a magnetic field. The $\mathbf{R}$-dependent Zeeman contribution in ε_μ is set to zero whenever the acceleration of the lattice is orthogonal to the magnetic field gradient.

The effect of the constant force $\boldsymbol{\mathcal{F}}_\mu$ on the Bloch wavefunctions is to induce a time-dependent translation in reciprocal space which is given by

$$\mathbf{k}(t) = \mathbf{k}_0 + \frac{\boldsymbol{\mathcal{F}}_\mu t}{\hbar}. \qquad (5.11)$$

Because of the periodicity of the lattice, the quasimomentum $\mathbf{k}(t)$ is restricted to the first Brillouin zone and the motion is periodic with a Bloch period t_B which depends on the direction and strength of the force applied. For example, the Bloch period for a force pointing from the Γ-point through the M-point is $t_B = \sqrt{3}\hbar k_L/|\boldsymbol{\mathcal{F}}_\mu|$
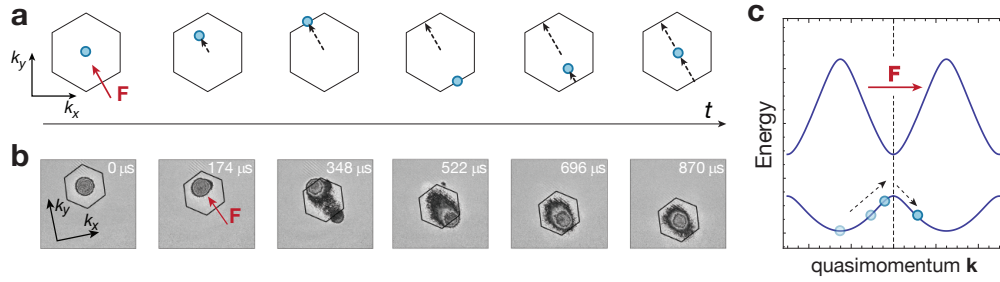
Figure 5.8.: Adiabatic motion of atoms in the lowest band. **(a)** Schematic periodic motion of the particles (blue circles) in the first BZ for a force **F** pointing as illustrated (red arrow). **(b)** Corresponding images of the quasimomentum distribution of the atoms during the adiabatic Bloch oscillation. Images of the condensed ^{87}Rb atoms loaded in the lattice are taken in the lab frame after band-mapping and TOF. Atoms are restricted to the first Brillouin zone (hexagons) because only the first band is populated during the adiabatic motion, as illustrated in **(c)**. Bands are plotted in a repeated zone scheme.

in the honeycomb lattice, while the Bloch period for a force pointing through the K-point is $t_B = 3\hbar k_L |\boldsymbol{\mathcal{F}}_\mu|$, simply because of the geometry of the Brillouin zone. It is important to note that the images we get after band mapping and TOF are taken in the lab frame. This means that we observe the BZ moving with respect to the atoms while the opposite happens in the co-moving frame as depicted in Fig. 5.7b. Given that the choice of reference frame does not affect the physics, the result of the forces is to move the atoms in the band according to eq. 5.11, as illustrated in Fig. 5.7c.

Phase factors from the adiabatic motion

If the force is sufficiently weak to restrict the dynamics to a single band n, the form of the Bloch wavefunctions is preserved, up to a phase factor, by substituting the quasimomentum with the time-dependent one, $\mathbf{k}(t)$

$$\tilde{\Psi}(t) = e^{i\eta(t)}\psi^n_{\mathbf{k}(t)}, \tag{5.12}$$

where $\psi^n_{\mathbf{k}}(\mathbf{r})$ are Bloch wavefunctions of the bare Hamiltoninan $H_0 = \mathbf{p}^2/(2m) + V_L(\mathbf{r})$ for the nth band. By substituting the ansatz 5.12 into the time-dependent Schrödinger equation for $\tilde{H}$, eq. 5.9, the phase factor $\eta(t)$ is derived. This is given by $\eta(t) = \varphi_{\text{dyn}}(t) + \phi_g$ that generically includes both a dynamical contribution

$$\varphi_{\text{dyn}}(\tau) = -\frac{1}{\hbar}\int_0^\tau \left[E_1\left(\mathbf{k} + \boldsymbol{\mathcal{F}}_\mu t\right) + \varepsilon_\mu + \varepsilon_{kin}\left(t\right)\right] dt \tag{5.13}$$
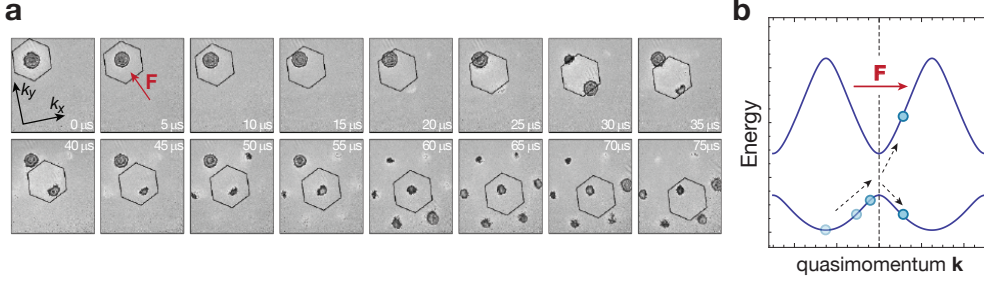
Figure 5.9.: Diabatic motion of atoms in the first and second band. **(a)** Images of the quasimomentum distribution of the atoms after band-mapping and TOF for the same motion illustrated in Fig. 5.8a. Due to the presence of a strong force, the motion of the atoms is non-adiabatic: Atoms outside the first Brillouin zone (hexagons) are populating higher bands. Their motion in the two lowest bands is illustrated in **(b)**.

and a geometric contribution

$$\phi_g = i \int_0^\tau \langle u_{\mathbf{k}(t)}^1 | \, \nabla_\mathbf{k} \, | u_{\mathbf{k}(t)}^1 \rangle \cdot \boldsymbol{\mathcal{F}}_\mu \, dt = i \int_C \langle u_\mathbf{k}^1 | \, \nabla_\mathbf{k} \, | u_\mathbf{k}^1 \rangle \cdot d\mathbf{k} \tag{5.14}$$

which depends only on the path C taken in the reciprocal space and corresponds to the Berry phase for any closed loop. An example of adiabatic motion of atoms in the hexagonal lattice is illustrated in Fig. 5.8.

Non-adiabatic motion

Transitions into higher bands occur when a strong external force is acting on the particles. In the context of electrons in solids this effect is known as the Landau-Zener breakdown, occurring if the applied electric field is strong enough for the electrons to be excited from the valence to the conduction bands [217]. In our case, we can not describe our system as a linear crossing of energy levels, as Landau and Zener do, but we can derive equivalent equations of motion that describe the evolution of the atoms in the two lowest bands of the honeycomb lattice. To find the equation of motion from the time-dependent Hamiltonian of eq. 5.9, we can make an ansatz for the wavefunction like $\Psi(t) = \alpha_1(t)\psi_{\mathbf{k}(t)}^1 + \alpha_2(t)\psi_{\mathbf{k}(t)}^2$. Analogously to what we have done before for a single band, we can derive the equation of motion for the coefficients α_1 α_2 from the Schrödinger equation

$$i\hbar\dot{\Psi} = (H_0 - \boldsymbol{\mathcal{F}}_\mu \cdot \mathbf{r})\Psi \tag{5.15}$$

where the common energy offsets ϵ_μ and ϵ_{kin}, not relevant for the dynamics, have been neglected. The equations of motion for atoms in the two lowest bands are

described by

$$i\hbar \begin{pmatrix} \dot{\alpha_1}(t) \\ \dot{\alpha_2}(t) \end{pmatrix} = \begin{pmatrix} E^1_{\mathbf{k}(t)} - \langle u^1_{\mathbf{k}(t)}| \, \boldsymbol{\mathcal{F}}_\mu \cdot \mathbf{r} \, |u^1_{\mathbf{k}(t)}\rangle & - \langle u^1_{\mathbf{k}(t)}| \, \boldsymbol{\mathcal{F}}_\mu \cdot \mathbf{r} \, |u^2_{\mathbf{k}(t)}\rangle \\ - \langle u^2_{\mathbf{k}(t)}| \, \boldsymbol{\mathcal{F}}_\mu \cdot \mathbf{r} \, |u^1_{\mathbf{k}(t)}\rangle & E^2_{\mathbf{k}(t)} - \langle u^1_{\mathbf{k}(t)}| \, \boldsymbol{\mathcal{F}}_\mu \cdot \mathbf{r} \, |u^1_{\mathbf{k}(t)}\rangle \end{pmatrix} \begin{pmatrix} \alpha_1(t) \\ \alpha_2(t) \end{pmatrix}.$$

(5.16)

When the force is strong, first and second band are coupled and atoms which are initially prepared in the lowest band can populate the second band during their motion in the Brillouin zone, as illustrated by the example in Fig. 5.9.

5.3.4. Effects of weak interactions

In the experiments described in this thesis we are studying weakly interacting bosons in a superfluid state where the interactions are repulsive. Their effects are not always negligible, as we already mentioned in Section 4.1.3. Weak interactions can result in instabilities when the particles move in the energy bands and have a non-zero quasimomentum. These instabilities put a limit on the timescales of coherent evolution of the wavefunction when particles are subjected to a force. The most significant sources of instability are summarized here, for a more detailed discussion we reference to the following experimental and theoretical studies [143, 218–223].

Dynamical and energetic instabilities

Dynamical and Landau instabilities are the two main sources of dephasing of the weakly interacting BEC. Both instabilities can occur in a lattice and depend on the quasimomentum of the condensate.

Energetic (Landau) instabilities are a common dissipative process for superfluids and they occur whenever the system can lower its energy by emitting phonons. Whether that is the case is determined by the energy dispersion of the excitation modes. If the spectrum has negative eigenvalues, the population of these modes will grow and the excitations will break the superfluidity. In free space, this instability corresponds to the criterion for superfluidity given by Landau, where the condensate with a group velocity larger than the sound velocity is energetically unstable to the presence of perturbations [224]. In a periodic potential, an analogous sound velocity can be derived from the excitation spectrum. In the tight binding limit and in absence of trapping potential the excitation spectrum is calculated analytically [219, 220, 225] and the sound velocity is approximated by $c^2 \approx U n_0 E_0(\mathbf{k})/\mathbf{k}^2$ where $E_0(\mathbf{k})$ is single particle energy spectrum in absence of interactions, $\mathbf{k}$ the quasimomentum of the excitations, U the interaction strength and n_0 is the population of each lattice site. The greater the interactions the less important the Landau instability will be.

While Landau instability is closely related to the thermal component of the gas and occurs only at finite temperatures, dynamical instability is instead a collective excitation of the condensate and it can happen even at $T = 0$ [221]. This instability
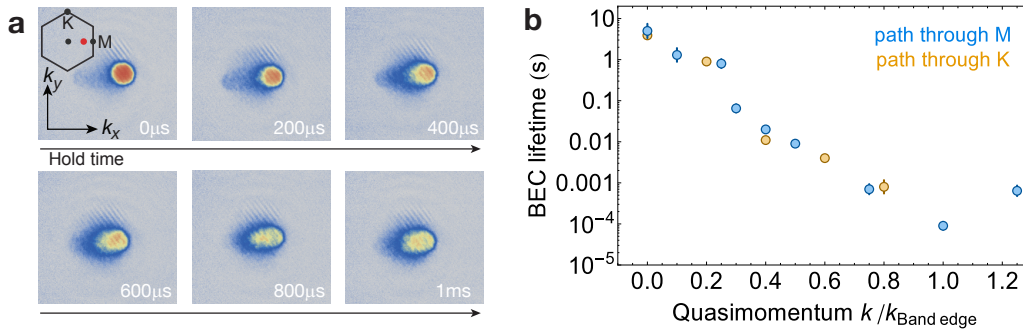
Figure 5.10.: **(a)** Evolution of the BEC ($\sim 5 \times 10^4$ atoms) in the lattice with increasing hold time. The initial quasimomentum of the condensate is represented in the schematic (red dot). Images are taken after band mapping with a short time-of-flight. Instabilities can deplete the condensate and modify the quasimomentum distribution on long timescales. **(b)** Log plot of typical lifetimes for a BEC of $\sim 5 \times 10^4$ atoms in a $1E_r$ lattice measured by monitoring the decrease of the maximum optical density over time. They are measured at different k-points along a path thoward the **K** or **M** point, k values are renormalized to the distance from the Γ point to the band edge, $k_{\text{Band edge}}$. Note that lifetimes close to the edge of the band are typically $\leq$1ms.

occurs only for weakly interacting particles in a periodic potential as a result of the interplay between the dispersion relation and nonlinearity of the Gross-Pitaevskii equation. The dynamical instabilities arise for a quasimomenta above a threshold $\mathbf{k}_c$, where the frequency of the excitation spectrum of the Bogoliubov modes has an imaginary component [219, 222, 226]. When this happens, an arbitrary small perturbation can grow exponentially in time. The growth of these unstable modes drives the system far away from the initial state, as observed and studied in 1D lattice experiments [221, 227, 228]. In the tight binding limit for a 1D lattice the instability sets in at the quasimomentum where the effective mass changes sign [219, 226]. Intuitively, this can be understood by noting that a sign inversion corresponds to the case of an effective attractive interaction which makes the system unstable.

Both instabilities occur in our case since the almost pure BEC is weakly interacting. Typical working parameters, like average particle number, densities and interaction strength for the array of tubes are derived and summarized in the appendix C. As illustrated in Fig. 5.10, we observed instabilities which decrease the lifetime of the condensate in the lattice when the atoms are prepared at a quasimomentum $\mathbf{k} \neq 0$. The images in Fig. 5.10a show an example of such growth of excitation modes which alters the initial state and destroys the condensates after some long hold time. We observed that the timescale for the growth of instabilities is strongly dependent on the quasimomentum and it changes by more than four orders of magnitude from the bottom of the first band to the zone edge, as illustrated in the

graph of Fig. 5.10b. The continuous decrease in lifetime indicates that both energetic and dynamical instabilities are present in our experimental realization. These instabilities put a limit on timescales for the motion of the atoms in the band.

In the experimental results of the following chapters, the atoms are in a superfluid state as they are loaded in shallow lattices $(1-5E_r)$ and interactions are weak and repulsive. When we apply a force to move the atoms in reciprocal space, we purposely employ oscillations which are fast enough to avoid the loss of coherence caused by the exponential growth of the instabilities. The most relevant effect of weak interactions that we need to account for is the initial quasimomentum spread of the weakly interacting BEC loaded in the lattice at $\mathbf{k} = 0$. In the following chapter, we will model it with a distribution $n(\mathbf{k})$ which represents the normalized quasimomentum distribution of the atoms in the lattice, approximated by a Gaussian with standard deviation $\sigma_{\mathbf{k}}$ whose spread depends on density and interaction strength.

5.4. Final remarks

In this chapter, we have introduced the experimental setup of the honeycomb lattice and we have illustrated standard techniques to probe and manipulate the state of atoms loaded into it. We have shown how atoms subjected to an external force can be moved in the energy band along a certain path in the Brillouin zone which we can choose experimentally. In the following chapters we will make use of Bloch oscillations to probe the topological properties of the lattice by probing how the eigenstates change when particles are moved in the Brillouin zone.

Chapter 6.

Aharonov-Bohm interferometry in the honeycomb lattice

As reviewed in Chapter 2, the physical properties of a lattice are encoded not only in the scalar dispersion of the bands, but also in the geometry of the band eigenstates. The ability to map the distribution of Berry curvature of an energy band is essential to its characterization as it determines its topological invariant. In this chapter we present the interferometric technique, extension of the Zak phase measurement technique presented in [57, 58], which we use to probe the topological properties associated with individual cones of the optical honeycomb lattice.

In Section 6.1.1, the interferometry around the Dirac cones is introduced and the analogy with the celebrated Aharonov-Bohm effect is illustrated. The experimental sequence is described in general terms in Section 6.1.2, then the details of the experimental realization are briefly presented in Section 6.2. Here, we also comment on the sources of systematic errors that can introduce non-negligible dynamical phases to the interferometric signal and we illustrate the theoretical model used to interpret the experimental results, Section 6.2.3. In Section 6.3, the experimental results of the measured Berry phases associated with the Dirac cones are presented. In Section 6.3.2, a self-referenced interferometry allows us to reduce systematic errors and to estimate an upper bound for the spread in Berry curvature. In Section 6.3.3, the interferometry is used to directly observe the motion of the fluxes in the Brillouin zone and their annihilation upon lattice imbalance. In Section 6.4, conclusions and future applications of this interferometric technique are briefly summarized. Additional details on eperimental parameters and numerical simultaions can be found in appendix D.

6.1. An interferometer to characterize Bloch bands' topology

To locally map the topological features of a Bloch band of the honeycomb lattice, we realize an atomic interferometer in momentum space. This experimental technique

a π Magnetic Flux   **b** π Berry Flux

Real space   Reciprocal space
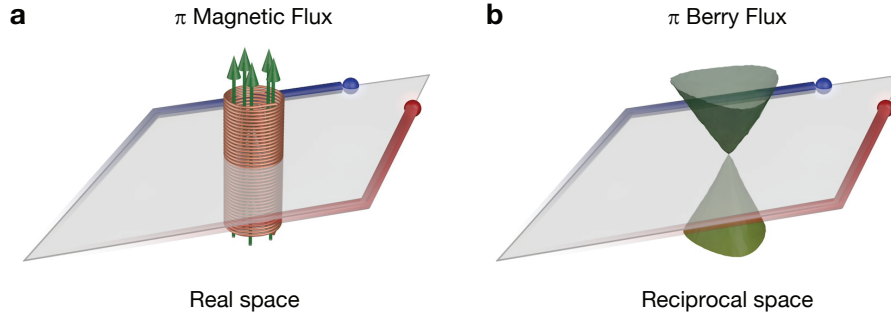
Figure 6.1.: In the Aharonov-Bohm effect **(a)**, electrons encircle a magnetic flux in real space, whereas in our interferometer **(b)**, the particles encircle the π-Berry flux of a Dirac point in reciprocal space. In both cases, the flux through the interferometer loop gives rise to a measurable phase difference.

is presented in this section.

6.1.1. The analogy with the Aharonov-Bohm effect

The Aharonov-Bohm effect [10] is one well known example of how a geometric phase can manifest itself when particles move adiabatically in a closed loop in the parameter space. In the specific example considered by Aharonov and Bohm, charged particles are moving around an infinite solenoid, source of a magnetic field. Even if the particles travel in a zero-field region where no force is acting on them, the magnetic flux confined inside the solenoid influences the eigenstates of the charged particles everywhere via the magnetic vector potential $\mathbf{A}(\mathbf{r})$. As a result, particles with charge q acquire a path-dependent phase shift due to the presence of a vector potential extending outside the coil. If two particles are moving along different paths, on the left and on the right of the solenoid (Fig. 6.1a), they acquire a phase difference due to the magnetic flux, Φ_B, through the enclosed area S. This measurable phase difference between particles is

$$\Delta\varphi = \frac{q}{\hbar} \oint_C \mathbf{A}(\mathbf{r})d\mathbf{r} = 2\pi\frac{\Phi_B}{\Phi_0} \tag{6.1}$$

where C is the contour of the enclosed area, $\Phi_0 = h/q$ is the flux quantum and $\Phi_B = \int_S \mathbf{B}(\mathbf{r})dS$.

The topological features of an energy band can be viewed as the analog of a magnetic field in reciprocal space generated by the Berry connection $\mathbf{A}^n(\mathbf{k})$, that plays the role of the vector potential $\mathbf{A}(\mathbf{r})$ for the neutral atoms in the optical lattice. The Berry curvature $\Omega^n(\mathbf{k})$ is thus equivalent to a magnetic field $\mathbf{B}$. The Dirac cones of the honeycomb lattice with their singular Berry fluxes correspond to the infinite and narrow solenoid. In analogy to an Aharonov-Bohm interferometer

that measures the total magnetic flux in real space, we can thus realize an atomic interferometer to measure the Berry flux of a certain energy band in momentum space. By adiabatically moving a condensate, our (ideally) point-like probe, in the lowest energy band of the honeycomb lattice, we can directly measure the topological properties associated with a Dirac cone, which have been presented in Chapter 3. Information on their distribution in reciprocal space can be gained by changing the area of the loop, i.e. the total flux going through the interferometer.

6.1.2. The sequence for the Aharonov-Bohm interferometry

The Aharonov-Bohm interferometry for ultracold atoms combines the motion due to a spin-dependent force, presented Section 5.3, with a spin-echo sequence [57, 58]. The protocol measures the phase difference picked up by the two spin components as they move in a loop in the Brillouin zone.

In our experimental realization, the spin-echo sequence employs two internal states of ^{87}Rb, $|\uparrow\rangle = |F = 2, m_F = 1\rangle$ and $|\downarrow\rangle = |F = 1, m_F = 1\rangle$ that have opposite magnetic moment. The interferometer sequence is illustrated in Fig. 6.2. It begins with the preparation of an almost pure ^{87}Rb BEC in the state $|\uparrow\rangle$ at quasimomentum $\mathbf{k} = 0$ in the lowest band of a $V_0 = 1.0(1) \, E_r$ deep lattice. The lattice depth has been chosen to be able to move the atoms adiabatically in the energy band on timescales on the order of few milliseconds.

Subsequently, the atoms are exposed to a microwave (MW) field resonant with the transition $|\uparrow\rangle \to |\downarrow\rangle$ of frequency ω_r which is described by following field $V_{\mathrm{MW}}(t) = \hbar\Omega \cos(\omega_r t)$, Ω being the Rabi frequency. The effect of the microwave is to coherently couple the two states. In the rotating frame, a $\pi/2$-microwave pulse will transform the spin states according to

$$|\downarrow\rangle \to \frac{1}{\sqrt{2}} \left(|\uparrow\rangle + |\downarrow\rangle \right) \tag{6.2}$$

$$|\uparrow\rangle \to \frac{1}{\sqrt{2}} \left(|\uparrow\rangle - |\downarrow\rangle \right) \tag{6.3}$$

while a π-pulse will flip the states as $|\uparrow\rangle \to -|\downarrow\rangle$ and $|\downarrow\rangle \to |\uparrow\rangle$. As illustrated in Fig. 6.2, in the step (i) a resonant $\pi/2$-microwave pulse creates a coherent superposition of $|\uparrow\rangle$ and $|\downarrow\rangle$ states. After this pulse each atom will be in the following state

$$|\psi\rangle = \frac{1}{\sqrt{2}} \left(|\uparrow, \mathbf{k} = 0\rangle - |\downarrow, \mathbf{k} = 0\rangle \right) \tag{6.4}$$

where $|\mathbf{k}\rangle$ indicates the Bloch wave of the first band with quasimomentum $\mathbf{k}$. Since we are working with N particles loaded in the lattice, we need to remember that product of these single particle states constitutes the many-body state. After the state preparation, a state-dependent force from a magnetic field gradient and an
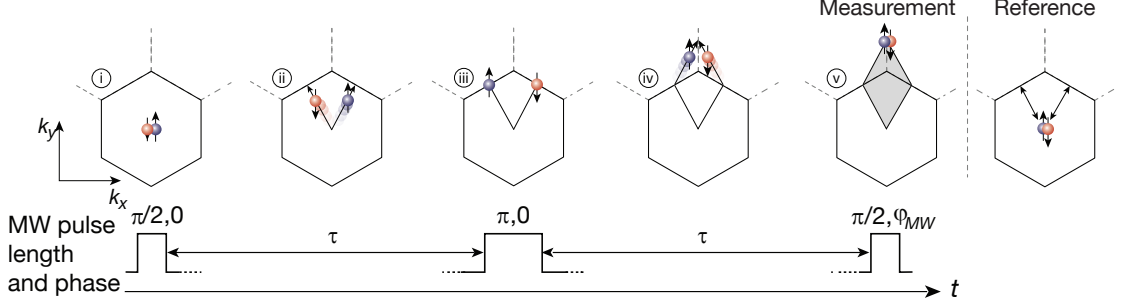
Figure 6.2.: Interferometer sequence. Hexagons indicate the first Brillouin zone and red (blue) spheres are atoms in the $|\downarrow\rangle$ ($|\uparrow\rangle$) state. The sequence of microwave pulses and the motion of particles in the energy band due to the applied forces are illustrated. The different steps of the protocol are described in the main text.

orthogonal state-independent force from the lattice acceleration move the atoms adiabatically along state-dependent paths in reciprocal space, which are described by the time-dependent quasimomentum $\mathbf{k}(t)$ of equation 5.11, (ii). The evolution of each atom is described by the time-dependent Hamiltonian for Bloch oscillations, see eq. 5.9, and the total state-dependent force $\boldsymbol{\mathcal{F}}$ is described by eq. 5.10. In the ideal case, the direction of the force is chosen such that the two spin components move symmetrically about a symmetry axis of the dispersion relation, i.e. $k_{x,\uparrow} = -k_{x,\downarrow}$ and $k_{y,\uparrow} = k_{y,\downarrow}$, as shown in figure. This ensures that two spin states of opposite magnetic moment sample the same dispersion relation at each point in time

$$E^1\left(\mathbf{k}(0) + \boldsymbol{\mathcal{F}}_{|\mu|}t\right) = E^1\left(\mathbf{k}(0) + \boldsymbol{\mathcal{F}}_{-|\mu|}t\right). \tag{6.5}$$

If that is the case, there is no energy difference between the spin states anywhere along the path. This means that after an evolution time t the dynamical phase $\varphi_{\text{dyn}}(t) = \int_0^t E^1(\mathbf{k}(0) + \boldsymbol{\mathcal{F}}t')dt'$ arising from the motion of each atom in the energy band is identical for both spin states and it will have no influence on the final measurement of the Berry phase. In this case the state of a particle reads

$$|\psi\rangle = \frac{e^{i\varphi_{\text{dyn}}(t)}}{\sqrt{2}}\left(|\uparrow, \mathbf{k} - \boldsymbol{\mathcal{F}}_{|\mu|}t\rangle - |\downarrow, \mathbf{k} + \boldsymbol{\mathcal{F}}_{|-\mu|}t\rangle\right). \tag{6.6}$$

If the orthogonality between the forces is imperfect, instead, the atoms in the two spin states will evolve differently and they will acquire different dynamical phases during the motion. These additional terms will contribute to the phase one measures at the end of the interferometry.

After an evolution time τ, a microwave π-pulse swaps the states $|\downarrow\rangle$ and $|\uparrow\rangle$ (iii). The two atomic wavepackets now experience a magnetic force pointing in the opposite direction along x, such that both spin components arrive at the same

quasimomentum $\mathbf{k}^{\text{fin}}$ after an additional evolution time τ (iv). At this point, the state of the atoms is given by the following superposition of $|\uparrow\rangle$ and $|\downarrow\rangle$ states

$$|\psi^{\text{fin}}\rangle \propto |\uparrow, \mathbf{k}^{\text{fin}}\rangle + e^{i\varphi}|\downarrow, \mathbf{k}^{\text{fin}}\rangle \tag{6.7}$$

with relative phase φ. Ideally, all the dynamical phases accumulated by the two spin states should be common because of the symmetry of the paths and the use of the spin-echo pulse, which eliminates the contribution to the dynamical phase related to the motion in the inhomogeneous magnetic field. In this case the phase φ consists of the geometric phase φ_B only. In reality experimental imperfections can introduce a difference in the dynamical phases accumulated by the two spin components, $\varphi_{\text{dyn},\downarrow}$, $\varphi_{\text{dyn},\uparrow}$. The final phase φ is given by

$$\varphi = \varphi_B + (\varphi_{\text{dyn},\downarrow} - \varphi_{\text{dyn},\uparrow}). \tag{6.8}$$

Finally, a read-out $\pi/2$-microwave pulse with a variable phase φ_{MW} is applied at the end of the motion (v). The microwave field changes as $V_{\text{MW}}(t) = \hbar\Omega\cos(\omega_r t - \varphi_{\text{MW}})$ and the $\pi/2$-pulse rotates the states according to

$$|\downarrow\rangle \rightarrow \frac{e^{i\varphi_{\text{MW}}/2}}{\sqrt{2}}\left(e^{i\varphi_{\text{MW}}/2}|\uparrow\rangle + e^{-i\varphi_{\text{MW}}/2}|\downarrow\rangle\right) \tag{6.9}$$

$$|\uparrow\rangle \rightarrow \frac{e^{-i\varphi_{\text{MW}}/2}}{\sqrt{2}}\left(e^{i\varphi_{\text{MW}}/2}|\uparrow\rangle - e^{-i\varphi_{\text{MW}}/2}|\downarrow\rangle\right) \tag{6.10}$$

and closes the interferometer. The final state becomes

$$|\psi^{\text{fin}}\rangle \propto e^{i\frac{\varphi+\varphi_{\text{MW}}}{2}}\left(\cos\left(\frac{\varphi_{\text{MW}}}{2} + \frac{\varphi}{2}\right)|\uparrow, \mathbf{k}^{\text{fin}}\rangle + i\sin\left(\frac{\varphi_{\text{MW}}}{2} + \frac{\varphi}{2}\right)|\downarrow, \mathbf{k}^{\text{fin}}\rangle\right). \tag{6.11}$$

The phase information is converted into spin population fractions that are given by

$$n_{\uparrow,\downarrow} = \frac{N_{\uparrow,\downarrow}}{N} = \frac{1}{2}\left(1 \pm \cos(\varphi + \varphi_{\text{MW}})\right) \tag{6.12}$$

where N is the total atom number and $N_{\uparrow,\downarrow}$ the atoms in a certain spin state. The accumulated phase φ can be measured by varying the phase φ_{MW}. It is important to note that, given the form of eq. 6.12, we can only measure the phase φ modulo π. This means, for example, that we can not distinguish the sign of the Berry phase when it is exactly $\pm\pi$.

In order to independently estimate any possible dynamical phase contribution and extract only the one of geometric origin, we additionally employ a 'zero-area' reference interferometer, comprising a V-shaped path (Fig. 6.2 (v)) realized by reversing the lattice acceleration after the π-microwave pulse in (iii). In this case, the measured phase consists only of a small dynamical phase difference introduced,

eventually, by the experimental imperfections.

6.2. Experimental details

Here, the experimental parameters and possible sources of residual systematic errors for the Aharonov-Bohm interferometry are summarized. We also comment on the effect of weak interactions on the interference fringes and present a simple theory model which we use to interpret the experimental results obtained in the weakly interacting case. Additional experimental details can be found in the appendix D.

6.2.1. Experimental parameters

The interferometry is performed in a $1.0(1)$ E_r lattice in which we load a Rubidum cloud of $\sim 4 \times 10^4$ condensed atoms. The lattice depth was chosen to have a large separation between the two lowest bands (~ 8 kHz at the Γ-point) such that the atoms can move adiabatically during the entire duration of the interferometer sequence which is fixed at $2\tau = 1.6$ ms. We quantify the adiabaticity of the motion for this range of forces by checking that the occupation of higher bands is negligible at the end of the interferometry. For interferometer paths ending near the Dirac point where the adiabaticity condition is hardest to fulfill, the population in the second band is $\sim 20\%$ of the total atom number. The value of τ has been chosen so that the effect of instabilities of the weakly interacting BEC can be neglected in first approximation. The trap frequencies of the combined blue-detuned lattice and dipole potential are $\omega_{x,y}/2\pi$=26.5(7) Hz and $\omega_z/2\pi$=183(2) Hz. Typical parameters for the array of tubes are summarized in appendix C.

To move the atoms in reciprocal space we combine the forces from field gradients and lattice acceleration. A magnetic field gradient $B' = 9.0(1)$ G/cm produces a fixed acceleration $|\mu\nabla B|/m$= 2.9(1) m/s^2 and creates a spin-dependent force along the x-axis. An orthogonal lattice acceleration a_L is realized by sweeping the frequency of the lattice beam three, as described in Section 5.3. The magnitude of this acceleration varies from 1 to 11 m/s^2 in the experimental runs. The atoms' final quasimomentum is set by the lattice acceleration according to

$$k_x^{\text{fin}} = 0 \ \text{ and } \ k_y^{\text{fin}} = 2ma_L\tau/\hbar. \tag{6.13}$$

As illustrated by the schematics of Fig. 6.3, different k_y^{fin} result in loops of different geometry that probe different portions of the Brilloiun zone. The absorption images in the bottom row show examples of the quasimomentum distribution detected after the interferometry. The detection sequence combines band-mapping with a Stern-Gerlach pulse that spatially separates the $|\uparrow\rangle$ and $|\downarrow\rangle$ states during time of flight.

As explained earlier, the spin-dependent motion of the atoms is created by a field
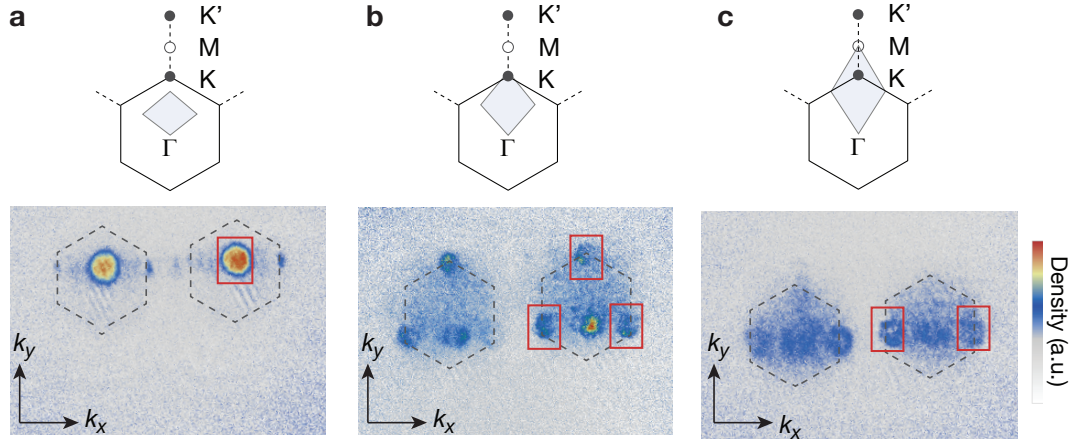
Figure 6.3.: Examples of band-mapped images taken after the interferometry and the detection sequence, as described in the main text. Schemes on top illustrate the paths taken in the Brillouin zone for each example. Atoms in the ↓ and ↑ internal states of ^{87}Rb are spatially separated (left and right in the images) by the Stern-Gerlach pulse to measure the populations $n_{\uparrow,\downarrow}$. The red regions of interest (ROI) highlight the ↓ atoms which have been addressed by all the microwave pulses and are counted in the final data analysis. The atoms outside the ROIs, e.g. see atoms in **(b)**, are the ones not addressed by all the microwave pulses due to the inhomogeneous magnetic field. Since they move along different paths in the Brillouin zone they are not analyzed. Depending on the end point of the loop we analyze one **(a)**, three **(b)** or two **(c)** clouds since the edge of the Brillouin zone (hexagons) Bragg reflects a fraction of the weakly interacting cloud. More details on the effect on the BZ edge and on weak interactions are in Sec. 6.2.3.

gradient. As a result, the microwave pulses of the protocol will not be resonant for the entire atomic cloud which has a finite size. This results in a fraction of atoms, about 10% in our case, which is not properly addressed by all the microwave pulses. These atoms travel along paths which are different from the ones of the interferometer loop and they will end at different locations in the Brillouin zone, as one can clearly note from the image in Fig. 6.3b. Moreover, the spatially varying detuning across the cloud reduces the maximum contrast of the interference fringes since atoms participating in the protocol will experience slightly different microwave rotations depending on their position in the inhomogeneous gradient.

To extract the phase after the interferometry, we count only the populations of atoms that have been addressed by all the microwave pulses of the interferometric protocol, i.e. atoms in the red boxes in Fig. 6.3. This selective analysis enhances our resolution since large part of the incoherent background is removed from the interference signal. The interference fringe for the fraction of atoms in the two spin states, $n_{\uparrow,\downarrow}$, is fitted with a sine function.

6.2.2. Canceling dynamical phases

As mentioned in Sec. 6.1.2, canceling the dynamical phase difference between the two spin states is necessary if we want to extract a quantitative estimate on the spread in Berry curvature from the phase of the interference fringes. Imperfections in alignment of the magnetic field gradient relative to the lattice, errors in the relative angles or intensities of the lattice beams, can introduce small path-dependent dynamical phases that contribute to our experimental uncertainty. Here these effects are briefly reviewed. More details on the different optimization procedures and on the system parameters can be found in the appendix D.

The dynamical phase difference between the two states for each half of the interferometer sequence is

$$\Delta\varphi_{\mathrm{dyn}} = \frac{1}{\hbar} \int_0^\tau \left[E^1\left(\mathbf{k} + \boldsymbol{\mathcal{F}}_\mu t\right) - E^1\left(\mathbf{k} + \boldsymbol{\mathcal{F}}_{-|\mu|}t\right) + \varepsilon_\mu\left(t\right) - \varepsilon_{-\mu}\left(t\right) \right] dt \qquad (6.14)$$

where the dynamical phase is defined by eq. 5.13. This contribution cancels when all of the following conditions are met:

- the magnetic field that enters in the definition of $\boldsymbol{\mathcal{F}}_\mu$ and of the Zeeman term ε_μ, have negligible time-dependent noise. To minimize the effect of magnetic field fluctuations, we use a low-noise power supply for the coil's current corresponding to a peak-to-peak field noise of $dB \simeq 240\ \mu$G, mostly at 50 Hz. To reduce the effect of background AC-noise, mostly at 50 Hz and reproducible from shot to shot, the beginning of the interferometer sequence is synchronized to the mains voltage. Furthermore, we keep the duration of the interferometer sequence fixed to probe the same portion of the 50-Hz cycle in each experimental run which thus adds a fixed dynamical phase contribution.

- the atoms travel along paths where the energy band is symmetric, which eliminates the first term in eq. 6.14. The symmetry of the energy bands about the symmetry axis of the interferometry has been checked with the Aharonov-Bohm sequence by comparing the measured phases along ideally symmetric paths, e.g. ending at k_y^{fin} or $-k_y^{\mathrm{fin}}$. The phase difference between the two types of loops should vanish when the dispersion is symmetric. Moreover, the angles between the lattice beams are measured to be $120(1)°$ and therefore introduce negligible systematic errors.

- the acceleration from lattice and gradient are orthogonal such that the magnitude of force $\boldsymbol{\mathcal{F}}_\mu$ is the same for the two spin-components and ε_μ is zero, i.e. the two spin states experience the same Zeeman energy shift along the path. The effect of the misalignment of the magnetic field gradient is reduced by the use of a spin-echo π-pulse which reverses the direction of motion of the atoms in the inhomogeneous magnetic field. In addition, the alignment of the
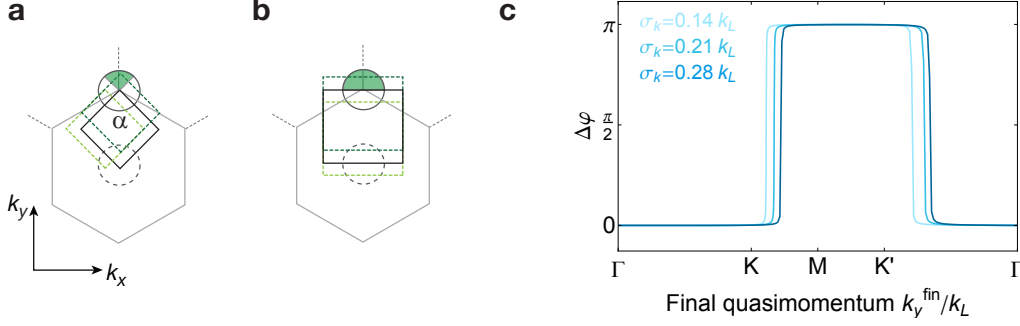
Figure 6.4.: Effect of the geometry of the loop combined with quasimomentum spread. **(a-b)** Examples of Interferometer loops ending at the **K** point with rhombic **(a)**, or rectangular **(b)** geometry, illustrating how the shape of the loops affects the fraction of the atoms that acquire a phase shift (green sectors of the circles). Light (dark) dashed green lines represent paths which have (have not) enclosed the Dirac point. For the interferometer loop given in **(a)**, only a minority of the atoms that cross the edge of the BZ is phase shifted. **(c)** Curves calculated for different quasimomentum spreads and fixed spread in Berry curvature, $\delta k_\Omega = 0.7 \times 10^{-4} k_L$, from the theory model, eq. 6.15-6.16.

gradient is fine-tuned by changing the current in the two Stern-Gerlach coils. For orthogonal gradient and lattice accelerations, the phase measured by the zero-area reference interferometer should be the same for loops ending at k_y^{fin} and $-k_y^{\text{fin}}$. Hence, a vanishing phase difference between the two types of loops sets the correct value of the current in the coils. From our calibrations, we estimate an error on the gradient alignment of at most $2°$.

6.2.3. Effects of atomic quasimomentum distribution

Due to the diluteness of the atomic cloud and the short timescales for the motion of the atoms in the band, the system can be considered as non-interacting in first approximation. The effects of dynamical instabilities are neglected in our modeling. We only account for the quasimomentum spread of the weakly interacting cloud to accurately relate the measured interferometer phases to the location and spread of the Berry flux in reciprocal space.

If the interferometric protocol is performed with a single particle in the periodic potential, the interferometric signal would be exactly described by eq. 6.12. In our experimental realization, instead, we need to account for the quasimomentum distribution of the particles in a lattice, which we parametrize by $n(\mathcal{K})$, with $\int n(\mathcal{K}) \, d^2\mathcal{K} = 1$. If there were no interactions, the distribution of the condensed atoms in reciprocal space would be a well localized Gaussian distribution where the widths of it are given by the frequencies of the harmonic trapping potential for
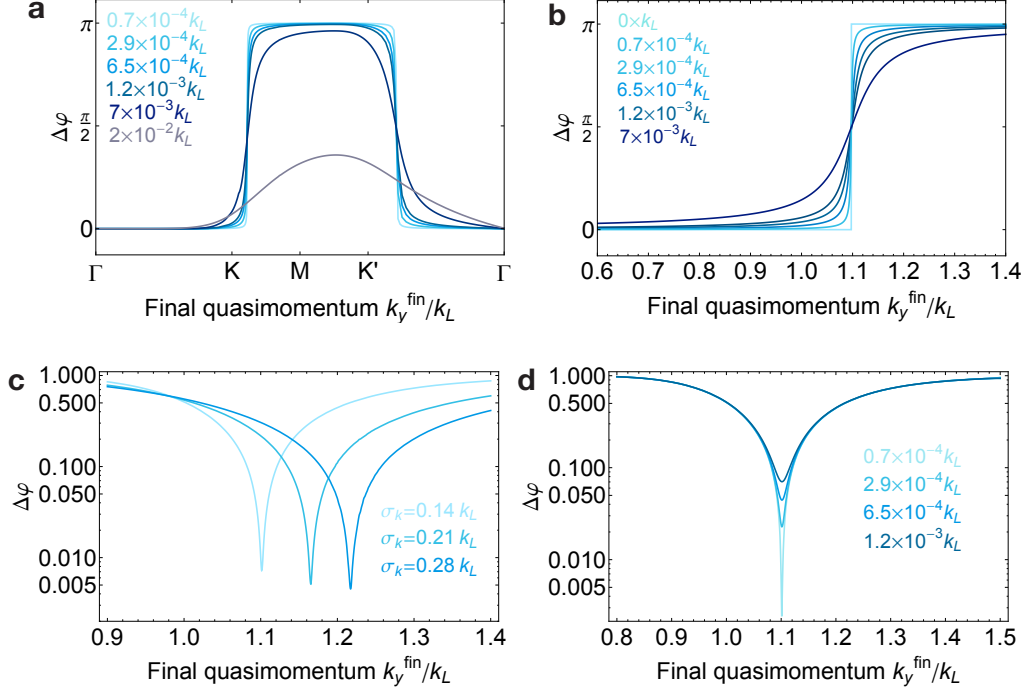
Figure 6.5.: Expected phase differences. Curves are calculated for different spreads in Berry curvature δk_Ω and $\sigma_{\mathbf{k}} = 0.14 k_L$. Note that for large spreads δk_Ω the phase difference does not reach the maximum value of π since a significant portion of the Berry curvature extends outside the area of the interferometer **(b)**. Zoom on the first phase jump **(a)**. **(c)** Effect of the quasimomentum spread on the decrease in contrast in proximity of a Dirac cone. Curves are calculated for different quasimomentum spreads and fixed spread in Berry curvature, $\delta k_\Omega = 0.7 \times 10^{-4} k_L$. **(d)** Expected contrast $\mathscr{C}$ in proximity of a Dirac cone calculated for different spreads in Berry curvature δk_Ω and a $\sigma_{\mathbf{k}} = 0.14 k_L$.

atoms in the lattice with effective mass $m^* = \hbar^2 (d^2 E^1/dk^2)^{-1}$. This distribution can be broadened by the presence of weak repulsive interactions. In order to account for the quasimomentum distribution of the atoms in the lattice and correctly model the experimental results, we need to average the interference fringe over the entire extension of the cloud, see the schematic of Fig. 6.4a for a visualization of the effect of momentum spread. We assume $n(\mathcal{K})$ to be Gaussian distribution of rms width $\sigma_{\mathbf{k}}$. The value of $\sigma_{\mathbf{k}}$ is measured before the start of the interferometer sequence and it is $\sigma_{\mathbf{k}} = 0.14(1) k_L$. To estimate the interference signal, we can consider an atom that has an initial quasimomentum $\mathcal{K} \neq 0$. In a loop that encloses a region S for atoms initially at $\mathbf{k}(0) = \Gamma$, this atom acquires the following Berry phase

$$\Phi(\mathcal{K}) = \int_S \Omega^1(\mathbf{k} + \mathcal{K}) \, d^2\mathbf{k} \tag{6.15}$$

where Ω^1 is the Berry curvature of the lowest band, described by eq. 2.35 and 3.19. The spread in Berry curvature δk_Ω is quantified by the half width at half maximum of the distribution of Berry curvature, eq. 3.19. By averaging the population fractions of the $\uparrow \downarrow$ states over the entire quasimomentum distribution of the cloud we get the total interference signal

$$n_\uparrow - n_\downarrow = \int \cos\left[\varphi_{MW} + \Phi(\mathcal{K})\right] n(\mathcal{K}) \, d^2\mathcal{K}$$
$$= \mathscr{C} \cos(\varphi_{MW} + \varphi). \tag{6.16}$$

The actual interference contrast in the experiment is imperfect due to inhomogeneous broadening of the microwave transition, population transfer to the second band in proximity of the Dirac point, and the heating associated with dynamical instability of the Gross-Pitaevskii equation. In modeling the data, we therefore globally rescale the predicted contrast $\mathscr{C}$ according to the maximum observed contrast for loops ending close to the Dirac point, i.e. $\mathscr{C}_{\exp} = \mathscr{C}_{\max} \times \mathscr{C}$.

The main effect for a highly localized localized Berry curvature and a relatively modest momentum spread is to shift the position of the phase jump along k_y, as shown in the graph of Fig. 6.4c, but not to change its sharpness, which relates, instead, to the spread of Berry curvature as the theory curves in Fig. 6.5a-b show. This is due to the fact that the Berry curvature is extremely well localized – essentially point-like when compared to the broader atomic quasimomentum distribution. If these two distributions have similar extents, instead, the smoothness of the phase jump will depend both on Berry curvature and atomic quasimomentum distributions.

The shift of the phase jump location (Fig. 6.4c) can be understood using simple geometric arguments, as it depends only on the distribution of the cloud in reciprocal space and the geometry of the interference loop. The phase jump and the minimum in the interference contrast occur when at least half of the particles have enclosed the Dirac point at the end of the loop. Because of the momentum spread, each atom has sampled a slightly different path in momentum space and may therefore have acquired a different geometric phase. If the interferometer loop has a rectangular shape and its extension is larger than the quasimomentum spread of the cloud, for example, the phase jump will occur exactly at the Dirac point (see Fig. 6.4b). For our rhombic paths, however, when the interferometry ends at the $\mathbf{K}(\mathbf{K}')$ point, only the atoms in the shaded sector of Fig. 6.4a have performed a loop which enclosed the Dirac point. The shape of this sector of the atomic cloud is given by the opening angle of the loop α, which is about $\alpha \sim 75°$ at the first Dirac point, and the fraction of atoms in the sector is determined by the distribution $n(\mathcal{K})$. The condition on the
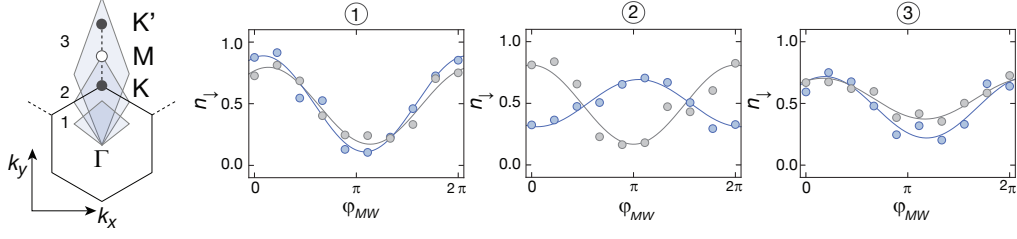
Figure 6.6.: Schematic: Changing the lattice acceleration realizes loops with different geometries (shaded areas, hexagon depicts the first Brillouin zone). The measured interference fringes for loops 1-3 are shown. The fractions of atoms in the state $|\downarrow\rangle$, $n_\downarrow$, are plotted as a function of the phase φ_{MW}. Measurement loop data are shown in blue and zero-area reference data are shown in gray with corresponding sinusoidal fits. The contrast is limited by inhomogeneous broadening of the microwave transition, the finite momentum spread of the condensate and, for large final quasimomenta, by dynamical instabilities.

phase jump at the **K**-point than reads

$$\int_{sector} n(\boldsymbol{\mathcal{K}})d^2\boldsymbol{\mathcal{K}} = \int_{-\infty}^{+\infty}\int_{k_y>k_x\cot(\alpha/2)} \frac{1}{2\pi\sigma^2}e^{-(k_x^2+(k_y-k_y^{\mathrm{fin}})^2)/(2\sigma^2)}dk_xdk_y = 0.5\,.$$
(6.17)

The position of the phase jump happens at a k_y^{fin} that is slightly shifted from the ideal case of $\sigma_{\mathbf{k}} = 0$. Regarding the smoothness of the phase jump, this is indicative of the spread in Berry curvature: a larger the spread results in a smoother change in the geometrical phase acquired along loops of increasing size, see Fig. 6.5. When the Berry curvature extends outside the area of the interferometer the maximum of the geometrical phase is lower than π, as it can be seen from the graph of Fig. 6.5.

6.3. Measurement of the Berry phase associated with the Dirac cones

In this section we present the experimental results obtained with the Aharonov-Bohm interferometry where we directly measured the Berry phase associated with the Dirac cones of a honeycomb optical lattice which has time-reversal symmetry.

6.3.1. Detecting the Berry fluxes

To detect the Berry fluxes and to locate them in the Brillouin zone, we perform a sequence of interferometric measurements in which we vary the region enclosed by the interferometer loop, as illustrated in the schematic of Fig. 6.6. This is achieved by varying the lattice acceleration to control the quasimomentum of the atoms at
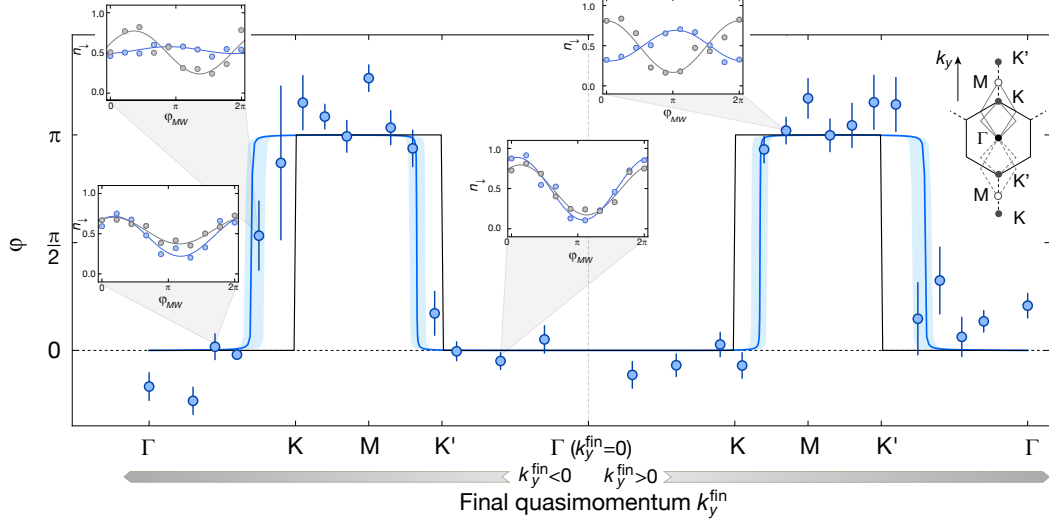
Figure 6.7.: Summary of phase shifts measured relative to the zero-area reference interferometer for loops of different final quasimomenta k_y^{fin}, as depicted in the inset on the right. Error bars denote fit uncertainties or standard deviations in case of averages. Lines are ab initio theory using a full band structure calculation with: no momentum spread $\sigma_{\mathbf{k}} = 0$ and perfectly localized Berry curvature $\delta k_\Omega = 0$ (black); $\sigma_{\mathbf{k}} = 0.21 k_L$ and $\delta k_\Omega \simeq 10^{-4} k_L$ (blue). δk_Ω is the HWHM of the Berry curvature distribution, see eq. 3.19. As explained in the main text, the shift in the phase jump results from the momentum spread $\sigma_{\mathbf{k}}$, while the broadening of the edges is caused by δk_Ω. The shaded area accounts for a variation in $\sigma_{\mathbf{k}} = 0.14$–$0.28 k_L$. Insets show the fraction of atoms $n_\downarrow$ detected in state $|\downarrow\rangle$ as a function of the phase φ_{MW} for selected quasimomenta. Measurement loop data (blue) and zero-area reference data (gray) are plotted.

the end of the loop, i.e. the parameter k_y^{fin} defined by eq. 6.13. Some examples of the interference fringes obtained after the Aharonov-Bohm interferometry are presented in Fig. 6.6 and 6.7 together with the sinusoidal fits from which the phase is extracted. For each loop geometry, the measured phase is compared with the phase obtained with the zero-area reference interferometry to extract the geometrical phase contribution. It can be seen from the graph 2 of Fig. 6.6 that we observe a clear phase difference of $\varphi \simeq \pi$ when one Dirac point is enclosed in the measurement loop. In contrast, we find a vanishing phase difference when zero or two Dirac points are enclosed in the loop, corresponding to the plots 1 and 3 in Fig. 6.6.

The interferometry is repeated for many different loops to map the change of the geometrical phase in proximity of the Dirac points. The resulting phase differences between measurement and reference loops are shown in Fig. 6.7. Here it can be seen that there's a clear jump of the phase from 0 to π for loops enclosing either the $\mathbf{K}$ or $\mathbf{K}'$ point. This phase goes back to zero when two fluxes are enclosed in the loop.

Small deviations of the phases from 0 or π can be attributed to shot to shot noise and residual systematic errors in the cancellation of dynamical phases. In fact, these contributions are generally different for the measurement and reference sequences as atoms move along different paths in the two cases. Additionally, magnetic field noise can change from shot to shot resulting in a different contribution to the dynamical phase for the two sets of data. Systematic errors are particularly relevant close to the phase jump, where the contrast is minimal, and small errors can influence the perceived direction of the phase jump. Nonetheless, given the sharpness of the phase change which goes to π, the data are fully consistent with the behavior expected for an inversion-symmetric lattice, where it is impossible to identify the sign of the singular Berry flux ($\pm\pi$) at the $\mathbf{K}$ and $\mathbf{K}'$ points.

The results are in good agreement with the theoretical predictions of our model, see eq. 6.16. In comparing data with theory, we account for heating during the sequence, more severe for longer traveled distance in the reciprocal space, by allowing a range of momentum spread of the BEC, $\sigma_{\mathbf{k}} = 0.14$–$0.28 k_L$. Here the minimum value corresponds to the independently measured momentum spread of the cloud before the beginning of the interferometer sequence (at $\mathbf{k} = 0$).

6.3.2. Auxiliary analysis near the Dirac point: characterizing the Berry curvature

As we have seen, systematic errors and small dynamical phases can still be present in the value of the phase obtained when comparing measurement and zero-area reference loop. To improve our measurement precision, we performed self-referenced interferometry in the vicinity of a Dirac point which eliminates the need for a separate reference measurement and thus minimizes systematic errors.

This self-referencing exploits the periodicity of the Brillouin zone and works as follows. As Fig. 6.8 illustrates, when the interferometry ends close to the edge of the Brillouin zone, some atoms will have crossed the edge of the zone and some will have not due to their finite momentum spread. Due to the periodicity of the reciprocal space, atoms ending the loop with a quasimomentum outside the first Brillouin zone are Bragg reflected and the quasimomentum $\mathbf{k}$ is shifted by one or more reciprocal lattice vectors to be restricted to the first Brillouin zone (left and right sectors in Fig. 6.8). Therefore, the effect of the edges of the three zones that touch at $\mathbf{K}$ is to "slice" the atomic cloud into sectors: atoms that have (left, right) or have not (bottom) crossed the edge of the zone, L, R, B, as labeled in Fig. 6.9. These slices are projected onto three different corners of the first BZ by the band-mapping technique and are well spatially separated in the pictures after time-of-flight expansion, as illustrated by the images in Fig. 6.3 and Fig. 6.8. The acquired phases of each sector of the cloud, φ_L, φ_R and φ_B, can thus be measured independently. As atoms in the bottom cloud will always be last to go past the
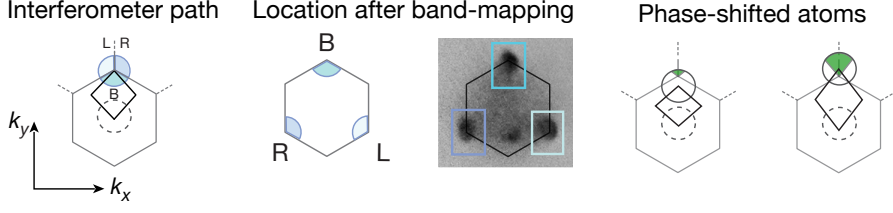
Figure 6.8.: Self-referenced interferometry at the Dirac point. Left: Interferometer path closing at the **K** point. Because of the initial momentum spread, the cloud (circle with colored sectors, not to scale) is split by the edges of the BZ. Middle: Band-mapping spatially separates the three different parts of the cloud onto three corners of the first BZ (schematic and image, where cloud sizes are dominated by in-situ size). Right: The fraction of atoms for which the Dirac point lies within the interferometer loop (green sectors) increases with final quasimomentum $\mathbf{k}^{\text{fin}}$.

Dirac points, they provide a new phase reference within the same shot, significantly reducing sensitivity to drifts in the experiment. We determine the phase shift of the L, R clouds, first to pass the first Dirac point, relative to atoms in the bottom cloud B according to

$$\varphi = \frac{\varphi_L + \varphi_R}{2} - \varphi_B. \tag{6.18}$$

The experimental results for the measured phase φ detected in proximity of the Brillouin zone's edge and around the **K** and **K'** points are illustrated in Fig. 6.9. The data show a sudden jump from 0 to π that occurs within a very small quasi-momentum range of $< 0.01\,k_L$. An arctangent fit to the experimental data gives a phase step of

$$\varphi = 0.95(10)\pi. \tag{6.19}$$

Both results are indicative of an extremely well localized π Berry flux. In order to give an estimate on the spread in Berry curvature, the results are compared with the theoretical model where we apply eq. 6.16 to calculate the phase of each interference fringe, substituting for the distribution $n(\mathcal{K})$ the distribution of one of the three slices of the full quasi-momentum distribution. The position of the phase jump is in excellent agreement with the model that includes the estimated momentum spread of $\sigma_{\mathbf{k}} = 0.15(1)k_L$. The steepness of the phase jump suggests a spread in Berry curvature on the order of

$$\delta k_\Omega \simeq 10^{-4} k_L, \tag{6.20}$$

corresponding to an energy offset between the A and B sites of $\Delta \simeq \mathrm{h} \times 3\,\mathrm{Hz}$ and of a ratio of energy gap at the Dirac cone to bandwidth of $\leq 3 \times 10^{-4}$.
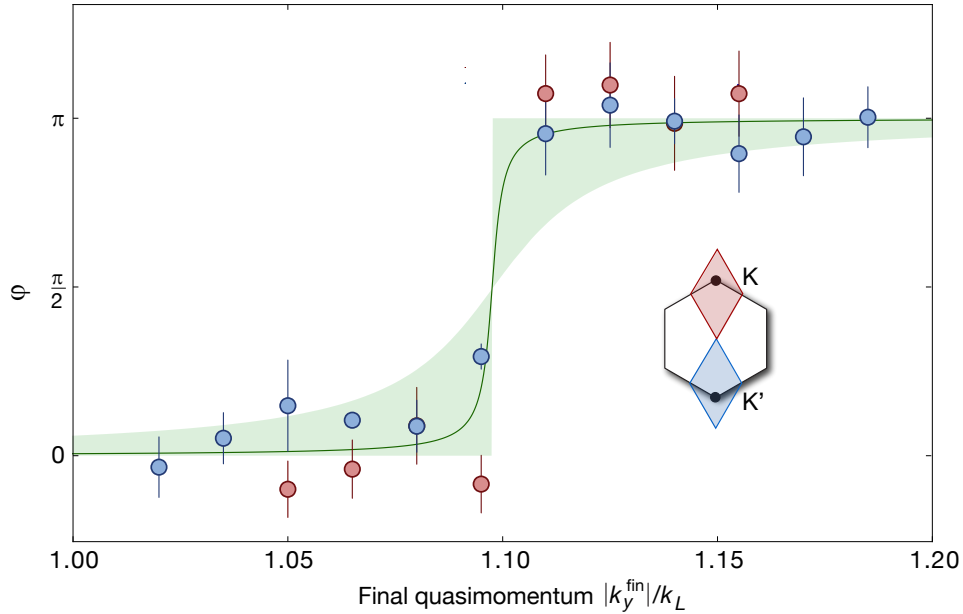
Figure 6.9.: Results from self-referenced interferometry at the Dirac point. Phase differences between atoms that have crossed the band edge (sectors L, R) and those that have not (sector B) versus final quasimomentum k_y^{fin} for paths close to the $\mathbf{K}$ ($\mathbf{K}'$) point in red (blue). The shaded region indicates a range $\delta k_\Omega = 0-12\times10^{-4}k_L$ for the spread in Berry curvature, whereas the line is calculated for $\delta k_\Omega \simeq 10^{-4}k_L$ using the model described in the main text, corresponding to an A-B offset of $\Delta \simeq \text{h} \times 3$ Hz. All theory curves are computed at a fixed momentum spread, $\sigma_{\mathbf{k}} = 0.15k_L$.

Analysis of the interference contrast

The location of the Dirac cone manifests itself not only through a sharp phase jump but also through a pronounced minimum in the interference contrast. All the measured contrasts of the full cloud are plotted in Fig. 6.10 together with the theory line calculated for the same parameters as the phase jump data in Fig. 6.9. First of all, the reduction in contrast at the first Dirac point agrees well with theory while the one at the second Dirac point has a worse agreement with our simple model. This is most likely due to instabilities that are more pronounced for paths ending close to the second Dirac point, as it can be seen from the images of the momentum distribution of the BEC in Fig. 6.11b and from the measured increase in cloud size plotted in Fig. 6.11a which is indicative of an increased momentum spread.

To constrain the possible spread in Berry curvature we analyze the contrast of the interference fringes close to the first phase jump since it is the one that is less affected by instabilities. The data of the contrast close to the first phase jump are presented in Fig. 6.10b. By comparing it with our theoretical model we extract an
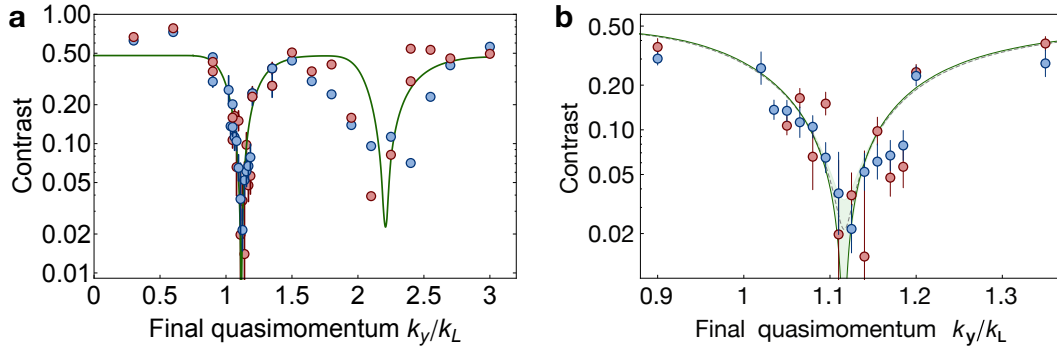
Figure 6.10.: **(a)** Full interference contrasts $\mathscr{C} = (n_\downarrow^{\max} - n_\downarrow^{\min})/(n_\downarrow^{\max} + n_\downarrow^{\min})$ of the interference fringes of the full cloud for all measured final quasimomenta k_y^{fin}. **K** **K′** points are at $1k_L$ and $2k_L$. Red (blue) data points represents contrast measured at positive (negative) k_y^{fin}, as in Fig. 6.9. Theory line is calculated for $\delta k_\Omega \simeq 10^{-4}k_L$ and a fixed momentum spread $\sigma_{\mathbf{k}} = 0.15k_L$. The agreement with the reduction of contrast at the second Dirac cone is worse since the spread $\sigma_{\mathbf{k}}$ of the theory curve is fixed and the model does not account for effects of dynamical instabilities. **(b)** Zoom on the contrast at the first Dirac point. Shaded region indicates a range $\delta k_\Omega = 0 - 12 \times 10^{-4}k_L$, green theory line is calculated for $\delta k_\Omega \simeq 10^{-4}k_L$, same parameters of Fig. 6.9. Dashed line is calculated for $\delta k_\Omega \leq 6 \times 10^{-4}k_L$, our conservative estimate. All calculations assume $\sigma_{\mathbf{k}} = 0.15\ k_L$.

upper bound for the spread of the Berry curvature around the Dirac cone of

$$\delta k_\Omega \leq 6 \times 10^{-4}k_L \tag{6.21}$$

which is our conservative estimate. This corresponds to a maximal A-B site offset of $\Delta \leq \mathrm{h} \times 12\,\mathrm{Hz}$ and a ratio of energy gap at the Dirac cone to bandwidth of $\leq 1 \times 10^{-3}$. The sharpness of the phase jump and the strong reduction of contrast down to our detection limit demonstrate that the interferometric protocol can map the Berry curvature with very high resolution.

Finally we would like to comment on the second band population for loops ending close to the Dirac point. Although the vanishing band gap precludes performing a perfectly adiabatic measurement in the immediate proximity of the Dirac point, the population in the second band is constrained by independent measurements to be $\leq 20\%$ of the total atom number. Numerical simulations of the full dynamics, which can be found in appendix D, showed that for a well localized Berry flux the effect of second band population is to shift of the position of the phase jump and of the reduced contrast. We find a moderate broadening of the contrast due to the second band population for small AB offsets Δ. These numerical results indicate that the comparison with our model gives us an upper bound on the localization of Berry curvature.
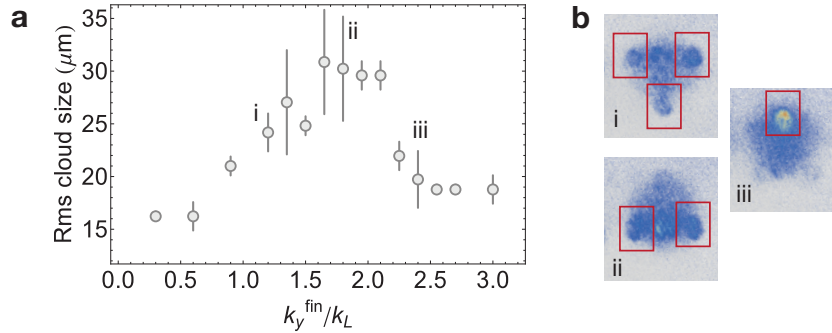
Figure 6.11.: Observed increase in quasimomentum spread. **(a)** Plot of rms cloud sizes from Gaussian fits to the atomic cloud after band mapping and short TOF. Data are averages and errors are standard deviations. An increase in cloud size is indicative of an increase in momentum spread. **(b)** Examples of images taken after band mapping and short TOF for some selected points.

6.3.3. Detecting the motion and annihilation of Dirac points

To verify the method's sensitivity to changes in Berry flux, we performed interferometry in a modified lattice potential. As explained in Section 3.2.3, we can change the position of the Berry fluxes in the Brillouin zone by imbalancing the powers of the lattice beams. In the experimental realization we change the power of two lattice beams (I_1, I_2) relative to the third (I_3). With this choice, the Dirac points move along the symmetry axis of the interferometer loop as illustrated in Fig. 6.12 and the condition on the symmetry of the paths in the energy band, eq. 6.5, is still satisfied. It follows that the lattice imbalance does not add any additional dynamical phase to the measured interference signal.

By using a fixed measurement loop that encloses only one Dirac point in the intensity-balanced case, we can measure the change of the geometric phase upon imbalancing the lattice beam's intensities. The motion of the Dirac points in and out of the area of the loop results in a geometrical phase which jumps from π to 0. The experimental results are presented in Fig. 6.12 where the observed phase is obtained by comparing the measurement and zero-area reference loops. The measured phases are in good agreement with theoretical predictions which take the value of δk_Ω from our best estimate, coming from the self-referenced data presented in the previous section.

Since the location of the fluxes can be controlled at will, we can now probe the modification of the topological features upon annihilation of the Berry fluxes. To observe the relative motion of the fluxes, the location of two Dirac points in the imbalanced lattice is mapped by using the self-referenced interferometry with paths ending near the **K** and the **K**′ point and enclosing up to two Dirac points. For the data in the vicinity of the second Dirac point we use the B cloud as a reference,
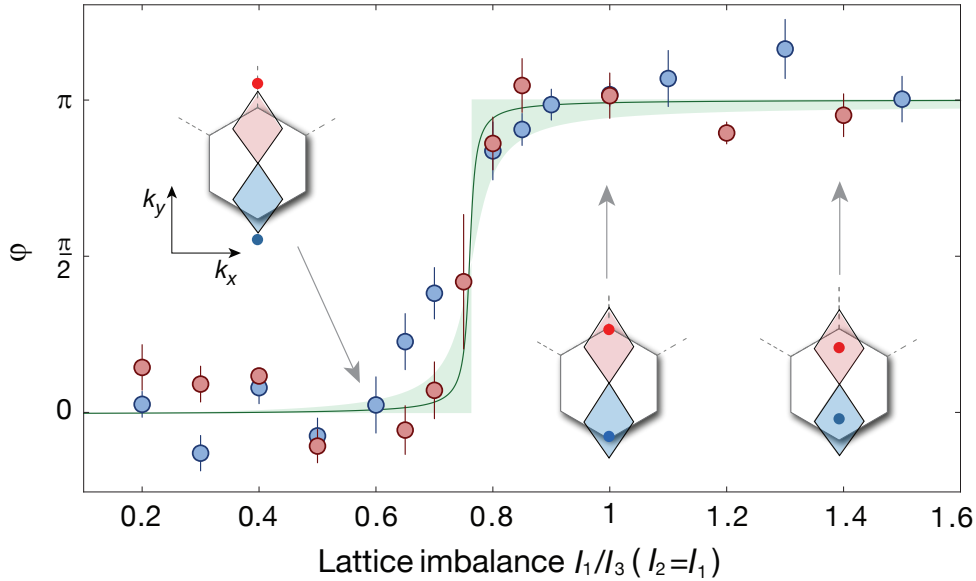
Figure 6.12.: Observing the movement of the Berry fluxes: Measured phase difference between the zero-area reference loop and measurement loop is plotted versus lattice imbalance around **K** (red) and **K'** (blue). Final quasimomentum is fixed at $k_y^{\text{fin}} = \pm 1.2 \, k_L$. Red and blue dots in the insets give the location of Dirac points for the indicated imbalances. Theory curve is calculated for lattice depth $V_0 = 1 \, E_r$, momentum spread $\sigma_{\mathbf{k}}=0.15 \, k_L$, and $\delta k_\Omega \simeq 10^{-4} k_L$. Shaded area corresponds to $\delta k_\Omega = 0 - 12 \times 10^{-4} k_L$.

with the label B now referring to the fraction of atoms in the front part of the cloud, $k_y > k_y^{\text{fin}}$, that are the first to sample the Berry flux of both Dirac points. We again apply eq. 6.18 to extract the geometrical phase. The results are shown in figure 6.13 where the measured phase jumps for different imbalance factors, $f = I_{1,2}/I_3$ are plotted. With decreasing imbalance $I_{1,2}/I_3 < 1$, the Dirac points and the associated fluxes move toward each other while preserving their distribution of Berry curvature. As a result, the range of final quasimomenta for which the interferometer encloses a single π flux narrows and both the upward and downward phase jumps shift towards the **M** point, as we observed. For a strong imbalance ($I_{1,2}/I_3=0.2$), the two Dirac points have annihilated at the **M** point, and no phase jump is detected for any loop size. This indicates the change of topology of the band.

At an intermediate imbalance ($I_{1,2}/I_3=0.7$), the position of the phase jump at $k_y^{\text{fin}} = 1.2k_L$ is in very good agreement with theory. The position of the second phase jump, instead, deviates by a $\simeq 10\%$ from the calculated value. This can likely be attributed to a combination of geometric imperfections of the imbalanced lattice potential that introduce additional dynamical phases, the second band population that shifts the location of the phase jump and of the minimum in contrast,
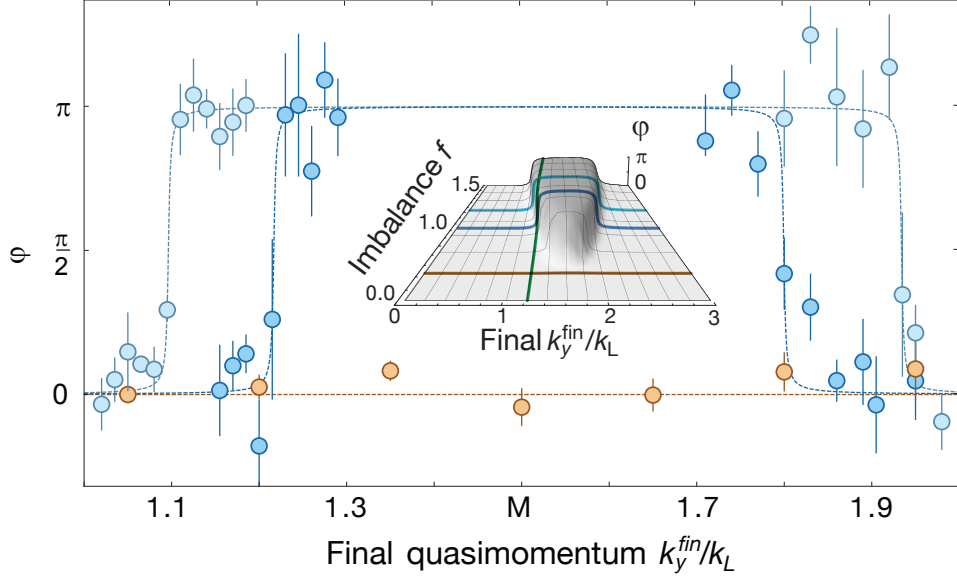
Figure 6.13.: Moving and merging the Berry fluxes: Self-referenced phase near **K** and **K**′ for an imbalance $I_{1,2}/I_3 = 1.0$ and $I_{1,2}/I_3 = 0.7$ in light and dark blue, highlighting the shift in the location of Berry flux. For a stronger imbalance of $I_{1,2}/I_3 = 0.2$ the Berry fluxes annihilate at the **M** point and no phase shift is observed (orange data). The orange data are phase differences between the measurement and reference loops for an imbalance of $I_{1,2}/I_3 = 0.2$. Curves are guides to the eye obtained by fitting the observed phase jump with an arctangent of slope fixed by our best estimate of the HWHM of the Berry curvature, $\delta k_\Omega \simeq 10^{-4} k_L$, from the data of Fig. 6.9. The inset shows the calculated Berry phase for loops with various final k_y^{fin} and lattice imbalances using the same $\sigma_{\mathbf{k}}$ and δk_Ω as above. Colored lines indicate parameters explored in the measurements.

and the increase in momentum spread due to instabilities which has been observed experimentally, as the results plotted in Fig. 6.11a illustrate. The inhomogeneous broadening of the quasimomentum distribution may play a major role for these loops since the position of the phase jump is quite sensitive to changes of the atomic distribution $n(\mathcal{K})$, especially when the opening angle of the interferometer is small. In our experimental realization the opening angle is $\alpha \sim 42°$ when two Dirac points are enclosed by the interferometer loop. The observed shift is compatible with the one expected from the model of eq. 6.17 when we approximate the effect of the instabilities with an asymmetric Gaussian distribution with standard deviations $\sigma_{kx} = 0.1 k_L$ and $\sigma_{ky} = 2.5\,\sigma_{kx}$.
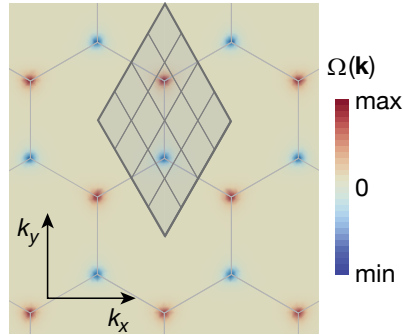
Figure 6.14.: Mapping the distribution of Berry curvature and measuring the Chern number of a band via Aharonov-Bohm interferometry: the interferometric protocol is performed along different small loops (gray rhombic paths) which cover the entire area of the Brillouin zone.

6.4. Final remarks and prospects

The results presented in this chapter demonstrate a versatile interferometric technique which allows us to measure local geometric phases along arbitrary closed paths in reciprocal space and to directly map the Berry curvature of an energy band with high quasimomentum resolution thanks to the use of a Bose-Einstein condensate.

We applied the Aharonov-Bohm interferometry to an optical honeycomb lattice which constitutes the extreme test case for this technique due to the Berry flux singularities imposed by the symmetries of the lattice potential. The measured π Berry phase demonstrates the winding of the band eigenstate around a Dirac cone of the lowest Bloch band. The sharpness of the observed phase jumps and the strong reduction of contrast down to our detection limit demonstrate the capability of the atom interferometry to detect extremely well localized topological features. Moreover, the Aharonov-Bohm interferometer allowed us to detect how the topological features are changed when the lattice is imbalanced. We directly observed the annihilation of the Berry fluxes which indicates the transition to a topologically trivial band structure.

The limitation to the present setup are dynamical instabilities which put a limit on the timescales of the interferometry and make it hard to be fully adiabatic in proximity of the Dirac points. Reducing these effects might be important when one wants to probe a less localized Berry curvature, where the effect of quasimomentum spread and second band population can modify the phase jump and the interference contrast in a non-trivial way. In future experiments these effects of interactions could be reduced by combining slower ramps with the use of a Feshbach resonance in an atomic species such as ^{39}K [229].

Despite this limitation, the interferometric technique proved to be suitable to resolve the distribution of Berry curvature of a single band by combining local mea-

surements of the geometric phases along small Aharonov-Bohm loops, as illustrated in Fig. 6.14. Since these local measurements would not be symmetric about a symmetry axis of the energy band, it would also be necessary to reconstruct the dynamical phases picked up by the two spin states during their motion in the Brillouin zone to subtract them from the signal. This can be done if the dispersion of the band can be precisely reconstructed by spectroscopic techniques. In this case, the interferometry would enable the full reconstruction of topological invariants such as Chern numbers [57].

In the present setup the interferometry could be used to observe the change of spread in Berry curvature and detect the sign of the Berry curvature at the inequivalent Dirac cones when an AB offset is introduced by tilting the beams' polarizations. Even more interesting would be to apply it to the honeycomb lattice when time-reversal symmetry is broken by periodic modulation [74, 82] of the lattice potential, to measure its non-zero Chern number and the change of sign of the Berry phase at the $\mathbf{K}(\mathbf{K}')$ points. The interferometry could potentially be applied to even more exotic modifications of the bands, like the one predicted for the Floquet spectrum of radiated graphene [230].

Multiband extensions of this work can enable measurements of Wilson loops and off-diagonal (non-Abelian) Berry connections and thus allow to fully reconstruct the complete geometric tensor of Bloch bands, as suggested in [107]. Extending outside the realm of cold atoms simulations, the highly non-linear phase jump we observed at the Dirac point may find application in precision force sensing when interactions are under control, as our sensitivity is comparable to the results presented in the following reference [231].

Chapter 7.

Stückelberg interferometry in the honeycomb lattice

In the previous chapter, the characterization of the geometrical features of a single Bloch band has been presented. In this chapter, we start to develop interferometric techniques for characterizing multi-band systems by looking at the non-adiabatic dynamics of atoms in the optical lattice. In Section 7.1, the non-adiabatic motion of atoms in the two lowest bands of the lattice is introduced. In Section 7.2, the Stückelberg interferometry is presented. As suggested in several proposals, this technique can allow the topological properties of the two bands to be extracted [232–234] as well as the dispersion of the honeycomb lattice to be precisely mapped [105, 106, 235]. In Section 7.2.2 the preliminary results of Stückelberg interferometry are presented. Conclusions and prospects are in Section 7.3. An extended discussion on topological properties of multi-band systems and their relation to non-adiabatic motion will be found in the thesis of Tracy Li [236].

7.1. Non-adiabatic motion in the two lowest bands

As discussed in Section 5.3.3, atoms can populate higher bands when they are subjected to a strong force and their motion in the first energy band is non-adiabatic. If other bands are separated from the lowest two by a large energy gap, the non-adiabatic transitions into the higher bands can be neglected. The equations of motion for the generic state $\psi(\mathbf{k}(t)) = \alpha_1(t)\psi_{\mathbf{k}}^1 + \alpha_2(t)\psi_{\mathbf{k}}^2$, linear combination of first and second band Bloch states, are described by the differential equations 5.16, in short notation

$$i\hbar\partial_t \begin{pmatrix} \alpha_1(t) \\ \alpha_2(t) \end{pmatrix} = \hat{H}_{\mathrm{dy}}(\mathbf{k}) \begin{pmatrix} \alpha_1(t) \\ \alpha_2(t) \end{pmatrix}. \tag{7.1}$$

For the results presented in the following section, the force is realized only via the lattice acceleration and it simplifies to $\boldsymbol{\mathcal{F}}_\mu = -m\mathbf{a}_L = -\mathbf{F}$ in $\hat{H}_{\mathrm{dy}}$. The unitary that evolves a state from $\mathbf{k}(0)$ to $\mathbf{k}(t)$ along a specific path C is the operator $\hat{U}_{\mathbf{k}(0)\to\mathbf{k}(t)} = \exp(-\int_0^t \hat{H}_{\mathrm{dy}}dt/\hbar)$ in this two-band model.
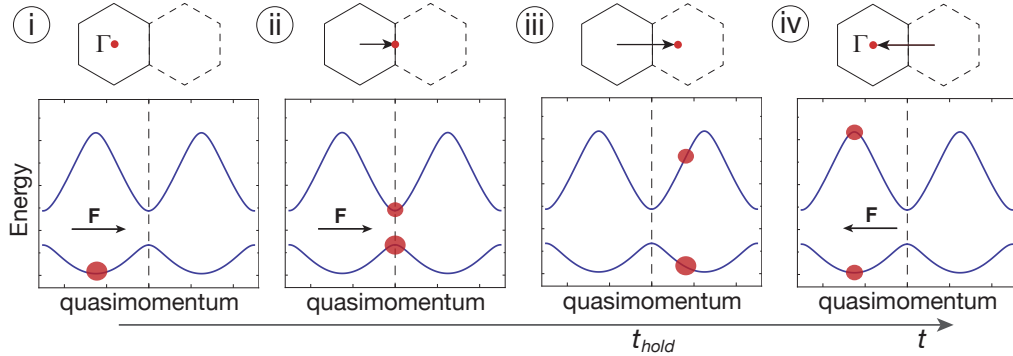
Figure 7.1.: Schematic sequence for the Stückelberg interferometry. It illustrates the motion of the atoms (red circles) in the Brillouin zone (schemes on top, arrows indicate the path) as well as their evolution in the two lowest energy bands for the main steps of the sequence described in the text.

7.2. Stüeckelberg interferometry

This interferometric protocol has been used in past works to measure energy difference between bands of an optical lattice [105, 235]. The precise calibration of the lattice depth is essential for reconstructing dynamical phases accumulated during the motion of atoms in the Brillouin zone and for measuring the Chern number of a band via the Aharonov-Bohm interferometry.

7.2.1. The experimental sequence

The general idea behind this interferometric protocol is to create a superposition state between the eigenstates of two bands which is used to probe the phases accumulated by the atoms during their time-evolution. In a simplified picture, Stückelberg interferometry consists of two partial Landau-Zener transitions and it can be viewed as the analogous of a Mach-Zehnder interferometer for particles populating the two lowest energy bands of a lattice. The role of the beam-splitter is played by the edge of the band, where the gap between first and second band is smaller and probability of exciting particles to the other band is higher. The result of the non-adiabatic motion is to create the desired coherent superposition of particles in the first and second band. To close the interferometer, the particles are moved across the edge of the band once more where they undergo an other 'beam splitter' operation.

Our experimental sequence is illustrated in Fig. 7.1. As for the Aharonov-Bohm interferometry, we start by loading a weakly interacting BEC in the lowest band of the lattice at $\mathbf{k} = 0$. Then, a strong force is applied onto the atoms by accelerating the lattice potential as described in Section 5.3.3, (i). The magnitude of the force is chosen so that only the first and second bands can be populated during the motion. The atoms are moved along a desired path in the Brillouin zone and their state

coherently evolves into a superposition of first and second band eigenstates (ii). The movement in reciprocal space is then stopped at a certain point $\mathbf{k}_1$ (iii) where the atoms are held for a variable amount of time, t_{hold}. During this hold time the eigenstates of the first and second band time evolve according to their eigenenergies and accumulate a different dynamical phase. After that, the force is applied again to transport the superposition state to a final quasimomentum $\mathbf{k}_2$ (iv). The atoms cross the edge of the Brillouin zone an other time to close the interferometer and to read out the phase difference between atoms in the first and second band. To detect the bands' populations, the atoms are released from the trap after band mapping and then imaged after 10 ms of TOF.

The evolution of the wavefunction is obviously more complicated than the simplified sequence we just described as it is governed by the differential equations 7.1 and mixing between the two band eigenstates happens all along the path. We can now describe the evolution of the states during the Stückelberg sequence in a more formal way. The time-evolution along a path is given by an operator $\hat{U}_{\mathbf{k}(0) \rightarrow \mathbf{k}(t)}$. The time-evolution of the states during the full Stückelberg interferometry sequence is described by the following product

$$\hat{U}_S = \hat{U}_2 \hat{D}(\mathbf{k}_1, t_{\text{hold}}) \hat{U}_1, \tag{7.2}$$

where $\hat{U}_1$ and $\hat{U}_2$ describe the effect of the two movements: $\mathbf{k}_0 \rightarrow \mathbf{k}_1$ from Γ to the hold point $\mathbf{k}_1$, and $\mathbf{k}_1 \rightarrow \mathbf{k}_2$ from $\mathbf{k}_1$ to the detection point $\mathbf{k}_2$. The unitary transformation $\hat{D}(\mathbf{k}_1, t)$ describes the evolution during the hold at $\mathbf{k}_1$ when the atoms accumulate a dynamical phase. The operator $\hat{D}$ is given by the following matrix

$$\hat{D}(\mathbf{k}_1, t) = \begin{pmatrix} \exp\left(-iE_{\mathbf{k}_1}^1 t_{\text{hold}}/\hbar\right) & 0 \\ 0 & \exp\left(-iE_{\mathbf{k}_1}^2 t_{\text{hold}}/\hbar\right) \end{pmatrix}. \tag{7.3}$$

The protocol starts with atoms in the lower band at $\mathbf{k}_0 = 0$, thus the initial state is $\psi_{\mathbf{k}_0}(0) = \psi_{\mathbf{k}_0}^1 = (1, 0)^T$ and the state at the end of the full sequence is given by

$$\begin{pmatrix} \alpha_1 \\ \alpha_2 \end{pmatrix} = \hat{U}_2 \hat{D}(\mathbf{k}_1, t_{\text{hold}}) \hat{U}_1 \begin{pmatrix} 1 \\ 0 \end{pmatrix}. \tag{7.4}$$

The probability to remain in the first band is most generally described by

$$P_1(t_{\text{hold}}) = |\langle \psi_{\mathbf{k}_2}^1 | \hat{U}_S | \psi_{\mathbf{k}_0}^1 \rangle|^2 = a_C + b_C \cos((E_{\mathbf{k}_1}^1 - E_{\mathbf{k}_1}^2)t_{\text{hold}}/\hbar + \varphi_{\text{dyn}}) \tag{7.5}$$

where we introduced the parameters a_C and b_C that depend on the probability of exciting atoms from the first to the second band along the specific path C taken in the Brillouin zone, and a dynamical phase φ_{dyn} accumulated during the motion in the two non-degenerate bands, $\varphi_{\text{dyn}} = \int (E_{\mathbf{k}(t)}^1 - E_{\mathbf{k}(t)}^2)/\hbar \, dt$. The probability of eq. 7.5 oscillates at a frequency given by the energy difference between the two bands

at the hold point $\mathbf{k}_1$ as a function of the hold time. This oscillating signal is used to precisely measure the energy difference between the bands.

Since we are using a weakly interacting BEC with a momentum spread $\sigma_{\mathbf{k}} \simeq 0.14 k_L$ and fast accelerations, we can treat the effect of the momentum spread similarly to what has been done for the measurements of the Berry phase (see equation 6.16), and calculate theory curves by averaging the interference signal of eq. 7.5 over the initial quasimomentum distribution $n(\boldsymbol{\mathcal{K}})$ as

$$P_1(t_{\text{hold}}) = \int | \langle \psi^1_{\mathbf{k}_2 + \boldsymbol{\mathcal{K}}} | \hat{U}_S | \psi^1_{\mathbf{k}_0 + \boldsymbol{\mathcal{K}}} \rangle |^2 \; n(\boldsymbol{\mathcal{K}}) \; d^2 \boldsymbol{\mathcal{K}}. \tag{7.6}$$

7.2.2. Mapping the energy difference between first and second band

By holding the atoms at different quasimomenta during the Stückelberg sequence, the energy difference between first and second band is mapped along a specific path in the Brillouin zone. The results are presented in Fig. 7.2. Thanks to the narrow initial quasimomentum distribution of the BEC, we were able to observe clear Stückelberg oscillations as a function of hold time, some examples are presented as insets in the figure. The contrast of these oscillations is limited by the probability of transferring atoms to the second band, i.e. the parameters a_C, b_C of eq. 7.5 which depend on the specific path taken in the Brillouin zone. For long holds, the contrast is also reduced by instabilities of the weakly interacting BEC and by the quasimomentum spread of the cloud according to which a range of frequencies is contributing to the observed oscillatory signal, see eq. 7.6. The energy difference between the first and second band is extracted from the oscillatory signal by fitting the data with a damped cosine function.

The experimental results of the measured energy differences are summarized in the main graph of Fig. 7.2. The frequencies of the observed oscillations agree very well with the energy differences we expect from the full band structure calculation combined with the quasimomentum averaging of eq. 7.6. By comparing the results with the predictions from theory, we observed that the effect of the momentum spread is to under (over) estimate the gap frequency where the band has positive (negative) curvature. Even if the energy difference in proximity of the $\mathbf{K}$ point cannot be measured because of a combination of momentum spread and instabilities setting in at a timescale comparable to the gap frequency, we find the energy difference close to the Dirac point to be $<10\%$ of the lattice bandwidth. This result is compatible with the presence of a small gap at the Dirac cone that has been measured via Aharonov-Bohm interferometry, see Section 6.3.2.

As one can notice from the theory curves in Fig. 7.2 obtained with and without averaging over the quasimomentum distribution, the effect of this spread is found to be minimal where the slopes of the energy bands are approximately linear. The
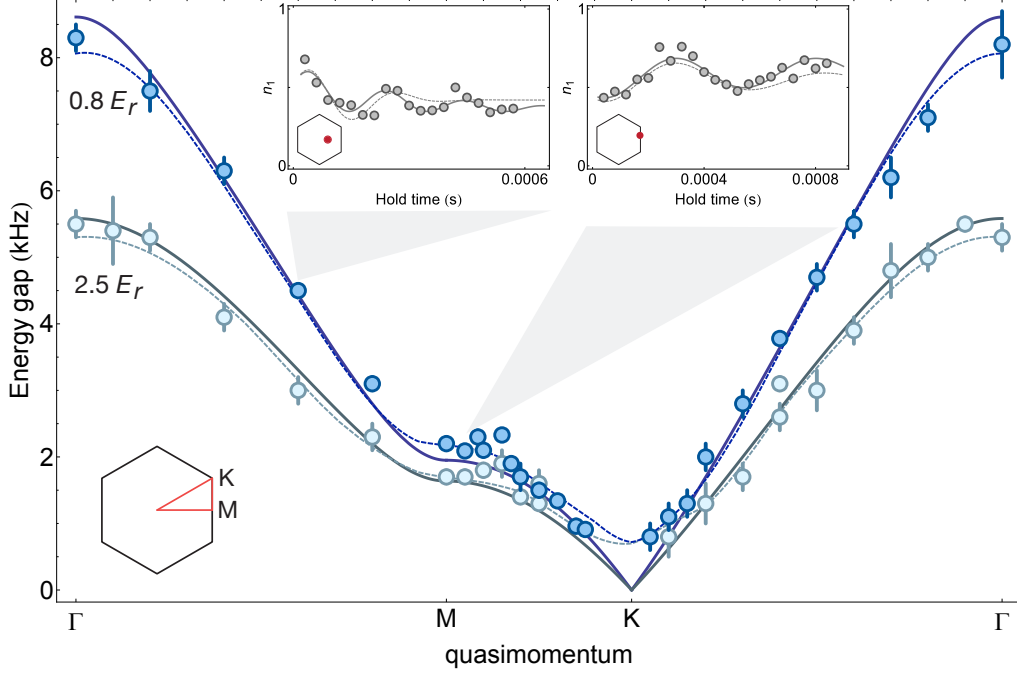
Figure 7.2.: Mapping of the dispersion relation via Stückelberg interferometry. The energy difference $(E_{\mathbf{k}}^1 - E_{\mathbf{k}}^2)/h$ between first and second band is measured at different quasimomenta $\mathbf{k}$ along the path depicted in the bottom inset (red triangle, hexagon is the first Brillouin zone). Error bars denote fit uncertainties. The accelerations used are $a_L = 44$ m/s^2 and $a_L = 38$ m/s^2, depending on the lattice depth and energy gap along the path taken. With these accelerations only the first and second band can be populated during the fast motion in the BZ. The observed Stückelberg oscillations are shown as insets for selected points of the main graph. The corresponding fits (solid lines) and scaled theory lines (dashed) are shown. The hold position in the BZ is also sketched. The contrast of the oscillatory signal is limited by the path-dependent transition probabilities and by the quasimomentum spread which damps the oscillatory signal for long holds. In the main graph the lines are ab initio theory using a full band structure calculation for the indicated lattice depths and no momentum spread. Dashed lines are calculated by accounting for an initial momentum spread of the BEC of $\sigma_{\mathbf{k}} = 0.14\ k_L$.

lattice depth can be precisely estimated by comparing the energy gap at these locations with value obtained from the full band structure calculation. The Stückelberg interferometry is routinely used to calibrate the lattice depth and to carefully balance the lattice potential by comparing oscillation frequencies at different points in the Brillouin zone. Despite the current limitations due to interactions, Stückelberg interferometry is also a valuable technique to detect and characterize the energy gap at the Dirac points when a large AB offset is introduced (≥ 1 kHz), as recently

Figure 7.3.: Initial phase of Stückelberg oscillations for interferometry along differently angled paths. **(a)** Example o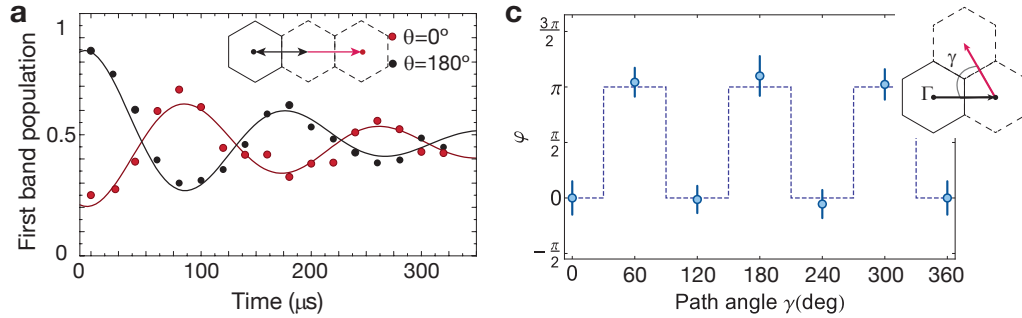f Stückelberg oscillations for two backtracked curves (0° and 180°) obtained in a 3 E_r lattice with an acceleration of $a_L =$80 m/s^2. Paths are shown as insets. **(b)** Summary of the measured phase differences referenced to the 0° path. Data are taken in a 3 E_r lattice. Schematic illustrates the paths taken during the interferometry.

realized in our experiment by tuning the polarizations of the lattice beams [237].

Initial phase of the Stückelberg oscillations

So far we neglected the information carried by the initial phase of the Stückelberg oscillatory signal. Without a hold time in the Stückelberg sequence, the following probability of remaining in the first band is measured at the end of the interferometry $P_1 = |\langle \psi^1_{\mathbf{k}_2}| \hat{U}_2 \hat{U}_1 |\psi^1_{\mathbf{k}_0}\rangle|^2 = |\langle \psi^1_{\mathbf{k}_2}| \psi_{\mathbf{k}_2}(t)\rangle|^2$. By comparing the initial phase of the oscillations along different paths we can gain information about the symmetries of the band eigenstates. We specifically looked at the Stückelberg oscillations when moving by two reciprocal lattice vectors, from Γ-point to Γ-point, as illustrated in Fig. 7.3. The final quasimomentum is $\mathbf{k}_2 = \mathbf{k}_0 + 2\mathbf{G}$, $\mathbf{G}$ being a reciprocal lattice vector. We accelerate by one reciprocal lattice vector into the next Brillouin zone, hold at Γ for a variable t_{hold} and accelerate again at different angles, ending at the Γ point in a neighboring Brillouin zone.

Even if the dispersion is the same along all the paths taken and it results in the same accumulated dynamical phase at the end of the motion, we observed a clear π phase shift between paths ending in neighboring zones. An example of such oscillations is presented in Fig. 7.3a where we compare paths at an angle of 0° and 180°. This phase shift indicates that the evolution and the final states reached are actually different not because of the energy probed along the path but because of the winding of the bands eigenstates is different in neighboring zones, feature which is also linked to the presence of two inequivalent Dirac points. The different orientation of the eigenstates of neighboring zones is also illustrated in chapter 3, see the plot in Fig. 3.4a. By comparing the phases of the oscillations along differently angled paths connecting Γ points the C$_3$ symmetry of the lattice is manifest since

the initial state evolves to the same final state for paths that are symmetric under 120° rotations, as the results in Fig. 7.3c illustrate.

The close connection between the phase of the Stückelberg oscillations and the geometric properties of the two bands has been recently derived and the non-adiabatic dynamics of particles in the lattice has been interpreted in terms of Wilson lines [237, 238]. Moreover, the topological properties of the two-band model have been extracted by studying the dynamical evolution of particles subjected to a strong force. We reference to the following work [237] for a more complete overview on such topic.

7.3. Final remarks

In this chapter, results of Stückelberg interferometry in the honeycomb lattice have been presented. It has been illustrated how the interferometry can be used to map the dispersion of the lattice along a specific path in the Brillouin zone. By comparing the measured oscillation frequencies with the ones expected from theory we can accurately estimate the lattice depth and map the dispersion of the lattice potential. This technique allows the dynamical phases acquired by particles moving in the energy band to be precisely reconstructed. This information is necessary to extend the Aharonov-Bohm interferometry to arbitrary paths in the Brillouin zone in order to measure the Chern number of a band.

Furthermore, we have shown that the phase of the oscillatory signal reveals the three-fold rotational symmetry of the lattice potential. Recent results from our lab taken in the strong force limit allowed the Wilson loop matrix to be reconstructed and they demonstrated the less trivial winding of the band eigenstates when the inversion symmetry is broken by a large energy offset between the A and B sites [237]. Stückelberg interferometry constitutes one possible and promising approach among the many proposed recently [86–88, 107, 239] to probe the topological features of multi-band systems without using state-dependent interferometric schemes. This would allow the invariants of such models to be reconstructed by combining measurements along different paths in the Brillouin zone.

Chapter 8.

Conclusion and outlook

This thesis presented a new experimental setup in which a honeycomb optical lattice has been implemented to study topological Bloch bands with ultracold atoms. The apparatus allows to cool bosons (^{87}Rb) and fermions (^{40}K) to condensation and degeneracy and it favors systematic studies of topological properties of bands with and without interactions between the particles thanks to the available Feshbach resonances for ^{40}K. In this thesis we described the honeycomb optical lattice for the cold atoms and we presented the geometrical features of its energy bands associated with the Dirac cones, which are analogous to the ones of solid state graphene. Contrary to the solid state case where there is little room to tune system parameters, the potential landscape can be adjusted at will. This enables us to engineer a band structure with or without offset between the two inequivalent sites of the unit cell as well as to tune the hopping amplitudes along the three tunneling directions. The high degree of control on the system parameters allows the geometrical features to be carefully tuned: The position of the Berry fluxes associated with the Dirac points and their spread in quasimomentum are controlled experimentally. This tunability facilitated the observation of the annihilation of the Dirac points upon lattice imbalance and it is a feature that one could take advantage of in future studies. In this thesis, we have also introduced techniques to detect and manipulate the state of the state of the atoms in the lattice. In particular, Bloch oscillations are a key ingredient for the detection of the topological properties of a Bloch band.

To probe the topological properties of the individual Dirac cones and to extract quantitative information about the spread in Berry curvature, an interferometric technique, the natural follow-up to the pioneering works carried out for cold atoms in 1D optical superlattices [57, 58], was studied. The key feature of this interferometry is the ability to measure the Berry phases associated with adiabatic motion of atoms in a band along arbitrary closed loops in reciprocal space. This Aharonov-Bohm interferometry allowed us to directly observe the π Berry phase associated with the Dirac cones of the lowest band of the lattice. Our results demonstrated the winding of the band eigenstate and the topological character of the conical intersections of the optical lattice. Moreover, the combined use of a Bose-Einstein condensate and the Bragg reflection at the edge of the zone greatly enhanced the

quasimomentum resolution of the interferometer, allowing us to give a quantitative upper bound on the spread in Berry curvature of the extremely narrow Berry flux of a cone. Furthermore, we exploited the local mapping of this technique and the high degree of control over the lattice structure to directly observe the topological phase transition associated with moving and merging Dirac cones. The annihilation of the fluxes of the cones is beyond the applicable strain levels in graphene [126, 140] but is universal to any honeycomb lattice potential, as demonstrated in several other wave systems in which this behavior has been observed, e.g. in photonic graphene [92]. In our experimental realization, the motion of the cones was detected with the interferometry, and the geometric phase associated with the cones was observed to disappear when the lattice was strongly imbalanced. The results of the interferometry presented in this thesis illustrate the capability of the protocol to locally detect geometrical features that are challenging to observe in real [17, 100–102] and synthetic [81, 82] materials by alternative techniques, like transport measurements.

In the last part of this thesis, preliminary results concerning interferometry between atoms in the two lowest bands of the lattice, possible extensions of the Aharonov-Bohm interferometry, have been introduced. The results from the Stückelberg interferometry illustrate how this technique can be used to precisely reconstruct the dispersion of the energy bands, a necessary information for reconstructing the Chern number via Aharonov-Bohm interferometry, as well as to gain information about the symmetries of the band eigenstates. Recently, Stückelberg interferometry combined with the analysis of population transfer has been used in our experimental setup to reconstruct Wilson loops in the presence of an energy offset between the A-B sites, and its eigenvalues have also been obtained [237].

Outlook

The observed winding of the band eigenstate around the Dirac cone and the high degree of control over the lattice structure highlight the potential of ultracold atoms as a versatile system to engineer topological bands and study them in a systematic manner. In the context of this thesis, we presented results obtained with a time-reversal and inversion symmetric lattice. By making use of the tunable honeycomb lattice potential one of these symmetries can be broken and novel topological bands can potentially be studied. The optical flux lattice, with its lowest flat band, is one prominent example [68, 135] as its properties are equivalent to those of charged particle in a uniform and strong magnetic field. Engineering strain as an effective source of strong pseudo-magnetic field is also an interesting direction for future studies on artificial magnetic fields in a honeycomb lattice [83, 84, 240]. Another intriguing direction of research consists of adding a periodic drive which would break the time-reversal symmetry of the system, as recently realized in several works [81, 82, 241]. The modulation of the potential would permit the implementation of novel topological Floquet bands with non-zero Chern number [74, 76, 136, 230] and,

possibly, spin-orbit coupling [21, 242], allowing a rich variety of topological bands to be explored.

For the results presented in this thesis, interactions between the particles were weak and they could be safely neglected to interpret the experimental results. The high degree of control over the lattice potential and interactions, advantages of cold atoms compared to other systems, can facilitate systematic studies on the interplay of topology and interactions with our experimental apparatus. It would be interesting to study the phase diagram of our lattice structure which has not been investigated in detail yet [94] but it is rich in novel exotic phases when interactions between different states and complex next-nearest-neighbors tunnelings are added, as pointed out in several works concerning both fermions and bosons [62, 95, 96, 206, 207, 243]. Interacting atoms prepared in p-bands of the honeycomb lattice are also an intriguing direction for future studies [244, 245].

Our results also highlighted the potential of the interferometric protocol for probing geometrical features with high quasimomentum resolution. The Aharonov-Bohm interferometry is suitable to fully resolve the distribution of Berry curvature over the entire Brillouin zone by combining local measurements of the geometric phases along small loops in reciprocal space. This would enable the full reconstruction of the topological invariants [57] in a large variety of lattice structures. Particularly interesting would be to apply it to bands with non-zero Chern number and, for example, detect a change of sign of the Berry phase at a Dirac point when time-reversal symmetry is broken in the honeycomb lattice. This technique could potentially be applied to even more exotic modifications of the bands, like the ones predicted for the Floquet spectrum of radiated graphene [246], to map out the local distribution of Berry curvature in the Brillouin zone. Moreover, as the results from the annihilation of the Dirac points demonstrate, the protocol facilitates the observation of topological phase transitions in such bands upon a controlled modification of the system parameters.

Multiband extensions of this work [107] would enable measurements of Wilson loops and off-diagonal Berry connections in systems with quantum spin-Hall effect [21, 22], as an example, and thus allow the complete geometric tensor of Bloch bands to be fully reconstructed. These techniques would therefore constitute a way of characterizing complex systems, e.g. measuring the $\mathbb{Z}_2$ invariant of the quantum spin-Hall effect [122], and reconstructing non-Abelian Berry connections. To conclude, the apparatus for cold atoms in a honeycomb optical lattice presented in this thesis is good playground for new studies on topological properties of Bloch bands.

Appendix A.

Complete derivation of the optical potential

Here the complete derivation of the optical potential is summarized. The potential is calculated in the most general way, considering polarization tilts and power imbalances. At the end we simplify the general results to the specific potentials cited and used in the main text.

The electric field of each wave, as parametrized in Chapter 3, is

$$\mathbf{E}_i(\mathbf{r}) = \sqrt{I_i}e^{i\mathbf{k}_i\mathbf{r}-i\omega_L t}(\cos(\theta_i)\hat{z} + \sin(\theta_i)e^{i\phi_i}(\hat{\mathbf{z}} \times \hat{\mathbf{k}}_i)) = \mathbf{E}_s + \mathbf{E}_p. \tag{A.1}$$

Because of the vector product $(\hat{\mathbf{z}} \times \hat{\mathbf{k}}_i)$ and of the orientations of the beams $\mathbf{k}_i$ defined in the main text (3.24) we get that the p-polarized (polarization in the plane of intersection, the x-y plane)

$$\mathbf{E}_p = e^{-i\omega_L t}(\sin(\theta_1)e^{i\mathbf{k}_1\mathbf{r}+i\phi_1}\hat{x} + \sin(\theta_2)e^{i\mathbf{k}_2\mathbf{r}+i\phi_2}(\hat{x}\cos(4\pi/3), \hat{y}\sin(4\pi/3))$$
$$+ \sin(\theta_3)e^{i\mathbf{k}_3\mathbf{r}+i\phi_3}(\hat{x}\cos(2\pi/3), \hat{y}\sin(2\pi/3))) \tag{A.2}$$

By transforming each component of the electric field in the $\sigma_\pm$ basis, as done in the main text, we get

$$\mathbf{E}_{\sigma_+} = \frac{1}{\sqrt{2}}e^{-i\omega_L t}(-\sin(\theta_1)e^{i\mathbf{k}_1\mathbf{r}+i\phi_1}\hat{x} + \sin(\theta_2)e^{i\mathbf{k}_2\mathbf{r}+i\phi_2}(\hat{x}\cos(\pi/3) + i\hat{y}\sin(\pi/3))$$
$$+ \sin(\theta_3)e^{i\mathbf{k}_3\mathbf{r}+i\phi_3}(\hat{x}\cos(-\pi/3) - i\hat{y}\sin(-\pi/3))) \tag{A.3}$$

and analogously for $\mathbf{E}_{\sigma_-}$. In a compact notation:

$$\mathbf{E}_{\sigma_\pm} = \frac{1}{\sqrt{2}}e^{-i\omega_L t+i\pi}\left(\sin(\theta_1)e^{i\mathbf{k}_1\mathbf{r}+i\phi_1} + \sin(\theta_2)e^{i\mathbf{k}_2\mathbf{r}\pm i4\pi/3+i\phi_2} + \sin(\theta_3)e^{i\mathbf{k}_3\mathbf{r}\pm i2\pi/3+i\phi_3}\right). \tag{A.4}$$

Now we can derive the interference patterns which define our periodic lattice

potential. The intensity pattern of the polarization out of plane of intersection is

$$I_s(\mathbf{r}) = |\mathbf{E}_s|^2 = \sum_{i,j=1}^{3} \sqrt{I_i I_j} \cos\theta_i \cos\theta_j e^{i((\mathbf{k}_i - \mathbf{k}_j)\mathbf{r})} \tag{A.5}$$

$$= \sum_{i=1}^{3} I_i \cos^2\theta_i + \sum_{i,j=1}^{3} \sqrt{I_i I_j} \cos\theta_i \cos\theta_j \cos((\mathbf{k}_i - \mathbf{k}_j)\mathbf{r}). \tag{A.6}$$

The arrangement of the minima of this pattern has a honeycomb symmetry. Similarly, we can derive the intensity pattern from the polarization decomposition of eq. A.3 for in-plane component of the polarization. Defining $\eta_i = (0, 4\pi/3, 2\pi/3)$ we get

$$I_p(\mathbf{r}) = |\mathbf{E}_p|^2 = |\mathbf{E}_+|^2 + |\mathbf{E}_-|^2 \tag{A.7}$$

$$= \frac{1}{2} \sum_{i,j=1}^{3} \sqrt{I_i I_j} \sin(\theta_i) \sin(\theta_j) e^{i((\mathbf{k}_i - \mathbf{k}_j)\mathbf{r} + i(\phi_i - \phi_j) + i\eta_i)} \tag{A.8}$$

$$+ \frac{1}{2} \sum_{i,j=1}^{3} \sqrt{I_i I_j} \sin(\theta_i) \sin(\theta_j) e^{i((\mathbf{k}_i - \mathbf{k}_j)\mathbf{r} + i(\phi_i - \phi_j) - i\eta_i)}. \tag{A.9}$$

Note that intensities of $\sigma_\pm$ polarizations are spatially displaced because the electric fields $\mathbf{E}_{\sigma_\pm}$ are out of phase. The sums in eq. A.7 can be simplified further to cancel out some terms. We then obtain

$$I_p(\mathbf{r}) = \sum_{i=1}^{3} I_i \sin^2\theta_i - \frac{1}{2} \sum_{i,j=1}^{3} \sqrt{I_i I_j} \sin\theta_i \sin\theta_j \cos((\mathbf{k}_i - \mathbf{k}_j)\mathbf{r} + \phi_i - \phi_j). \tag{A.10}$$

When the polarizations are laying in the plane of intersection, the interference has the minima arranged in a triangular pattern and has a maximum intensity of $9/2I_0$ in the balanced case ($I_i = I_0$), half of the honeycomb one. Plots of these intensity profiles can be found in the main text, Chapter 3.

To calculate the optical potential we have to multiply by the dipole potential U_{dip} of eq. 3.20 which is dependent on polarization and m_F state. We write it in a short notation as

$$U_{\text{dip}} = (U_1 + 2U_2 - g_F m_F \mathcal{P}(\mathbf{r})(U_1 - U_2)) I(\mathbf{r}) \tag{A.11}$$

where we introduced the effective dipole potentials $U_{1,2}$ of the $D_{1,2}$ transitions for readability, which are

$$U_{1,2} = \frac{\pi c^2 \Gamma_{1,2}}{2\omega_{1,2}^3} \left(\frac{1}{\omega_{1,2} - \omega_L} + \frac{1}{\omega_L + \omega_{1,2}} \right) \tag{A.12}$$

and the polarization $\mathcal{P}$ is spatially dependent in our lattice configuration. Thus the

potential is decomposed in a state-independent and a state-dependent part

$$V_L = (U_1 + 2U_2)I_s + (U_1 + 2U_2 - g_F m_F \mathcal{P}(\mathbf{r})(U_1 - U_2))I_p \tag{A.13}$$

$$= (U_1 + 2U_2)(I_s + |E_+|^2 + |E_-|^2) - g_F m_F (U_1 - U_2)(|E_+|^2 - |E_-|^2). \tag{A.14}$$

The state-dependent part of the potential, linear in m_F number, can be mapped onto an effective magnetic field whose magnitude depends on the detuning of the optical potential from the D-lines, which defines the factor $U_1 - U_2$. The strength of this term can be tuned with a polarization tilt or a field offset tilt. Given our geometry and detunings, the state-dependent part can be further simplified as

$$V_L = (U_1 + 2U_2)(I_s + |E_+|^2 + |E_-|^2) - \frac{\sqrt{3}g_F m_F (U_1 - U_2)}{2} \sum_{i,j=1}^{3} \cos((\mathbf{k}_i - \mathbf{k}_j)\mathbf{r}). \tag{A.15}$$

In our experimental realization, the state-dependent term can be neglected because of the large detuning from both lines which results in $U_1 - U_2 \approx 0$ and also because of the choice of out of plane linear polarizations which sets I_p to zero in the ideal case. Other schemes, like the flux lattice, make use of this state-dependent and spatially-dependent term to purposely create artificial spin-orbit coupling [65, 68]. The different configurations of the lattice associated with different state-dependent potentials could be probed by, e.g., driving band-selective microwave transitions between different hyperfine states of the atoms loaded in the lattice.

If only two beams have imperfect polarizations, i.e. $\theta_1 = \theta_2 = \theta \neq 0$, the potential is created by the interference pattern I_p of eq. A.7 which is

$$I_p = 2I_0 \sin^2 \theta (1 + \cos((\mathbf{k}_1 - \mathbf{k}_2)\mathbf{r} + \phi_1 - \phi_2)). \tag{A.16}$$

To model small imperfections of the beams' polarizations, we can thus define the 1D lattice potential as $A \sin((\mathbf{k}_1 - \mathbf{k}_2)\mathbf{r})$. The energy offset $\Delta/2$ of an A or B well can be calculated from this expression at one of the minima of the honeycomb potential, i.e. $\mathbf{r}_A, \mathbf{r}_B$. It follows that $\Delta/2 = A\sqrt{3}/2$, equation which defines the amplitude A and thus the potential of eq. 3.30 quoted in the main text.

Appendix B.

Density distributions of atoms in a harmonic trap

Here we consider a gas trapped in a three-dimensional harmonic trap

$$V_{ho}(\mathbf{r}) = \frac{m}{2}(\omega_x^2 x^2 + \omega_y^2 y^2 + \omega_z^2 z^2). \tag{B.1}$$

The real space and momentum distribution of an atomic gas are determined by its statistical distribution. The calculation of finite temperature properties is considerably simplified by taking a semi-classical approach, the Thomas-Fermi approximation, valid for large atom numbers [142, 143]. Here, the real-space density distribution in the harmonic potential is calculated by integrating over all momenta. For example, starting from a Fermi gas with a semiclassical statistical distribution given by

$$f_F(\mathbf{r}, \mathbf{p}) = \frac{1}{e^{(\frac{\mathbf{p}^2}{2m} + V_{ho} - \mu)/k_B T} + 1}, \tag{B.2}$$

the Fermi-Dirac density distribution $n_F(\mathbf{r})$ can be obtained by averaging over all momenta $\mathbf{p}$ to get [144, 159]

$$n_F(\mathbf{r}) = -\frac{1}{\lambda_{dB}^3} \mathrm{Li}_{3/2}\left(-e^{-(V_{ho}(\mathbf{r}) - \mu)/k_B T}\right), \tag{B.3}$$

with $\lambda_{dB} = \sqrt{2\pi\hbar^2/(mk_B T)}$ is the de Broglie wavelength, μ the chemical potential and $\mathrm{Li}_{3/2}$ the polylogarithm of order $3/2$. In the high temperature limit, this distribution reduces to the Gaussian Boltzmann distribution

$$n_{MB}(\mathbf{r}) = \frac{N}{\pi^{3/2}\sigma_x \sigma_y \sigma_z} e^{-x^2/\sigma_x^2 - y^2/\sigma_y^2 - z^2/\sigma_z^2} \tag{B.4}$$

with $\sigma_i^2 = k_B T/m\omega_i$. For the case of bosons with semiclassical statistical distribution given by

$$f_B(\mathbf{r}, \mathbf{p}) = \frac{1}{e^{(\frac{\mathbf{p}^2}{2m} + V_{ho} - \mu)/k_B T} - 1} \tag{B.5}$$

the atoms start to macroscopically occupy the single-particle ground state. The distribution of atoms in the trap n_B is thus composed of two different distributions, the one of condensed atoms and the one of thermal atoms [142]. The role of weak repulsive interactions is also important in determining the distribution of the condensed atoms. Due to scattering the atoms will redistribute in the harmonic trap. The density distribution n_B of the BEC is modified and is given by the Thomas-Fermi parabolic distribution [142]

$$n_B(\mathbf{r}) = \frac{1}{g} \left(\mu - V_{ho}(\mathbf{r}) \right) \tag{B.6}$$

where g is the amplitude of the contact potential.

The real space distribution of atoms in the trap as well as the ballistic expansion of atoms during TOF, that maps momentum into position according to $\mathbf{r}_i(t) = \mathbf{r}_i(0)(1 + \omega_i^2 t^2)^{-1/2}$, are markedly different for a thermal gas, degenerate fermions and condensed bosons. To correctly relate the density distribution measured by absorption imaging with the distributions we just mentioned, we should remember that we detect the column density $n_{col}(x, y)$ defined in Chapter 4 and we actually integrate the distributions along the z direction to derive the fitting functions from which we extract temperatures and atom numbers.

Appendix C.

System parameters for weakly interacting bosons in the lattice

As mentioned in Chapter 5, interactions, even when weak, can play an important role in determining the ground state wavefunction, the excitation spectrum and the stability of the condensate. As described in the main text, the 2D lattice without additional vertical confinement results in a periodic array of elongated tubes with high filling factors. Here we summarize the tubes' parameters from which we infer mean atom numbers, densities and interaction strengths in the weakly interacting regime, i.e. $na_s^3 \ll 1$. These results are derived from Gross-Pitaevskii (see eq. 4.9) with the lattice in the tight-binding limit, where each lattice site can be approximated by an harmonic trapping potential. In this case, the stationary Gross-Pitaevskii equation (GPE) can be treated analytically. Of course this is a coarse approximation which can give us a qualitative idea about the energy scales and the relevant system's parameters. If the particles in the lattice are strongly correlated and the filling factors are low, the Bose-Hubbard model [247–250] is more suitable for describing the properties of the system.

We consider weakly interacting ^{87}Rb atoms in a harmonic trap with chemical potential μ. We assume the lattice to be in the x-y plane, while along z the atoms are confined only by the harmonic trap. Following the standard derivation of the GPE for particles in a lattice [143], we can subtitute the field operators in the many-body Hamiltonian with complex numbers and make the usual ansatz for the manybody wavefunction of condensed atoms loaded in each tube of the kind $\Psi(x_i, y_i) = \sum_i w_i(x_i, y_i)\phi_i(z)$ where $w_i(x, y)$ is the Wannier function of the tube i located at position (x_i, y_i) which defines the radial part of the wavefunction, and $\phi_i(z)$ is the interaction broadened wavefunction along the z-direction, where there is no periodic potential. From this approximation, one derives a stationary Gross-Pitaevskii equation for interaction broadened wavefunction ϕ_i of each tube which is

$$\left(\tilde{g}|\phi_i|^2 + \frac{1}{2}m(\omega_z^2 z^2 + \omega_x^2 x_i^2 + \omega_y^2 y_i^2) - \mu \right) \phi_i(z) = 0 \qquad (C.1)$$

with ω_i being the trap frequencies. Here we approximated each lattice well with an

harmonic trap for simplicity. We also assume $\omega_x = \omega_y = \omega_r$, which is the case in the experimental realization. The renormalized 1D scattering length is $\tilde{g}$ defined as $\tilde{g} = g \int |w(x,y)|^4 dx dy$ and it can be found by approximating the Wannier function of the atoms at a site i with the ground state of the harmonic oscillator that describes the lattice potential [251]. The harmonic oscillator length is given by $l_r^2 = \hbar/m\omega_r$ and it depends on the lattice depth through the on-site trap frequency ω_r. We find a value of $\tilde{g} \approx 2g\hbar/(ml_L^2) = g \times 5.5 \ \mu\text{m}^{-2}$ for ^{87}Rb in a 1 E_r lattice. Moreover, given our trapping parameters $l_r \gg a_s$, this means that, even if we are more tightly confined along the radial direction compared to the axial one, the system is still fully three-dimensional.

The profile of the broadened wavefunction is derived from eq. C.1

$$|\phi_i(z)|^2 = \frac{\mu - 0.5m\left(\omega_z^2 z^2 + \omega_x^2 x_i^2 + \omega_y^2 y_i^2\right)}{\tilde{g}}. \tag{C.2}$$

The Thomas-Fermi boundary along z is found to be

$$z_{TF}(x_i, y_i) = \sqrt{\frac{2\mu - 0.5m\omega_r^2(x_i^2 + y_i^2)}{m\omega_z^2}}. \tag{C.3}$$

The number of particles in each tube N_i is calculated from the following integral

$$N_i(x_i, y_i) = \int_{-z_{TF}}^{z_{TF}} |\phi_i(z)|^2 dz = \frac{2m}{3\tilde{g}} z_{TF}(x_i, y_i)^3 \omega_z^2. \tag{C.4}$$

The number of particles in each tube defines the chemical potential via the equation $N_T = \sum_i N_i$, with N_T being the total atom number. For a large system, $N \gg 1$, the chemical potential can be estimated within the continuum approximation by calculating the following integral analytically: $N_T = V^{-1} \int N_i dx dy$ where the volume V is the unit cell volume $V = 3\sqrt{3}d_L^2/2$. The resulting chemical potential is

$$\mu = \frac{\hbar\bar{\omega}_{ho}}{2} \left(\frac{15 N_T m \tilde{g} V}{4\pi\hbar^2 \bar{l}_{ho}}\right)^{2/5} \tag{C.5}$$

with $\bar{\omega}_{ho} = (\omega_r^2 \omega_z)^{1/3}$ being the geometrical mean of the trap frequencies and $\bar{l}_{ho}^2 = \hbar/(m\bar{\omega}_{ho})$ the corresponding oscillator length.

For $N_T = 4 \times 10^4$ particles in a 1 E_r lattice combined with a harmonic trap with frequencies $\omega_i = 2\pi$ (24 Hz, 24 Hz, 180 Hz), typical for the experiments, we get a value of $\mu/h \sim$500 Hz. For these parameters we evaluate a Thomas-Fermi boundary along the radial direction of $\mathbf{r}_{TF} \sim 20 \ \mu$m by computing the minimum distance at which the atom number in a tube is zero, i.e. setting $N_i(\mathbf{r}_{TF}) = 0$. This value of the radius $\mathbf{r}_{TF}$ for the parameters cited above is comparable to the cloud size we

measure experimentally for atoms imaged in situ. The number of populated tubes is $N_{tubes} \sim 7000$, with a peak of 36 atoms in the central tube. The interaction parameter of each tube is evaluated from the integral $U_{I,i} = \tilde{g} \int_{-z_{TF}}^{z_{TF}} |\phi_i(z)|^4 / N_i(z)^2 dz$ where we have normalized the wavefunction ϕ_i to one. Within the continuum approximation the integral is solved analytically to find $U_{I,i} = 3\tilde{g}/(5z_{TF}(x_i, y_i))$. The average density, tube lengths and interaction strengths of our array of tubes are estimated by using the ratio N_i/N_T as a weight

$$l_{tubes} = \sum 2N_i z_{TF}/N_T \sim 8 \ \mu\text{m} \tag{C.6}$$

$$U_{I,tubes} = \sum U_{I,i} N_i/N_T \sim h \times 14 \ \text{Hz} = 3.5 \cdot 10^{-3} \ E_r \tag{C.7}$$

$$n_{1D} = \sum N_i^2/(2z_{TF}N_T) \sim 6 \ \mu\text{m}^{-1}. \tag{C.8}$$

This small value of the average interaction strength $U_{I,tubes}$ justifies the assumption of weakly interacting regime for the ^{87}Rb atoms loaded in the optical lattice. Finally, we can compare the average interaction strength with the hopping in a 1 E_r lattice: $U_{I,tubes}/J \sim 1 \times 10^{-2} \ll 1$.

For the 3 E_r lattice we used for the results presented in Chapter 7, we find similar tubes' parameters, specifically: $l_{tubes} \sim 5 \ \mu\text{m}$, $n_{1D} \sim 5 \ \mu\text{m}^{-1}$ and $U_{I,tubes} \sim h \times 21 \ \text{Hz} = 5 \cdot 10^{-3} \ E_r$ and $U/J \sim 0.1$.

Appendix D.

Additional details on the Aharonov-Bohm interferometry

D.1. Experimental parameters

Lattice calibration and acceleration parameters

The interferometry is performed in a shallow lattice of 1.0(1) E_r and has been calibrated by using the Stückelberg interferometry introduced in the last chapter. The lattice depth has been chosen to have a large separation between the two bands away from the Dirac point such that the atoms can move adiabatically during the sequence of duration $2\tau = 1.6$ ms. This value has been chosen to avoid instabilities of weakly interacting BEC while being slow enough to fulfill the adiabaticity condition in a 1 E_r lattice. We quantify the adiabaticity of the motion for this range of forces by checking that the occupation of higher bands is negligible at the end of the interferometry. This is done by bringing the atoms back to the Γ-point, followed by a band-mapping sequence to extract the population of the atoms in the different bands. For interferometer paths ending near the Dirac point, where the adiabaticity condition is hardest to fulfill, the population in the second band is at most $\sim 20\%$ of the total atom number. We have verified that the excited-band population near the Dirac point does not appreciably affect our measurement by numerically integrating the Schrödinger equation for the two-band model. More on this numerics can be found in Section D.4.

Detection

The fractions of atoms in the two spin states, $n_{\uparrow,\downarrow}$, are measured by standard absorption imaging. After band-mapping (410 μs of ramp duration), a Stern-Gerlach pulse of 9.5 ms is applied to spatially separate the $|\uparrow\rangle$ and $|\downarrow\rangle$ states during time of flight. While this imaging can perfectly distinguish atoms that occupy opposite sides of the Brillouin zone, due to the short TOF of 10ms the imaged size of the atomic cloud is still a convolution of the quasimomentum and real-space distributions.

Microwave pulses

To simplify the interpretation of the results, the microwave pulses need to be short compared to the evolution time τ. To this end, we use 40W of microwave power to drive the transitions between the different hyperfine states, this results in a Rabi frequency of $2\pi\times33$ kHz and in a 15 μs π-pulse for the $|1,0\rangle \to |2,1\rangle$ transition, and in a $2\pi\times21$ kHz Rabi frequency with a 24 μs π-pulse for the $|1,1\rangle \leftrightarrow |2,1\rangle$. Thanks to the high power, the microwave π-pulse transfers most of the atoms, about 90%, to the desired state despite the broadening of the microwave transition in the inhomogeneous potential. The atoms that are not addressed by all the microwave pulses travel along different paths in reciprocal space and can thus be separated from the rest of the signal, as shown in the examples of Fig. 6.3 in the main text.

D.2. Minimizing dynamical phases and systematic errors

In order to reduce the dynamical phase contribution to the observed interference signal we investigated all the possible sources of systematic errors.

Magnetic field noise

Time-dependent fluctuations of the magnetic field are the dominant source of noise in the interferometry sequence and contribute to the dynamical phase and to shifts of the resonance for the microwave pulses that will result in an imperfect spin-echo sequence. To minimize the effect of magnetic field fluctuations, we use a low-noise power supply for the coil's current (FUG supply, type NTN750M-15) which has a residual ripple of $dI/I \simeq 3 \times 10^{-4}$ at 20A the set current in the experimental runs. This corresponds to a peak-to-peak field noise of $dB \simeq 240 \times \mu$G, mostly at 50 Hz. We add a inductive load in series to the coil to reduce high frequency noise. Since the current needs $\sim$ 2s to stabilize to this noise level and we don't want to oscillate the atoms in the energy bands for this long as the condensate will be depleted by instabilities, the experimental sequence begins with atoms in the internal state $|F = 1, m_F = 0\rangle$. The magnetic field gradient is turned on 2s before the interferometer sequence starts and a 15 μs microwave π-pulse transfers the atoms in $|1,0\rangle$ to $|2,1\rangle$ to start the spin-echo sequence.

The ambient AC-noise is $\simeq$4 mG peak-to-peak close to the science cell, corresponding to $\sim$5 kHz noise on the microwave resonance frequency. To reduce it, the beginning of the interferometer sequence is synchronized to the 50 Hz-line and we keep the duration of the interferometer sequence fixed to probe the same portion of the 50 Hz noise in each experimental run. With this choice, the dynamical phase associated with the 50 Hz noise is a fixed contribution that cancels out when we
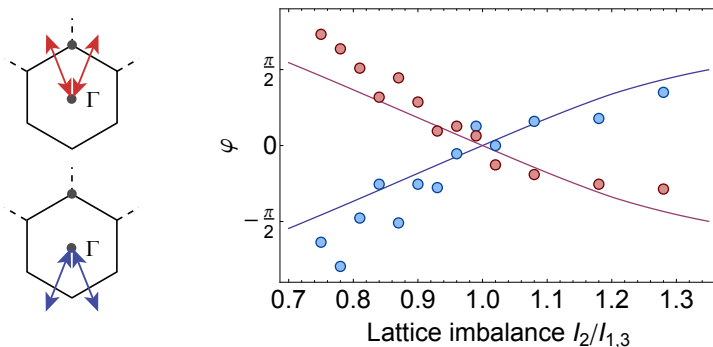
Figure D.1.: Effect of lattice imbalance. Plot of the phases measured with the interferometry for zero-area reference loops performed upwards (red) and downwards (blue), as illustrated by the schemes on the left. By changing the lattice imbalance ($I_2/I_{1,3}$) different dynamical phases are measured. Theory lines that account for the distortion of the energy band upon imbalance are also plotted.

compute the phase difference between measurement and reference curves.

Optimizing the lattice balance

The lattice balance along the symmetry axis of the interferometer loop is checked with the Stückelberg interferometry and with the Aharonov-Bohm sequence by comparing the measured phases along two 'zero-area' loops performed in opposite directions, i.e. with the first part of the motion ending at k_y or $-k_y$ as the scheme in Fig. D.1 illustrates. A lattice imbalance can add a path-dependent dynamical phase which is different for the particles moving along the left or the right path of the interferometer loop. Since $E_1(\mathbf{k}) = E_1(-\mathbf{k})$ because of time-reversal symmetry, the difference in dynamical phase picked up by the two spin components has opposite sign for the upwards and downwards loops (red and blue in Fig. D.1). This can be seen by writing down the dynamical phases in a more explicit form

$$\Delta\varphi_{dyn,+k_y} = \varphi_{dyn,\downarrow,+k_y} - \varphi_{dyn,\uparrow,+k_y}$$

$$= \int_0^\tau E_1(|\boldsymbol{\mathcal{F}}_x|t, |\boldsymbol{\mathcal{F}}_y|t)dt - \int_0^\tau E_1(-|\boldsymbol{\mathcal{F}}_x|t, |\boldsymbol{\mathcal{F}}_y|t)dt$$

$$= \int_0^\tau E_1(-|\boldsymbol{\mathcal{F}}_x|t, -|\boldsymbol{\mathcal{F}}_y|t)dt - \int_0^\tau E_1(|\boldsymbol{\mathcal{F}}_x|t, -|\boldsymbol{\mathcal{F}}_y|t)dt = -\Delta\varphi_{dyn,-k_y}. \qquad \text{(D.1)}$$

A vanishing phase difference between the phases measured for the two sequences with upwards and downwards paths corresponds to the balanced case. An example of a balancing curve is presented in Fig. D.1.
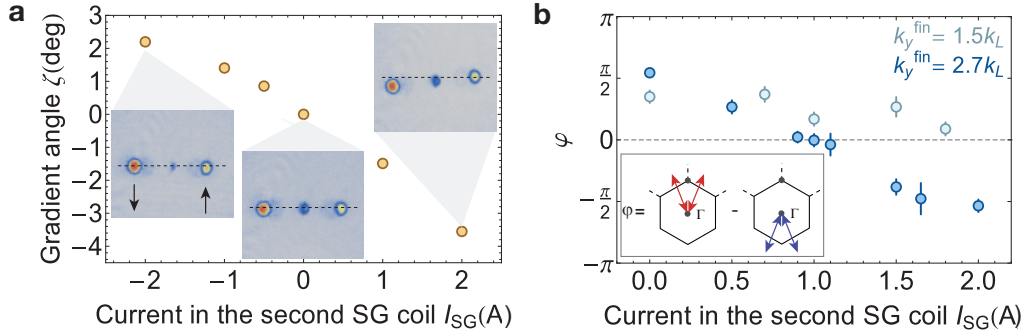
Figure D.2.: Alignment of the magnetic field gradient. **(a)** A current through a second Stern-Gerlach (SG) coil fine-tunes the direction of the spin-dependent force, i.e. the angle $\zeta(I_{SG})$ relative to $\zeta(I_{SG} = 0)$ which sets the 0° angle. Examples of imaged $\uparrow, \downarrow$ atoms at selected currents I_{SG} are shown. **(b)** Example of alignment curves: phase difference between zero-area reference loops performed upwards and downwards (see inset) is measured at different I_{SG} for loops of different lengths. Total distances traveled along y, k_y^{fin}, are $k_y^{\text{fin}} = 2.7k_L$ (dark blue), $k_y^{\text{fin}} = 1.5k_L$ (light blue). The phase difference vanishes for orthogonal gradient and lattice acceleration. Interferometry for long paths, i.e. large k_y^{fin}, is more sensitive on imperfect alignment of the forces.

Alignment of the B-field gradient

An imperfect orthogonality between the force from the gradient and the one from the lattice modifies not only the trajectories of the two states in the Brillouin zone but also the magnitude of the total force, i.e. all the terms in the dynamical phase of eq. 6.14. The effect of this systematic error is diminished by the use of a spin-echo π-pulse which reduces the the Zeeman term contribution in the dynamical phase φ_{dyn} to the following path-dependent term

$$\int_0^{2\tau} \Delta\varepsilon_\mu = \mu \, |a_L| \, \tau^3 \cos(\gamma) \nabla B \qquad (\text{D.2})$$

which arises from the differential motion of the two spin states in the inhomogeneous field gradient. Here γ is the angle between the force from the gradient and the one from the lattice acceleration a_L. This is likely a dominant source of systematic error at large $\left|k_y^{\text{fin}}\right|$, i.e. large lattice accelerations. In addition, we fine-tune the alignment of the force from the gradient relative to the one from the lattice acceleration. This is done by tuning the current in the two Stern-Gerlach coils. For orthogonal gradient and lattice accelerations, the phase measured by the zero-area reference interferometer should be independent of the length of the path, k_y^{fin}. Hence, to optimize the direction of the gradient, we measure the phase of the 'zero-area' reference loop for
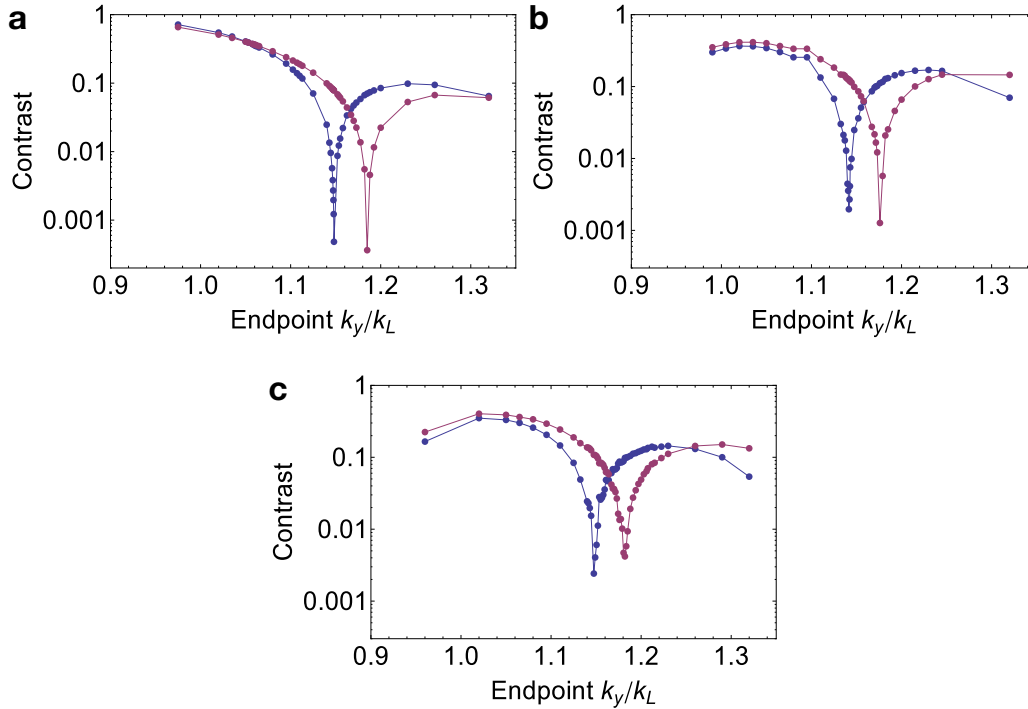
Figure D.3.: Results from the numerical simulation of the interferometry sequence in the two-band model in proximity of the Dirac point. The results are obtained with a momentum spread of $\sigma_{\mathbf{k}} = 0.14 k_L$ and three different A-B offsets, $\Delta = 0$, $\Delta = 3$ Hz and $\Delta = 12$ Hz from **a** to **c**. Blue points are the results obtained when only the population in the first band is analyzed, the red ones include both first and second band signals. The sharpness of the features is not significantly affected by the second band population, especially when the Berry curvature is extremely well localized.

opposite lattice accelerations and different currents of the fine-tuning coil, the results are presented in Fig. D.2. The phase difference between the loops performed in opposite directions, k_y^{fin} and $-k_y^{\mathrm{fin}}$, should vanish for orthogonal gradient and lattice acceleration. By comparing them, we set the current in the second Stern-Gerlach coil to 1A. From our calibrations we estimate an error on the gradient alignment of at most 2°.

D.3. Effect of second band population

In proximity of the Dirac point it is hard to fulfill the adiabaticity condition because of the extremely small energy gap. We observed a partial transfer of atoms to the second band for loops ending close to the Dirac point, where the first and second band populations are detected together at the end of the interferometry. In order
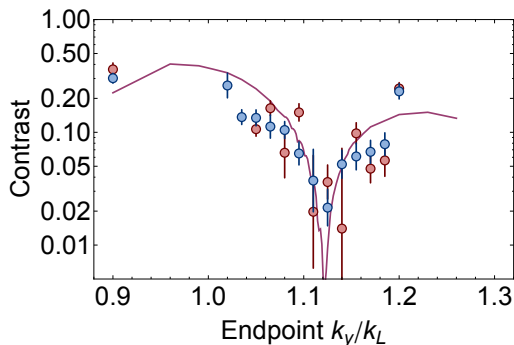
Figure D.4.: Comparison of the numerical results for $\Delta = 12$ Hz with the data of the interference contrast. The theory curve has been only shifted to match the position of the observed minimum in contrast which depends on the spread $\sigma_{\mathbf{k}}$. No scaling is applied to the curve.

to check that the effect of the second band population is not to sharpen the phase jump and the contrast feature, we numerically evolved the states of the $\uparrow$ and $\downarrow$ particles according to the equation of motion for the non-adiabatic case, which we have introduced in the main text, see eq. 5.16. The full contrast of the interference fringes are calculated by averaging over the quasimomentum distribution $n(\mathbf{k})$. The simulations are done for an AB offset of $\Delta = 0$ Hz, $\Delta = 3$ Hz and $\Delta = 12$ Hz, and the numerical results are illustrated in the graphs of Fig. D.3 where the contrast obtained by analyzing only the first band population or the first and second band together are plotted. It can be seen that detecting both first and second band mostly results in a shift of the position of minimum contrast in all three cases. Moreover, the second band population results in a less pronounced contrast in the case of a larger energy gap Δ and larger spread in Berry curvature. From these simulations we can conclude that comparing the data in proximity of the Dirac point to theory does give an upper bound on the spread in curvature. Finally, it is interesting to note that the numerical simulation captures quite well the observed decrease in contrast, see Fig. 6.10b in the main text. Specifically, it predicts the decreased contrast which has been observed in proximity of the Dirac point and it matches the data remarkably well without any additional rescaling, as illustrated in Fig. D.4 where the data are overlaid with the curve obtained for $\Delta = 12$ Hz. This seem to indicate that the decrease in contrast is mostly due to second band population rather than imperfections in the spin-echo sequence and instabilities, which seem to play a minor role.

D.4. Effect of finite size and harmonic trapping potential

The discrete translational symmetry of the optical lattice can be broken by the presence of an harmonic trap. In order to understand the effect of the harmonic potential on the Aharonov-Bohm results, the harmonic trap is added to the Hamiltonian of the lattice which becomes

$$\hat{H}_{\text{tb}} = -\sum_{\langle i,j \rangle} J(\hat{c}_i^\dagger \hat{c}_j + \text{h.c.}) + \kappa \sum_i \hat{c}_i^\dagger \hat{c}_i \; i^2. \tag{D.3}$$

The spring constant κ is defined as $\kappa = m\omega_r^2 d_L^2/2 = \text{h} \times 1.8 \; 10^{-4}J$, where ω_r is the radial harmonic trap frequency and $J \sim \text{h} \times 1.3$ kHz. The Hamiltonian is diagonalized to find the energy spectrum and the eigenstates of this system. With the discrete translational symmetry broken, we can expect to find both delocalized states with a well-defined quasimomentum and localized states consisting of many quasimomentum components. Therefore, we look at the single-particle density of states (DOS) to check for the presence of a gap at the Dirac cones and to analyze the energy spectrum of the system. The DOS is $\text{DOS}(E) = N \sum_i \delta(E - E_i)$ and we normalize it to the total number of counts such that $\sum_i \text{DOS}(E_i) = 1$. The DOS is obtained numerically by binning the eigenvalues into small energy intervals. The results for system of $\sim$2400 lattice sites and $J = \text{h} \times 1.3$ kHz, as in the experimental realization, are presented in Fig. D.5. The graphs a-b show that a gap opens at the Dirac point due to the finite system's size in absence of a harmonic confinement and that the density of states resembles the one for the tight binding model of a honeycomb lattice, with van Hove singularities at $\pm J$ and the DOS approaches zero for $E \sim 0$ [126]. Note also the presence of zero energy modes in the spectrum due to finite system size. When the harmonic potential is added, the DOS does not drop to zero as in the non-trapped case. The spectrum, plot in Fig. D.5d, shows the presence of small gaps in proximity of $E = 0$ which appear due to the broken spatial symmetry of the potential. These gaps are at most $\sim \text{h} \times 15$ Hz for the trap parameters and the number of sites we used. Since the system size is smaller than the actual one, this value is giving us an order of magnitude for the value of the gaps opened by the broken translational symmetry. A very similar value is extracted for the lattice with an additional next-nearest neighbor hopping term, $J' = 0.1J$.

Since the harmonic potential is varying slowly compared to the lattice spacing, it is reasonable to assume that lattice is locally homogeneous. In order to better understand the effect of the harmonic trap, we therefore made use of local density approximation and compared the DOS calculated analytically with the numerical result. The local density of states of atoms in the trap corresponds locally to the density of states (LDS) of the homogeneous lattice, $\rho_0(E)$. The analytic form of ρ_0 for a hexagonal lattice can be found for example in [126]. The local density of states
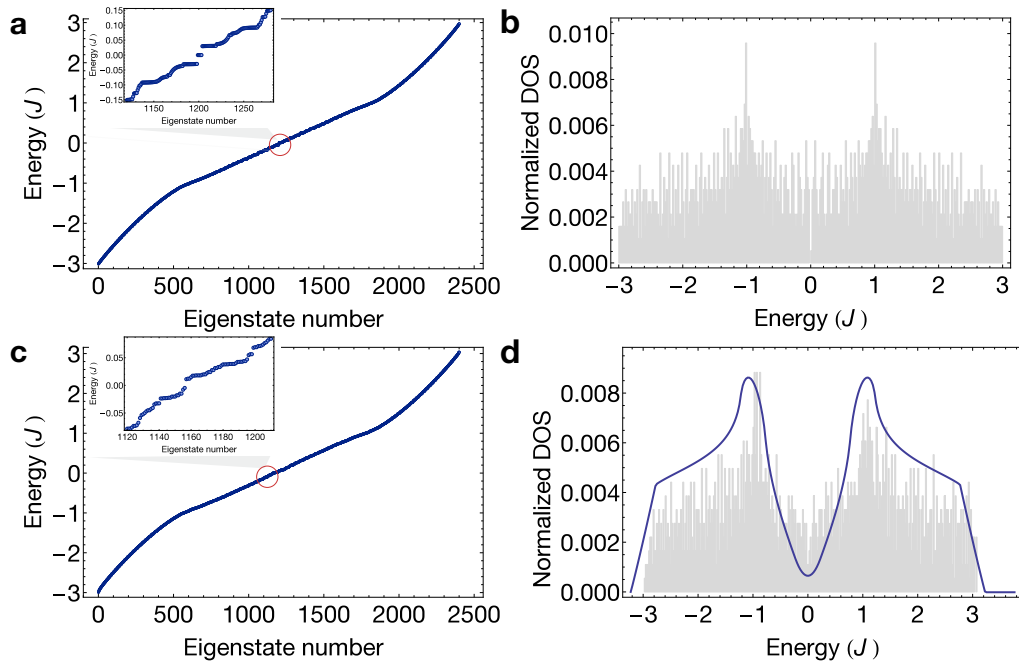
Figure D.5.: Single particle energy spectrum without (hard-wall boundary conditions) (**a**) and with harmonic trapping potential (**c**), calculated for ~ 2400 sites, $\Delta = 0$ and $J = \text{h} \times 1.3$ kHz. (**b**)-(**d**) corresponding DOS. In (**d**) the solid line is obtained by local density approximation, as explained in the text.

is solely shifted by the energy of the harmonic potential, $\rho_{\text{LDA}}(E, i) = \rho_0(E - \kappa i^2)$ and the global density of states is found by summing the local density of states over all lattice sites, $\text{DOS}_{\text{LDA}}(E) = N \sum_i \rho_{\text{LDA}}(E, i)$ where N is a normalization constant such that DOS is normalized to one and can be compared with the numerical results. The global DOS calculated with the local density approximation is shown in Fig. D.5d. Its behavior (solid line) is very similar to the one of the numerics: the DOS increases in the middle of the spectrum and no large gap is opened on a global scale. Similar results have been obtained in the following reference [252] where it is shown that local density approximation captures quite well the effect of a weak harmonic trapping potential, and moreover, that the characteristic spectrum survives locally in the trap, provided the confining potential varies over a length scale much larger than the extent of a unit cell. This is certainly our scenario given the small value of κ. To compare our results with the ones in [252], we also numerically estimated the radially averaged local density of states away from the trap center, defined as $\text{LDOS}(\mathbf{r}_i) = N \sum_n \sum_i |\psi_n(i)|^2 \delta(E - E_n)$, $\psi_n(i)$ being the nth eigenstate at position r_i. The LDOS calculated for 10, 20 and 50 sites away from the center of the harmonic potential is plotted in Fig. D.6. The behavior of the LDOS is in qualitative agreement with the one in [252]: the van Hoove singularities are
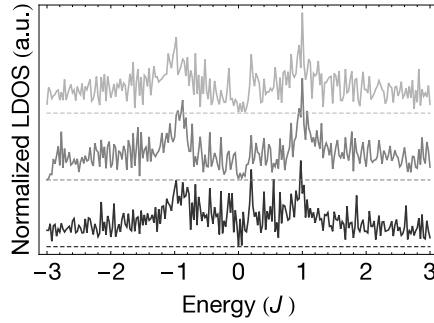
Figure D.6.: Normalized local density of states for 10, 20 and 50 sites away from the trap center, from light to dark gray respectively. Curves are shifted for visualization purposes, dashed lines represent the zero of the DOS for each set. The LDOS resembles the shape of the density of states of the homogeneous lattice case. At larger distances away from the center its features are smoothened.

smoothen and the shape of the DOS close to $E = 0$ starts to be modified only far away from the trap center. The binning of our numerics does not allow to extract a quantitative measure of the local energy gap between the two bands but it indicates the qualitative agreement with local density approximation, at least in the center of the harmonic trap where the density is highest.

To better visualize the effect of the harmonic trap, we also computed the Hamiltonian of eq. D.3 on a cylindrical geometry: we keep periodic-boundary conditions along x and open boundaries along y. The harmonic trapping potential is only along y. By doing so, we can still Fourier transform the creation and annihilation operators along the x-direction

$$\hat{c}_{x_j,y_j} = \frac{1}{N_x} \sum_{k_x} e^{-ik_x x} \hat{c}_{k_x,y_j} \tag{D.4}$$

while keeping open boundary conditions along y. By using this expansion for the operators $\hat{c}_{x_j,y_j}$, the tight binding Hamiltonian of the hexagonal lattice is rewritten as

$$\hat{H}_L = -J \sum_j (\hat{c}^\dagger_{k_x,2i} \hat{c}_{k_x,2i+1} + \text{h.c.}) - J \sum_j (\hat{c}^\dagger_{k_x,2i} \hat{c}_{k_x,2i-1} (e^{ik_x d_L/2} + e^{-ik_x d_L/2}) + \text{h.c.}) \tag{D.5}$$

where we made a distinction between even and odd sites to distinguish the A and B sites along the y-direction. This Hamiltonian is analogous to a zigzag chain for a graphene monolayer [111, 126]. The dispersion along k_x is directly found by diagonalizing such Hamiltonian with or without a harmonic potential of the kind $H_{ho} = \kappa \sum_i \hat{c}^\dagger_{k_x,i} \hat{c}_{k_x,i} \, i^2$. The results are illustrated in Fig. D.7. In absence of harmonic trap, the system has two distinct bands with edge modes at $E = 0$.
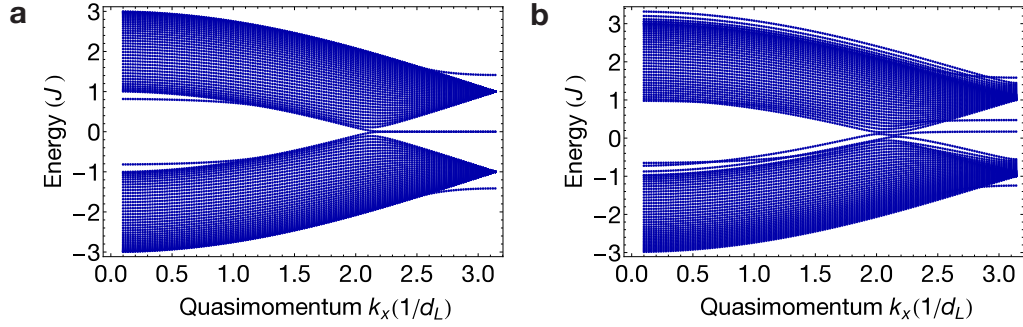
Figure D.7.: **(a)** Numerical results for a cylindrical geometry with 40 sites along x and without harmonic trap. When the trap is added **(b)**, the bands start to mix close to $E = 0$.

The larger the system size the denser the spectrum will become, approaching the tight binding limit of the hexagonal lattice with vanishing gap at the Dirac points $(k_x d_L = 2\pi/3)$. When the harmonic trap is added, the bands start to mix and small gaps open in proximity of $E = 0$. With increasing system size, the upper and lower bands will mix more, up to the point where there is no clear separation in energy between the two and many states will have energy close to zero, increasing the DOS in the middle of the spectrum. The results of this model qualitatively agree with what we see with the full numerics. The gaps we get in proximity of the Dirac point with our system size (~ 90 sites along the radial direction) are on the order of h×10 Hz with this model.

Bibliography

[1] J. B. Listing, "Vorstudien zur Topologie", Vandenhoeck und Ruprecht, Gttingen (1848) (cit. on p. 1).

[2] P. Wilson, *Curved Spaces: From Classical Geometries to Elementary Differential Geometry* (Cambridge University Press, 2007) (cit. on pp. 1, 7, 9).

[3] M. V. Berry, "Quantal Phase Factors Accompanying Adiabatic Changes", Proc. R. Soc. Lond. A **392**, 45–57 (1984) (cit. on pp. 1, 7, 9, 14, 18).

[4] R. Y. Chiao and Y.-S. Wu, "Manifestations of Berry's Topological Phase for the Photon", Phys. Rev. Lett. **57**, 933–936 (1986) (cit. on p. 1).

[5] P. G. Kwiat and R. Y. Chiao, "Observation of a nonclassical Berry's phase for the photon", Phys. Rev. Lett. **66**, 588–591 (1991) (cit. on p. 1).

[6] D. Suter, G. C. Chingas, R. A. Harris, and A. Pines, "Berry's phase in magnetic resonance", Molecular Physics **61**, 1327–1340 (1987) (cit. on p. 1).

[7] R. Tycko, "Adiabatic Rotational Splittings and Berry's Phase in Nuclear Quadrupole Resonance", Phys. Rev. Lett. **58**, 2281–2284 (1987) (cit. on p. 1).

[8] T. Bitter and D. Dubbers, "Manifestation of Berry's topological phase in neutron spin rotation", Phys. Rev. Lett. **59**, 251–254 (1987) (cit. on p. 1).

[9] W. P. Su, J. R. Schrieffer, and A. J. Heeger, "Solitons in Polyacetylene", Phys. Rev. Lett. **42**, 1698–1701 (1979) (cit. on pp. 1, 16).

[10] Y. Aharonov and D. Bohm, "Significance of Electromagnetic Potentials in the Quantum Theory", Phys. Rev. **115**, 485–491 (1959) (cit. on pp. 1, 10, 82).

[11] B. Simon, "Holonomy, the Quantum Adiabatic Theorem, and Berry's Phase", Phys. Rev. Lett. **51**, 2167–2170 (1983) (cit. on pp. 1, 10).

[12] F. Wilczek and A. Zee, "Appearance of Gauge Structure in Simple Dynamical Systems", Phys. Rev. Lett. **52**, 2111–2114 (1984) (cit. on pp. 1, 7, 10, 11).

[13] Y. Aharonov and J. Anandan, "Phase change during a cyclic quantum evolution", Phys. Rev. Lett. **58**, 1593–1596 (1987) (cit. on pp. 1, 10).

[14] D. J. Thouless, M. Kohmoto, M. P. Nightingale, and M. den Nijs, "Quantized Hall Conductance in a Two-Dimensional Periodic Potential", Phys. Rev. Lett. **49**, 405–408 (1982) (cit. on pp. 1, 2, 14, 15).

[15] K. von Klitzing, "The quantized Hall effect", Rev. Mod. Phys. **58**, 519–531 (1986) (cit. on p. 2).

[16] K. v. Klitzing, G. Dorda, and M. Pepper, "New Method for High-Accuracy Determination of the Fine-Structure Constant Based on Quantized Hall Resistance", Phys. Rev. Lett. **45**, 494–497 (1980) (cit. on p. 2).

[17] Y. Zhang, Y.-W. Tan, H. L. Stormer, and P. Kim, "Experimental observation of the quantum Hall effect and Berry's phase in graphene.", Nature **438**, 201–4 (2005) (cit. on pp. 2, 5, 21, 112).

[18] M. Z. Hasan and C. L. Kane, "Colloquium : Topological insulators", Rev. Mod. Phys. **82**, 3045–3067 (2010) (cit. on p. 2).

[19] X.-L. Qi and S.-C. Zhang, "Topological insulators and superconductors", Rev. Mod. Phys. **83**, 1057–1110 (2011) (cit. on p. 2).

[20] F. D. M. Haldane, "Model for a Quantum Hall Effect without Landau Levels: Condensed-Matter Realization of the Parity Anomaly", Phys. Rev. Lett. **61**, 2015–2018 (1988) (cit. on pp. 2–4, 40).

[21] C. L. Kane and E. J. Mele, "Quantum Spin Hall Effect in Graphene", Phys. Rev. Lett. **95**, 226801 (2005) (cit. on pp. 2, 15, 113).

[22] C. L. Kane and E. J. Mele, "Z_2 Topological Order and the Quantum Spin Hall Effect", Phys. Rev. Lett. **95**, 146802 (2005) (cit. on pp. 2, 4, 15, 113).

[23] B. A. Bernevig and S.-C. Zhang, "Quantum spin hall effect", Phys. Rev. Lett. **96**, 106802 (2006) (cit. on p. 2).

[24] M. König, S. Wiedmann, C. Brne, A. Roth, H. Buhmann, L. W. Molenkamp, X.-L. Qi, and S.-C. Zhang, "Quantum Spin Hall Insulator State in HgTe Quantum Wells", Science **318**, 766–770 (2007) (cit. on p. 2).

[25] D. C. Tsui, H. L. Stormer, and A. C. Gossard, "Two-dimensional magnetotransport in the extreme quantum limit", Phys. Rev. Lett. **48**, 1559–1562 (1982) (cit. on p. 2).

[26] R. B. Laughlin, "Anomalous quantum hall effect: an incompressible quantum fluid with fractionally charged excitations", Phys. Rev. Lett. **50**, 1395–1398 (1983) (cit. on p. 2).

[27] K. B. Davis, M. O. Mewes, M. R. Andrews, N. J. van Druten, D. S. Durfee, D. M. Kurn, and W. Ketterle, "Bose-Einstein Condensation in a Gas of Sodium Atoms", Phys. Rev. Lett. **75**, 3969–3973 (1995) (cit. on pp. 2, 45).

[28] M. H. Anderson, J. R. Ensher, M. R. Matthews, C. E. Wieman, and E. A. Cornell, "Observation of Bose-Einstein Condensation in a Dilute Atomic Vapor", Science **269**, 198–201 (1995) (cit. on pp. 2, 45).

[29] M. R. Matthews, B. P. Anderson, P. C. Haljan, D. S. Hall, C. E. Wieman, and E. A. Cornell, "Vortices in a Bose-Einstein Condensate", Phys. Rev. Lett. **83**, 2498–2501 (1999) (cit. on p. 2).

[30] K. W. Madison, F. Chevy, W. Wohlleben, and J. Dalibard, "Vortex Formation in a Stirred Bose-Einstein Condensate", Phys. Rev. Lett. **84**, 806–809 (2000) (cit. on p. 2).

[31] M. R. Andrews, D. M. Kurn, H.-J. Miesner, D. S. Durfee, C. G. Townsend, S. Inouye, and W. Ketterle, "Propagation of Sound in a Bose-Einstein Condensate", Phys. Rev. Lett. **79**, 553–556 (1997) (cit. on p. 2).

[32] D. M. Stamper-Kurn, A. P. Chikkatur, A. Görlitz, S. Inouye, S. Gupta, D. E. Pritchard, and W. Ketterle, "Excitation of Phonons in a Bose-Einstein Condensate by Light Scattering", Phys. Rev. Lett. **83**, 2876–2879 (1999) (cit. on p. 2).

[33] B. DeMarco and D. S. Jin, "Onset of Fermi Degeneracy in a Trapped Atomic Gas", Science **285**, 1703–1706 (1999) (cit. on p. 2).

[34] S. Inouye, M. R. Andrews, J. Stenger, H.-J. Miesner, D. M. Stamper-Kurn, and W. Ketterle, "Observation of Feshbach resonances in a Bose-Einstein condensate", Nature **392**, 151–154 (1998) (cit. on p. 2).

[35] C. Chin, R. Grimm, P. Julienne, and E. Tiesinga, "Feshbach resonances in ultracold gases", Rev. Mod. Phys. **82**, 1225–1286 (2010) (cit. on pp. 2, 50).

[36] Z. Hadzibabic, P. Krüger, M. Cheneau, B. Battelier, and J. Dalibard, "Berezinskii-Kosterlitz-Thouless crossover in a trapped atomic gas", Nature **441**, 1118–1121 (2006) (cit. on p. 2).

[37] I. Bloch, J. Dalibard, and W. Zwerger, "Many-body physics with ultracold gases", Rev. Mod. Phys. **80**, 885–964 (2008) (cit. on pp. 2, 29).

[38] D. Jaksch, C. Bruder, J. I. Cirac, C. W. Gardiner, and P. Zoller, "Cold Bosonic Atoms in Optical Lattices", Phys. Rev. Lett. **81**, 3108–3111 (1998) (cit. on p. 3).

[39] M. Greiner, O. Mandel, T. Esslinger, T. W. Hänsch, and I. Bloch, "Quantum phase transition from a superfluid to a Mott insulator in a gas of ultracold atoms", Nature **415**, 39–44 (2002) (cit. on p. 3).

[40] B. Paredes, A. Widera, V. Murg, O. Mandel, S. Flling, I. Cirac, G. V. Shlyapnikov, T. W. Hnsch, and I. Bloch, "Tonks-Girardeau gas of ultracold atoms in an optical lattice", Nature **429**, 277 (2004) (cit. on p. 3).

[41] T. Kinoshita, T. Wenger, and D. S. Weiss, "Observation of a One-Dimensional Tonks-Girardeau Gas", Science **305**, 1125–1128 (2004) (cit. on p. 3).

[42] U. Schneider, L. Hackermller, S. Will, T. Best, I. Bloch, T. A. Costi, R. W. Helmes, D. Rasch, and A. Rosch, "Metallic and Insulating Phases of Repulsively Interacting Fermions in a 3D Optical Lattice", Science **322**, 1520–1525 (2008) (cit. on p. 3).

[43] R. Jördens, N. Strohmaier, K. Günter, H. Moritz, and T. Esslinger, "A Mott insulator of fermionic atoms in an optical lattice", Nature **455**, 204–207 (2008) (cit. on p. 3).

[44] J. Billy, V. Josse, Z. Zuo, A. Bernard, B. Hambrecht, P. Lugan, D. Clément, L. Sanchez-Palencia, P. Bouyer, and A. Aspect, "Direct observation of Anderson localization of matter waves in a controlled disorder", Nature **453**, 891–894 (2008) (cit. on p. 3).

[45] T Lahaye, C Menotti, L Santos, M Lewenstein, and T Pfau, "The physics of dipolar bosonic quantum gases", Reports on Progress in Physics **72**, 126401 (2009) (cit. on p. 3).

[46] J. G. Danzl, E. Haller, M. Gustavsson, M. J. Mark, R. Hart, N. Bouloufa, O. Dulieu, H. Ritsch, and H.-C. Ngerl, "Quantum Gas of Deeply Bound Ground State Molecules", Science **321**, 1062–1066 (2008) (cit. on p. 3).

[47] K.-K. Ni, S. Ospelkaus, M. H. G. de Miranda, A. Pe'er, B. Neyenhuis, J. J. Zirbel, S. Kotochigova, P. S. Julienne, D. S. Jin, and J. Ye, "A High Phase-Space-Density Gas of Polar Molecules", Science **322**, 231–235 (2008) (cit. on p. 3).

[48] M. Aidelsburger, M. Atala, S. Nascimbène, S. Trotzky, Y.-A. Chen, and I. Bloch, "Experimental Realization of Strong Effective Magnetic Fields in an Optical Lattice", Phys. Rev. Lett. **107**, 255301 (2011) (cit. on p. 3).

[49] M. Aidelsburger, M. Atala, M. Lohse, J. T. Barreiro, B. Paredes, and I. Bloch, "Realization of the Hofstadter Hamiltonian with Ultracold Atoms in Optical Lattices", Phys. Rev. Lett. **111**, 185301 (2013) (cit. on p. 3).

[50] H. Miyake, G. A. Siviloglou, C. J. Kennedy, W. C. Burton, and W. Ketterle, "Realizing the Harper Hamiltonian with Laser-Assisted Tunneling in Optical Lattices", Phys. Rev. Lett. **111**, 185302 (2013) (cit. on p. 3).

[51] W. S. Bakr, J. I. Gillen, A. Peng, S. Fölling, and M. Greiner, "A quantum gas microscope for detecting single atoms in a Hubbard-regime optical lattice", Nature **462**, 74–77 (2009) (cit. on p. 3).

[52] J. F. Sherson, C. Weitenberg, M. Endres, M. Cheneau, I. Bloch, and S. Kuhr, "Single-atom-resolved fluorescence imaging of an atomic Mott insulator", Nature **467**, 68–72 (2010) (cit. on p. 3).

[53] W. S. Bakr, A. Peng, M. E. Tai, R. Ma, J. Simon, J. I. Gillen, S. Flling, L. Pollet, and M. Greiner, "Probing the SuperfluidtoMott Insulator Transition at the Single-Atom Level", Science **329**, 547–550 (2010) (cit. on p. 3).

[54] N. Gemelke, X. Zhang, C.-L. Hung, and C. Chin, "In situ observation of incompressible Mott-insulating domains in ultracold atomic gases.", Nature **460**, 995–998 (2009) (cit. on p. 3).

[55] G. Roati, E. de Mirandes, F. Ferlaino, H. Ott, G. Modugno, and M. Inguscio, "Atom Interferometry with Trapped Fermi Gases", Phys. Rev. Lett. **92**, 230402 (2004) (cit. on p. 3).

[56] Y. Shin, M. Saba, T. A. Pasquini, W. Ketterle, D. E. Pritchard, and A. E. Leanhardt, "Atom Interferometry with Bose-Einstein Condensates in a Double-Well Potential", Phys. Rev. Lett. **92**, 050405 (2004) (cit. on p. 3).

[57] D. A. Abanin, T. Kitagawa, I. Bloch, and E. Demler, "Interferometric Approach to Measuring Band Topology in 2D Optical Lattices", Phys. Rev. Lett. **110**, 165304 (2013) (cit. on pp. 3–5, 81, 83, 102, 111, 113).

[58] M. Atala, M. Aidelsburger, J. T. Barreiro, D. Abanin, T. Kitagawa, E. Demler, and I. Bloch, "Direct measurement of the Zak phase in topological Bloch bands", Nature Physics **9**, 795–800 (2013) (cit. on pp. 3–5, 14, 81, 83, 111).

[59] P. T. Ernst, S. Gotze, J. S. Krauser, K. Pyka, D.-S. Luhmann, D. Pfannkuche, and K. Sengstock, "Probing superfluids in optical lattices by momentum-resolved Bragg spectroscopy", Nat Phys **6**, 56–61 (2010) (cit. on p. 3).

[60] A. S. Sørensen, E. Demler, and M. D. Lukin, "Fractional Quantum Hall States of Atoms in Optical Lattices", Phys. Rev. Lett. **94**, 086803 (2005) (cit. on p. 3).

[61] N. R. Cooper and J. Dalibard, "Reaching Fractional Quantum Hall States with Optical Flux Lattices", Phys. Rev. Lett. **110**, 185301 (2013) (cit. on p. 3).

[62] S. Raghu, X.-L. Qi, C. Honerkamp, and S.-C. Zhang, "Topological Mott Insulators", Phys. Rev. Lett. **100**, 156401 (2008) (cit. on pp. 3, 113).

[63] V. Bretin, S. Stock, Y. Seurin, and J. Dalibard, "Fast Rotation of a Bose-Einstein Condensate", Phys. Rev. Lett. **92**, 050403 (2004) (cit. on p. 3).

[64] F. Gerbier and J. Dalibard, "Gauge fields for ultracold atoms in optical superlattices", New Journal of Physics **12**, 033007 (2010) (cit. on pp. 3, 4, 16).

[65] J. Dalibard, F. Gerbier, G. Juzeliūnas, and P. Öhberg, "Colloquium: Artificial gauge potentials for neutral atoms", Rev. Mod. Phys. **83**, 1523–1543 (2011) (cit. on pp. 3, 117).

[66] N. Goldman, G. Juzeliūnas, P. Öhberg, and I. B. Spielman, "Light-induced gauge fields for ultracold atoms", Reports on Progress in Physics **77**, 126401 (2014) (cit. on p. 3).

[67] Y.-J. Lin, R. L. Compton, K. Jiménez-García, J. V. Porto, and I. B. Spielman, "Synthetic magnetic fields for ultracold neutral atoms", Nature **462**, 628–632 (2009) (cit. on p. 3).

[68] N. Cooper, "Optical Flux Lattices for Ultracold Atomic Gases", Phys. Rev. Lett. **106**, 175301 (2011) (cit. on pp. 3, 34, 65, 112, 117).

[69] A. Celi, P. Massignan, J. Ruseckas, N. Goldman, I. Spielman, G. Juzeliūnas, and M. Lewenstein, "Synthetic Gauge Fields in Synthetic Dimensions", Phys. Rev. Lett. **112**, 043001 (2014) (cit. on p. 3).

[70] Y.-J. Lin, K. Jiménez-García, and I. B. Spielman, "Spin-orbit-coupled Bose-Einstein condensates", Nature **471**, 83–86 (2011) (cit. on p. 3).

[71] M. Beeler, R. Williams, K. Jiménez-García, L. J. Leblanc, A. R. Perry, and I. B. Spielman, "The spin Hall effect in a quantum gas", Nature **498**, 201–204 (2013) (cit. on p. 3).

[72] B. Stuhl, H. Lu, L. Aycock, D. Genkina, and I. Spielman, "Visualizing edge states with an atomic Bose gas in the quantum Hall regime", ArXiv e-prints (2015) (cit. on p. 3).

[73] M. Mancini, G. Pagano, G. Cappellini, L. Livi, M. Rider, J. Catani, C. Sias, P. Zoller, M. Inguscio, M. Dalmonte, and L. Fallani, "Observation of chiral edge states with neutral fermions in synthetic Hall ribbons", ArXiv e-prints (2015) (cit. on p. 3).

[74] T. Kitagawa, E. Berg, M. Rudner, and E. Demler, "Topological characterization of periodically driven quantum systems", Phys. Rev. B **82**, 235114 (2010) (cit. on pp. 3, 102, 112).

[75] A. Hemmerich, "Effective time-independent description of optical lattices with periodic driving", Phys. Rev. A **81**, 063626 (2010) (cit. on p. 3).

[76] N. Goldman and J. Dalibard, "Periodically Driven Quantum Systems: Effective Hamiltonians and Engineered Gauge Fields", Physical Review X **4**, 031027, 031027 (2014) (cit. on pp. 3, 112).

[77] J. Struck, C. Ölschläger, M. Weinberg, P. Hauke, J. Simonet, A. Eckardt, M. Lewenstein, K. Sengstock, and P. Windpassinger, "Tunable Gauge Potential for Neutral and Spinless Particles in Driven Optical Lattices", Phys. Rev. Lett. **108**, 225304 (2012) (cit. on p. 4).

[78] D. Jaksch and P. Zoller, "Creation of effective magnetic fields in optical lattices: the Hofstadter butterfly for cold neutral atoms", New Journal of Physics **5**, 56 (2003) (cit. on p. 4).

[79]   M. Atala, M. Aidelsburger, M. Lohse, J. T. Barreiro, B. Paredes, and I. Bloch, "Observation of chiral currents with ultracold atoms in bosonic ladders", Nature Physics **10**, 588–593 (2014) (cit. on p. 4).

[80]   D. R. Hofstadter, "Energy levels and wave functions of Bloch electrons in rational and irrational magnetic fields", Phys. Rev. B **14**, 2239–2249 (1976) (cit. on p. 4).

[81]   M. Aidelsburger, M. Lohse, C. Schweitzer, M. Atala, J. Barreiro, N. Cooper, I. Bloch, and N. Goldman, "Measuring the Chern number of Hofstadter bands with ultracold bosonic atoms", Nat Phys (cit. on pp. 4, 112).

[82]   G. Jotzu, M. Messer, R. Desbuquois, M. Lebrat, T. Uehlinger, D. Greif, and T. Esslinger, "Experimental realization of the topological Haldane model with ultracold fermions", Nature **515**, 237–240 (2014) (cit. on pp. 4, 40, 74, 102, 112).

[83]   N. Levy, S. A. Burke, K. L. Meaker, M. Panlasigui, A. Zettl, F. Guinea, A. H. C. Neto, and M. F. Crommie, "Strain-Induced PseudoMagnetic Fields Greater Than 300 Tesla in Graphene Nanobubbles", Science **329**, 544–547 (2010) (cit. on pp. 4, 112).

[84]   B. Tian, M. Endres, and D. Pekker, "Landau levels in strained optical lattices", ArXiv e-prints (2015) (cit. on pp. 4, 112).

[85]   H. Price and N. Cooper, "Mapping the Berry curvature from semiclassical dynamics in optical lattices", Phys. Rev. A **85**, 1–12 (2012) (cit. on p. 4).

[86]   A. Dauphin and N. Goldman, "Extracting the Chern Number from the Dynamics of a Fermi Gas: Implementing a Quantum Hall Bar for Cold Atoms", Phys. Rev. Lett. **111**, 135302 (2013) (cit. on pp. 4, 109).

[87]   P. Hauke, M. Lewenstein, and A. Eckardt, "Tomography of Band Insulators from Quench Dynamics", Phys. Rev. Lett. **113**, 045303 (2014) (cit. on pp. 4, 109).

[88]   M. Killi, S. Trotzky, and A. Paramekanti, "Anisotropic quantum quench in the presence of frustration or background gauge fields: A probe of bulk currents and topological chiral edge modes", Phys. Rev. A **86**, 063632 (2012) (cit. on pp. 4, 109).

[89]   P. Delplace, D. Ullmo, and G. Montambaux, "Zak phase and the existence of edge states in graphene", Phys. Rev. B **84**, 195452 (2011) (cit. on p. 4).

[90]   N. Goldman, J. Dalibard, A. Dauphin, F. Gerbier, M. Lewenstein, P. Zoller, and I. B. Spielman, "Direct imaging of topological edge states in cold-atom systems", Proceedings of the National Academy of Science **110**, 6736–6741 (2013) (cit. on p. 4).

[91] K. K. Gomes, W. Mar, W. Ko, F. Guinea, and H. C. Manoharan, *Designer Dirac fermions and topological phases in molecular graphene*, 2012 (cit. on p. 4).

[92] M. C. Rechtsman, Y. Plotnik, J. M. Zeuner, D. Song, Z. Chen, A. Szameit, and M. Segev, "Topological Creation and Destruction of Edge States in Photonic Graphene", Phys. Rev. Lett. **111**, 103901 (2013) (cit. on pp. 4, 112).

[93] T. Jacqmin, I. Carusotto, I. Sagnes, M. Abbarchi, D. D. Solnyshkov, G. Malpuech, E. Galopin, A. Lemaître, J. Bloch, and A. Amo, "Direct Observation of Dirac Cones and a Flatband in a Honeycomb Lattice for Polaritons", Phys. Rev. Lett. **112**, 116402 (2014) (cit. on p. 4).

[94] P. Soltan Panahi, J. Struck, P. Hauke, A. Bick, W. Plenkers, G. Meineke, C. Becker, P. Windpassinger, M. Lewenstein, and K. Sengstock, "Multicomponent quantum gases in spin-dependent hexagonal lattices", Nature Physics **7**, 434–440 (2011) (cit. on pp. 4, 113).

[95] D. S. Lühmann, O. Jürgensen, M. Weinberg, J. Simonet, P. Soltan-Panahi, and K. Sengstock, "Quantum phases in tunable state-dependent hexagonal optical lattices", Phys. Rev. A **90**, 013614 (2014) (cit. on pp. 4, 34, 63, 113).

[96] I. Vasić, A. Petrescu, K. Le Hur, and W. Hofstetter, "Chiral bosonic phases on the Haldane honeycomb lattice", Phys. Rev. B **91**, 094502 (2015) (cit. on pp. 4, 63, 113).

[97] P. Dietl, F. Piéchon, and G. Montambaux, "New Magnetic Field Dependence of Landau Levels in a Graphenelike Structure", Phys. Rev. Lett. **100**, 236405 (2008) (cit. on pp. 4, 25).

[98] T. Oka and H. Aoki, "Photovoltaic Hall effect in graphene", Phys. Rev. B **79**, 081406 (2009) (cit. on p. 4).

[99] T. Kitagawa, T. Oka, A. Brataas, L. Fu, and E. Demler, "Transport properties of nonequilibrium systems under the application of light: Photoinduced quantum Hall insulators without Landau levels", Phys. Rev. B **84**, 235108 (2011) (cit. on p. 4).

[100] Y. Liu, G. Bian, T. Miller, and T.-C. Chiang, "Visualizing Electronic Chirality and Berry Phases in Graphene Systems Using Photoemission with Circularly Polarized Light", Phys. Rev. Lett. **107**, 166803 (2011) (cit. on pp. 5, 112).

[101] C. Hwang, C.-H. Park, D. A. Siegel, A. V. Fedorov, S. G. Louie, and A. Lanzara, "Direct measurement of quantum phases in graphene via photoemission spectroscopy", Phys. Rev. B **84**, 125422 (2011) (cit. on pp. 5, 112).

[102] K. S. Novoselov, A. K. Geim, S. V. Morozov, D Jiang, M. I. Katsnelson, I. V. Grigorieva, S. V. Dubonos, and A. A. Firsov, "Two-dimensional gas of massless Dirac fermions in graphene.", Nature **438**, 197–200 (2005) (cit. on pp. 5, 21, 112).

[103] B Wunsch, F Guinea, and F Sols, "Dirac-point engineering and topological phase transitions in honeycomb optical lattices", New Journal of Physics **10**, 103027 (2008) (cit. on p. 5).

[104] G. Montambaux, F. Piéchon, J.-N. Fuchs, and M. O. Goerbig, "Merging of Dirac points in a two-dimensional crystal", Phys. Rev. B **80**, 153412 (2009) (cit. on pp. 5, 25).

[105] A. Zenesini, D. Ciampini, O. Morsch, and E. Arimondo, "Observation of Stückelberg oscillations in accelerated optical lattices", Phys. Rev. A **82**, 065601 (2010) (cit. on pp. 5, 103, 104).

[106] S. Shevchenko, S. Ashhab, and F. Nori, "Landau Zener Stueckelberg interferometry", Physics Reports **492**, 1–30 (2010) (cit. on pp. 5, 103).

[107] F. Grusdt, D. Abanin, and E. Demler, "Measuring $\mathbb{Z}_2$ topological invariants in optical lattices using interferometry", Phys. Rev. A **89**, 043621 (2014) (cit. on pp. 5, 15, 102, 109, 113).

[108] A. Shapere and F. Wilczek, *Advanced Series in Mathematical Physics: Volume 5, Geometric Phases in Physics* (World Scientific, Singapore, 1989) (cit. on p. 7).

[109] J. W. Zwanziger, M Koenig, and A Pines, "Berry's Phase", Annual Review of Physical Chemistry **41**, 601–646 (1990) (cit. on p. 7).

[110] S. Kobayashi and K. Nomizu, *Foundations of Differential Geometry*, v. 1 () (cit. on p. 7).

[111] B. Bernevig and T. Hughes, *Topological Insulators and Topological Superconductors* (Princeton University Press, 2013) (cit. on pp. 7, 15, 133).

[112] F. Wilczek and A. Shapere, *Geometric Phases in Physics*, Advanced series in mathematical physics (World Scientific, 1989) (cit. on pp. 7, 8).

[113] J. Sakurai and J. Napolitano, *Modern Quantum Mechanics* (Addison-Wesley, 2011) (cit. on p. 9).

[114] R. G. Chambers, "Shift of an Electron Interference Pattern by Enclosed Magnetic Flux", Phys. Rev. Lett. **5**, 3–5 (1960) (cit. on p. 10).

[115] A. Tonomura, N. Osakabe, T. Matsuda, T. Kawasaki, J. Endo, S. Yano, and H. Yamada, "Evidence for Aharonov-Bohm effect with magnetic field completely shielded from electron wave", Phys. Rev. Lett. **56**, 792–795 (1986) (cit. on p. 10).

[116] Y. Makeenko, "Brief introduction to Wilson loops and large N", Physics of Atomic Nuclei **73**, 878–894 (2010) (cit. on p. 11).

[117] N. W. Ashcroft and N. D. Mermin, *Solid State Physics* (Saunders College Publications, 1976) (cit. on p. 12).

[118] G. H. Wannier, "The Structure of Electronic Excitation Levels in Insulating Crystals", Phys. Rev. **52**, 191–197 (1937) (cit. on p. 13).

[119] W. Kohn, "Construction of Wannier Functions and Applications to Energy Bands", Phys. Rev. B **7**, 4388–4398 (1973) (cit. on p. 13).

[120] D. Xiao, M.-C. Chang, and Q. Niu, "Berry phase effects on electronic properties", Rev. Mod. Phys. **82**, 1959–2007 (2010) (cit. on pp. 14, 39).

[121] J. Zak, "Berry's phase for energy bands in solids", Phys. Rev. Lett. **62**, 2747–2750 (1989) (cit. on p. 14).

[122] L. Fu and C. L. Kane, "Time reversal polarization and a Z_2 adiabatic spin pump", Phys. Rev. B **74**, 195312 (2006) (cit. on pp. 15, 113).

[123] D. N. Sheng, Z. Y. Weng, L. Sheng, and F. D. M. Haldane, "Quantum Spin-Hall Effect and Topologically Invariant Chern Numbers", Phys. Rev. Lett. **97**, 036808 (2006) (cit. on p. 15).

[124] R. Yu, X. L. Qi, A. Bernevig, Z. Fang, and X. Dai, "Equivalent expression of $\mathbb{Z}_2$ topological invariant for band insulators using the non-Abelian Berry connection", Phys. Rev. B **84**, 075119 (2011) (cit. on p. 15).

[125] D. R. Yarkony, "Diabolical conical intersections", Rev. Mod. Phys. **68**, 985–1013 (1996) (cit. on p. 16).

[126] A. H. Castro Neto, F. Guinea, N. M. R. Peres, K. S. Novoselov, and A. K. Geim, "The electronic properties of graphene", Rev. Mod. Phys. **81**, 109–162 (2009) (cit. on pp. 16, 18, 21, 41, 112, 131, 133).

[127] D. P. DiVincenzo and E. J. Mele, "Self-consistent effective-mass theory for intralayer screening in graphite intercalation compounds", Phys. Rev. B **29**, 1685–1694 (1984) (cit. on p. 21).

[128] V. P. Gusynin and S. G. Sharapov, "Unconventional Integer Quantum Hall Effect in Graphene", Phys. Rev. Lett. **95**, 146801 (2005) (cit. on p. 21).

[129] G. W. Semenoff, "Condensed-Matter Simulation of a Three-Dimensional Anomaly", Phys. Rev. Lett. **53**, 2449–2452 (1984) (cit. on p. 21).

[130] J. Ibañez Azpiroz, A. Eiguren, A. Bergara, G. Pettini, and M. Modugno, "Self-consistent tight-binding description of Dirac points moving and merging in two-dimensional optical lattices", Phys. Rev. A **88**, 033631 (2013) (cit. on p. 25).

[131] H. J. Metcalf and P. van der Straten, *Laser Cooling and Trapping* (Springer, 2.edition, 2002) (cit. on pp. 30, 52).

[132] C. Cohen-Tannoudji, J. Dupont-Roc, and G. Grynberg, *Atom-photon interactions: basic processes and applications*, Wiley-Interscience publication (J. Wiley, 1992) (cit. on p. 30).

[133] J. Dalibard and C. Cohen-Tannoudji, "Dressed-atom approach to atomic motion in laser light: the dipole force revisited", J. Opt. Soc. Am. B **2**, 1707–1720 (1985) (cit. on p. 30).

[134] R. Grimm, M. Weidemüller, and Y. B. Ovchinnikov, "Optical Dipole Traps for Neutral Atoms", Advances in Atomic Molecular and Optical Physics **42**, 95–170 (2000) (cit. on p. 30).

[135] N. R. Cooper and J. Dalibard, "Optical flux lattices for two-photon dressed states", EPL (Europhysics Letters) **95**, 66004 (2011) (cit. on pp. 34, 112).

[136] S. K. Baur, M. H. Schleier-Smith, and N. R. Cooper, "Dynamic optical superlattices with topological bands", Phys. Rev. A **89**, 051605 (2014) (cit. on pp. 34, 112).

[137] N. Marzari, A. A. Mostofi, J. R. Yates, I. Souza, and D. Vanderbilt, "Maximally localized Wannier functions: Theory and applications", Rev. Mod. Phys. **84**, 1419–1475 (2012) (cit. on pp. 38, 39).

[138] E. Blount, *Formalisms of band theory*, edited by F. Seitz and D. Turnbull, Vol. 13, Solid State Physics (Academic Press, 1962), pp. 305 –373 (cit. on p. 39).

[139] R. D. King Smith and D. Vanderbilt, "Theory of polarization of crystalline solids", Phys. Rev. B **47**, 1651–1654 (1993) (cit. on p. 39).

[140] V. Pereira, A. Castro Neto, and N. Peres, "Tight-binding approach to uniaxial strain in graphene", Phys. Rev. B **80**, 045401 (2009) (cit. on pp. 41, 112).

[141] L. Tarruell, D. Greif, T. Uehlinger, G. Jotzu, and T. Esslinger, "Creating, moving and merging Dirac points with a Fermi gas in a tunable honeycomb lattice.", Nature **483**, 302–5 (2012) (cit. on p. 41).

[142] C. J. Pethick and H. Smith, *Bose Einstein Condensation in Dilute Gases* (Cambridge University Press, Cambridge, 2001) (cit. on pp. 45, 47, 54, 60, 119, 120).

[143] L. P. Pitaevskii and S. Stringari, *Bose Einstein Condensation* (Clarendon Press, Oxford, 2003) (cit. on pp. 45, 48, 60, 78, 119, 121).

[144] W. Ketterle and M. Zwierlein, "Making, probing and understanding ultracold Fermi gases", Nuovo Cimento Rivista Serie **31**, 247–422 (2008) (cit. on pp. 45, 46, 48, 60, 119).

[145] T. Best, "Interacting Bose-Fermi mixtures in optical lattices", PhD thesis (Johannes Gutenberg-Universität Mainz, 2011) (cit. on p. 45).

[146] G. Roati, "Quantum degenerate Potassium-Rubidium mixtures", PhD thesis (Universitá degli studi di Trento, 2003) (cit. on p. 45).

[147] T. Rom, "Bosonische und fermionische Quantengase in dreidimensionalen optischen Gittern: Präparation, Manipulation und Analyse", PhD thesis (Ludwig-Maximilian-Universität München, 2009) (cit. on pp. 45, 58).

[148] U. Schneider, "Interacting Fermionic Atoms in Optical Lattices - A Quantum Simulator for Condensed Matter Physics", PhD thesis (Johannes Gutenberg-Universität Mainz, 2010) (cit. on p. 45).

[149] S. Will, "Interacting bosons and fermions in three-dimensional optical lattice potentials", PhD thesis (Johannes Gutenberg-Universität Mainz, 2011) (cit. on p. 45).

[150] T. Li, "An Apparatus for Probing Fermions in a Quasi-Two-Dimensional Geometry", Master's thesis (Ludwig-Maximilians-Universität München, 2011) (cit. on pp. 45, 50, 52, 54).

[151] M. Boll, "A 2D+ -3D MOT system for producing laser-cooled K-Rb mixtures", Master's thesis (Ludwig-Maximilians-Universität München, Johannes Gutenberg Universität Mainz, 2011) (cit. on pp. 45, 51, 53).

[152] M. Reitter, "Ultracold Fermions in a novel 2D setup", Master's thesis (Ludwig-Maximilians-Universität München, 2012) (cit. on pp. 45, 51, 53, 56).

[153] K. Huang, *Statistical Mechanics* (John Wiley & Sons, 2nd edition, 1987) (cit. on p. 45).

[154] A. Fetter and J. Walecka, *Quantum Theory of Many-Particle Systems* (Dover Publications, 2003) (cit. on p. 45).

[155] S. N. Bose, "Plancks Gesetz und Lichtquantenhypothese", Z. Physik **26**, 178181 (1924) (cit. on pp. 45, 46).

[156] A. Einstein, "Quantentheorie des einatomigen idealen Gases", Sitzungsber. Preuss. Akad. Wiss., phys.-math **23**, 114 (1925) (cit. on pp. 45, 46).

[157] E. Fermi, "Sulla quantizzazione del gas perfetto monoatomico", Rend. Lincei **3**, 145–149 (1926) (cit. on p. 45).

[158] P. A. M. Dirac, "On the Theory of Quantum Mechanics", Proceedings of the Royal Society of London A: Mathematical, Physical and Engineering Sciences **112**, 661–677 (1926) (cit. on p. 45).

[159] D. A. Butts and D. S. Rokhsar, "Trapped Fermi gases", Phys. Rev. A **55**, 4346–4350 (1997) (cit. on pp. 46, 119).

[160] Y. Castin, "Basic theory tools for degenerate Fermi gases", Proceedings of the Enrico Fermi Varenna School on Fermi gases (2007) (cit. on pp. 46, 48).

[161] A. J. Leggett, "Bose-Einstein condensation in the alkali gases: Some fundamental concepts", Rev. Mod. Phys. **73**, 307–356 (2001) (cit. on p. 46).

[162] F. Schwabl, *Quantum Mechanics* (Springer Berlin Heidelberg, 2007) (cit. on p. 47).

[163] J. Weiner, V. S. Bagnato, S. Zilio, and P. S. Julienne, "Experiments and theory in cold and ultracold collisions", Rev. Mod. Phys. **71**, 1–85 (1999) (cit. on p. 47).

[164] F. Dalfovo, S. Giorgini, L. P. Pitaevskii, and S. Stringari, "Theory of Bose-Einstein condensation in trapped gases", Rev. Mod. Phys. **71**, 463–512 (1999) (cit. on pp. 48, 49).

[165] S. Stringari, C. Wieman, and S. italiana di fisica, *Bose-Einstein Condensation in Atomic Gases: Proceedings of the International School of Physics "Enrico Fermi", Varenna on Lake Como, Villa Monastero, 7-17 July 1998*, Bose-Einstein Condensation in Atomic Gases (IOS Press, 1999) (cit. on p. 48).

[166] L. P. Pitaevskii, "Vortex lines in an imperfect bose gas", Soviet Physics JETP-USSR **13** (1961) (cit. on p. 48).

[167] E. Gross, "Structure of a quantized vortex in boson systems", Il Nuovo Cimento Series 10 **20**, 454–477 (1961) (cit. on p. 48).

[168] N. Bogoliubov, "On the theory of superfluidity", J. Phys. **11**, 2332 (1947) (cit. on p. 48).

[169] C. Raman, M. Köhl, R. Onofrio, D. S. Durfee, C. E. Kuklewicz, Z. Hadzibabic, and W. Ketterle, "Evidence for a Critical Velocity in a Bose-Einstein Condensed Gas", Phys. Rev. Lett. **83**, 2502–2505 (1999) (cit. on p. 49).

[170] H. Feshbach, "Unified theory of nuclear reactions", Annals of Physics **5**, 357–390 (1958) (cit. on p. 49).

[171] U. Fano, "Effects of Configuration Interaction on Intensities and Phase Shifts", Phys. Rev. **124**, 1866–1878 (1961) (cit. on p. 49).

[172] K. Goral, T. Khler, S. A. Gardiner, E. Tiesinga, and P. S. Julienne, "Adiabatic association of ultracold molecules via magnetic-field tunable interactions", Journal of Physics B: Atomic, Molecular and Optical Physics **37**, 3457 (2004) (cit. on p. 49).

[173] T. Köhler, K. Góral, and P. S. Julienne, "Production of cold molecules via magnetically tunable Feshbach resonances", Rev. Mod. Phys. **78**, 1311–1361 (2006) (cit. on p. 49).

[174] D. Steck, "Rubidium 85 D line data", Physics, 31 (2001) (cit. on p. 50).

[175] T. G. Tiecke, "Feshbach resonances in ultracold mixtures of the fermionic quantum gases ^{6}Li and ^{40}K", PhD thesis (University of Amsterdam, 2009) (cit. on p. 50).

[176] H. Hu, X.-J. Liu, and M. Modugno, "Expansion of a quantum degenerate boson-fermion mixture", Phys. Rev. A **67**, 063614 (2003) (cit. on p. 50).

[177] F. Ferlaino, C. D'Errico, G. Roati, M. Zaccanti, M. Inguscio, G. Modugno, and A. Simoni, "Erratum: Feshbach spectroscopy of a K-Rb atomic mixture [Phys. Rev. A 73, 040702 (2006)]", Phys. Rev. A **74**, 039903 (2006) (cit. on p. 50).

[178] G. Roati, F. Riboli, G. Modugno, and M. Inguscio, "Fermi-Bose Quantum Degenerate $^{40}K - ^{87}Rb$ Mixture with Attractive Interaction", Phys. Rev. Lett. **89**, 150403 (2002) (cit. on p. 50).

[179] E. G. M. van Kempen, S. J. J. M. F. Kokkelmans, D. J. Heinzen, and B. J. Verhaar, "Interisotope Determination of Ultracold Rubidium Interactions from Three High-Precision Experiments", Phys. Rev. Lett. **88**, 093201 (2002) (cit. on p. 50).

[180] A. Marte, T. Volz, J. Schuster, S. Dürr, G. Rempe, E. G. M. van Kempen, and B. J. Verhaar, "Feshbach Resonances in Rubidium 87: Precision Measurement and Analysis", Phys. Rev. Lett. **89**, 283202 (2002) (cit. on p. 50).

[181] P. A. Ruprecht, M. J. Holland, K. Burnett, and M. Edwards, "Time-dependent solution of the nonlinear Schrödinger equation for Bose-condensed trapped neutral atoms", Phys. Rev. A **51**, 4704–4711 (1995) (cit. on p. 50).

[182] J. L. Roberts, N. R. Claussen, S. L. Cornish, E. A. Donley, E. A. Cornell, and C. E. Wieman, "Controlled Collapse of a Bose-Einstein Condensate", Phys. Rev. Lett. **86**, 4211–4214 (2001) (cit. on p. 50).

[183] M. Zaccanti, C. D'Errico, F. Ferlaino, G. Roati, M. Inguscio, and G. Modugno, "Control of the interaction in a Fermi-Bose mixture", Phys. Rev. A **74**, 041605 (2006) (cit. on p. 50).

[184] S. Ospelkaus, C. Ospelkaus, L. Humbert, K. Sengstock, and K. Bongs, "Tuning of Heteronuclear Interactions in a Degenerate Fermi-Bose Mixture", Phys. Rev. Lett. **97**, 120403 (2006) (cit. on p. 50).

[185] J. L. Bohn, "Cooper pairing in ultracold ^{40}K using Feshbach resonances", Phys. Rev. A **61**, 053409 (2000) (cit. on p. 50).

[186] T. Loftus, C. A. Regal, C. Ticknor, J. L. Bohn, and D. S. Jin, "Resonant Control of Elastic Collisions in an Optically Trapped Fermi Gas of Atoms", Phys. Rev. Lett. **88**, 173201 (2002) (cit. on p. 50).

[187] C. A. Regal, C. Ticknor, J. L. Bohn, and D. S. Jin, "Tuning $p-$Wave Interactions in an Ultracold Fermi Gas of Atoms", Phys. Rev. Lett. **90**, 053201 (2003) (cit. on p. 50).

[188] L. Cook and T. Hanna, "^{40}K Feshbach Resonances - private communication", (cit. on pp. 50, 59).

[189] K. Dieckmann, R. J. C. Spreeuw, M. Weidemüller, and J. T. M. Walraven, "Two-dimensional magneto-optical trap as a source of slow atoms", Phys. Rev. A **58**, 3891–3895 (1998) (cit. on p. 53).

[190] J. Catani, P. Maioli, L. De Sarlo, F. Minardi, and M. Inguscio, "Intense slow beams of bosonic potassium isotopes", Phys. Rev. A **73**, 033415 (2006) (cit. on p. 53).

[191] S. Chaudhuri, S. Roy, and C. S. Unnikrishnan, "Realization of an intense cold Rb atomic beam based on a two-dimensional magneto-optical trap: Experiments and comparison with simulations", Phys. Rev. A **74**, 023406 (2006) (cit. on p. 53).

[192] W. Ketterle, K. B. Davis, M. A. Joffe, A. Martin, and D. E. Pritchard, "High densities of cold atoms in a *dark* spontaneous-force optical trap", Phys. Rev. Lett. **70**, 2253–2256 (1993) (cit. on p. 53).

[193] J. Weiner, V. S. Bagnato, S. Zilio, and P. S. Julienne, "Experiments and theory in cold and ultracold collisions", Rev. Mod. Phys. **71**, 1–85 (1999) (cit. on p. 53).

[194] L. G. Marcassa, G. D. Telles, S. R. Muniz, and V. S. Bagnato, "Collisional losses in a K-Rb cold mixture", Phys. Rev. A **63**, 013413 (2000) (cit. on p. 53).

[195] G. Modugno, C. Benkő, P. Hannaford, G. Roati, and M. Inguscio, "Sub-Doppler laser cooling of fermionic ^{40}K atoms", Phys. Rev. A **60**, R3373–R3376 (1999) (cit. on pp. 53, 63).

[196] M. Landini, S. Roy, L. Carcagní, D. Trypogeorgos, M. Fattori, M. Inguscio, and G. Modugno, "Sub-Doppler laser cooling of Potassium atoms", Phys. Rev. A **84**, 043432 (2011) (cit. on p. 53).

[197] D. R. Fernandes, F. Sievers, N. Kretzschmar, S. Wu, C. Salomon, and F. Chevy, "Sub-Doppler laser cooling of fermionic ^{40}K atoms in three-dimensional gray optical molasses", EPL (Europhysics Letters) **100**, 63001 (2012) (cit. on pp. 53, 63).

[198] M. Greiner, I. Bloch, O. Mandel, T. W. Hänsch, and T. Esslinger, "Exploring Phase Coherence in a 2D Lattice of Bose-Einstein Condensates", Phys. Rev. Lett. **87**, 160405 (2001) (cit. on pp. 54, 68, 70).

[199] E. Majorana and M. Inguscio, "Oriented atoms in a variable magnetic field", in *Ettore Majorana Scientific Papers*, edited by G. Bassani (Springer Berlin Heidelberg, 2006), pp. 113–136 (cit. on p. 54).

[200] M. Brown-Hayes and R. Onofrio, "Optimal cooling strategies for magnetically trapped atomic Fermi-Bose mixtures", Phys. Rev. A **70**, 063614 (2004) (cit. on p. 58).

[201] M. Schleier-Smith, "Private communication", (cit. on p. 59).

[202] E. Hecht, *Optics* (Addison-Wesley, 2002) (cit. on p. 62).

[203] C.-L. Hung, X. Zhang, L.-C. Ha, S.-K. Tung, N. Gemelke, and C. Chin, "Extracting densitydensity correlations from in situ images of atomic quantum gases", New Journal of Physics **13**, 075019 (2011) (cit. on p. 62).

[204] C.-L. Hung, X. Zhang, N. Gemelke, and C. Chin, "Accelerating evaporative cooling of atoms into Bose-Einstein condensation in optical traps", Phys. Rev. A **78**, 011604 (2008) (cit. on p. 63).

[205] Y.-J. Lin, A. R. Perry, R. L. Compton, I. B. Spielman, and J. V. Porto, "Rapid production of ^{87}Rb Bose-Einstein condensates in a combined magnetic and optical potential", Phys. Rev. A **79**, 063631 (2009) (cit. on p. 63).

[206] X. Li, S. S. Natu, A. Paramekanti, and S. Das Sarma, "Chiral spin superfluidity and spontaneous spin Hall effect of interacting bosons", ArXiv e-prints (2014) (cit. on pp. 63, 113).

[207] Jürgensen, O. and Sengstock, K. and Lühmann, D.-S., "Twisted complex superfluids in optical lattices", ArXiv e-prints (2015) (cit. on pp. 63, 113).

[208] T. A. Savard, K. M. O'Hara, and J. E. Thomas, "Laser-noise-induced heating in far-off resonance optical traps", Phys. Rev. A **56**, R1095–R1098 (1997) (cit. on pp. 67, 71).

[209] R. Jáuregui, N. Poli, G. Roati, and G. Modugno, "Anharmonic parametric excitation in optical lattices", Phys. Rev. A **64**, 033403 (2001) (cit. on pp. 67, 71).

[210] M. Prevedelli, T. Freegarde, and T. Hnsch, "Phase locking of grating tuned diode lasers", Appl. Phys. B, S241–S248 (1995) (cit. on p. 68).

[211] J. Bernardoff, "A setup for imprinting artifcial magnetic fields on ultracold atoms", Master's thesis (Ludwig-Maximilians-Universität München, 2013) (cit. on p. 68).

[212] F. Gerbier, A. Widera, S. Fölling, O. Mandel, T. Gericke, and I. Bloch, "Interference pattern and visibility of a Mott insulator", Phys. Rev. A **72**, 053606 (2005) (cit. on pp. 68, 69).

[213] F. Gerbier, S. Trotzky, S. Fölling, U. Schnorrberger, J. Thompson, A. Widera, I. Bloch, L. Pollet, M. Troyer, B. Capogrosso-Sansone, N. Prokof'ev, and B. Svistunov, "Expansion of a Quantum Gas Released from an Optical Lattice", Phys. Rev. Lett. **101**, 155303 (2008) (cit. on p. 68).

[214] P. L. Gould, G. A. Ruff, and D. E. Pritchard, "Diffraction of atoms by light: The near-resonant Kapitza-Dirac effect", Phys. Rev. Lett. **56**, 827–830 (1986) (cit. on p. 70).

[215] M. Ben Dahan, E. Peik, J. Reichel, Y. Castin, and C. Salomon, "Bloch Oscillations of Atoms in an Optical Potential", Phys. Rev. Lett. **76**, 4508–4511 (1996) (cit. on p. 72).

[216] E. Peik, M. Ben Dahan, I. Bouchoule, Y. Castin, and C. Salomon, "Bloch oscillations of atoms, adiabatic rapid passage, and monokinetic atomic beams", Phys. Rev. A **55**, 2989–3001 (1997) (cit. on p. 72).

[217] C. Zener, "Non-Adiabatic Crossing of Energy Levels", Proceedings of the Royal Society of London A: Mathematical, Physical and Engineering Sciences **137**, 696–702 (1932) (cit. on p. 77).

[218] L. D. Landau and E. M. Lifshitz, *Fluid Mechanics* (Oxford: Pergamon, 1987) (cit. on p. 78).

[219] B. Wu and Q. Niu, "Landau and dynamical instabilities of the superflow of Bose-Einstein condensates in optical lattices", Phys. Rev. A **64**, 061603 (2001) (cit. on pp. 78, 79).

[220] M. Machholm, C. J. Pethick, and H. Smith, "Band structure, elementary excitations, and stability of a Bose-Einstein condensate in a periodic potential", Phys. Rev. A **67**, 053613 (2003) (cit. on p. 78).

[221] L. Fallani, L. De Sarlo, J. E. Lye, M. Modugno, R. Saers, C. Fort, and M. Inguscio, "Observation of Dynamical Instability for a Bose-Einstein Condensate in a Moving 1D Optical Lattice", Phys. Rev. Lett. **93**, 140406 (2004) (cit. on pp. 78, 79).

[222] M. Modugno, C. Tozzo, and F. Dalfovo, "Role of transverse excitations in the instability of Bose-Einstein condensates moving in optical lattices", Phys. Rev. A **70**, 043625 (2004) (cit. on pp. 78, 79).

[223] O. Morsch and M. Oberthaler, "Dynamics of Bose-Einstein condensates in optical lattices", Rev. Mod. Phys. **78**, 179–215 (2006) (cit. on p. 78).

[224] L. Landau, E. Lifshits, and L. Pitaevskii, *Statistical Physics*, Course of theoretical physics pt. 2 (Pergamon Press, 1980) (cit. on p. 78).

[225] D. van Oosten, P. van der Straten, and H. T. C. Stoof, "Quantum phases in an optical lattice", Phys. Rev. A **63**, 053601 (2001) (cit. on p. 78).

[226] A. Smerzi, A. Trombettoni, P. G. Kevrekidis, and A. R. Bishop, "Dynamical Superfluid-Insulator Transition in a Chain of Weakly Coupled Bose-Einstein Condensates", Phys. Rev. Lett. **89**, 170402 (2002) (cit. on p. 79).

[227] M. Cristiani, O. Morsch, N. Malossi, M. Jona-Lasinio, M. Anderlini, E. Courtade, and E. Arimondo, "Instabilities of a Bose-Einstein condensate in a periodic potential: an experimental investigation", Opt. Express **12**, 4–10 (2004) (cit. on p. 79).

[228] F. S. Cataliotti, L Fallani, F Ferlaino, C Fort, P Maddaloni, and M Inguscio, "Superfluid current disruption in a chain of weakly coupled BoseEinstein condensates", New Journal of Physics **5**, 71 (2003) (cit. on p. 79).

[229] G. Roati, M. Zaccanti, C. D'Errico, J. Catani, M. Modugno, A. Simoni, M. Inguscio, and G. Modugno, "^{39}K Bose-Einstein Condensate with Tunable Interactions", Phys. Rev. Lett. **99**, 010403 (2007) (cit. on p. 101).

[230] Y. T. Katan and D. Podolsky, "Modulated Floquet Topological Insulators", Phys. Rev. Lett. **110**, 016802 (2013) (cit. on pp. 102, 112).

[231] A. K. Tuchman and M. A. Kasevich, "Phase-Slip Interferometry for Precision Force Measurements", Phys. Rev. Lett. **103**, 130403 (2009) (cit. on p. 102).

[232] J.-N. Fuchs, L.-K. Lim, and G. Montambaux, "Interband tunneling near the merging transition of Dirac cones", Phys. Rev. A **86**, 063613 (2012) (cit. on p. 103).

[233] L.-K. Lim, J.-N. Fuchs, and G. Montambaux, "Mass and Chirality Inversion of a Dirac Cone Pair in Stückelberg Interferometry", Phys. Rev. Lett. **112**, 155302 (2014) (cit. on p. 103).

[234] A. Alexandradinata, X. Dai, and B. A. Bernevig, "Wilson-loop characterization of inversion-symmetric topological insulators", Phys. Rev. B **89**, 155114 (2014) (cit. on p. 103).

[235] S. Kling, T. Salger, C. Grossert, and M. Weitz, "Atomic Bloch-Zener Oscillations and Stückelberg Interferometry in Optical Lattices", Phys. Rev. Lett. **105**, 215301 (2010) (cit. on pp. 103, 104).

[236] T. Li, "PhD thesis, in preparation", (cit. on p. 103).

[237] T. Li, L. Duca, M. Reitter, F. Grusdt, E. Demler, M. Endres, M. Schleier-Smith, I. Bloch, and U. Schneider, "Experimental reconstruction of Wilson lines in Bloch bands", ArXiv e-prints (2015) (cit. on pp. 108, 109, 112).

[238] M. Endres, "Private communication", (2014) (cit. on p. 109).

[239] N. Goldman, A. Kubasiak, P. Gaspard, and M. Lewenstein, "Ultracold atomic gases in non-Abelian gauge potentials: The case of constant Wilson loop", Phys. Rev. A **79**, 023624 (2009) (cit. on p. 109).

[240] F. Guinea, M. I. Katsnelson, and A. K. Geim, "Energy gaps and a zero-field quantum Hall effect in graphene by strain engineering", Nat Phys **6**, 30–33 (2010) (cit. on p. 112).

[241] J. Struck, M. Weinberg, C. Ölschläger, P. Windpassinger, J. Simonet, K. Sengstock, R. Höppner, P. Hauke, A. Eckardt, M. Lewenstein, and L. Mathey, "Engineering Ising-XY spin-models in a triangular lattice using tunable artificial gauge fields", Nature Physics **9**, 738–743 (2013) (cit. on p. 112).

[242] J. Struck, J. Simonet, and K. Sengstock, "Spin-orbit coupling in periodically driven optical lattices", Phys. Rev. A **90**, 031601 (2014) (cit. on p. 113).

[243] W. Zheng, H. Shen, Z. Wang, and H. Zhai, "Magnetic Order Driven Topological Transition in the Haldane-Hubbard Model", ArXiv e-prints (2015) (cit. on p. 113).

[244] C. Wu and S. Das Sarma, "$p_{x,y}$-orbital counterpart of graphene: Cold atoms in the honeycomb optical lattice", Phys. Rev. B **77**, 235107 (2008) (cit. on p. 113).

[245] C. Wu, "Orbital Ordering and Frustration of p-Band Mott Insulators", Phys. Rev. Lett. **100**, 200406 (2008) (cit. on p. 113).

[246] Y. Tenenbaum Katan and D. Podolsky, "Generation and manipulation of localized modes in Floquet topological insulators", Phys. Rev. B **88**, 224106 (2013) (cit. on p. 113).

[247] M. P. A. Fisher, P. B. Weichman, G. Grinstein, and D. S. Fisher, "Boson localization and the superfluid-insulator transition", Phys. Rev. B **40**, 546–570 (1989) (cit. on p. 121).

[248] D. Jaksch, C. Bruder, J. I. Cirac, C. W. Gardiner, and P. Zoller, "Cold Bosonic Atoms in Optical Lattices", Phys. Rev. Lett. **81**, 3108–3111 (1998) (cit. on p. 121).

[249] W. Krauth and N. Trivedi, "Mott and Superfluid Transitions in a Strongly Interacting Lattice Boson System", EPL (Europhysics Letters) **14**, 627 (1991) (cit. on p. 121).

[250] W. Zwerger, "MottHubbard transition of cold atoms in optical lattices", Journal of Optics B: Quantum and Semiclassical Optics **5**, S9 (2003) (cit. on p. 121).

[251] D. S. Petrov, G. V. Shlyapnikov, and J. T. M. Walraven, "Regimes of Quantum Degeneracy in Trapped 1D Gases", Phys. Rev. Lett. **85**, 3745–3749 (2000) (cit. on p. 122).

[252] J. K. Block and N. Nygaard, "Honeycomb optical lattices with harmonic confinement", Phys. Rev. A **81**, 053421 (2010) (cit. on p. 132).